

**Benchtap Nanocontact Replication via
Unconventional Polycarbonate Molding: from
Fingerprint Phantom, Designed Nanostructure, to
Superhydrophobicity**

by

Clayton William Schultz

B.Sc., Simon Fraser University, 2014

Thesis Submitted in Partial Fulfillment of the
Requirements for the Degree of
Doctor of Philosophy

in the
Department of Chemistry
Faculty of Science

© Clayton William Schultz 2021

SIMON FRASER UNIVERSITY

Summer 2021

Copyright in this work rests with the author. Please ensure that any reproduction or re-use is done in accordance with the relevant national copyright legislation.

Declaration of Committee

Name: Clayton William Schultz

Degree: Doctor of Philosophy

Title: Benchtop Nanocontact Replication via Unconventional Polycarbonate Molding: from Fingerprint Phantom, Designed Nanostructure, to Superhydrophobicity

Committee:

Chair: Paul Li
Professor, Chemistry

Hua-Zhong Yu
Supervisor
Professor, Chemistry

Vance Williams
Committee Member
Professor, Chemistry

Loren Kaake
Committee Member
Associate Professor, Chemistry

Michael Adachi
Examiner
Assistant Professor, Engineering Science

Michael Serpe
External Examiner
Professor, Chemistry
University of Alberta

Abstract

In this thesis, a benchtop protocol for one-to-one replication of micro and nanostructures is described. Polycarbonate (PC) replicas are constructed via unconventional solvent-assisted molding using a polydimethylsiloxane (PDMS) negative to imprint the softened PC. The versatility of this protocol is highlighted by the broad array of applications that have been explored, from the preparation of 3D fingerprint phantoms and replication of designed nanostructures, to the creation of superhydrophobic surfaces. To achieve the best molding performance we characterized how solvent compatibility, time, and physical disruption modulate degree of crystallization and the PC morphology. By making an impression of a fingerprint into solvent-softened PC and casting it with PDMS, a 3D reproduction of the fingerprint (namely, a fingerprint phantom) can be created. Such a phantom contains all three levels of details on human fingerprints. The phantoms are detected by conventional optical and capacitive fingerprint scanners and match well with the original fingerprints. Improved fingerprint scanners and algorithms which enhance security by detecting third level details (such as sweat pores) could be developed using these phantoms as imaging standards. Replicas of structural “masters” with much smaller features than fingerprints can be constructed with this protocol; length scales down to 100 nm can be successfully replicated across large (>10 cm) areas. Confirmed with electron and atomic force microscopy, PC replicas are as effective as masters, enabling the duplication and preservation of expensive lithographically designed masters. Exact reproduction of a nanostructured master is important for lowering the cost of fabricating materials which utilize micro/nanoscale features, such as electronics, optics, sensors, and structural elements. It has been shown that the growth and development of crystalline spherulites are interrupted and limited by the molding operation. Understanding how crystallization can be regulated during solvent assisted molding is essential for developing nanofabrication techniques that utilize other polymers susceptible to crystallization. Controlled PC crystallization was further utilized to fabricate superhydrophobic PDMS. The porous network of spherulites developed is rough on the μm -scale while the spherulites consist of nanoscale tendrils. By casting PDMS from PC the extensive multi-scale roughness is transferred, producing PDMS with an optimized water contact angle of $172\pm 1^\circ$ and a sliding angle less than 1° . The performance of the superhydrophobic PDMS is superior to those constructed with more elaborate laser etching and plasma sputtering techniques.

Keywords: Nanoreplication; Solvent-assisted molding; Benchtop method; Biometric Fingerprint Phantoms; Superhydrophobicity

Dedication

This thesis represents the culmination of my efforts to make the world a better place. This thesis is dedicated to all those who fight for a better, safer, cleaner, and healthier world.

Acknowledgements

First and foremost, thank you to my wife for her continual emotional (and financial) support through this process. When I was stressed out or overwhelmed by my research, she helped to ground me and make things feel normal. The life and experiences she has shared me outside of the scientific arena, helped keep me motivated. Without her, my spirit and drive for research would not have survived. Thank you for the joy and love we have shared over this past decade. I look forward to our future together and all the adventures and experiences we will share.

I would also like to thank my family for their support during my PhD. They understood how important this work is to me and supported me any way they could. Beyond the support, throughout my life they encouraged me to think and to try and understand the world around me, fostering the scientist within me.

Without the opportunity and push given to me by my senior supervisor Dr. Hogan Yu I would not have even started this degree. At a time when I was without direction, he gave me a path to follow, which has led me to here and now. Throughout my degree, he has been patient and honest with me, which has helped me to develop my research and writing skills. Beyond the research itself, he has provided me opportunities to build my other professional and leadership skills. It is very obvious he truly cares for his students; I aspire to one day lead a group like he does and have the kind of impact on others he has had on me.

Within Yu group I met several mentors and lifelong friends who had an immensely positive impact on my life. Jessica Wong mentored me in many aspects of research, she was patient and always willing to help others succeed. Some of the foundational ideas in this project were devised with her help and support. Samuel Weng supported me when I first began research, his infectious happy attitude made research and being in the lab fun. Lishen Zhang became a student around the same time as myself, where our researches aligned we developed a strong collaborative spirit. As a colleague, ally, and sometimes rival he pushed me to be at my best.

I would also like to thank the members of my supervisory committee for their advice and direction during committee meetings. The perspective and knowledge they brought to committee meetings helped to expand my research and challenge what I thought I knew.

I always left meetings with a sense of hope and new ideas to take my research further. Beyond that, they were always happy to help or discuss concepts with me at my request.

Table of Contents

Declaration of Committee	ii
Abstract	iii
Dedication	v
Acknowledgements	vi
Table of Contents	viii
List of Tables	x
List of Figures	xi
List of Acronyms	xvii
Chapter 1. General Introduction	1
1.1. Fingerprint Biometrics	1
1.1.1. The Structure of Fingerprints	1
1.1.2. Fingerprint Classification and Matching	2
1.1.3. Classes of Fingerprint Sensors	6
1.2. Fabrication of Nanostructures	9
1.2.1. Conventional Nanofabrication Methods	9
1.2.2. Nanostructure Replication Methods	12
1.3. Superhydrophobic Materials	16
1.3.1. Interfacial Energy and Surface Wetting	16
1.3.2. The Wenzel and Cassie-Baxter Wetting States	19
1.3.3. Fabricating Polymeric Superhydrophobic Surfaces	22
1.4. Polymeric Materials for Nanofabrication	24
1.4.1. Polycarbonate	25
1.4.2. Polydimethylsiloxane	28
1.4.3. Thermodynamics of Polycarbonate Crystallization	31
1.4.4. Solvent-Induced Crystallization (SINC) of Polycarbonate	39
1.5. Research Objective and Thesis Structure	45
Chapter 2. Techniques and Methods	46
2.1. Scanning Electron Microscopy	46
2.2. Atomic Force Microscopy	51
2.3. Contact Angle Goniometry	56
Chapter 3. Fabrication of 3D fingerprint phantoms via unconventional polycarbonate molding	58
3.1. Introduction	59
3.2. From 3D PC Mold to PDMS Fingerprint Phantom	61
3.3. Microscopic imaging of the mold and phantom	64
3.4. Optimization of phantom fabrication	69
3.5. Conclusion	70
3.6. Experimental	70
3.7. Supporting Information	71

Chapter 4. Three-Dimensional Conductive Fingerprint Phantoms Made of Ethylene-Vinyl Acetate / Graphene Nanocomposite for Evaluating Smartphone Scanners.....	73
4.1. Introduction.....	74
4.2. Fabrication and characterization of 3D fingerprint phantoms made of EVA-G.....	77
4.3. Phantom Testing with Standalone Capacitive Scanner and Smartphones.....	83
4.4. Conclusions.....	88
4.5. Experimental Section.....	88
4.6. Supporting Information	90
Chapter 5. Benchtop one-to-one replication across length scales from 100 nm to 10 cm via ambient polycarbonate molding.....	95
5.1. Introduction.....	96
5.2. Nanocontact replication using PC at the Micro- and Nanoscale.....	98
5.3. Optimization of Replication Parameters.....	102
5.4. Distinction from Conventional Single-step Molding and Application Potential ...	107
5.5. Conclusion.....	112
5.6. Experimental	112
5.7. Supporting Information	114
Chapter 6. Superhydrophobic Polydimethylsiloxane via Nanocontact Molding of Solvent Crystallized Polycarbonate: Optimized Fabrication, Mechanistic Investigation, and Application Potential.....	120
6.1. Introduction.....	121
6.2. Optimized fabrication of superhydrophobic PDMS via nanocontact molding of solvent treated PC.....	122
6.3. Structural characterization and Mechanistic Insights	126
6.4. Comparison with state-of-the-arts and application potentials	135
6.5. Conclusion.....	137
6.6. Experimental	138
6.7. Supporting Information	139
Chapter 7. Concluding Remarks and Future Directions.....	146
7.1. Concluding Remarks	146
7.2. Future Directions	147
7.2.1. Development of Universal Phantoms.....	147
7.2.2. Extended Nanoreplication Applications.....	148
7.2.3. Improved and Applied Superhydrophobic Surfaces	151
References.....	157

List of Tables

Table 4-1: Imaging of fingerprint phantoms with several smartphone capacitive scanners	86
Table 5-1: Feature dimensions of the DVD-ROM master, PDMS template, and PC replica fabricated by benchtop one-to-one nanocontact replication.	99
Table 5-2: Resolutions of traditional nanoreplication methods on popular engineering plastics.....	108
Table 6-1: Comparison of the state-of-the-art methods of preparing superhydrophobic PDMS. Wetting properties (contact angle and sliding angle) and calculated f value of superhydrophobic PDMS substrates fabricated via different methods.	135

List of Figures

Figure 1-1: Structure of friction ridges: cross section of finger tissue.	2
Figure 1-2: The three classes of fingerprints (A) whorl, (B) loop, and (C) arch.....	2
Figure 1-3: Process of fingerprint feature extraction: (A) Fingerprint Image, (B) Binarized fingerprint image, (C) Binarized image with fingerprint minutiae identified in red.....	3
Figure 1-4: Hypothetical matching score distribution; Red: imposter attempts, Green: genuine attempts.....	5
Figure 1-5: Working principle of an optical fingerprint sensor.	7
Figure 1-6: Working principle of a capacitive fingerprint sensor.....	8
Figure 1-7: Working principle of a thermal fingerprint sensor.....	8
Figure 1-8: Working principle of ultrasound fingerprint sensor.	9
Figure 1-9: Schematic of EBL. (A) Substrate with resist material spin coated onto the surface. (B) Electron beam exposure. (C) Substrate after development.	10
Figure 1-10: Schematic of Photolithography. (A) with a negative resist, (B) with a positive resist.	11
Figure 1-11: Schematic view of Nanoreplication. (A) Lithographically designed master. (B) Casting of PDMS from master. (C) PDMS “replica”. (D) Molding of prepolymer/precursor film on substrate. (E) prepolymer/precursor curing. (F) 1:1 replica of master.	14
Figure 1-12: Solvent Assisted Molding Schematic. (A) Application of solvent and stamp to polymer film. (B) Solvent-assisted molding of polymer film. (C) Resulting patterned polymer surface.	16
Figure 1-13: Intramolecular forces at surface of matter.	16
Figure 1-14: Diagram of a droplet on a surface showing the three interfacial energies and contact angle of the droplet.	18
Figure 1-15: Images of hydrophobicity in nature. (A) Lotus leaf, (B) Dragonfly.	18
Figure 1-16: Different states of water droplet on surfaces. (A) Water droplet on a smooth surface. (B) Water droplet on a rough surface in the Wenzel state. (C) Water droplet on a rough surface in the Cassie-Baxter state.....	20
Figure 1-17: Schematic view of Droplet on a surface with hierarchical roughness. Left inset shows magnified a section of features under the droplet.....	21
Figure 1-18: Schematic plot of the energy barrier between the Cassie-Baxter and Wenzel states. ⁴⁰	22
Figure 1-19: Synthesis of polycarbonate from phosgene and salt of bisphenol A	25
Figure 1-20: Unit cell diagram for polycarbonate based on bis-phenol A	27
Figure 1-21: Scheme of cross-linking reaction for silicone network formation	29
Figure 1-22: Schematic diagram of amorphous and crystalline polymer chains	32
Figure 1-23: Typical DSC curve for a polymer: T _g -glass transition, T _c -crystallization temperature, T _m -Melting temperature and the decomposition of the polymer. ⁹³	33
Figure 1-24: Gibbs free energy of formation of a nucleus as a function of its size. ⁹⁰	34

Figure 1-25: Schematic of a polymer lamella.....	35
Figure 1-26: A series of AFM phase images obtained on a BA-C8 film at room temperature. (A) An embryo; (B) a short lamella (founding lamella) developed from the embryo shown in a (C–F). The growth of the founding lamella; (G–P) branching and splaying apart of the subsidiary lamellae. ⁹⁰	36
Figure 1-27: AFM phase images of poly(ϵ -caprolactone) hedrite growing at 56 °C; the images in (b), (c) and (d) correspond to elapsed times of 244, 290, and 551 min, respectively, with respect to the image in (a). ⁹⁸	37
Figure 1-28: SEM image of a complete spherulite formed in solvent treated PC.	37
Figure 1-29: AFM phase image obtained on a BA-C12 film. Three induced nuclei are observed at about 15 nm away from the parent lamella. ⁹⁰	38
Figure 2-1: Thermionic electron gun containing a tungsten filament (F), Wehnelt electrode (W), ceramic high-voltage insulator (C) and an o-ring seal (O) to the lower part of the TEM column An autobias resistor (R_b) (actually located inside the high-voltage generator) is used to generate a potential difference between (W) and (F), thereby controlling the electron-emission current. Arrows denote the direction of electron flow that gives rise to the emission current.....	47
Figure 2-2: Schematic diagram of a scanning electron microscope. The same x- and y-scan waveforms are applied to the SEM column and to the display device. Signal from a detector modulates the brightness of the display. .	49
Figure 2-3: Schematic dependence of the interaction volume and penetration depth, as a function of the kinetic energy E_0 and atomic number Z of the primary electrons.	49
Figure 2-4: Qualitative behavior of the force between tip and sample as function of tip-sample distance.	52
Figure 2-5: Schematic drawing of a typical AFM setup.	52
Figure 2-6: Comparison sketch of line profiles measured with a high aspect ratio probe tip (A) and a wide probe tip (B). The profiles of the trench recorded by each tip are shown in red.....	54
Figure 2-7: ScanAsyst-Air tip geometry, A) SEM image of ScanAsyst-Air tip B) side view C) front view.....	54
Figure 2-8: TEM image of AFM tip (a) before and (b) after the wear test with 10 nN normal force for 10 mm sliding distance of Si (100) specimen.....	55
Figure 2-9: Sketch of a goniometer setup. A basic goniometer consists of a light source, an adjustable sample stage, a dispensing system (e.g. motorized syringe connected to a needle by tubing), a camera to record video, and a computer for data analysis.	56
Figure 2-10: Schematic of sliding angle (A) and contact angle hysteresis (B) measurements.	57
Figure 3-1: Fabrication of 3D fingerprint phantoms via solvent-assisted polycarbonate (PC) molding. (A) Finger to be impressed on PC. (B) Fingerprint impression molded on a PC plate serving as the 3D template (mold). (C) PDMS fingerprint phantom casted from the PC mold. The bottom insets show how fingerprint features were “copied” to PC and subsequently	

replicated to a PDMS phantom (color code: pink-finger, dark blue-PC mold, and beige-PDMS phantom).	61
Figure 3-2: Matching of 3D PDMS phantoms with original fingerprints. (A) Fingerprint with a loop core. (B) Fingerprint with a whorl core. (C) Fingerprint with a tented arch core. Top row of each section: optical images of actual finger (left) and corresponding phantom (right) output from the same fingerprint scanner. Bottom row: binarized representation of fingerprint pattern with results of minutiae identification and matching algorithm overlaid. Similarity scores between original and phantom are displayed on the binarized phantom images (top left corner).	62
Figure 3-3: Optical imaging of the PC fingerprint mold (left) and PDMS phantom (right). (A)/(A') shows the entire fingerprint, which represents the first level details; (B)/(B') a magnified section showing the fingerprint core; (C)/(C') selected second level details such as islands (I), incipient (under developed) ridges (II), delta (III), and bifurcation (IV); (D)/(D') a high magnification image showing the third level details, i.e., sweat pores along a fingerprint ridge (as highlighted).	64
Figure 3-4: Profilometry imaging of PC fingerprint mold and PDMS phantom. Profiled 3D images of (A) PC mold, (B) PDMS phantom, and their respective cross section along the red line.	65
Figure 3-5: Scanning electron microscopy (SEM) imaging of PC fingerprint mold (left) and matching PDMS fingerprint phantom (right). (A)/(A') Low magnification images of ridges; (B)/(B') images of a single ridge surface; (C)/(C') images of spherulites in PC mold and their impressions in the PDMS phantom; (D)/(D') high magnification images of an individual spherulite and its impression. The insets in (A)/(A') display water drops on the respective surfaces and corresponding contact angles.	68
Figure 4-1: Fabrication of EVA-G fingerprint phantom from a real finger via thermal molding. (A) Schematic view of the thermal molding process (grey: PC, black: EVA-G). (B) PC with molded impression of fingerprint on the surface. (C) EVA-G phantom cast from the PC mold.	77
Figure 4-2: (A) Optical image of the source fingerprint on a fingertip; (B) magnified optical image of fingerprint ridges at the fingertip core; (C) optical image of the fingerprint phantom corresponding to the fingerprint shown in (B); (D) Magnified optical image of several ridges on the phantom; (E) SEM image of fingerprint ridges on the phantom; (F) magnified SEM image of the highlighted region in E. Various pairs of matching minutiae (second-level details) are highlighted in B and C with red circles, such as the core (I), a delta (II), an island (III), and a ridge bifurcation (IV). Third-level details (sweat pores) are circled in blue in D and F.	79
Figure 4-3: Profilometry images of (A) PC mold with the impression of a fingerprint and (B) the corresponding EVA-G phantom. The bottom insets show cross-section profile along the red line in the associated image.	80
Figure 4-4: Impedance spectroscopy of thermally molded EVA-G nanocomposites (30 wt %). (A) Representative Nyquist plot. The top-right inset displays the current as a function of applied DC voltage. (B) Electrical conductivity (σ) and complex permittivity (ϵ^*) of as a function of the frequency (f) for the impedance measurements.	82

- Figure 4-5: Fingerprint matching between the original fingerprint and the EVA-G phantom with a capacitive scanner. (A) Image of a real fingerprint captured with a capacitive scanner used to make the PC mold. (A') Image of the EVA-G fingerprint phantom cast from the PC mold. (B) Binarized depiction of the original fingerprint with location of minutiae indicated by tailed circles. (B') Binarized depiction of the image of the EVA-G phantom, the circles connected with a red line are minutiae for matching. (C) Magnified image of the highlighted area in (A); (C') Magnified image of the corresponding area in the EVA-G phantom. 83
- Figure 4-6: Operation of smartphones with an EVA-G fingerprint phantom. (A) EVA-G phantom taped to a finger and imaged with the smartphone fingerprint scanner. (B) Examples of enrolled fingerprint profiles, partial fingerprints captured by the scanner during the initial enrollment; triangles indicate minutiae locations. Minutiae in the prospective and enrolled fingerprints are compared for a match. Green triangles in the enrolled profiles indicate matching minutiae, red indicate no-match. An accepted match is indicated by a green checkmark. (C) Smartphone unlocked after matching the phantom with an enrolled fingerprint profile. 86
- Figure 5-1: Benchtop one-to-one nanocontact replication of a DVD-ROM master to create an identical PC replica. Schematic illustration of the preparation of a PDMS template and the subsequent solvent-assisted molding to create a PC replica of the original DVD master; AFM images of (A) the original DVD-ROM as the master, (B) the PDMS template cast from the DVD-ROM, (C) the PC replica. 98
- Figure 5-2: SEM imaging of microscale pit arrays prepared via benchtop nanocontact replication. (A) Silicon/SU8 master, (B) PDMS template cast from the master, (A') PC replica of the master, (B') Second generation PDMS template cast from the PC replica. All images are tilted at 30° to measure the feature height/depth. 100
- Figure 5-3: Nanocontact replication of nanohole arrays. Atomic force microscopy (AFM) images of a nanohole array fabricated on a thin PMMA film on a silicon substrate (A), the PDMS template cast from the “master” (B), and the PC replica molded from the PDMS template (C). Inset below each image is the profile of the respective surface along the red line. Inset in each image is a zoom-in of a single nanoscale feature. 101
- Figure 5-4: Crystallization of acetone-treated PC plates confined by nanocontact molding. (A) PC treated with acetone for the indicated period of time. (B) PC molded with a PDMS template (cast from a BD-R disc) right after the solvent treatment for the same period of time as in (A). Simple schematics of the treatment applied to the PC surface are displayed as the top insets. (C) High-magnification images of the molded PC plates shown in (B). 104
- Figure 5-5: (A) Volume of acetone absorbed by the PC plate (solid circles) and PDMS template (open circles) during nanocontact replication as a function of acetone treatment time before molding. (B) Profiles of PC molded with the back of a boxcutter (Exacto blade) after acetone treatment. PC was treated for 10 to 40 s as color coded in the corresponding curves; the arrow indicates the direction of increased treatment time. 106

- Figure 5-6: Fabrication of PDMS microchannel plates from the PC replica of a silicon/SU8 master. (A) Lithographically prepared silicon/SU-8 master with 14 rectangular relieves (0.5 mm wide and 50 μm high); (B) PDMS template cast from the master, adorned with microfluidic channels; (C) PC replica of the master molded with the PDMS template; (D) Second-generation PDMS microchannel plate cast from the PC replica. Inlet holes were punched into the PDMS plate, which was adhered to a glass substrate; embedded microchannels were filled with a dye solution to test their efficacy. 109
- Figure 5-7: Nanocontact replication of a security label with subwavelength diffractive structures. (A) Nickel master for making security labels provided by Nanotech Nanosecurity Corp.; (B) PDMS template cast from the nickel master; (C) PC replica molded from the PDMS template; (D) Second-generation PDMS template cast from the PC replica; (E) Second-generation PC replica molded from the second-generation PDMS template. In all cases, optical images are shown on the left, while the corresponding AFM image showing the microscopic morphology is shown on the right. The bottom-right Inset in each optical image is a magnified section (letter G). 110
- Figure 6-1: Fabrication of superhydrophobic PDMS via nanocontact molding of solvent-treated PC. (A) PC plate (2.5 \times 2.5 cm²) before acetone treatment. (B) PC plate after acetone treatment. (C) PDMS molded from the acetone-treated PC template. The bottom right inset of each image shows a water droplet on the surface and the measured contact angle. The right side inset is a schematic representation of the fabrication process (gray: PC, red: acetone, dark grey: PDMS). 123
- Figure 6-2: Optimization of the preparation protocol for superhydrophobic PDMS. PC treatment and PDMS casting conditions are listed in the left inset table. Solvent: solvent used to treat PC; Time: how long solvent is applied; Quenching: non solvent used to stop the treatment; Diluent: solvent used to dilute PDMS; PDMS/h-PDMS: ratio of PDMS to h-PDMS (wt %). The solid black line indicates a contact angle of 150 $^\circ$ (superhydrophobic) and the dashed line denotes a contact angle of 170 $^\circ$ 124
- Figure 6-3: Contact angle (A) and optical transmittance at 500 nm (B) through PC (black) and PDMS (red) as a function of solvent treatment time. The inset photos in (A) show water droplets on the molded PDMS surfaces prepared from 60 and 80 s treatment of PC with acetone. The top right inset in (B) shows the optical transmittance of unmodified PC and PDMS across the visible spectrum, respectively. 126
- Figure 6-4: SEM images of acetone treated PC plates and PDMS casts. (A) PC was treated with acetone for up to 120 s, then the acetone film was blown off with compressed air or left to evaporate. These PC plates (left) were used as templates for molding the corresponding PDMS (right). Acetone treatment conditions for each row are shown on the PC image. Areas of interest are highlighted with red circles. (B) Schematic view of amorphous PC (left) and of a semi-crystalline PC spherulite (right). 128
- Figure 6-5: 3D Profilometry images of PDMS molded from PC templates treated with acetone for 60 s (A), 75s (B), and 80 s (C), respectively. The vertical relief

is represented on a color scale bar from blue to red. Cross-section profiles are shown as insets below each image.....	130
Figure 6-6: Histograms of roughness features on PDMS molded from PC templates treated with acetone for 60 s (A), 75s (B), and 80 s (C), respectively. ..	132
Figure 6-7: SEM images of a PC spherulite (A) and the impressions molded with neat PDMS (B), h-PDMS (C), 75/25 (w/w) PDMS/h-PDMS (D), PDMS diluted with 20% (w/w) hexane (E), and PDMS diluted with 20% (w/w) toluene (F), respectively.....	133
Figure 6-8: Superhydrophobic PDMS (2.5×2.5 cm ²) patterned by UV/Ozone treatment. (A) Array of hydrophilic spots, (B) Array of hydrophilic spots connected by channels. Diluted color ink solutions were used for better visualization.	136
Figure 7-1: (a) Ice on a superhydrophobic anti-icing surface. The asperities with tips indented into the ice (indicated by arrows) are very likely to be damaged during icing (water solidification) and/or deicing (ice removal). (b) Ice on the same surface sitting lower on the asperities during the next icing events. The ice-solid contact area increases from (a) to (b).	154

List of Acronyms

ΔG	Gibbs Free Energy
ΔH	Enthalpy
ΔS	Entropy
AAO	Anodized Aluminum Oxide
ABS	Acrylonitrile butadiene styrene
AFM	Atomic Force Microscopy
AKD	Alkylketene Dimer
CAH	Contact Angle Hysteresis
CNT	Carbon Nanotubes
CT	Computed Tomography
CVD	Chemical Vapor Deposition
DAK	Dialkylketone
DCM	Dichloromethane
EBL	Electron-beam Lithography
EVA	Ethylene-vinyl acetate
EVA-G	Ethylene-vinyl acetate embedded with graphene nanoplatelets
FAR	False Acceptance Rate
FIB	Focused Ion-beam Lithography
FP	Fingerprint
FRR	False Rejection Rate
FT-IR	Fourier-Transform Infrared Spectroscopy
GNP	Graphene nanoplatelets
HAI	Hospital acquired infections
h-PDMS	Hard-polydimethylsiloxane
HSQ	Hydrogen Silsesquioxane
H_v	Heat of vaporization
IAFIS	Integrated Automated Fingerprint Identification System
k_B	Boltzmann constant
LLDPE/EBA	Linear low-density polyethylene/ethylene butyl acrylate
MRI	Magnetic Resonance Imaging
PC	Polycarbonate
PDMS	Polydimethylsiloxane

PE	Polyethylene
PFPE	Perfluoropolyether
PMMA	Polymethylmethacrylate
PP	Polypropylene
PS	Polystyrene
PSI	Pounds per square inch
PTFE	Polytetrafluoroethylene
PU	Polyurethane
PVC	Poly(vinyl-chloride)
Ra	Arithmetic average roughness
Rpm	Average maximum peak height
RPM	Rotations per Minute
Rvm	Average maximum valley depth
SA	Sliding Angle
SEM	Scanning Electron Microscopy
SINC	Solvent-induced Crystallization
SLIPS	Slippery liquid-infused porous surfaces
T_g	Glass transition temperature
T_m	Melting temperature
V_m	Molar volume
X	Material specific interaction parameter
XRD	X-ray diffraction
Z	Complex Impedance
Z'	Real Impedance
Z''	Imaginary Impedance
γ_{lv}	Liquid-vapor interface
γ_{sl}	Solid-liquid interface
γ_{sv}	Solid-vapor interface
δ	Hildebrand Solubility Parameter
σ	Conductivity
ϵ	Complex Permittivity
ϵ'	Real Permittivity
ϵ''	Imaginary Permittivity

Chapter 1.

General Introduction

This chapter provides the background knowledge and literature reviews that are essential to appreciate the research topics (projects) described in this thesis. Fundamentals of fingerprint biometrics and fingerprint scanners are described first, followed by the introduction of conventional nanofabrication techniques and advanced soft-lithography methods. The principles behind superhydrophobicity are then presented along with a summary of common fabrication materials and methods. Next, the two polymeric materials (polycarbonate and PDMS) that are key to this thesis research and their properties are briefly introduced. This chapter is concluded with a short statement of the research objective and an outline of the thesis structure.

1.1. Fingerprint Biometrics

1.1.1. The Structure of Fingerprints

Friction ridges are located on the skin that covers our palms and fingers along with the soles of our feet and toes. The skin here is hairless and covered in raised ridges, the epidermis is thicker and lacks sebaceous glands (exocrine glands that secrete oils).^{1,2} The presence of these ridges aids sensory abilities and is thought to improve friction when grasping, though their purpose is still not fully understood.³ Ridges are three-dimensional structures with irregular and varied dimensions, ridges may have pores along them and are separated by narrow furrows or valleys.¹ The morphology of ridges varies throughout the body, but are most defined and complex on the tips of our fingers and toes.^{1,2}

Skin throughout the body has three layers: the epidermis (outermost layer), dermis (middle layer), and hypodermis (inner layer).¹ The hypodermis made of connective tissues and fat provides insulation and padding, it is thicker beneath friction ridges.¹ The dermis is made of connective tissue. Its function is to provide structural reinforcement to skin. In the finger ridges the dermis houses nerves, blood vessels, and sweat glands.^{1,2} Structures in the dermis known as papillae connect the dermis to the epidermis, in most of our skin they are small and sparse.¹ Where friction ridges form, they are larger and densely

arranged into pairs of snaking parallel lines, producing friction ridges. The arrangement between the papillae of the dermis and epidermis is illustrated in the cross section shown in Figure 1-1. Epidermis, the top layer of skin, constitutes the protective boundary between our bodies and the outside world. As shown in Figure 1-1, it is comprised of a basal layer of cells (germinative cells) which continually create a column of new cells, these cells (keratinized cells) harden, flatten, and die to create a durable outer layer of skin.¹

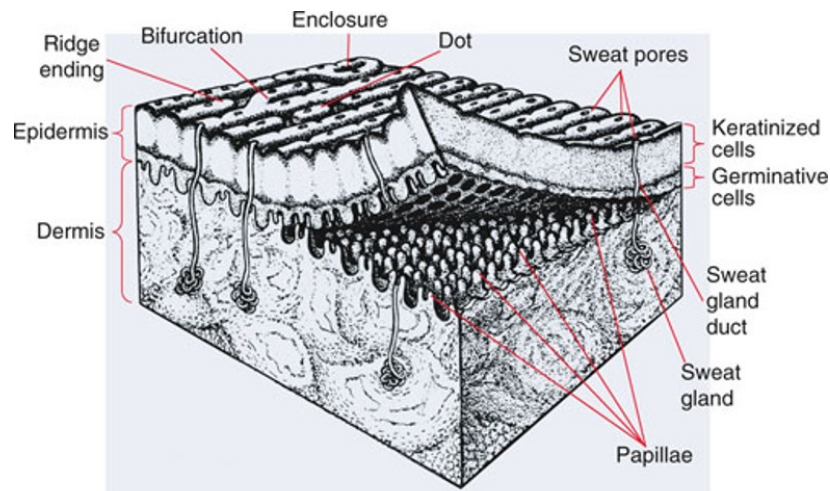


Figure 1-1: Structure of friction ridges: cross section of finger tissue.
 Reprinted with permission from Ref. 1. Copyright (2009), Springer.

1.1.2. Fingerprint Classification and Matching

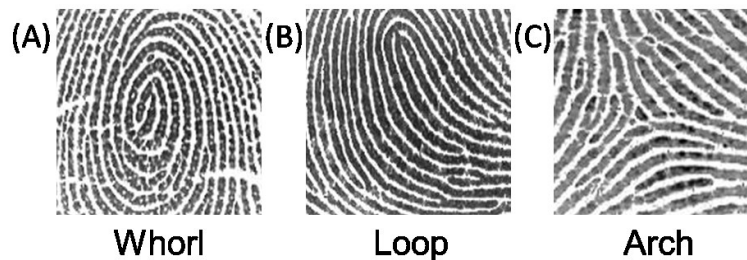


Figure 1-2: The three classes of fingerprints (A) whorl, (B) loop, and (C) arch.

The friction ridges on fingertips are arranged in a complex pattern of adjacent ridges. These arrangements are centered around a “core”, a point ridges seem to emanate from which can belong to one of several classes; 1) whorls (Figure 1-2A) that spiral outward from a central point at or near the middle of the fingertip; 2) loops (Figure 1-2B) that begin on one side of the fingertip moving up into the center of the finger and returning

back to the side it originated from; 3) arches (Figure 1-2C) that start at one edge of the finger slope upward toward the middle of the fingertip, then back down.

Matching between fingerprints can be conducted by a variety of methods that all work by identifying the position of ridges and comparing their locations between prints; today this is done with algorithms.^{4,5} Fingerprint matching algorithms have two distinct stages, the first being feature extraction is illustrated in Figure 1-3. First, any fingerprint image (latent, fingerprint cards, fingerprint scanner) is uploaded; an image of my left index finger is shown in Figure 1-3A. The software performs filtering on the image to improve contrast then identifies the ridges from the background, the image is then binarized (pixels are converted to either 1 or 0, representing black and white respectively) with ridges in black on a white background (Figure 1-3B).^{4,6} With the image binarized, the algorithm can identify minutiae, the relative location and direction of minutiae (where ridges differentiate and where ridges cross) are recorded and labelled in red (Figure 1-3C). The fingerprint, or more aptly the locations of its minutiae is now ready for matching.

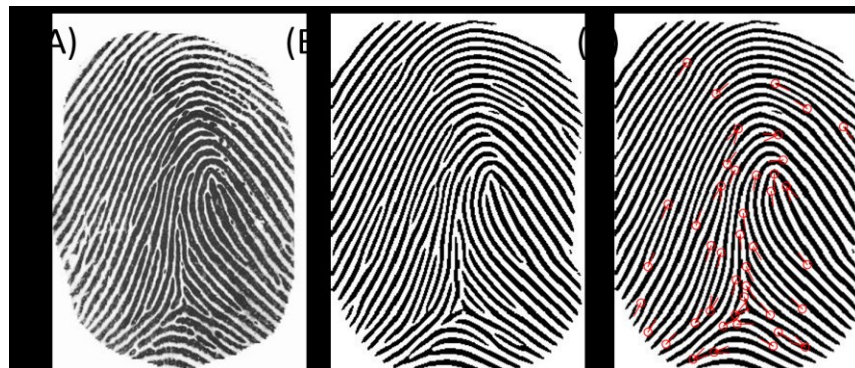


Figure 1-3: Process of fingerprint feature extraction: (A) Fingerprint Image, (B) Binarized fingerprint image, (C) Binarized image with fingerprint minutiae identified in red.

Fingerprint matching algorithms employ a variety of methods to compare the similarity of fingerprints. It is insufficient to simply overlay two fingerprint images for comparison; even the same fingerprint will produce a different image if the parameters of fingerprint sampling are not identical. This so-called intraclass variation can result from differences in finger pressure, finger placement, rotation, imaged area, skin dryness, and the fingerprint capture method (latent or scanned), along with the inherent malleability of tissue.⁶ Therefore images must be compared based on how similar they are, and a threshold (an arbitrary value) must be set for distinguishing a match from a mismatch.

The most common and most familiar method to compare fingerprints is minutiae matching. To perform minutiae matching the ridges in the binarized image are thinned by the software until they are all 1 pixel wide, creating a “skeleton” of the ridges.^{6,7} Minutiae points are extracted by analyzing 3 x 3 pixel windows along each pixel of a ridge. If a ridge pixel has only 1 black adjacent pixel it is a ridge ending, if a ridge has 2 adjacent pixels it is a normal fingerprint ridge, and if a ridge has 3 adjacent pixels it is a bifurcation (where ridges split).⁷ With these broad categories most minutiae can be identified by software for subsequent matching.

With minutiae located, the algorithm compares and matches minutiae in the fingerprints being compared. The software finds the most similar minutiae pair and uses them to align the fingerprints being compared.^{6,7} Next the algorithm determines correspondence, minutiae that are located close enough between the two images are deemed to be matching while minutiae without an analog in the other image are not.⁶ Based on the number of matching pairs and how closely they match, a similarity score is output. If the similarity score is above a threshold value, the fingerprints are considered a match.

Other techniques for matching fingerprints have also been explored. Fingerprint ridges hold additional information in the position of ridges which are not part of minutiae and the details of ridges themselves (third level details). Sometimes minutiae are difficult to resolve, especially in poor quality fingerprints, or in the case of small partial prints there may not be enough minutiae for a strong comparison. In an effort to incorporate information from all ridges, algorithms have been developed that separate the fingerprint image into many smaller regions which are filtered and tessellated with respect to the core and then directly compared with other prints.⁸ In essence, each section is locally filtered improving contrast.⁸ By delocalizing and enhancing smaller sections the algorithm can better deal with the natural distortions in fingerprint images and make direct comparison between ridges.⁸

More sophisticated algorithms that analyze even more fingerprint data have been devised. A system for detecting and matching third level details in fingerprints was developed by A. K. Jain et.al.⁹ Gabor filters are applied to facilitate identification and isolation of elements with different frequency and spatial direction. This filtering algorithm is capable of differentiating pores along ridges. Because a single ridge can contain many

pores, they contribute to the uniqueness of fingerprint signature, this information can be collected from a given fingerprint.⁹ Moreover, pore matching, when used in conjunction with minutiae-based matching, contributed to significant improvement in the accuracy of fingerprint matching.⁹ This significant matching accuracy improvement is primarily observed when cross-referencing small and partial fingerprints.⁹

The boundaries of fingerprint matching are being pushed in an effort to make fingerprint biometrics more secure while maintaining its ease of use. When algorithms compare fingerprints a finite amount of information is collected, and a similarity score is calculated. This value must be above a predefined value for a match. This creates two possible sources of error, either a false rejection or a false match that are intrinsically and inexorably linked. The similarity scores of genuine and imposter fingerprints will vary due to image quality, fingerprint condition, and the number of matching minutiae, see Figure 1-4.¹⁰ If the matching threshold (the required score) is increased the false acceptance rate (FAR) will be reduced because less imposter attempts have a sufficient score, however, as the matching threshold increases the false rejection rate (FRR) increases because more genuine fingerprints will have insufficient scores. Neither is desirable, however, we tend to favor a low FAR for forensic applications and a low FRR for rapid identification (borders, security systems).^{9,10} This problem worsens when cross-referencing fingerprints in large databases, as the number of enrolled fingerprints for an counterfeit to compare with increases the odds of it finding a strong enough match increases the FAR.^{11,12} The only way to simultaneously lower both FAR and FRR is to acquire more information for comparison through a combination of better fingerprint matching algorithms, which consider all levels of fingerprint detail, and better fingerprint imaging technologies to clearly recognize the aforementioned detail.

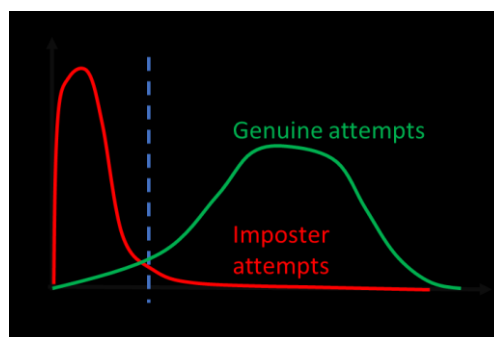


Figure 1-4: Hypothetical matching score distribution; Red: imposter attempts, Green: genuine attempts.

1.1.3. Classes of Fingerprint Sensors

Images used for fingerprint matching purposes are acquired through two general methods. Fingerprint images can be acquired by enhancing the pattern of fingerprint oil left when a finger contacts a surface, these are called latent prints and are primarily collected at crime scenes for law enforcement purposes. The other kind of fingerprints are intentional images for cataloging or biometric applications. The most familiar form of fingerprinting is fingerprint inking, where ridges are coated with a thin layer of ink which is transferred to a specially designed paper form under supervision. These physical prints were traditionally kept on file in large databases for manual comparison.⁵ Manually searching for a match in such databases was incredibly slow and labor-intensive; digitization of fingerprint databases not only reduce the storage spaces but also enables automated fingerprint matching.⁵ The adoption of data digitization has increased both the accuracy and the speed of fingerprint matching. The biggest database in the world, the Integrated Automated Fingerprint Identification system (IAFIS), came online in 1999.^{4,5} It contains fingerprint records of nearly 150 million individuals.^{4,5}

Devices to quickly and accurately image fingerprints have been in development for decades, development has accelerated with their inclusion into phones, beginning with the iPhone in 2013.¹³⁻¹⁵ Fingerprint sensors are based on a variety of imaging techniques that perform the same function; differentiating fingerprint ridges from furrows with high fidelity under varied conditions.

Optical Sensors

The most conceptually simple are optical sensors that simply take an image of light reflected by a fingerprint. Light is emitted toward the fingerprint through optical elements (often a prism or array of prisms) and a camera acquires the reflected signal (light) from the fingerprint.^{13,14} The ridges of the fingerprint absorb light while the furrows between ridges do not, light instead reflects off the prism air interface, creating excellent contrast between ridges and furrows.¹⁴ This working principles is illustrated in Figure 1-5; reflected light is shown as solid lines and the hypothetical path of absorbed light is shown as dashed lines. Variations of this principle exist such as using an array of smaller prisms to make up the imaging surface, this reduces the prism and device size but reduces overall

resolution.^{14,16} An array of fiber optics can also be used in place of the prism, the working principle remains the same.

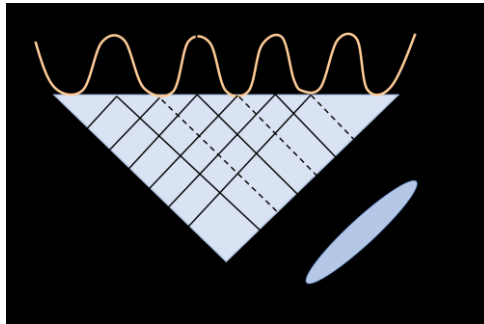


Figure 1-5: Working principle of an optical fingerprint sensor.

Capacitive Sensors

Solid state sensors measure the physical properties of finger ridges and convert them to a digitized pattern of ridges and valleys, such systems were proposed in the 1980s and realized in the 1990s.^{13,14} Capacitance based solid state fingerprint sensors construct fingerprint images with a 2D array of micro capacitor plates. A schematic of a capacitive scanner is shown in Figure 1-6. The array consists of capacitor plate pairs that have a baseline capacitance maintained by internal circuitry. When a finger is applied, the finger tissue acts as a third capacitive “plate” in the system, separated by the insulating layer atop the sensor. The finger interacts with the electric field between the plates and small electrical charges build up at the surface of the finger when it is pressed against the sensor.¹⁴ The capacitance (C) is determined by;¹⁴

$$C = k \epsilon_0 (A/d) \quad (1)$$

where k is the relative permittivity or dielectric constant, ϵ_0 is the vacuum permittivity, A is the surface area of the capacitor, and d is the distance between the electrodes (finger and microplates) of the capacitor.¹⁴ Under ridges the finger tissue is closer to the plates (smaller d) resulting in a stronger interaction than in the valleys. Parasitic capacitance with the finger decreases the baseline capacitance and subsequently leads to change in the output voltage of the corresponding capacitive plate cell. The change in output voltage is converted into the intensity value of a pixel in the resultant fingerprint image.¹³ Capacitance based fingerprint scanners can be made smaller and thinner than optical based scanners. The small form factor of capacitance-based fingerprint scanners made

them highly desirable to the smartphone industry, as the new phones are becoming thinner and lighter. As a result, it has become ubiquitous in smartphones. It is, however, more expensive, compared to optical sensors to fabricate large area sensors (i.e. full handprint sensors). Another drawback of the capacitive scanner is that too much or too little moisture at the fingertips will lead to inaccurate recording of the fingerprint. For instance, wet fingers will output inaccurate images while dry fingers can produce low contrast images.

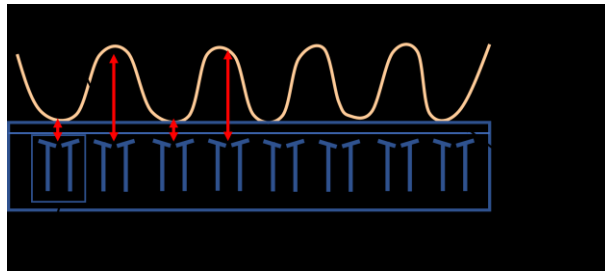


Figure 1-6: Working principle of a capacitive fingerprint sensor.

Thermal Sensors

Another class of solid-state sensors are thermal based fingerprint sensors that are made from a silicon base with pixels of pyroelectric materials.¹⁴ This sensor functions by monitoring the change in the rate of heat transfer at each pixel. The sensor's surface is maintained at a constant temperature by default. This sensor is programmed to re-establish that default temperature, when a finger is pressed against it, by changing the rate of heat transfer at each pixel.^{13,14,17} Ridges transfer heat from the sensor faster than the air between them, resolving the print. A schematic of a thermal sensor is shown in Figure 1-7. Thermal sensors overcome the issues with skin condition but have their own deficiencies. Thermal sensor images disappear as the chip reaches thermal equilibrium, obscuring ridges. These sensors cannot operate on hot days where the temperature differential is not very high. Also, this sensor consumes considerably more power because of the constant heating required.

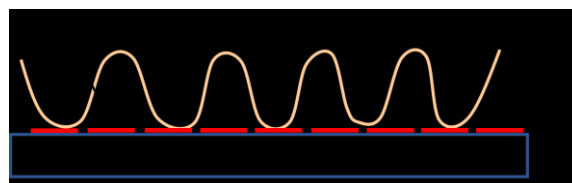


Figure 1-7: Working principle of a thermal fingerprint sensor.

Acoustic Sensors

The final class of fingerprint sensors are acoustic (ultrasound) sensors, shown in Figure 1-8. An array of sensor cells made from a senders and receiver image the fingerprint.^{14,18} The distance to the skin is determined by the time it takes for acoustic pulses from the sender to reach the receiver.¹⁴ Ultrasound sensors are unaffected by differences in skin condition and skin hydration that affect other imaging methods. This sensor is capable of providing a more accurate measurement of finger ridge topography.¹³ While the most accurate, these sensors are rather large and take longer to acquire a single image, thus limiting their application.^{13,14} Recent research has focused on reducing the size of these systems while maintaining functionality.^{18,19}

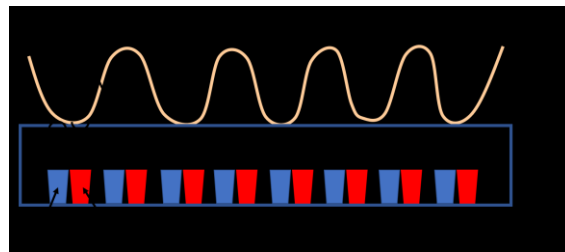


Figure 1-8: Working principle of ultrasound fingerprint sensor.

1.2. Fabrication of Nanostructures

1.2.1. Conventional Nanofabrication Methods

Nanostructures of a master are fabricated via conventional nanofabrication techniques. Nanofabrication processes generate arbitrary patterns with features having dimensions of <100 nm.²⁰ The most common and well-established conventional nanofabrication techniques are photolithography, laser lithography, focused ion beam lithography (FIB) and electron-beam lithography (EBL).²⁰ These techniques are top-down approaches that create patterns through the selective etching of the substrate.^{20,21} Incredibly complex and detailed patterns can be fabricated with these methods. They are, however, limited by the high instrument and operating costs, which restrict the majority of researchers from accessing these state-of-art instrumentations. These methods also have low throughput, are limited to planar fabrication, and are incompatible with nonstandard fabrication materials.²⁰ These drawbacks have precipitated the development of associated nanoreplication techniques.

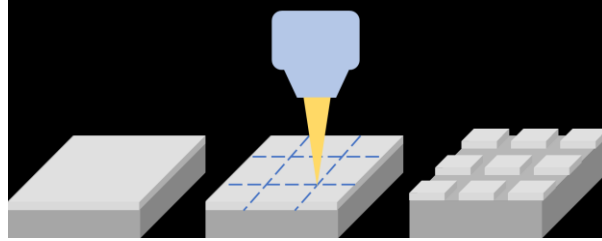


Figure 1-9: Schematic of EBL. (A) Substrate with resist material spin coated onto the surface. (B) Electron beam exposure. (C) Substrate after development.

EBL (Figure 1-9) is a serial process (features are written one at a time), making it quite slow relative to most nanofabrication methods such as photolithography and molding.^{20,21} Despite the slow fabrication speed, EBL is an essential tool for creating new nanostructures because it does not require a pre-existing mask or template. Two main factors dictate the resolution and fidelity of EBL; the electron beam and the resist being patterned. The parameters that are essential to produce high-resolution patterns are the probe size and the flux (i.e., $\mu\text{C}/\text{cm}^2$) of the electron beam. The optimum parameters being as small of an electron probe as possible while the flux of the electron probe is as high as possible. The electron beam is generated by an electron source, some common electron sources are tungsten, cerium hexaboride, and lanthanum hexaboride. These are examples of hot cathodes, high temperature (typically between 1800-2800 K) are used to overcome the work function and emit electrons.²² Hexaboride based electron sources are capable of outputting higher beam current, a highly desirable parameter, due to their lower work function.²² A source capable of producing high beam current enables the use of smaller spot sizes that are essential when writing high-resolution patterns without sacrificing the write speed.^{20,22} A lower current beam would require multiple passes over an area (which could introduce error) and require a prohibitively long treatment time.^{20,22}

Nanofabrication techniques like EBL rely on a resist, a thin layer of material spin coated onto the substrate, which is sensitive to the lithographic element. The resist that is etched (Figure 1-9A) is just as important as the electron beam; how smoothly and accurately it can be treated by the beam, and its sensitivity to electrons can drastically change the fabricated nanostructures.²¹ After electron beam irradiation (Figure 1-9B), the substrate is etched with a developer (solvent that removes either treated (positive) or untreated (negative) resist). Figure 1-9C illustrates the etching of a positive resist. Combinations of multiple resist layers having different etching properties and sensitivities to different developers can be used to fabricate unique 3D structures.²¹ The resolution as

determined by the critical dimension for a variety of organic and inorganic resists has been investigated. The resolution of organic and inorganic resists ranges from ~90 nm to ~5 nm, with polymethylmethacrylate (PMMA) and hydrogen silsesquioxane (HSQ) both achieving ~5 nm resolutions.²¹

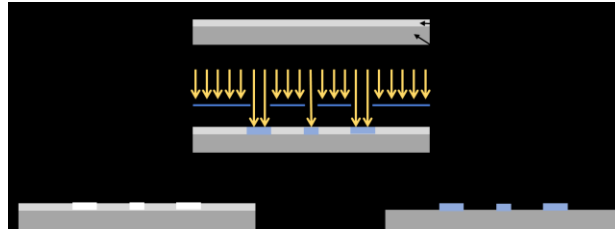


Figure 1-10: Schematic of Photolithography. (A) with a negative resist, (B) with a positive resist.

Photolithography is a nanofabrication process in which light is used to transfer a pattern from a photomask to a substrate. The substrate may be made of a photosensitive material or coated in a photoresist that is either broken down or cured when exposed to light or extreme UV radiation. Photolithography is shown schematically in Figure 1-10. The most obvious advantage of photolithography over EBL is speed. Photolithography is capable of patterning larger areas simultaneously. For example, a modern photolithography tool using 193 nm light can pattern a surface to a resolution of 38 nm and generate 1×10^{12} features per second.²³ Through careful engineering of photomasks and a combination of projection lenses, these features can be made smaller than the wavelength of light used.²³ These mask masters are often fabricated via electron and ion beam lithographic techniques that offer superior resolution and fidelity, but at the expense of throughput and time. As a result, complicated masks can be extremely expensive and are one of the main factors in the cost of photolithography.

In addition to costly mask fabrication, photolithography is limited by surface morphology, susceptibility to contaminants, and feature size variations. Photolithography, being a projection process, is limited to flat surfaces because changes in the distance between the mask and substrate surface will lead to blurring of the projected image and subsequently affect the size of the patterned features.²³ Photolithography is extremely sensitive to surface contaminants because they can interfere with the projection of radiation, leading to mistakes in the resulting pattern, necessitating their operation in facilities that have designated cleanrooms. Features generated by photolithography are

also susceptible to variation in the size of a few percent due to thermal and spatial distortions that are caused by minute changes in the pattern of light hitting the surface.^{20,23}

Through conventional nanofabrication techniques a limitless compendium of features and devices can be fabricated on a variety of surfaces. Nowhere is the power and versatility more apparent than in the electronics industry, where sophisticated semiconductor microchips are fabricated through a complex series of fabrication steps. The complexity of microchips had grown exponentially since their development in the 1960s, the minimum size of features has decreased from $\sim 20 \mu\text{m}^{24}$ to sub-10 nm,²⁵ allowing more components to be packed into them. At the current limit of 5 nm, transistors have a density of 170 million per square millimeter.²⁶

There is no denying the raw power of conventional nanofabrication technologies, however, fabrication is growing exceedingly complex, microchips can take 3 months to fabricate and have over 1000 steps. This increased complexity has increased the probability of error and subsequently contributed to high costs. While unconventional nanofabrication, such as nanoreplication (also known as nanoimprint lithography), cannot replace the conventional nanofabrication processes entirely, it is a more cost-effective and higher throughput technique to fabricate nanostructures. Due to its high throughput, nanoreplication becomes even more attractive when fabricating features over large areas. Diffraction gratings or self-cleaning surfaces, whose characteristics/performance do not deteriorate due to the presence of a few molding defects are prime examples. Nanoreplication substrates must be capable of conforming to master/cast features during molding. Polymers are great substrates for replication because it can be deformed rather easily with the aid of heat or solvent. The process of molding is inherently simpler to carry out and does not require state-of-the-art instrumentations, making it more accessible for research, education, and the general public.

1.2.2. Nanostructure Replication Methods

Unconventional nanofabrication techniques, such as nanoreplication, were invented to address the limitations of conventional nanofabrication. Whitesides' research group spearheaded the development of nanoreplication techniques that use a patterned template (master) to generate (via casting) an inverse replica pattern on the corresponding cast (stamp). The stamp is used to mold a substrate generating a 1-to-1 copy of the master

called a replica. They developed a number of replication techniques that include replica molding, microtransfer molding, micromolding in capillaries and solvent-assisted molding; these techniques are often referred to as soft lithography because of the “soft” nature of the stamp and/or substrate.²⁷⁻³⁰ Elastomeric stamps made from PDMS were used by the Whitesides group to pattern substrates by physically moving materials on the substrate surface. This portion of the thesis will be devoted to categorizing and differentiating protocols relevant to nanoreplication, such as replica and solvent-assisted molding.

A key element of nanoreplication is the stamp. The properties and morphology of the stamp have tremendous influence on the morphology of the replicated patterns. Stamps can be divided into two general categories; hard pattern transfer elements and soft pattern transfer elements.²⁰ Hard stamps (used in replica molding) are often made from silicon, quartz, and metals like copper. They are categorized as ‘hard’ because of their rigidity. The rigidity of these materials reduces local deformations and can sustain high pressures.²⁰ These hard stamps, which exhibit low thermal expansion characteristics, are usually used in conjunction with thermally cured polymers. Quartz-based stamps are transparent in the UV region allowing UV curable polymers to be crosslinked while the stamp is in contact with the mold.²⁰ Hard molds, however, have issues with non-planar surfaces because of their inherent structural or physical rigidity. Insufficient stamp-to-mold contact in areas of high curvature can lead to incomplete pattern transfer.²⁰ Materials used in hard molds, which are intrinsically higher in surface free energy, require a release layer to facilitate the demolding process (i.e., decoupling of the stamp from the substrate) and to prevent surface fouling.²⁰ Rigid hard molds can also catastrophically fail by cracking, which is caused by too much pressure during molding and/or molding an uneven substrate.

Soft molds, which are elastomers, were developed to replicate features onto curved surfaces and non-rigid or non-uniform (not flat) surface morphologies. When a soft mold or stamp is prepared by casting an uncured liquid polymer against a topographically patterned master, which is usually prepared by conventional nanofabrication techniques, it is referred to as soft lithography. A number of polymers, such as Polyurethane (PU), PDMS, and perfluoropolyether (PFPE), can be adapted as stamp materials^{20,31} PDMS is the most widely used material for soft lithography. There are several key characteristics that made PDMS ubiquitous in soft lithography. PDMS is a liquid at room temperature before crosslinking, facilitating the production of templates by casting. It is optically

transparent above a wavelength of 280 nm enables molding of UV cured materials. The inherently low interfacial free energy (21.6 mN/m) eases the separation of mold from the substrate. PDMS exhibit high elasticity, stamps based on PDMS can easily be separated from rigid templates without breaking or cracking. It is, therefore, an ideal material for nanoreplication. Another benefit of molding with PDMS is its ability to conform to curved, rigid, and soft topographic surfaces. PDMS is durable and chemically inert toward most materials being patterned or molded. It is chemically resistant to many solvents and is permeable to gases, which prevents the entrapment of gas bubbles at the stamp-to-template interface. PDMS is also rather inexpensive. Replication with PDMS, in theory, can be performed over relatively large areas (>5 cm²).³²

Although PDMS has many merits, it suffers from a few drawbacks. PDMS is known to swell in organic solvents, such as acetone, toluene, and hexane(s). Organic solvent-induced swelling will lead to deformation and change the dimensions of features that reside on the surfaces of the PDMS stamp/mold.³² The softness of PDMS, which is susceptible to physical deformation, restricts it from replication processes that require high pressure. Due to the inherently low Young's modulus of PDMS, it is also challenging for PDMS to maintain replicated features that are sub-100-nm and structures that have high-aspect-ratios.³² These features are susceptible to deform and collapse under their own weight.³²

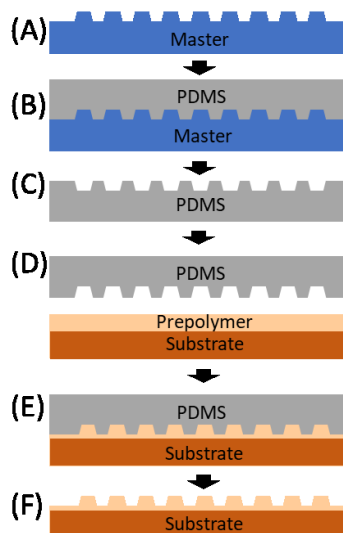


Figure 1-11: Schematic view of Nanoreplication. (A) Lithographically designed master. (B) Casting of PDMS from master. (C) PDMS “replica”. (D) Molding of prepolymer/precursor film on substrate. (E) prepolymer/precursor curing. (F) 1:1 replica of master.

Replica molding (represented in Figure 1-11A-C) is a process for shaping liquid polymer precursor using a rigid master that has been produced by conventional nanofabrication techniques (Figure 1-11A). The liquid precursor is subsequently cured against the master (Figure 1-11B). The resulting “replica” shown in Figure 1-11C, is the final product of replica molding and may be made from several UV curing or thermoplastic polymers. When the replica is applied to reproduce the original pattern into a different polymer it is called a template or stamp. Common techniques for this step are nanoimprint lithography, and solvent-assisted molding (Figure 1-11D). For nanoimprint lithography, the liquid precursor (which is applied as a thin layer to the substrate surface) is photo or thermally curable.²⁰ After curing in contact with PDMS stamp (Figure 1-11E) a 1:1 replica of the master is reproduced (Figure 1-11F).

In solvent-assisted molding, an appropriate solvent is used to soften the polymer film of interest before an elastomeric mold is stamped (

Figure 1-12). Solvent induced softening not only facilitates pattern transfer from an elastomeric stamp but also permits the process to be conducted at ambient temperatures. As shown in

Figure 1-12A, the application and role of solvent can vary, sometimes a polymer solution is applied to either a substrate or the mold; in other variations the solvent is applied to a polymer film on the substrate or to the mold before its application.^{20,32} The solvent swells or dissolves the polymer rendering it soft and easy to mold, solvent assisted molding can therefore be conducted without significant pressure or specialized molding equipment (

Figure 1-12B).²⁰ PDMS is commonly used as the pattern transfer element because it is permeable to gases, the solvent can evaporate during molding while the polymer is in conformal contact with the PDMS mold. Solvent removal solidifies the polymer and sets the molded features (

Figure 1-12C).^{20,32}

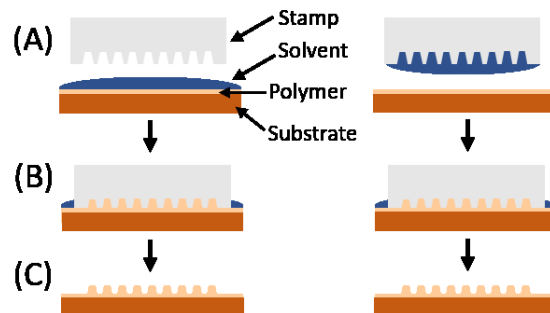


Figure 1-12: Solvent Assisted Molding Schematic. (A) Application of solvent and stamp to polymer film. (B) Solvent-assisted molding of polymer film. (C) Resulting patterned polymer surface.

Solvent-assisted molding has two primary benefits; 1) it is conducted at ambient temperature eliminating the deleterious effects of repeated cycles of heating and cooling; 2) the elastomeric stamps used can conform to nonuniform and nonplanar surfaces, improving pattern transfer and facilitating molding of large areas.^{20,32} The main drawbacks of solvent-assisted molding are related to swelling. Swelling of the elastomeric master can distort its topographical features and subsequently lead to distortion in the replicated structures. Swelling and subsequent shrinking of the molded polymer can also lead to distortion in the molded features. Solvent-assisted molding has been limited to polymer-solvent combinations that do not lead to polymer recrystallization. This is because crystallites will distort and deform molded structures, because of this the solvent-assisted molding potential of many polymer-solvent pairs (such as PC and acetone) have been overlooked.

1.3. Superhydrophobic Materials

1.3.1. Interfacial Energy and Surface Wetting

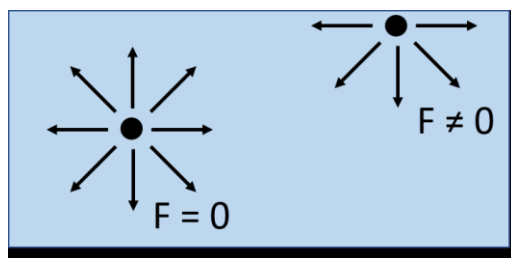


Figure 1-13: Intramolecular forces at surface of matter.

Knowledge of interfacial tensions between solids, liquids, and gases is key to understanding hydrophobicity and how it will be modulated in Chapter 5. Atoms/molecules

at the surface of matter have fewer neighbors than those in the bulk, this creates a net attractive force toward the bulk material as illustrated in Figure 1-13.^{33,34} As a result, when matter is in a fluid state the molecules at the surface are in a dynamic equilibrium with molecules in the bulk.^{33,34} The difference in forces manifests as surface tension in fluids. This force acts to reduce the surface area of a free liquid by minimizing the total number of surface molecules.³³ Liquids tend to adopt a spherical shape if unperturbed (i.e., in the absence of gravity and free from liquid-solid interaction) because spheres have the lowest total surface area. Surface tension in solids, however, is insufficient to overcome the energies of covalent or ionic bonds between atoms/molecules. At ambient conditions, solids, therefore, do not and cannot rearrange spontaneously to minimize their surface area.^{33,34}

The field of surface science examines the physical and chemical phenomena that occur at interfaces of two phases (i.e., solid-liquid, solid-vapor, solid-vacuum, and liquid-vapor interfaces). For instance, a free-standing drop of water has a single interface, the liquid-vapor interface (γ_{lv}). Two additional interfaces are introduced to the system when the water droplet comes into contact with the surface of a solid (Figure 1-17). These phases are a solid-vapor interface (γ_{sv}) and a solid-liquid interface (γ_{sl}).³³ Minimizing the total energy of these three interfaces is achieved by changing the shape and footprint of the droplet on the solid surface.^{33,34} When the solid is dry the interfacial energy is defined as γ_{sv} , if that same area is covered in a liquid film, the γ_{sv} interface is replaced by a γ_{sl} and a γ_{lv} interface.³³ The relationship between the interfacial energies is illustrated numerically in equation (2):³³

$$S = \gamma_{sv} - (\gamma_{sl} + \gamma_{lv}) \quad (2)$$

where S is defined as the spreading power. If $S > 0$, the sum of γ_{sl} and γ_{lv} is less than the γ_{sv} interfacial energy, the liquid droplet will spread on the solid surface. The formation of a liquid thin film is necessary to minimize the total energy of the system.^{33,34} When $S < 0$, only partial wetting occurs, because the interfacial energy of the solid is lower. In this instance, the liquid droplet will assume a shape that minimizes the total interfacial energy of the system. In partial wetting, the liquid droplet will adopt a spherical cap shape. The shape and equilibrium contact angle of this liquid droplet can be used to assess the surface energy of the solid. The equilibrium contact angle is defined by the tangent angle of the liquid-vapor interface at the three-phase contact line (Figure 1-14).

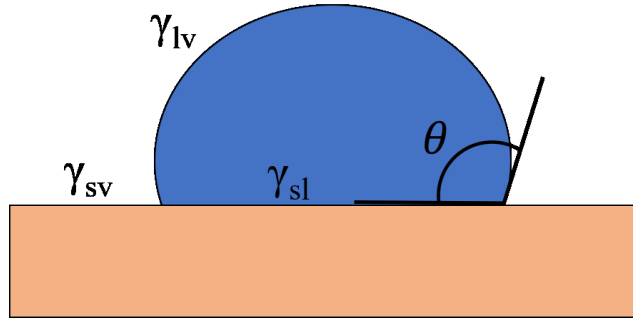


Figure 1-14: Diagram of a droplet on a surface showing the three interfacial energies and contact angle of the droplet.

The contact angle of a droplet is related to the respective interfacial energies by the Young-Dupre Equation:³⁵

$$\cos\theta_c = \frac{(\gamma_{sv}-\gamma_{sl})}{\gamma_{lv}} \quad (3)$$

This equation is an idealized representation of a droplet with a single contact angle. It does not consider hysteresis of the advancing and receding edges of the droplet.³⁵ The advancing and receding edges of the droplet can have different contact angles depending on how the droplet came to rest. In addition, the equation is derived under the assumption that the surface of the solid is completely smooth and flat.

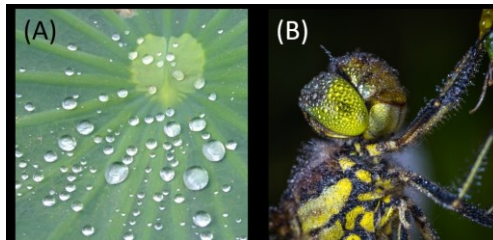


Figure 1-15: Images of hydrophobicity in nature. (A) Lotus leaf, (B) Dragonfly.

There are three classifications of surface energies: 1) hydrophilic surfaces, the observed water contact angle these surfaces is between 0° and 90°; 2) hydrophobic surfaces, they belong to a class of material that is capable of producing water contact angle above 90°; 3) superhydrophobic surfaces, they are a subset of hydrophobic surfaces that can achieve a water contact angle greater than 150°. For flat surfaces described by the Young-Dupre equation the water contact angle can vary from 0° on high energy surfaces like glass, up to 120° on low energy surfaces such as fluorinated polymers i.e. polytetrafluoroethylene (PTFE).^{33,34} However, there are numerous examples of

superhydrophobic surfaces in nature (contact angle $>150^\circ$), such as the sacred lotus leaf ($\sim 160^\circ$) and the bodies of many insects (Figure 1-15).³³ Droplets of water can easily roll off the surfaces of lotus leaves, removing dirt and dust in the process. This process of self-cleaning has become known as the lotus effect.^{33,34} How is it that plants and insects can create such hydrophobic surfaces?

1.3.2. The Wenzel and Cassie-Baxter Wetting States

Electron microscopy analyses revealed that the surfaces of the sacred lotus leaf are highly textured, indicating that superhydrophobicity is a synergistic product of both surface chemistry and textured surfaces. These textured surfaces consist of micro- and nano-scale hierarchical structures that amplify the effect of the surface chemistry.³⁶ The increase in surface roughness increases the effective surface area in a given region of the solid. The water droplet will adopt a near-spherical shape to minimize the size of this interface, and thus exposing more of the solid-gas interface.

The increase in hydrophobicity due to surface roughness was first identified and described by Robert N. Wenzel. Wenzel theorized that droplets of liquid are to conform to the topography of a rough surface, increasing the area of the solid-liquid interface.^{33,35,37} The effect of surface roughness on contact angle is described by the Wenzel equation which modulates the contact angle on a flat surface by a roughness factor (r):

$$\cos\theta_w = r\cos\theta_e \quad (4)$$

where $\cos\theta_w$ is the Wenzel contact angle and $\cos\theta_e$ is the Young's contact angle (a contact angle one would obtain if the surface of interest is chemically and topographically homogeneous). The roughness factor in the Wenzel equation acts to amplify the intrinsic surface free energy of the solid surface; when θ_e is below 90° cosine is positive so an increase in the roughness factor will make the surface more hydrophilic and reduce the contact angle. When θ_e is above 90° cosine is negative, in this case an increase in the roughness factor causes the surface to be more hydrophobic and contact angle increases.^{33,34,37} An illustration of a water droplet in a Wenzel state is shown in Figure 1-16B, compared with that of a droplet on a smooth surface (Figure 1-16A) there is an obvious increase in the effective surface area of the solid-liquid interface.

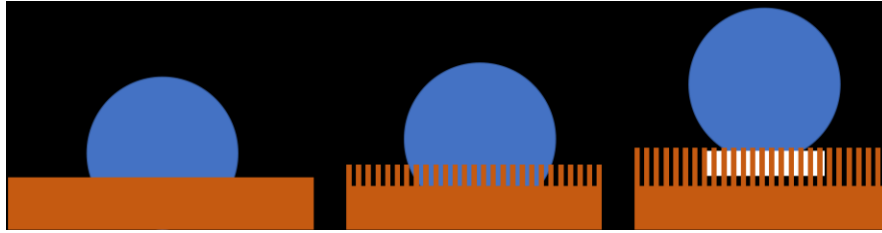


Figure 1-16: Different states of water droplet on surfaces. (A) Water droplet on a smooth surface. (B) Water droplet on a rough surface in the Wenzel state. (C) Water droplet on a rough surface in the Cassie-Baxter state.

A Wenzel state assumes that a liquid droplet would conform to the topography of the solid. As the surface roughness increases, it is also possible that the liquid cannot fill the small spaces between these features. Instead, the liquid sits atop these features (Figure 1-16C). This scenario can be described by the Cassie-Baxter formula:^{33,34}

$$\cos\theta_{CB} = f_s \cos\theta_e - (1 - f_s) \quad (5)$$

Where f_s is the fraction of solid in contact with the liquid and $\cos\theta_{CB}$ is the Cassie-Baxter contact angle. The most significant difference between the Cassie-Baxter and Wenzel equations is the modulation of contact angle compared to a flat surface. In the Wenzel treatment, surface roughness serves to amplify the effects of existing surface chemistry by the factor r . Conversely in the Cassie-Baxter case, the effect of surface chemistry is reduced by the factor f_s . This factor is the fraction of solid in contact with the liquid.^{33,34} This equation can be interpreted as a weighted mean of the contact angle of a liquid droplet on the surface and in vapor (which is 180°).^{33,34} This equation indicates that the apparent surface free energy of the solid decreases (i.e., increase in observed water contact angle) as the effective surface area in contact with the droplet decreases.

Each of these equations are tailored to specific liquid-solid interactions. Young's equation is developed under the assumption that the solid's surface is perfectly flat and homogeneous. Although it is adequate to evaluate ideal surfaces, its application is limited. This is because few surfaces are completely flat or homogeneous.³³ The equation proposed by Wenzel assumes complete wetting of a homogeneous surface and takes surface roughness into consideration, while the Cassie-Baxter equation assumes partial wetting and the formation of a composite surface.^{33,38}

Surface morphology has been found to play a key role in the modulation of hydrophobicity and determines what type of state a liquid droplet will assume.^{39,40} A plethora of research has concluded that hierarchical surface roughness on the micro- and nano-scale is essential to achieve superhydrophobicity.³⁴⁻⁴¹ Microscale and nanoscale roughness on their own will increase the hydrophobicity of a surface, but not to the same degree as in synergy.³⁹ As shown in Figure 1-17, hierarchical roughness vastly increases the surface area of the solid. In practice the water contact angle obeys the behavior described by Wenzel when surface roughness is mild ($r_s < 2$) and follow the Cassie-Baxter behavior as the surface roughness increases (i.e., surfaces that have the appropriate hierarchical roughness as illustrated in Figure 1-17).^{34,38} There is, however, no defined boundary between these two states. Behavior of the liquid droplets is also influenced by the mechanism in which they are formed or delivered to the surface. For example, the Wenzel behavior is more favorable when the water droplet is formed from vapor condensation.⁴⁰ In some instances, these states can co-exist. For instance, physically pressing a water droplet, which exhibits Cassie-Baxter state, can cause its transition into the Wenzel state.⁴⁰

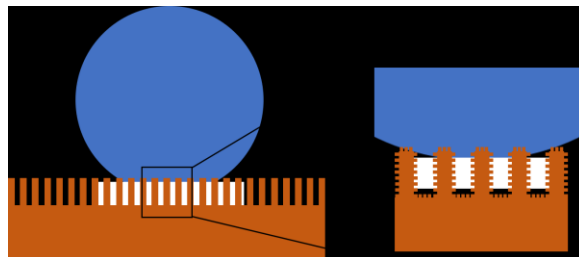


Figure 1-17: Schematic view of Droplet on a surface with hierarchical roughness. Left inset shows magnified a section of features under the droplet.

The co-existence of the Wenzel and Cassie-Baxter states is seen on the sacred lotus leaf, where high contact angle droplets that slide easily and adhere strongly to the surface are both present.³⁹ Even on homogeneously rough surfaces both types of droplets can form based on the force and angle with which they contacted the surface.³⁹ Droplets can also change state from a Cassie-Baxter to Wenzel state, existing in a transitional state where roughness features are partially filled.⁴⁰ Figure 1-18 shows a hypothetical free energy barrier between the states, the size of the energy barrier depends on the depth of roughness features the droplet must impregnate to fully wet the surface.⁴⁰ The Cassie-Baxter state is metastable and will transit to the Wenzel state if feature size is shallow

enough or the intrinsic hydrophobicity of the material is low enough that the free energy barrier can be overcome.⁴⁰

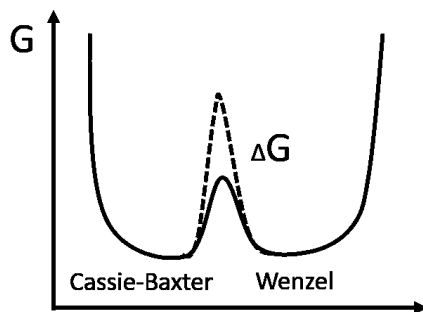


Figure 1-18: Schematic plot of the energy barrier between the Cassie-Baxter and Wenzel states.⁴⁰

Reprinted with permission from Ref. 40. Copyright (2009), *PNAS*.

1.3.3. Fabricating Polymeric Superhydrophobic Surfaces

Through study of superhydrophobicity in the nature, an understanding of the criterion for superhydrophobicity was achieved.^{34,36} The two key criteria that all superhydrophobic surfaces have are 1) the surface chemistry is of a low interfacial energy material; 2) surface must have hierarchical roughness on both the micro and nanoscale.³⁶ The first artificial superhydrophobic surface was composed of alkylketene dimer (AKD) and dialkylketone (DAK).⁴² A melted AKD/DAK mixture was cast onto glass and allowed to cool, during cooling the mixture began to crystallize, generating a rough surface morphology after 3 days of crystallization.⁴² Contact angle on the rough AKD reached 174°, a gargantuan increase from 109° on flat AKD.⁴² SEM investigation showed that AKD formed a fractal like structure with ~30 μm spheroids adorned with ~1 μm flakelike structures (hierarchical roughness).⁴² AKD has a rather low melting point of 66-67 °C and is opaque, both these properties inhibit its widespread application, but the framework for designing superhydrophobic materials proved invaluable.

Fluoropolymers, which have intrinsically low surface free energies, are attractive materials for creating superhydrophobic surfaces.³⁴ Although fluoropolymers have low surface free energies, hierarchical surface roughness is still essential to achieve superhydrophobicity. The surface of the fluoropolymer can be roughened to produce superhydrophobic materials through various processes. PTFE, also known as Teflon, becomes superhydrophobic when etched with oxygen plasma. This generated a contact

angle of 168° through a simple top-down process.⁴³ Simply stretching a PTFE membrane was found to produce a superhydrophobic surface. Stretching the membrane creates voids at the surface, reducing the effective contact area to the water droplet.⁴⁴ To mitigate the limited solubility of fluorinated polymers, they are often mixed with other polymer blends and copolymers to create superhydrophobic surfaces.^{45,46} Casting of fluorinated copolymers under humid conditions created a transparent and superhydrophobic material.⁴⁵ These methods rely on the inherent hydrophobicity of fluorinated polymers, while the surface morphology is controlled through deposition and etching processes.

Fluorinated polymers can also be applied as surface layers through chemical vapor deposition (CVD) to a template that has rough surface morphology. A carbon nanotube array that has inherently rough topography was coated with PTFE through CVD to generate a superhydrophobic material.⁴⁷

Though the surface energy of organosilanes is not as low as fluorinated compounds, they are capable of superhydrophobicity when applied with the appropriate surface morphologies.⁴⁸ For example, trimethylmethoxysilane ($(\text{CH}_3)_3\text{Si}(\text{OCH}_3)$) deposited on silicon and glass formed a superhydrophobic surface, with the deposited material building up to generate surface roughness.⁴⁹

Polymers often have low interfacial energies, similar to the waxy compounds employed by superhydrophobic vegetation, which has led to their application in superhydrophobic surfaces. Polymers can be restructured or reorganized in several ways; Erbil et al. constructed superhydrophobic polypropylene (PP) by a casting process. Fast evaporation of the solvent facilitated the formation of a porous surface that also has the necessary hierarchical surface roughness.⁵⁰ In a similar process, polyethylene (PE) is made superhydrophobic. The thin-film of PE was produced by casting a solution of PE dissolved in a mixture of solvent/non-solvent. Controlled crystallization of PE, subsequently, leads to the formation of a highly porous array of microstructures adorned with nanostructured crystallites.⁵¹ Porous microsphere/nanofiber composite films of polystyrene (PS), also exhibit superhydrophobic properties. This composite film is produced by electrostatic spinning a solution of 7 wt % PS/DMF solution.⁵² Treating a PC surface with the proper solvent under humid conditions was also found to produce a superhydrophobic surface by crystallizing the amorphous polymer into microscale spherulites with nanoscale tendrils.^{53,54} Polyamide⁵⁵ and poly(vinyl chloride) (PVC)⁵⁶ have

similarly been transformed into superhydrophobic materials by solvent-induced crystallization.

Controlling the rate of nucleation and crystallization of amorphous polymers are key to produce superhydrophobic surfaces. These parameters control the size, morphology, and distribution of roughness features. They are modulated to produce surfaces with specific properties, such as superhydrophobicity while maintaining optical transparency. The rate of crystallization is controlled by the solvent compatibility; which must be able to swell the polymer network but not fully dissolve the polymer.⁵⁰⁻⁵⁶ A mixture of solvent and non-solvent can be used to modulate the amount of swelling and rate of nucleation.^{50,52} The simplicity of solvent treatment is attractive for generating superhydrophobic interfaces over large areas quickly and economically.

The materials that can be made superhydrophobic are diverse in range. These materials, intrinsically hydrophobic, are made superhydrophobic through the appropriate surface roughening.

To further understand and optimize hydrophobic surfaces, researchers designed superhydrophobic surfaces with defined micro and nanoscale features to fully elucidate their effects.⁵⁷⁻⁶³ Micro and nanofabrication techniques can also be used to produce the necessary hierarchical roughness in PDMS cast from it.^{62,63} Anodized aluminum oxide (AAO) was used either as a mold or a “template” to fabricate superhydrophobic nanopillar arrays of polyacrylonitrile,⁵⁷ PVC⁵⁸ and PC.⁵⁹ The AAO has an array of parallel pores arranged in a honeycomb structure. The pore size, which ranges from a few micrometers to less than 100 nm, is tunable. While dependent on the material and structure shape, general trends in microstructure size and spacing that inform current research were determined.

1.4. Polymeric Materials for Nanofabrication

In this section of the introduction the primary polymers (PC and PDMS) used in this study will be described. Along with the thermodynamics that dictate their physical state and interactions with small molecular solvents.

1.4.1. Polycarbonate

Polycarbonates are thermoplastics which have a carbonate ester along their polymer backbone.⁶⁴ There are several methods to fabricate PC, the most commercially significant method is through the reaction of a dihydroxy compound with phosgene.^{64,65} Bisphenol A, the most commonly used dihydroxy compound for PC is deprotonated to produce a disodium salt (diphenoxide).⁶⁴ This salt is reacted with phosgene through interfacial polymerization under mild conditions (10-35 °C) to produce PC as shown in Figure 1-19.⁶⁴ The basic aqueous phase containing the disodium salt and the organic phase (often dichloromethane) containing phosgene.⁶⁴

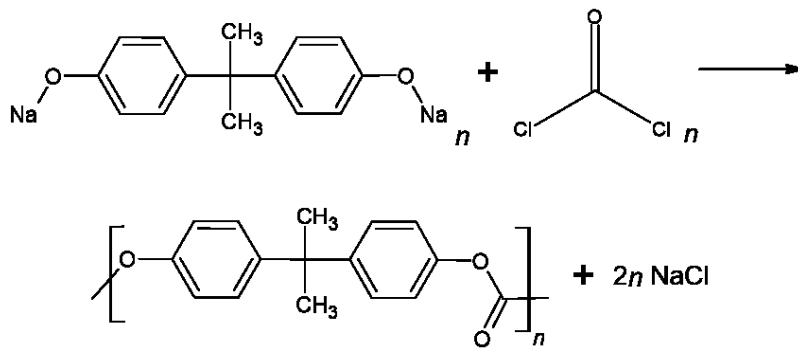


Figure 1-19: Synthesis of polycarbonate from phosgene and salt of bisphenol A

While PC can be produced from a wide range of hydroxyl containing compounds, in practice only PC made from diphenyl compounds such as bisphenol A have been commercially significant.^{64,65} As such when discussing PC, bisphenol A PC is usually what is being referred to. The physical properties that define PC result from several factors: (1) the molecule is symmetrical, (2) carbonate groups are polar but separated by aromatic hydrocarbons, (3) benzene rings along the polymer backbone restrict flexibility, (4) the repeat unit is quite long.⁶⁴

The most interesting property of PC is its impact strength, which is much higher than other pure polymers. Polymer chains are held together by polar interchain attraction between ester groups and also the stacking of benzene rings along the polymer chains.⁶⁴ It is however the stiffness of PC which defines its impact strength; the restricted flexibility of the polymer prevents chains from packing closely together, resulting in a higher free volume.⁶⁴ When stresses are applied to PC, intrachain rearrangement can occur to absorb energy. Commercial PC typically has a molecular weight between 20,000 and 50,000 g/mol which contributes its impact resistance and high resistance to creep.⁶⁴ It is difficult

for PC to rearrange, even under significant pressure and up to 140 °C, because the long inflexible chains cannot achieve large scale rearrangement.⁶⁴

Based on the presence of benzene rings and the polar carbonate component, PC should be capable of crystallization. However even when held above its T_g (145 °C) it takes several days for significant crystallization to develop.⁶⁴⁻⁶⁶ The free energy barrier for long inflexible PC chains to rearrange is high. When crystallized, PC chains arrange according to the unit cell shown in Figure 1-20. The polymer chains adopt a rhombic crystal structure as shown at the top of Figure 1-20. The a , and b cell constants are 11.9 Å and 10.1 Å respectively, four polymer chains are contained within the cell.⁶⁴ Adjacent polymer chains are oriented so the carbonate moiety is in the same plane as the methyl moieties on neighboring polymers.⁶⁴ More interesting is the c cell constant along the polymer chain, which is 21.5 Å, a long repeat unit.⁶⁴ Along the c -axis crystalline PC segments are arranged such that there is stacking between the rings structures with the methyl groups along the pivotal carbon chain pointing toward the back of the carbonate moiety (Figure 1-20).^{64,66} Due to the rigid backbone of crystalline PC and the significant degree of interchain attraction, the melting point (T_m) of PC is rather high (250 °C).⁶⁴ Aging, annealing, and crystallizing PC will however reduce the impact strength by increasing the density of chains and lowering the free volume, inhibiting intrachain relaxation.⁶⁴

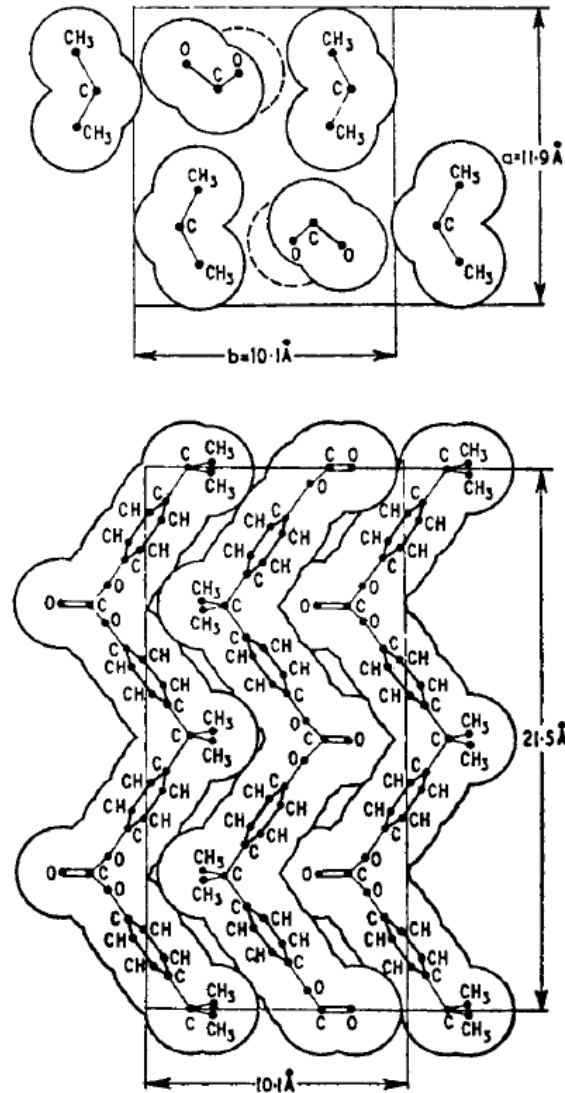


Figure 1-20: Unit cell diagram for polycarbonate based on bis-phenol A
 Reprinted with permission from Ref. 64. Copyright (1999), Elsevier.

Being difficult to crystallize, PC is produced in an amorphous state. It is characterized by high optical transparency in the visible spectrum (~90%). Upon crystallization PC exhibits haziness as voids and inconsistencies in polymer density develop, causing light to scatter. Typically, PC had a slight yellow color due to impurities, which was masked by blue dyes; modern methods of producing PC have higher purity and are virtually colorless.⁶⁴ PC is resistant to hydrolysis by dilute acidic and basic solutions due to the hydrophobicity of the benzene rings, however it dissolves easily in organophilic hydrolysing solvents like ammonia.⁶⁴ Solvents with a solubility parameter within $1.4 \text{ MPa}^{1/2}$ of PC ($19.4\text{-}19.8 \text{ MPa}^{1/2}$) are capable of solvating PC.⁶⁴ However many

of the solvents that can solvate PC are poor solvents, having different types of intermolecular forces.⁶⁵ This is the case for acetone, which can penetrate the polymer network, even though it does not have any specific interaction that stabilizes the polymer.^{64,65} As a result PC can crystallize out of the mixture to a more thermodynamically stable crystalline state.^{65,67} In contrast, if there is some kind of stabilizing interaction between the polymer and solvent, PC will remain in solution. Dichloromethane for example interacts with the carbonate group through its hydrogen moieties, preventing crystallization.^{64,65}

PC can be damaged by UV light, which over time causes a dulling of the surface through the formation of microscopic cracks.⁶⁴ These cracks can serve as failure points, reducing the impact strength of the polymer.⁶⁴ Fortunately PC is a good absorber of UV and the depth of UV degradation is low (0.075-0.125 cm), however this is still a problem for thin films.⁶⁴ These effects can be mitigated by UV absorbing additives.

In research, blends of polycarbonates with other materials are often tested, blends of PC and acrylonitrile butadiene styrene (ABS) have excellent mechanical properties and can be efficiently molded.⁶⁴ PC blends are made with the general objective of improving the physical properties of another polymer such as PMMA by blending in PC.^{68,69} The partitioning of additives into these PC blends has also been explored to develop functional polymers.⁷⁰

1.4.2. Polydimethylsiloxane

PDMS belongs to a class of polymers called organosilicons or commonly, silicones. These are characterized by the presence of carbon-silicon bonds. More specifically, as a siloxane, PDMS has a backbone of silicon-oxygen bonds.⁷¹⁻⁷⁴ PDMS is available in several forms which may differ in their viscosity, appearance, and physical properties based on the formulation of the polymer itself and additives present. Most often it is supplied in PDMS kits which contain a base⁷⁵ and curing agent.⁷⁶ The base kit contains prepolymer, short chains of PDMS (~60 repeat units) terminated with vinyl groups.⁷³ The curing agent contains shorter PDMS chains (~10 repeat units) which include methylhydrosilane moieties.⁷³ The hydrosilane moieties can react with the vinyl group in a hydrosilylation reaction where an Si-C bond is formed. This reaction, which is illustrated in Figure 1-21, is catalyzed by a platinum catalyst, often Karstedt's catalyst.⁷⁷ The reaction

between the vinyl end groups of the base and the hydrosilanes along the curing agent backbone lead to an extensively crosslinked polymer.^{71,73}

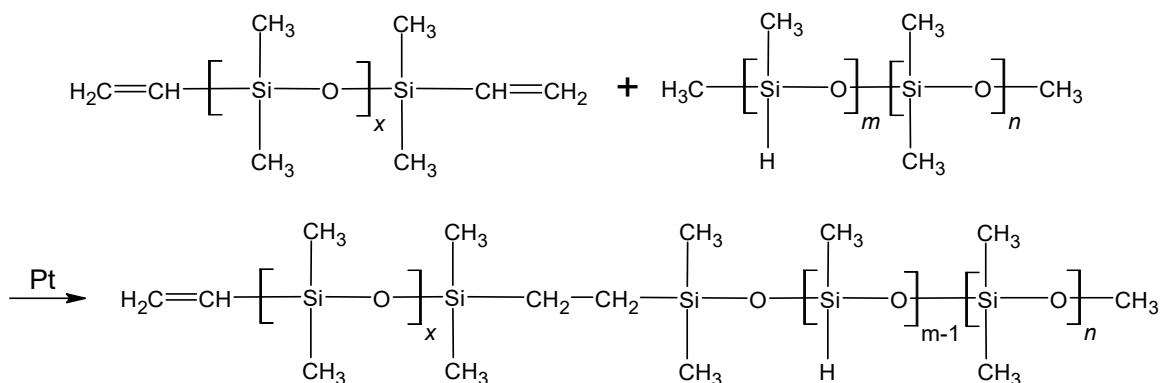


Figure 1-21: Scheme of cross-linking reaction for silicone network formation

Reprinted with permission from Ref. 73. Copyright (2005), Elsevier.

Depending on the amount of cross-linking between PDMS chains its properties can vary from a viscous oil to a durable elastomer. The properties can be further modified by the addition of fillers like silicon dioxide to the polymer network.⁷⁸ Thanks to this versatility and its agreeable properties, e.g. it is inert, non-toxic, optically transparent, UV resistant, and high gas permeability, PDMS is applied to a plethora of domestic and research applications. Depending on the formulation, it can serve as a release agent, a sealant, adhesive, water repellent, biomedical device, anti-foam agent, food additive, or lubricant.⁷²

The backbone structure of PDMS has low degree of steric hindrance compared to carbon-carbon or carbon-oxygen bonds because of the reduced likelihood of side groups (compared to C-C bonds) and increased bond length.⁷⁹ For this reason PDMS has a very low T_g of $-123\text{ }^\circ\text{C}$ and T_m of $-43\text{ }^\circ\text{C}$,⁷² the energy barrier from molecular motion being quite low. For this same reason PDMS is extremely soft, having a Young's modulus of 1.3-3 MPa depending on curing temperature.⁸⁰ Higher temperature facilitates greater cross-linking and a consequently harder polymer.⁸⁰ For comparison the Young's modulus of PC is 4 orders of magnitude higher. Despite being "soft", PDMS is known to be a durable elastomer, which results from its heavily cross-linked internal structure and ability to deform under stress.

PDMS is resistant to hydrophilic solvents but tends to swell when exposed to common hydrophobic solvents (e.g. acetone, dichloromethane, alkanes, triethylamine, xylene).^{71,78} Swelling generally correlated with similarity to the solubility parameter of PDMS (14.9-15.59 MPa^{1/2}).⁷¹ PDMS has high gas permeability because the highly flexible Si-O-Si backbones are capable of extensive long range motion.⁷⁸ Intermolecular forces in PDMS are also weak, allowing gases to permeate the matrix with relative ease.⁷⁸

Microfluidic systems are important for many applications such as biochemical analysis, chemical sensing, and cell-assays.⁸¹ Microfluidics offers benefits of reduced size, reagent volumes, rapidity, portability, and design flexibility.⁸¹ PDMS is desirable as a substrate for microfluidics because it can conform to a mold before curing, enabling cheap and easy fabrication of PDMS microfluidics with defined structures. The elastomeric nature of cured PDMS allows conformal contact with flat glass and polymer surfaces, useful for reversible or irreversible bonding.⁸¹ The transparency of PDMS is also advantageous for microfluidic applications, keeping it compatible with most optical detection methods.⁸¹ PDMS microfluidic systems for countless organic and inorganic molecules have been designed, with varied targets such as DNA,⁸² cobalt,⁸³ and dopamine.⁸⁴

Many analytical chemistry applications take advantage of the permeability of PDMS and the subsequent partitioning of compounds into PDMS.⁷⁸ Gas Chromatography columns coated with PDMS as a stationary phase are widely used because PDMS can uniformly coat the column and handle thermal cycling.⁷⁸ Analytes in a PDMS coated column are generally partitioned based on the degree of hydrophobic interactions.⁷⁸ The partitioning of organics from aqueous solutions into PDMS has been applied to perform extractions. By extracting a larger amount of analyte higher sensitivity can be achieved.⁷⁸ This has been applied to extract and analyze dangerous pollutants like polycyclic aromatic hydrocarbons,⁸⁵ and pesticides from common matrixes like soil, air, and water.⁷⁸

PDMS has been explored as a surface coating, because the strength of the Si-O-Si backbone imparts thermal stability and chemical inertness.⁸⁶ Anti-corrosion coatings on metal surfaces are made with PDMS, which was often mixed with another polymer or modified with additives.⁸⁶ PDMS membranes resistant to biofouling have also been designed by incorporating additives which inhibit biofilm formation and have biocidal

properties.⁸⁷ Being optically transparent, PDMS coatings can be applied when optical clarity is a concern, such as anti-reflection coatings for solar cells.⁸⁸

1.4.3. Thermodynamics of Polycarbonate Crystallization

In this research PC crystallization is either impeded or promoted depending on the application. To effectively control the degree of crystallization it is necessary to understand the factors that drive it. Further, an understanding of the nucleation and growth mechanisms will help relate the structures formed in PC to different stages of crystallization. Thermodynamics proves an excellent framework to analyze PC crystallization.

Molecular chains of polymers rearrange into an ordered structure that is energetically favored during crystallization. These ordered structures maximize dipole-dipole, H-bonding, and van der Waals interactions that stabilize polymer chains in crystalline arrangements.⁸⁹ Individual polymer chains tend to cooperatively organize and develop into crystalline arrangements where the backbones of polymers align.⁸⁹⁻⁹¹ In the amorphous state (Figure 1-22A), molecular chains of polymer do not exhibit long-range order. Instead, these polymer chains twist and tangle with one another, occupying space haphazardly. In the crystalline state (Figure 1-22B), regions of long-range order develop as polymer chains align with the adjacent polymer chains. Polymer chains can (and typically do) fold back over to align with themselves, forming structures called lamellae (Figure 1-22B). The degree of crystallinity and the corresponding size of lamellae depend on the crystallization conditions. As illustrated in the schematic, not all polymer chains arrange into lamellae, some remain in an amorphous or semi ordered state between sections of lamellae.^{90,91} Whether a polymer crystallizes is affected by many factors, such as the molecular structure of the polymer, thermal history (if it has previously crystallized or melted) and purity. For example, linear polymer chains that are long and flexible tend to crystallize, because they can easily rearrange and conform into tightly packed structures.⁸⁹ In contrast, a stiff polymer backbone, which limits the polymer's ability to rotate and conform, can inhibit polymer crystallization.⁸⁹ Side groups also affect crystallization. Isotactic polymers tend to crystallize favorably due to strong interchain and dipole-dipole interactions. On the contrary, atactic polymers are less likely to form lamellae due to steric hindrance.⁸⁹ Branching of polymer is deleterious to crystallization, packing of polymer chains difficult and less energetically favorable in branched polymers.⁸⁹ The rate

of cooling, annealing temperature and annealing time are other important factors that influence the crystallinity of a polymer. Polymers such as PC thermally crystallize incredibly slowly (on the order of weeks).^{65,92} Additives and impurities can also affect crystallization, either by disrupting order between polymer chains or serving as spacers and nucleation sites.⁹²



Figure 1-22: Schematic diagram of amorphous and crystalline polymer chains.

The attractive forces that facilitate crystallization, however, also restrict the mobility of polymer chains. These polymer chains can become entangled, akin to noodles, without any semblance of order. The temperature at which the polymer chains become mobile is the glass transition temperature (T_g). Below T_g , bulk polymers are slightly flexible and fracture when exceeding its elastic modulus, because these polymer chains are immobilized by intermolecular forces. These intermolecular forces are overcome at temperatures above T_g . Under this condition, polymers are soft and flexible (i.e. rubbers) because chains can slip past each other to conform to macroscopic stresses. In a typical differential scanning calorimetry (DSC) curve (Figure 1-23), the heat capacity of the polymer increases around the T_g as energy is used to overcome intermolecular forces and converted to molecular motion of the polymer chains. At temperatures above T_g , polymer chains are sufficiently mobile that they can crystallize to attain a state of lower free energy. This state of lower free energy is attained by maximizing the sum of the intermolecular attractions (i.e., the formation of microcrystalline domains) and the entropy of the polymer chains. These are, however, two opposing driving forces. The point at which the overall crystallization rate is highest is defined as the crystallization temperature (T_c). This phase transition is exothermic and present only in crystalline and semi-crystalline polymers. For crystalline and semi-crystalline polymers, a melting temperature (T_m) exists. At this

endothermic phase transition, polymers melt to a viscous liquid, suggesting that crystallites are thermally disrupted. Polymers are rendered amorphous again by melting.

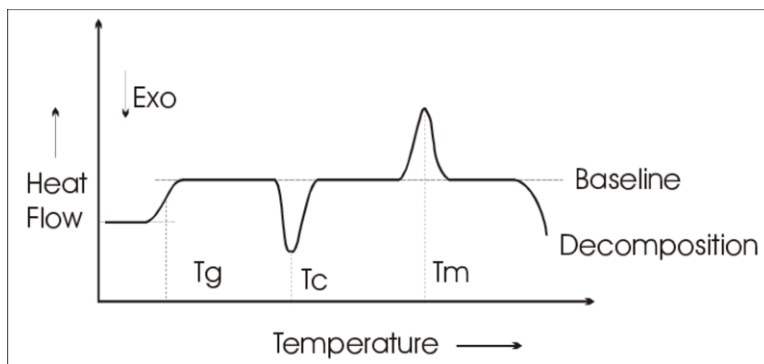


Figure 1-23: Typical DSC curve for a polymer: T_g-glass transition, T_c-crystallization temperature, T_m-Melting temperature and the decomposition of the polymer.⁹³

Reprinted with permission from Ref. 93. Copyright (2003), *Universität Potsdam*.

Other techniques can be applied to alter the physical properties of polymers in the absence of temperature variation. Plasticizers are typically added to polymers to promote plasticity and flexibility.^{65,92} The apparent improvement in elastic modulus is attributed to the intercalation of plasticizers between polymeric chains. They function as spacer molecules that push the polymeric chains away from each other and consequently increase the free volume of each polymer chain. The increased free volume has the same effect as increased temperature, allowing polymer chains greater freedom to conform and rearrange.^{65,92} Studies have demonstrated that the addition of a plasticizer to a pristine polymer sample will lead to depression in the T_g.^{65,92} Solvents are excellent plasticizers for polymers. They can easily penetrate into the polymer network because of their small size.^{65,92} PC, for example, which takes 2 weeks to thermally crystallize can crystallize in 3 minutes at room temperature when plasticized with small molecule solvents (acetone, ethyl acetate).^{65,92} The aromatic rings, which contribute significant steric hindrance in the polymer backbone, make PC stiff and crystallization difficult. This hinderance can, however, be overcome by the larger free volume afforded through solvent penetration.^{65,92}

Unlike conventional crystals, crystalline polymers consist of crystalline domains separated by amorphous regions. Crystalline lamellae tied together with semi-ordered and amorphous polymer. At the lamellae growth front polymer crystals often branch/splay or incite further crystallization nearby.^{90,91} Extensive branching leads crystals to most often

form spherical arrangements called spherulites.^{90,91} Spherulites can range in size from micro to millimeter depending on the polymer and growth conditions.⁹⁴

Crystal nucleation begins with the formation of an embryo, a region within the polymer that randomly exhibits increased alignment of molecular chains, termed homogeneous nucleation. Nucleation can also be incited by contaminants or impurities which provide a surface (with a lower free energy barrier) to grow from, which is termed heterogeneous nucleation. Initially embryonic growth is energetically unfavorable and the embryo may disappear. Once the embryo grows beyond a critical size, it becomes energetically favorable for the crystalline domain to grow larger. This can be attributed to the decrease in surface-to-volume ratio and enthalpy of crystallization outpacing the increase in surface energy (Figure 1-24).⁹⁰ Atomic Force Microscopy (AFM) has been applied to directly image embryo formation and disintegration in thermally crystallizing PC.⁹⁵

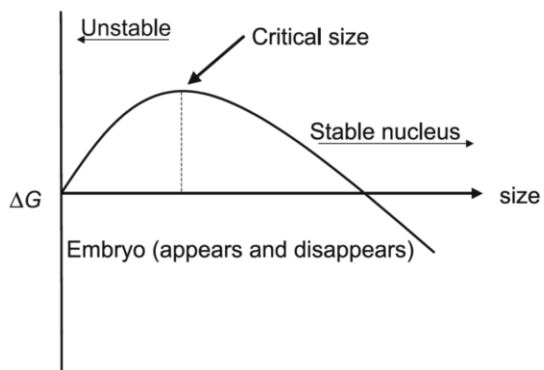


Figure 1-24: Gibbs free energy of formation of a nucleus as a function of its size.⁹⁰ Reprinted with permission from Ref. 90. Copyright (2005), *Springer*.

Once the embryo has grown beyond its critical size the embryo becomes a nucleus and begins to grow continuously from two ends.^{90,91} At these growth fronts amorphous polymer conforms and rearranges to the pre-existing crystalline arrangement to form the initial lamellae of the spherulite. A general 3D schematic of a lamella is shown in Figure 1-25, the growth fronts are located on the sides. Depending on the conditions, lamellae can grow from these fronts with varying degrees of isotropy.⁸⁶ Polymer chains wind into and out of the structure like wires in a switchboard, twisting back in is energetically unfavorable, but this is offset by the enthalpic stabilization between the aligned sections of the polymer chains.^{90,91,94} It is common for the polymer chains be only partially incorporated into lamellae, polymers also do not always re-enter the lamellae directly

adjacent to where they exited.⁹¹ Figure 1-25 shows chains exhibiting both adjacent re-entry and switchboard like re-entry.

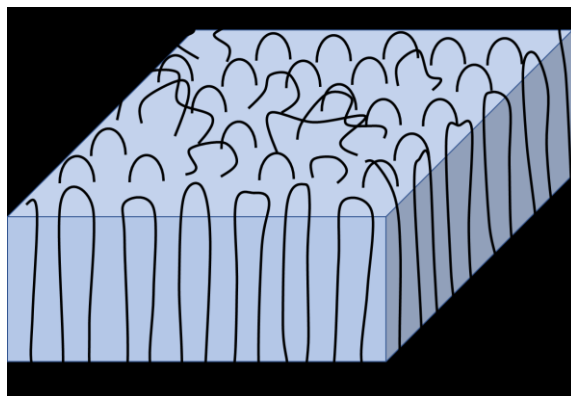


Figure 1-25: Schematic of a polymer lamella.

Polymer crystal propagation starts with the formation of a lamella. The initial lamella developed from the nucleus is termed the founding lamella because all subsequent lamellae will develop from it and its influence on the surrounding polymers.^{90,91} The founding lamella grows on its own for a considerable length, in crystallizable PC samples (ester group replaced with a flexible carbon chain) it was observed with AFM to grow to over 1 μm before other lamellae began to develop and grow outward from the nucleus.⁹⁰ In this research the length of the flexible carbon chain is denoted in the abbreviated BA-C n , where the n indicates the length of the carbon chain.⁹⁰ Time-resolved AFM images of the entire process are shown in Figure 1-26. A white dot in the phase contrast AFM image indicates the formation of a nucleus (Figure 1-26A) that serves as the nucleation point of the founding lamella, which grows outward in two directions (Figure 1-26, B-F). After 186 minutes (Figure 1-26G), growth of subsidiary lamellae starts to develop from the edges of the founding lamella. These subsidiary lamellae become larger and increase in number as the reaction progresses (Figure 1-26, I-P).

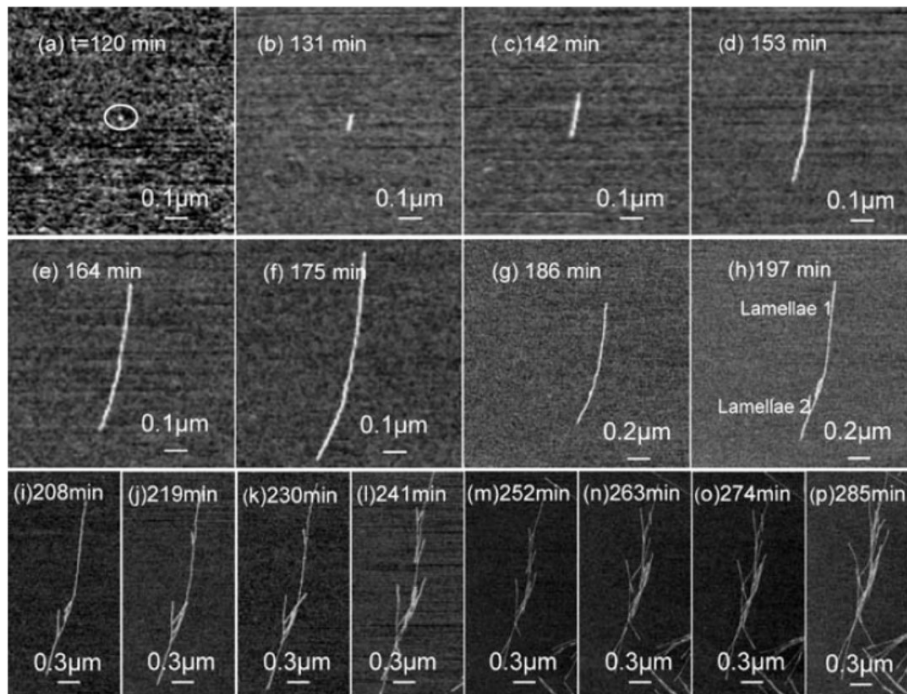


Figure 1-26: A series of AFM phase images obtained on a BA-C8 film at room temperature. (A) An embryo; (B) a short lamella (founding lamella) developed from the embryo shown in a (C–F). The growth of the founding lamella; (G–P) branching and splaying apart of the subsidiary lamellae.⁹⁰

Reprinted with permission from Ref. 90. Copyright (2005), Springer.

As the subsidiary lamellae become larger and more numerous, they become nucleation sites for additional lamellae growth. The founding and initial subsidiary lamellae grow considerably without much nucleation, developing into a spherulite skeleton. This spherulite skeleton subsequently grows into a spherulite as additional lamellae splay off from them.^{90,91} Studies of polystyrene and polypropylene have shown that initially only a few dominate lamellae develop, forming the “skeleton”.^{91,96,97,98} AFM analysis indicated that at early stages of crystallization (Figure 1-27A) only a few straight lamellae are emanating from the core. Interstitial spaces between the lamellae penetrate quite deep into the growing crystallite.⁹⁸ This interstitial space is filled with lamellae as the crystallization proceeds (Figure 1-27, B to D). These lamellae form either by nucleating from the dominant lamellae or from screw dislocations in the growing interstitial lamellae. Propagation of these subsidiary lamellae subsequently leads to further splaying and branching.⁹⁸ The morphology of crystallites eventually evolve into 3D spherulites as shown by scanning electron microscopy (SEM) analysis (Figure 1-28).

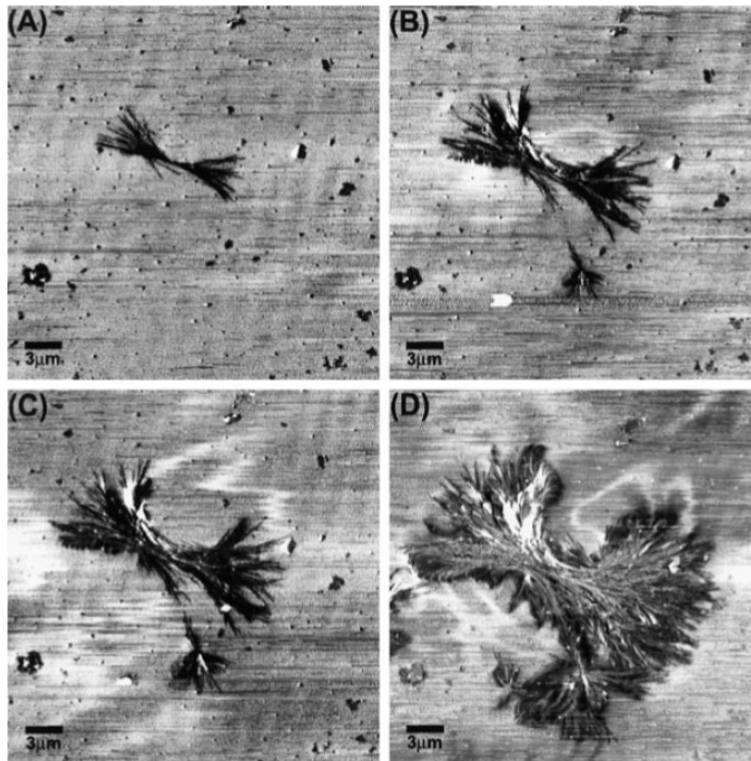


Figure 1-27: AFM phase images of poly(ϵ -caprolactone) hedrite growing at 56 °C; the images in (b), (c) and (d) correspond to elapsed times of 244, 290, and 551 min, respectively, with respect to the image in (a).⁹⁸

Reprinted with permission from Ref. 98. Copyright (2000), *Elsevier*.

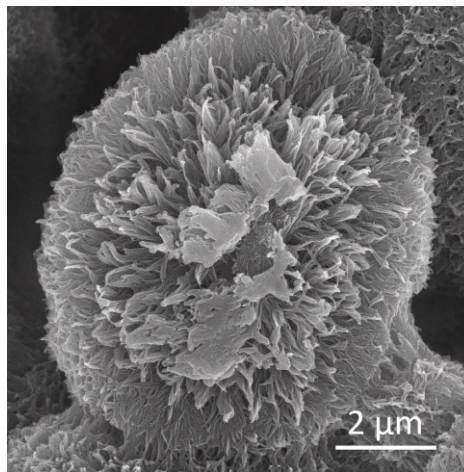


Figure 1-28: SEM image of a complete spherulite formed in solvent treated PC.

Pre-existing lamellae initiate crystallization at their edges by affecting this balance between stability and disorder. As discussed earlier, not all the polymer chains may incorporate into a nearby lamellae, which leaves part of the chain free to interact with the

amorphous matrix. Partially incorporated polymers have less mobility and therefore less entropy, resulting in increased crystallization incited by these chains.⁹¹ Moreover, their presence and restricted movement disturbs the amorphous matrix, reducing the entropy of neighboring unincorporated chains and inciting nucleation.⁹¹ Figure 1-29 illustrates the nucleation of crystallization near lamellae, small developing lamellae can be seen near the edges of a mature lamellae.⁹¹ It is clear that the new crystallites are not building off the existing lamellae, they are developing ~10 nm away from the existing crystalline domains out of disturbed polymer chains.⁹¹ In subsequent AFM images some of these lamellae can be seen developing further, while other embryos completely disappear because they did not reach a critical size.⁹¹

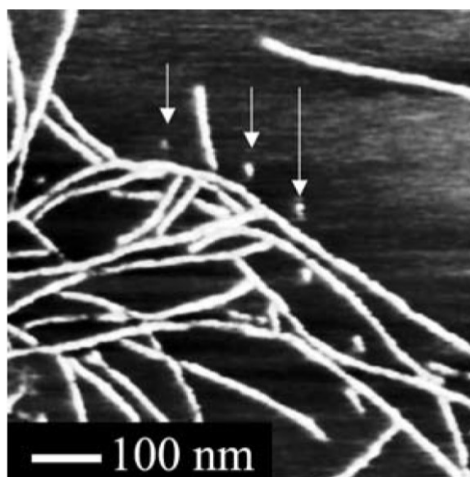


Figure 1-29: AFM phase image obtained on a BA-C12 film. Three induced nuclei are observed at about 15 nm away from the parent lamella.⁹⁰

Reprinted with permission from Ref. 90. Copyright (2005), *American Chemical Society*.

The growth rate of polymer crystallites fluctuates between T_g and T_m . At temperatures just above T_g , polymer chains are quite immobile, making reorganization difficult.^{90,91} As the temperature increases and polymer chains become more mobile the rate of growth increases. This increase in the rate of growth, which is limited by the diffusion of polymer chains, has been confirmed experimentally.⁹⁹ The growth of crystallites, however, are suppressed at elevated temperatures (near T_m) where the formation of ordered structures are less thermodynamically favored and decompose more easily. Additionally, the increased mobility of polymer chains at high temperature facilitates polymer to fold into the lamellae and adjust their conformation. Which results in fewer partially trapped polymers to incite branching through secondary crystallization.⁹¹

Polymer crystallization can be modeled thermodynamically by considering the Gibbs free energy (ΔG) of the reaction.^{100,101}

$$\Delta G = \Delta H - T\Delta S \quad (6)$$

The enthalpy (ΔH) of crystallization is negative due to increased interactions, such as dipole-dipole, H-bonding, and van der Waals, between neighbouring chains of polymer in crystalline lamellae. On the other hand, (ΔS) is negative for molecular systems becoming ordered. The magnitude of enthalpy is directly correlated to the size of the crystallites. Therefore, the melting of large crystallites occurs at higher temperatures, where the entropic contribution dominates. Melting (T_m) of the crystallites occur when the change in Gibbs free energy equals to zero ($\Delta G = 0$).^{100,101} Although this is an over simplified thermodynamics model, the inherent competition between entropy and enthalpy is vital to understand polymer crystallization, particularly when solvent incites the crystallization process.¹⁰⁰

1.4.4. Solvent-Induced Crystallization (SINC) of Polycarbonate

Some solvents can induce crystallization in polymers by forcing the molecular chains apart (much like a plasticizer), which gives them more freedom to conform, allowing molecular motion at lower temperature (a lower T_g). Solvent treatment can even induce rapid crystallization in polymers with stiff backbones which are difficult to crystallize. This apparent lowering of T_g can be explained/predicted by considering changes in Gibbs free energy through the Flory-Huggins solution theory. The Flory-Huggins solution theory attempts to model polymer solvation thermodynamically using a lattice model to account for the great dissimilarity in polymer and solvent size.^{101,102}

In the Flory-Huggins theory the polymer and solvent molecule are assumed to occupy spaces in a 3D lattice. This lattice consists of N sites of equal volume v_0 , the number of molecules in the lattice are defined as n_1 and n_2 for the respective species.¹⁰¹⁻
¹⁰⁴ The model also defines the degree of polymerization of the species as x_1 and x_2 , allowing for consideration of polymer blends as well. The model critically assumes that the volume of each monomer of polymer, solvent molecule, and the lattice volume are all equal.¹⁰¹⁻¹⁰⁴ Thus the volume occupied by a polymer or solvent in the lattice is defined as:

$$V_i = n_i x_i v_0 \quad (7)$$

and the volume fraction (ϕ_1) of a solvent in the lattice is:

$$\phi_1 = \frac{n_1}{n_1 + n_2 x_2} = \frac{n_1}{N} \quad (8)$$

while the volume fraction (ϕ_2) of a polymer in the lattice is:

$$\phi_2 = \frac{n_2 x_2}{n_1 + n_2 x_2} = \frac{n_2 x_2}{N} \quad (9)$$

The entropy of a polymer chain is dominated by the number of possible configurations for the chains. By assuming the chains are ideal (the number of conformations available to the polymer is same in free space and in solution), the entropy of a polymer molecule can be defined by the volume available to it for translational motion.^{102,105} The entropy for a molecule can then be written as:

$$S_i = k_B \ln V_i \quad (10)$$

where S_i is the entropy and k_B is the Boltzmann constant ($1.38064852 \times 10^{-23} \text{ m}^2 \text{ kg s}^{-2} \text{ K}^{-1}$). To calculate the change in entropy the entropy of the polymer and solvent in their pure state are subtracted from their entropy as a mixture:

$$\Delta S^M = n_1 S_1^m + n_2 S_2^m - n_1 S_1^p - n_2 S_2^p \quad (11)$$

where m denotes mixture and p denotes pure. By plugging equations (6 and 8) in for the solvent and polymer in their pure forms and as mixtures the equation simplifies to:

$$\Delta S^M = n_1 k_B \ln(n_1 + n_2 x_2) + n_2 k_B \ln(n_1 + n_2 x_2) - n_1 k_B \ln(n_1) - n_2 k_B \ln(n_2 x_2) \quad (12)$$

$$\Delta S^M = -k_B \left(n_1 \ln\left(\frac{n_1}{n_1 + n_2 x_2}\right) + n_2 \ln\left(\frac{n_2 x_2}{n_1 + n_2 x_2}\right) \right) \quad (13)$$

The terms in the natural logs are the volume fractions defined earlier:

$$\Delta S^M = -k_B (n_1 \ln(\phi_1) + n_2 \ln(\phi_2)) \quad (14)$$

The entropy of mixing a polymer and solvent will not be as large as two small molecules mixing because the polymer can occupy a more limited subset of states. The

entropy of polymer mixing will however always be positive due to the increasing number of available states, indicating that mixing of polymer and solvent is thermodynamically favorable.

Mixing is entropically favored, however, an enthalpic change also occurs as the environment of polymers and solvent molecules changes. There are three interactions to consider, polymer-polymer, solvent-solvent, and polymer-solvent interactions, which are defined as w_{11} , w_{22} , and w_{12} , respectively. The change in the total interaction is defined as:

$$\Delta w = w_{12} - \frac{w_{22} + w_{11}}{2} \quad (15)$$

For each Δw there is a material specific interaction parameter (X):

$$X_{12} = \frac{z}{k_B T} (\Delta w) \quad (16)$$

where z is the coordination number of the lattice and T is the temperature. It is rather impractical to measure the totality of interactions, so X_{12} is often estimated using Hildebrand solubility parameters (δ), a numerical representation of the degree of interaction between molecules.^{106,107} It is the square root of the cohesive energy density which encompasses all dipole, van der Waals, and H-bonding forces and does not discriminate between them. The cohesive energy density is calculated from the heat of vaporization (H_v) divided by the molar volume (V_m):^{106,107}

$$\delta = \sqrt{\frac{\Delta H_v - RT}{V_m}} \quad (17)$$

The closer the solubility parameters of the polymer and solvent are, the more likely they are to be compatible and mix; X_{12} can be defined as:

$$X_{12} = \frac{V(\delta_1 - \delta_2)^2}{RT} \quad (18)$$

where V is the volume of a polymer segment.

With X_{12} the enthalpy can be defined as:¹⁰⁴

$$\Delta H^M = k_B T \phi_1 \phi_2 X_{12} \quad (19)$$

The total Gibbs free energy for the mixing of a polymer and solvent can then be defined as:

$$\Delta G^M = RT(n_1 \ln(\phi_1) + n_2 \ln(\phi_2) + \phi_1 \phi_2 X_{12}) \quad (20)$$

In this equation n has been converted to moles by converting from k_B to R (8.3144 J·K⁻¹·mol⁻¹) through multiplying by Avogadro's number ($N_A * k_B = R$).

In summary, when mixing of polymer and solvent is favorable, which correlates to an increase in the entropy (outcompetes the decrease in the enthalpy of the system), the formation of polymer crystallites is thermodynamically unfavorable. In this case the solvent dissolves the polymer. The increase in entropy can be attributed to increased free volume and conformational freedom of the polymer chains, while the change in enthalpy is associated with the change in intermolecular interactions (dipole, van der Waals, H-bonding). As the dissimilarity between the polymer and solvent increases the enthalpy increases. If the polymer and solvent are too dissimilar the enthalpy will be too high, and such a solvation will not be favorable.

The enthalpy of the pure solvent and polymer will be rather low, molecules are generally quite stable in pure form. If the solvent molecule does not interact favorably with the polymer, the enthalpy of the mixture increases significantly. In this case, the mixed state (solvated polymer) is not particularly stable, and the polymer crystallizes to reduce the enthalpy of the polymer and expel solvent from the crystals, further reducing enthalpy. Crystallization will proceed if the enthalpy change can thermodynamically overcome the large loss of entropy associated with crystallization and expulsion of solvent. There is of course a limit to how dissimilar the polarity and molecular interactions of the solvent and polymer can be, if the enthalpy of mixing is too high, the polymer will be insoluble. The best solvents for polymer crystallization are relatively poor small molecule solvents; which because of favorable entropy of mixing, penetrate the polymer network to swell it, but do not stabilize the polymer enough to fully dissolve it.

Once crystallized, PC becomes insoluble in acetone due to increased enthalpy of crystallized PC, which can now outcompete the entropy of mixing. Stacking between the ring structures along the c -axis of crystalline PC segments stabilize the crystalline structure.^{64,66} The carbonate moieties in PC line up with the methyl moieties on adjacent chains, reducing repulsion.^{64,66} In contrast, enthalpically favorable interactions between

PC and acetone are minimal, there are no hydrogen bonding sites to interact with the carboxyl groups on either species. Acetone also does not interact with the aromatic rings along the PC chains which are responsible for stabilizing the crystallized form of PC.

Turska and colleagues, investigated the kinetics of SINC of PC with several solvents included dichloromethane (DCM) and acetone, a good and relatively poor solvent respectively.^{108,109} Both solvents penetrated and swelled the polymer network, but the kinetics of swelling by acetone were much faster, swelling 10 μm films in 3~5 min compared to at least 15 min for DCM.¹⁰⁸ This was attributed to the smaller size of acetone, facilitating its penetration into the polymer matrix.^{108,109}

Calorimetry measurements of the SINC process were performed, the swelling and crystallization processes were identified by the heat evolved. When treated with DCM swelling occurs first followed by crystallization over the next 10-30 min, as identified by two peaks.¹⁰⁸ In contrast, when treated with acetone the swelling and crystallization processes occur simultaneously and only one peak is present. Visual analysis of the swelling and crystallization fronts was performed. The acetone swelling followed by the crystallization fronts moved at the same rate through the polymer film, the whole process terminated in 3-5 min.^{108,109} This behavior fits with the description above, the less polar DCM has more favorable enthalpic interactions with PC, which increases the free energy barrier for rearrangement in crystalline domains, slowing the process. In acetone treated PC the energy barrier to crystallization is lower, and acetone incites heterogeneous nucleation as indicated by the monodispersed size of spherulites.¹⁰⁸ DSC measurements showed that acetone crystallized samples have a higher degree of crystallinity and higher melting point; more total polymer crystallized into larger (more stable) crystalline domains.¹⁰⁸

Polymer crystals are nowhere near perfect, the high energy barriers to rearrangement imposed by their entangled nature (and stiffness in the case of PC) lead imperfect crystallization. The morphology of crystallized PC depends on the length of time PC is annealed in crystallizing conditions as illustrated by the DCM studies referenced earlier.^{108,109} Polymer crystals therefore exist in metastable states dictated by the fastest processes that can overcome the free energy barrier. The height of this barrier is determined by the conditions; i.e. the compatibility of the solvent applied, the presence of plasticizers to increase the free volume, and the thermal history of the polymer (pre-

existing crystalline or semi-crystalline domains to incite crystallization).^{90,91,100} Based on their lower energy barrier of rearrangement, less perfect (smaller) crystals will develop faster but will also be less stable and susceptible to rearrangement into more perfect crystals characterized by a greater lamellae thickness; this is the process occurring during annealing.

The T_m of PC after SINC can give insight into the metastable state PC settled into. Analysis of PC crystallized with acetone vapor illustrates this relationship, when treated for a short time (0.7 hr) the first melting peak for PC is 171°C and increases steadily to 179°C as the treatment time is increased to 56 hr.⁶⁷ T_m can be directly correlated with lamellae thickness based on the fold surface free energy ($\sigma_e = 94 \text{ erg/cm}^3$) heat of fusion per unit volume ($\Delta H_f^\circ = 1.1 \times 10^9 \text{ erg/cm}^3$) and the melting temperature of a perfect crystal ($T_m^\circ = 318 \text{ }^\circ\text{C}$) by equation 21:⁶⁷

$$T_m = T_m^\circ \left(1 - \frac{2\sigma_e}{l\Delta H_f^\circ} \right) \quad (21)$$

The lamellae thickness was calculated to have increased from 67.7 Å to 72.6 Å over the treatment. The imperfect crystals form quickly in the first hour, afterwards the much slower rearrangement process can occur based on the pre-existing lamellae.⁶⁷ During the process of lamellae thickening the crystallinity of the PC increased, indicating amorphous PC was being consumed. During the annealing, amorphous sections near lamellae may form fringed micelles or be incorporated into crystals, along with rearrangement of fully and partially incorporated PC chains.⁶⁷ The depressed T_m of PC treated with DCM compared to acetone illustrate the influence of kinetics on crystallization. In DCM, which is a better solvent for PC, the kinetically faster smaller lamellae are the only ones capable of forming. Extending treatment time increases the T_m , but the crystal perfection is limited by the initial lamellae which formed. In comparison, after 30 min of acetone immersion the T_m of both melting peaks of PC are higher than PC treated with DCM at much higher temperatures and for much longer.¹⁰⁸ Since larger lamellae have enough energy to form at the onset, the initial population of lamellae will contain more of them.

1.5. Research Objective and Thesis Structure

As described in section 1.2, conventional nanofabrication methods rely on expensive equipment and are time consuming. Replication methods enable existing masters to be copied at a much lower cost, but still require precise set-up and conditions. Therefore, a bench-top technique that can replicate many masters with diverse properties is highly sought after in resource limited, academic, and commercial setting. The objective of this thesis is to develop such a bench-top nanocontact replication system and explore its application for fingerprint phantoms, micro/nanostructure replication, and superhydrophobic surface fabrication.

This thesis is compiled in a non-traditional manner; it consists four main chapters of results (which are essentially slightly modified publications) and three periphery chapters of general introduction and conclusions. Besides this present chapter, which serves as the general introduction of the background knowledge and literature review of topics relevant to the thesis research, Chapter 2 is to introduce the prominent methods used in this research to characterize materials' surface structures and relevant properties; SEM, AFM, and contact angle goniometry. Chapter 3 will discuss the replication of fingerprints to fabricate novel 3D fingerprint phantoms for developing sensors with higher resolution and more precise algorithms. Built upon this success, fabrication of conductive fingerprint phantoms for developing capacitive fingerprint sensors is detailed in Chapter 4. Chapter 5 presents the development and optimization of the replication protocol and its efficacy is illustrated by replicating masters across several length scales from microfluidics to nanostructure arrays. Straightforward fabrication of superhydrophobic PDMS from crystallized PC templates is presented in Chapter 6. Finally, Chapter 7 summarizes the major findings of this work and outlines future directions for this research.

Chapter 2. Techniques and Methods

Both the mechanistic and applied facets of this research are concerned with the surface/interface of the materials. Fingerprint and nanostructure replication applications require careful comparison of surface features to confirm fidelity. Development of superhydrophobic properties on a material is dictated by an interplay of micro and nanostructures. Concurrently, polymer crystallization can be monitored by observing the development of semi-crystalline spherulites. Scanning electron microscopy (SEM) and AFM, two of the most powerful surface imaging techniques, as well as surface wetting studies were primarily used to characterize PC and PDMS surfaces. SEM is an excellent tool for observing spherulite growth and monitoring fidelity over many length scales. AFM provides 3D topographical information which is invaluable to studying nanoreplication fidelity. Wetting characterization represents an important measure of success for developing superhydrophobic self-cleaning surfaces.

2.1. Scanning Electron Microscopy

SEM was used extensively in this research and in the field of nanoreplication, thus a short explanation of its principles is warranted. Typically, conventional microscopes have difficulty above 1000x magnification. Optical microscopes are limited by the wavelength of the imaging radiation and cannot resolve features much smaller than it based on the Abbe diffraction limit:

$$d = \frac{\lambda}{2n \sin \theta} \quad (22)$$

At the energies applied in electron microscopy, the electrons have a wavelength of 0.027-0.0009 nm, far below the wavelength of light used in optical microscopy.¹¹⁰ Like light the electrons interact with the atoms of the surface, the signals produced (light, electrons) are collected with detectors. Images produced by SEM have achieved ~1 nm resolution.^{110,111}

To begin, we start with the source of the electrons, which is typically a tungsten filament, LaB₆ or Schottky emitter, or a field emission tip.^{111,112} The electron “gun” typically consists of a cathode (one of the aforementioned electron sources) held at high negative potential to produce the electrons, and an electron accelerating region to guide them

toward the sample.¹¹¹ A typical tungsten electron gun is shown in Figure 2-1, the V-shaped wire labelled (F) is the tungsten cathode. It is heated with a DC current to 2700 K, at which point it begins to emit electrons via thermionic emission.¹¹¹ Thermionic emission occurs when electrons have enough energy to escape from the conduction band to the vacuum level (the energy of a stationary electron outside of the surface).¹¹¹ As the temperature is increased more electrons are capable of escaping. Tungsten is used as an electron source because of its extremely high cohesive energy density and melting point (3650 K).^{111,112} It can withstand the high temperatures needed to overcome the work function (Φ) of tungsten (4.5 eV); the energy difference between the top of the conduction band and the vacuum level.¹¹¹

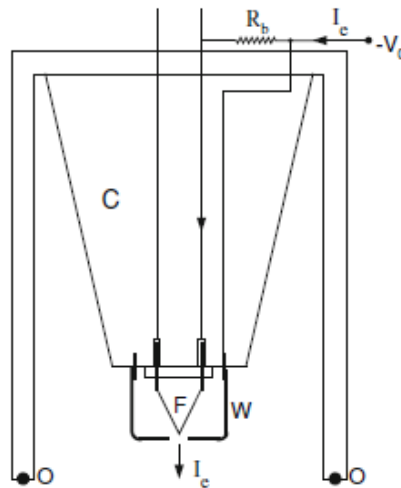


Figure 2-1: Thermionic electron gun containing a tungsten filament (F), Wehnelt electrode (W), ceramic high-voltage insulator (C) and an o-ring seal (O) to the lower part of the TEM column. An autobias resistor (R_b) (actually located inside the high-voltage generator) is used to generate a potential difference between (W) and (F), thereby controlling the electron-emission current. Arrows denote the direction of electron flow that gives rise to the emission current.

Reprinted with permission from Ref. 111. Copyright (2016), Springer.

An alternative approach is to use a material with a smaller work function, requiring less heating.¹¹¹ LaB_6 is the preferred material in this case. A crystal of LaB_6 is heated to 1400-2000 K by passing current through it.¹¹¹ These electrodes provide comparable emission current to a tungsten electrode but in a smaller area, consequently the electron beam produced can be focused over a smaller area.¹¹¹ While relatively expensive, LaB_6 sources last longer because of their lower operating temperature.

Surrounding both the LaB₆ and tungsten filaments is a Wehnelt cylinder (W), a metal electrode surrounding the filament apart from a small hole for the electron beam.¹¹¹ The Wehnelt cylinder effectively controls emission current through a negative potential, which inhibits electrons from leaving the cathode except very near its tip which is situated near the hole in the cylinder where the potential is less negative.¹¹¹ By increasing the negative bias the emitting area and emission current are decreases.¹¹¹ Through a resistor (R_b), the voltage applied to the filament is reduced compared to the Wehnelt cylinder.¹¹¹ The resistor helps stabilize emission current; as current increases, the voltage bias increases which suppresses emission in a negative feedback loop.¹¹¹ The resistance can also be manually modulated to easily vary the bias and control emission current.^{111,112}

Emission can be enhanced by applying an electrostatic field to the cathode surface, which lowers the work function and enables emission at lower temperatures.¹¹¹ This is known as the Schottky effect, Schottky sources require temperatures of only 1800 K to provide sufficient emission.¹¹¹ If the electrostatic field is sufficiently high, electrons can escape the surface via quantum tunnelling, which is known as field emission.¹¹¹ The electric field provides enough velocity to electrons for the quantum tunnelling probability to be high.¹¹¹ Field emission guns do not require any thermal excitation.¹¹⁰⁻¹¹²

Regardless of the electron source, the beam is focused onto the sample by ring-like axially symmetric magnetic lenses called condenser lenses. These lenses focus the beam to be as small as possible, because the beam size determines the resolution.^{110,111} A schematic representation of an SEM is shown in Figure 2-2, the condenser lenses are just under the electron gun. Unlike optical microscopes or TEM which perform traditional imaging, SEM analysis is performed via a raster scan.¹¹¹ Instead of irradiating the whole sample and focusing the image, small sections are irradiated by the SEM, each representing a “pixel” in the final image.^{110,111} Rastering of the electron beam is achieved by the scan coils (shown in Figure 2-2) which generate a magnetic field to deflect the electron beam.¹¹¹ To increase image magnification the size of the scanned area is decreased while the number of pixels stays the same, each “pixel” covering a smaller area. The resolution is therefore limited by the size of the beam, if it becomes larger than the “pixel” signal from outside it will be erroneously collected.

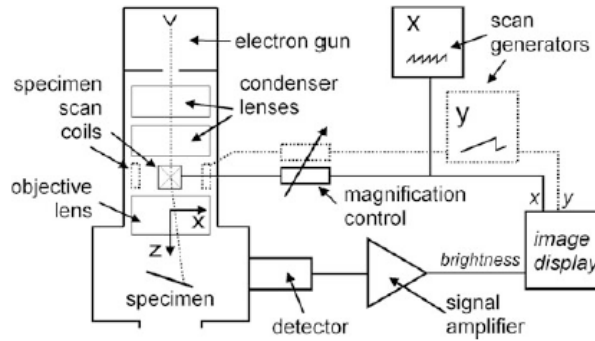


Figure 2-2: Schematic diagram of a scanning electron microscope. The same x- and y-scan waveforms are applied to the SEM column and to the display device. Signal from a detector modulates the brightness of the display.

Reprinted with permission from Ref. 111. Copyright (2016), Springer.

When the accelerated (primary) electrons reach a surface, they are scattered by elastic and inelastic collisions. The inelastic collisions involve “forward” scattering (by interacting with atomic electrons) with deflections less than 90° and fractional energy loss.¹¹¹ After numerous collisions the electrons eventually come to rest and are absorbed, the maximum depth this occurs at is called the penetration depth.¹¹¹ Beneath the area subjected to the electron beam exists an interaction volume where primary electrons are absorbed. This area, shown in Figure 2-3, is wider than the beam spot due to lateral scattering.^{111,112} The volume of this area is determined by the kinetic energy of electrons (lower energy electrons come to rest sooner), and the size of atomic nuclei (larger nuclei deplete the electrons via elastic scattering).¹¹¹

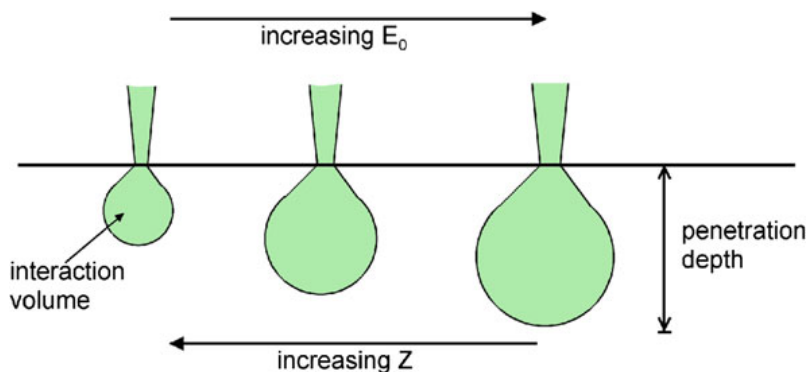


Figure 2-3: Schematic dependence of the interaction volume and penetration depth, as a function of the kinetic energy E_0 and atomic number Z of the primary electrons.

Reprinted with permission from Ref. 111. Copyright (2016), Springer.

Any energy lost by primary electrons during inelastic scattering is transferred to atomic electrons it collides with.^{110,111} Some of this energy is expended to escape from the atomic orbital, the rest becomes kinetic energy of the newly released electron (secondary electrons).¹¹¹ Secondary electrons will also interact with the material and scatter inelastically, most expend their energy and come to rest within the material.¹¹¹ Secondary electrons produced close to the surface (< 2 nm) may escape so the signal produced by them is primarily from the surface of the material.^{111,112} Primary electrons can yield between 0.1-10 secondary electrons depending on the electron energy and material properties.¹¹¹ The amount of secondary electrons is also influenced by topography, yield is lowest when the beam is perpendicular and increases as the angle deviates from surface-normal.¹¹¹ This has the effect of highlighting areas where height changes since more secondary electrons are emitted.

Secondary electrons are collected with an Everhart-Thornley detector. Electrons are first accelerated toward a mesh with a positive bias of several hundred volts, then further toward a scintillator with a bias of several thousand volts.^{110,111} The scintillator is a cathodoluminescent material which emits light when bombarded by electrons, i.e. phosphor, light emitting plastic, and garnet (oxide).¹¹¹ Higher energy electrons will produce a greater number of photons.¹¹¹ Light from the scintillator is then directed into a photomultiplier tube, which absorbs photons and produces photoelectrons to generate a signal.¹¹¹

Electrons that scatter elastically and with a scattering angle greater than 90° are called backscatter electrons.^{110,111} Since very little energy is transferred in their collisions, backscatter electrons have similar kinetic energies to the primary beam.¹¹¹ The backscattering coefficient increases with atomic number, since the atomic nucleus is responsible for elastic scattering. Backscatter electron images will show contrast variation due to chemical composition while secondary electron images primarily show topography.^{111,112} Backscatter electrons are produced as deep as half the penetration depth, since the other half of the energy is needed to leave the material.¹¹¹

Backscatter electrons can be detected with a scintillator/photomultiplier tube system, but this is inefficient since their high energy makes them rather unresponsive to electric fields used to collect electrons.¹¹¹ The Robinson detector, a ring shaped scintillator placed just below the objective lens and above the sample stage was designed to improve

efficiency.¹¹¹ It is rather large, in order to cover most angles and collect more backscatter electrons.¹¹¹ Light produced in the detector is guided by internal reflection to a photomultiplier tube, generating a signal.¹¹¹ Solid state detectors with large areas were designed under the same principle.¹¹¹ Doped silicon dioxide consisting of a n-type and p-type layer is used.¹¹¹ Backscatter electrons excite electrons within the detector to the conduction band, producing a current within the detector.¹¹¹

Since this research is primarily concerned with the surface topography secondary electron imaging proved useful. The non-conductive materials (PC, PDMS) imaged herein were coated with conductive gold and iridium, which allowed backscatter electron imaging, and localized the backscatter electron signal at the surface for useful topographical analysis as well.

2.2. Atomic Force Microscopy

AFM is an important characterization technique for precisely measuring the topography of a surface. For its incredible sensitivity, AFM is used extensively to analyze the products of nanofabrication and the roughness of surfaces. AFM imaging was used extensively in this work to analyze and compare masters and replicas.

The development of AFM was precipitated by the development of scanning tunnelling microscopy, wherein the electron tunnelling current between an atomically sharp tip and the surface is measured to achieve a very accurate determination of their separation.^{113,114} The tunnelling current manifests at a distance of 0.5-1 nm and increases exponentially as the tip sample distance is decreased.¹¹³ This current is used to both measure and control the tip sample distance via a feedback mechanism.¹¹³ Piezoelectric actuator elements facilitate the precise movement of the tip.¹¹³ Scanning tunnelling microscopy is however limited to conductive surfaces.^{113,114}

The principles of scanning tunneling microscopy were applied to measure surface topography through other interactions. AFM was developed by measuring the attractive and repulsive forces that manifest between a tip and a surface instead of the current.^{113,115} As a tip is brought into contact with a surface, 3 different regions manifest in the force curve (Figure 2-4). Initially the tip is too far from the surface for interaction and the force is negligible, as the tip approaches the surface an attractive force develops, generated by

Van der Waals interactions caused by instantaneous polarization of atoms.¹¹³ At very small distances (a few angstroms) the repulsive force builds up rapidly due to overlap of electronic orbitals. For any attractive force, there are two points, as shown in Figure 2-4, with that value on opposite sides of the curve. Care must be taken to consistently measure on one side of the curve to maintain a consistent relationship between force and sample distance.¹¹³

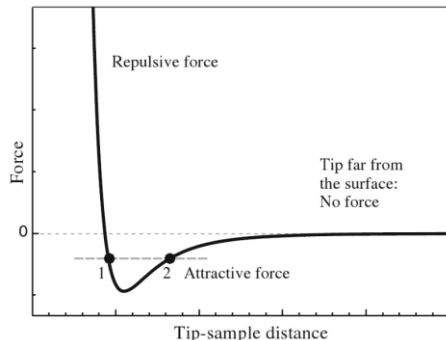


Figure 2-4: Qualitative behavior of the force between tip and sample as function of tip-sample distance.

Reprinted with permission from Ref. 113. Copyright (2015), *Springer*.

The key components of an AFM that allow for the precise measurement of force between a sample and the tip are shown in Figure 2-5. The tip is mounted onto a cantilever which acts as a spring and has a known spring constant.^{113,116} The deflection of the cantilever is conventionally measured with a laser beam that is reflected off the back of the cantilever tip toward a split photodiode.^{113,116} The movement of the sample or the tip is controlled by piezoelectric elements like in a scanning tunnelling microscope. To measure the topography of a surface the AFM tip is raster scanned across it and the deflection the tip is measured.¹¹⁶ AFM has several imaging modes that differ in how the tip interacts with the surface during the raster scan.

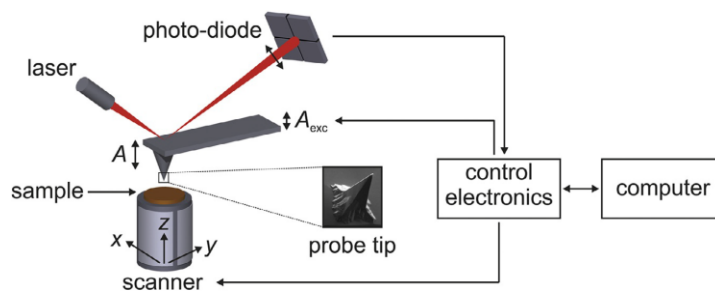


Figure 2-5: Schematic drawing of a typical AFM setup.

Reprinted with permission from Ref. 116. Copyright (2017), *Elsevier*.

The contact or static mode of operation is the simplest and original operating mode for AFM. The probe tip is brought to close proximity with the surface and first “snaps” into contact due to the attractive forces then is bent by the repulsive forces as shown in Figure 2-4. By Hooke’s law ($F = -kz$) the distance (z) the cantilever is bent by the surface can be translated to a force between the tip and sample based on the known spring constant (k) of the AFM tip.^{113,116} As the tip is raster scanned across the surface the force/tip deflection is monitored and kept at a constant value by changing the z -position via a feedback loop.^{113,116,117} By keeping the force constant the distance between the tip and sample are kept constant, the change in the z -position therefore corresponds to the surface topography. Contact mode has some distinct disadvantages, the lateral forces and repulsion between the tip and surface may damage both and the signal to noise ratio is lower than dynamic scanning modes.^{116,117}

Dynamic scanning methods were developed shortly after AFM was invented to overcome the issues associated with contact mode operation. In dynamic scanning modes the cantilever is excited to at or near its resonance frequency.^{113,116} As the vibrating tip is brought close to the surface the amplitude of the cantilever oscillation changes (generally decreases) due to Van der Waals and other electrostatic interactions.^{113,116,117} The amplitude is monitored and the z -position is controlled via a feedback to maintain a constant oscillation.¹¹⁶ During oscillation at the apex of the force curve the tip briefly taps the surface providing information about the nanomechanical properties of the surface.^{113,116} Tapping mode enables acquisition of topographical images with nanoscale resolution while limiting damage to the tip and surface.¹¹⁶ This mode is important for imaging “soft” surfaces such as polymers and biological materials which would be destroyed by constant tip sample interaction.¹¹³

Modern AFMs have incredible vertical sensitivity (< 0.1 nm), while the lateral resolution is several nanometers depending on tip geometry.^{113,117} Since AFM images are a convolution of the probe and surface geometry, the quality of an AFM image is directly correlated to the quality of the AFM tip.¹¹⁷ The smaller the end of the tip, the more precisely the surface topography can be measured.¹¹⁸ The most common AFM tips are silicon and silicon nitride (Si_3N_4) tips, Si tips can be made sharper than Si_3N_4 but Si_3N_4 tips are harder and can be made thinner.^{118,119} The merits of both materials are combined in hybrid tips.¹¹⁹ AFM tips are generally square pyramidal shaped and the angle of the sides dictates the types of structures that can be imaged. High aspect ratio tips will be more effective at

imaging high aspect ratio surface features at the cost of mechanical strength, this is qualitatively illustrated in Figure 2-6.

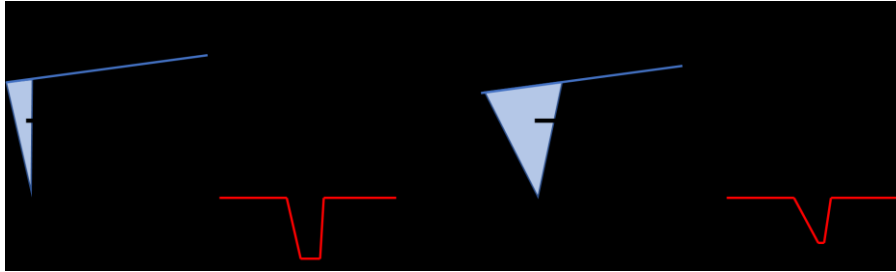


Figure 2-6: Comparison sketch of line profiles measured with a high aspect ratio probe tip (A) and a wide probe tip (B). The profiles of the trench recorded by each tip are shown in red.

Cantilevers with integrated tips are commonly constructed from Si and Si₃N₄ by lithography and wet etching.^{117,119} Metals like tungsten and nickel can also be used, these cantilevers must have a low resistance to help dissipate electric charge.¹¹⁹ Cantilevers have 2 common shapes, rectangular (like a diving board) and triangular (two arms meet at an apex where the tip is located).¹¹⁷ Si probes typically have rectangular cantilevers while Si₃N₄ probes typically have triangular cantilevers.¹¹⁷ AFM images in this thesis were recorded with ScanAsyst-Air tips; an SEM image of a ScanAsyst-Air tip is shown in Figure 2-7A. These triangular Si₃N₄ tips have a resonant frequency of 70 kHz and spring constant of 0.4 N/m.¹²⁰ Tips are between 2.5 to 8 μm in height with a front angle (FA) and back angle (BA) of 15 ± 2.5° and 25 ± 2.5° respectively as shown in Figure 2-7B.¹²⁰ The tip is not quite at the end of the cantilever, it is setback 5 μm. The side angle (SA) that determines tip width is 17.5 ± 2.5° (Figure 2-7C), and the radius of the tip end is 2 nm.

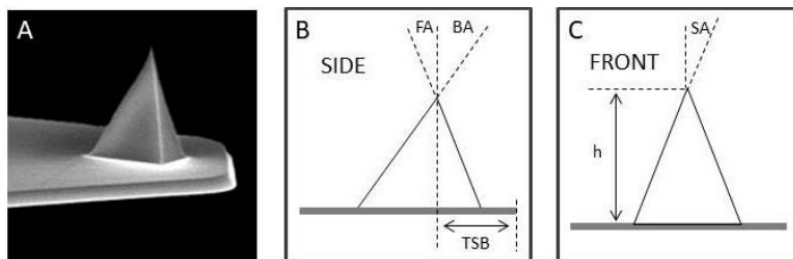


Figure 2-7: ScanAsyst-Air tip geometry, A) SEM image of ScanAsyst-Air tip B) side view C) front view.

Reprinted with permission from Ref. 120. Copyright (2020), 4D Labs.

Wear on AFM tips is a concern, tips are inherently damaged during contact with the surface.¹¹⁸ The development of tapping mode helped to minimize wear by reducing the

amount of contact with the surface. The force applied, sliding speed, and sliding distance can all affect wear rate.¹¹⁸ Harder specimens, particularly rough ones, also increase the wear rate because of abrasion by roughness features.¹¹⁸ As greater force is applied to the tip (by bringing it close to the surface) the wear rate increases. Figure 2-8 shows an AFM tip before and after a wear test to simulate normal use, it is clear that the end of the tip has been significantly blunted decreasing the resolution of the tip. At higher speeds more debris accumulates on the tip, obfuscating its function.¹¹⁸

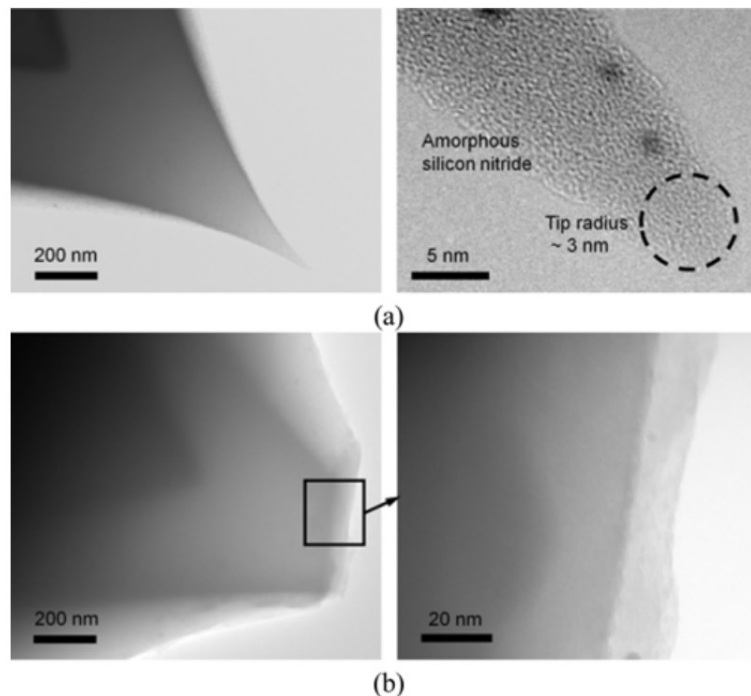


Figure 2-8: TEM image of AFM tip (a) before and (b) after the wear test with 10 nN normal force for 10 mm sliding distance of Si (100) specimen.

Reprinted with permission from Ref. 118. Copyright (2014), Springer.

The primary surfaces imaged in this thesis are soft polymers, particularly PDMS. On soft materials the repulsive force builds up less rapidly as the material can be deformed by the probe tip.¹²¹ The indentation depth can be quite significant, on neat PDMS the max indentation depth was 86 nm.¹²² Such deformation obscures boundary of the surface, the AFM tip feels an increased pull on force and a greatly increased pull off force compared to a hard surface.¹²² Large pull off forces can cause imaging errors and put torsional stress on the AFM tip. Incomplete elastic recovery of the adjacent surface can introduce further imaging errors.¹²² The tip can also become soiled by soft materials that are picked up by the tip while in contact with the surface.¹¹⁸ These issues can be mitigated on PDMS via

plasma or UV/ozone treatment, which generates a harder silica like layer, reducing the pull-on force from 5.9 to 0.2 nN and the pull-off force from 43.1 to 1.7 nN.¹²²

2.3. Contact Angle Goniometry

The wetting characteristics of a surface are defined by the contact angle of a water droplet on the surface. The exact edges of the interfaces can be difficult to discern along with the contact angle; to accurately image droplets the contact angle goniometer is used.¹²³ A schematic of a typical goniometer is shown in Figure 2-9. The sample is placed on a stage which is situated between a camera and a light source. A droplet is dispensed onto the surface by a syringe or pipette. The droplet blocks light, making a well-defined silhouette of the widest part (middle) of the droplet. Fitting software is applied to track the edge of the droplet and quantify the contact angle.

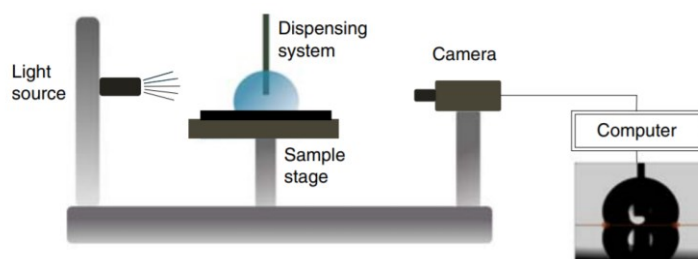


Figure 2-9: Sketch of a goniometer setup. A basic goniometer consists of a light source, an adjustable sample stage, a dispensing system (e.g. motorized syringe connected to a needle by tubing), a camera to record video, and a computer for data analysis.

Reprinted with permission from Ref. 123. Copyright (2018), *Nature Publishing Group*.

Another criterion for superhydrophobic surfaces is adhesion between the droplet and surface. The force necessary to achieve roll-off decreases as the surface becomes more hydrophobic. The two states that are used to describe the interaction between liquid droplets and rough surfaces differ in the amount of effective contact area. Water droplets in the Wenzel state are strongly pinned to the surface due to greater surface-to-water contact.^{33,34} In contrast, surface-to-water contact is significantly less in the Cassie-Baxter state. As a result water droplets adhere weakly to the surface, facilitating their movement along it.^{33,34} For this reason, the Cassie-Baxter state is desired when designing superhydrophobic/self-cleaning surfaces, while the undesirable pinning of water observed in the Wenzel state can attract more water and leave deposits of dissolved solids on surfaces upon drying.^{33,34}

The performance of superhydrophobic surfaces can be quantified by sliding angle (SA) and contact angle hysteresis (CAH) analyses. A schematic of SA and CAH measurement is presented in Figure 2-10A and B respectively. SA is the angle at which a surface must be tilted for a stationary droplet to roll off. To measure it a droplet is placed on the surface and it is slowly tilted until the droplet slides, that angle is the SA. A low SA indicates that the adhesion between the surface and droplet is relatively low. CAH is measured by adding and removing water from a droplet on a surface. Small aliquots of water are added to the water droplet, when the contact line of the droplet expands the advancing contact angle is measured.^{33,34,124} Conversely, the receding contact angle is recorded when the contact line shrinks while removing small aliquots of water from the water droplet.^{33,34,61,124} The difference between the advancing and receding angles is the CAH; a low CAH ($<10^\circ$) is associated with low adhesion to the surface and the Cassie-Baxter state.^{34,40} Since the water droplet is loosely adhered to the surface, the boundaries of the droplet can easily move. Because both SA and CAH are measures of adhesion of water droplet to the surface of interest, their values are often quite similar. Studies of superhydrophobic materials will normally report one of these to indicate the wetting state of the droplet (Wenzel or Cassie-Baxter).^{123,125}

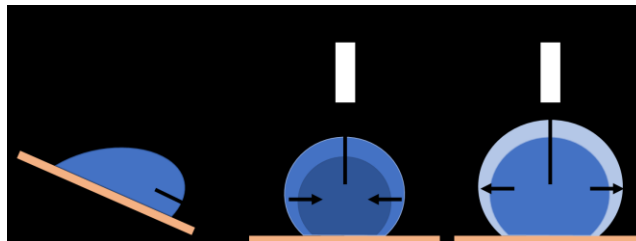


Figure 2-10: Schematic of sliding angle (A) and contact angle hysteresis (B) measurements.

How SA and CAH are related is still the topic of debate.^{123,125} Some research has found that the angle at the trailing end of a sliding droplet corresponds to the receding contact angle and the leading end contact angle corresponds to the advancing contact angle.¹²⁵ On some materials such as fluorinated silicon the SA and CAH will be the same, while on materials like alkyl ketene dimer (AKD) the CAH can be much larger.¹²⁵ Additionally, sliding angle depends on droplet size while contact angle hysteresis does not.¹²³ Both methods are indirect measures of adhesion between the droplet and the surface, but it is important to distinguish which one is being reported and why. In this thesis, SA is reported for its mechanistic similarity to the desired self-cleaning behavior.

Chapter 3. Fabrication of 3D fingerprint phantoms via unconventional polycarbonate molding

Fingerprint biometrics is a valuable and convenient security tool; every fingerprint is highly detailed and unique, we always have them on “hand”. Herein is described a novel bench-top technology of making 3D fingerprint replicas (namely, fingerprint phantoms) by exploring a unique microfabrication approach using conventional polymeric materials, to aid the development of reliable and accurate fingerprint biometrics. By pressing an impression of human fingerprints onto plastic substrates (e.g., polycarbonate chips), followed by casting with polydimethylsiloxane (PDMS, a popular elastomer), I can produce a flexible, nanoscale detailed, 3D reproduction of the fingerprint (phantoms). By testing with standard optical and capacitive fingerprint scanners (including smartphone capacitive sensors), I have shown that all three levels of fingerprint details can be precisely recorded and match well with the original fingerprint. Superior to artificial fingerprint patterns, these phantoms have the exact 3D features of fingerprints and introduce no variability compared to human sampling, which make them perfect targets for standardizing fingerprint scanners and for biometric applications.

Note: this chapter is adapted with modifications from:

Schultz, C. W., Wong, J. X. H., Yu, H.-Z., Fabrication of 3D Fingerprint Phantoms via Unconventional Polycarbonate Molding *Sci. Rep.* **2018**, 8, 9613. Copyright (2018) Nature.

I performed most of the experimental work and drafted the paper; Jessica Wong (a Masters student in Yu lab) helped with initial experimental design and manuscript proof-reading. Dr. Hogan Yu supervised the entire project and helped with writing the paper.

3.1. Introduction

The pattern of friction ridges on our fingertips form unique patterns known as fingerprints that are popularly adapted for personal identification. Forensic science relies heavily on fingerprints collected at crime scenes as evidence; fingerprint scanning systems at borders, corporate buildings, and in our mobile devices (smartphones, pads, and laptops), keep our personal identity and data safe. In all situations, fingerprint identification relies on the collection of fingerprint data for comparison and matching. Historically fingerprints were recorded by smearing ink on the fingertip and pressing it onto paper to form physical fingerprint impressions.⁵ Today fingerprints are often recorded for subsequent matching with digital fingerprint scanners either standalone or as part of a mobile device. For perspective, telecommunication experts predict that 40% of all smartphones worldwide will incorporate a fingerprint scanner, a significant increase from 30% in 2016.¹²⁶ Fingerprint scanners would be ubiquitous by 2020 as most new phones (regardless of price range) include them as default.¹²⁶ Their recording mechanisms are varied; optical scanners observe lighting differences absorbed/reflected by the ridges and valleys; capacitive scanners utilize an array of micro-capacitors to resolve capacitance difference between ridges and air; ultrasound scanners record ridge location by detecting the echo of projected acoustic pulses.¹

Fingerprint scanners are supposed to be robust to accommodate a wide range of user conditions, and accurate to ensure correct fingerprint matching, which are in fact facing challenges of spoofing and attacking with “synthetic” fingerprints.¹² Fingerprint scanners are typically first evaluated with sine wave and ronchi grating targets, which have defined feature size, relief, and grey levels.¹²⁷ By imaging targets the scanner’s resolution can be determined, its sensitivity adjusted, and operating parameters calibrated. Subsequently, actual fingerprints are sampled for quality and matching analysis with these scanners. Sampling people is costly, time consuming, and has many sources of uncontrollable errors (pressure, finger condition, sweat level, and fingerprint type) from user input. To reduce development costs manufacturers look for alternatives to testing real people, creating a demand for “phantoms” (*vide infra*) that bear the same structural and physical characteristics of human fingerprints.

An imaging phantom (or just “phantom”) is a specially designed object that mimics the properties of tissues/organs to test biomedical diagnostic devices (MRI, CT, and

ultrasound machine as examples) for accuracy and resolution calibration.¹²⁸⁻¹³⁰ The physical properties and dimensions of phantoms are accurately defined to facilitate more precise calibrations. Many types of phantoms with a large range of complexity exist today, from simple blocks of gelatinous water of certain densities to full body phantoms containing a bone-analog skeletal system, fake organs, and tissue regions mimicking muscle, skin, and fatty tissue.^{128,129} The development of patterned phantoms to test fingerprint scanners has been in demand due to the exponential increase of adapting fingerprint biometric systems for both stationary and mobile electronics as mentioned above.^{5,126,128} Non-permanent gelatin phantoms can be readily constructed by molding impressions of fingers into crafting plastics (Utile Plast™, Freeplastic™) and silicone rubbers. Gelatin phantoms approximate finger ridge relief and electrical resistance of human tissue well; however these gelatin phantoms dry out and distort quickly, for which they are not suitable for practical calibration applications.^{11,131} The state-of-the-art approach to fabricate fingerprint phantoms is the adaptation of 3D printing technology and the generation of a 3D image from a 2D fingerprint scan (simulating the ridges).¹³² Another notable progress in this field is the development of polydimethylsiloxane (PDMS) phantoms molded from a simulated ridge pattern etched in silicon, which was developed earlier by Lu *et al.* to test ultrasound scanners.¹⁸

Herein, is reported a bench-top technique to construct 3D fingerprint phantoms, for which PC is “reinvented” as an ideal candidate for solvent-assisted microcontact molding. Fingerprint impressions are first molded into a solvent-softened PC substrate (“the mold”), which serves as an enduring template (the “mold”) to cast 3D fingerprint phantoms with PDMS, the most popularly used elastomer for micro/nanofabrication. These permanent 3D replicas are derived from real fingerprint impressions with nanoscale features precisely reproduced.

3.2. From 3D PC Mold to PDMS Fingerprint Phantom

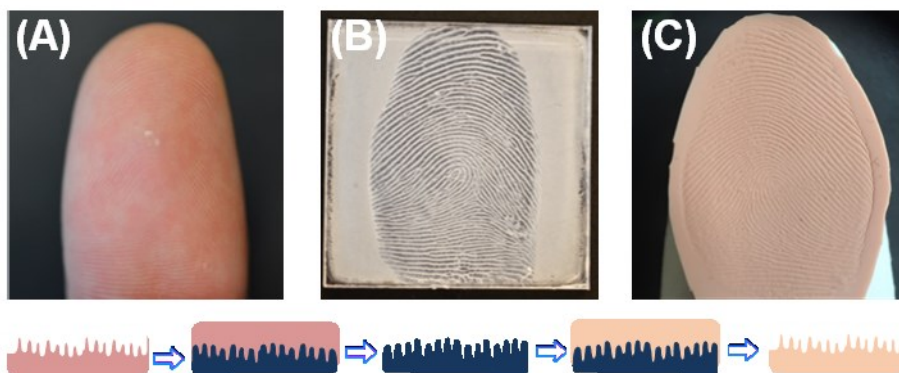


Figure 3-1: Fabrication of 3D fingerprint phantoms via solvent-assisted polycarbonate (PC) molding. (A) Finger to be impressed on PC. (B) Fingerprint impression molded on a PC plate serving as the 3D template (mold). (C) PDMS fingerprint phantom casted from the PC mold. The bottom insets show how fingerprint features were “copied” to PC and subsequently replicated to a PDMS phantom (color code: pink-finger, dark blue-PC mold, and beige-PDMS phantom).

The procedure to make fingerprint phantoms is not complicated, 3D physical “negatives” were first constructed on polycarbonate (PC) plates, followed by casting PDMS phantoms thereof (Figure 3-1). To begin with, a thin film of acetone was sprayed onto the PC plate, which penetrates the polymer network at the surface of PC causing it to swell and soften.^{59,133-135} Upon pressing with a finger, swollen PC chains are rearranged between fingerprint ridges and into pores to form a highly detailed PC “negative” of finger ridge relief, i.e., a reusable 3D mold (Figure 3-1B). Mild skin dryness can be felt upon exposure to acetone during fingerprint molding, however, the procedure is relatively safe because acetone does not penetrate the lipid layer to enter the bloodstream (to damage the skin).¹³⁶ Next step is the microcontact casting using PDMS to produce the 3D fingerprint phantom (Figure 3-1C). Microcontact molding was originally invented to copy defined micro/nano-patterns from silicon masters;^{20,137-139} here its unique application to replicate fingerprints via the creation of a highly-detailed 3D plastic mold was explored.

A few precautions should be taken when a fingerprint phantom is fabricated. The finger was rolled from one edge of the fingernail to the other to copy the entire ridge pattern. Demolding of the fingerprint phantom from the PC mold must be done carefully; after fingerprint molding the PC surface is no longer smooth, the PDMS phantom conforming to the roughness creates a large degree of adhesion between the surfaces.

On account of the flexibility of PDMS, the flat phantom can then be attached to a glove tip or wrapped around a finger before testing, which improves the usability (Figure 3-1C). These fingerprint phantoms were constructed in 2-3 hours without using any sophisticated instrumentation; the materials are inexpensive PC plates and standard PDMS kits. In comparison, the wearable phantoms fabricated by Engelsma *et al.* explored a special computer algorithm to map and convert a 2D fingerprint image to a 3D molds,¹³² which were focused on high resolution 3D printing and imaging processing technology. The PDMS phantoms created by Lu *et al.* were from designed silicon masters by adapting advanced lithography techniques in a clean room.¹⁸

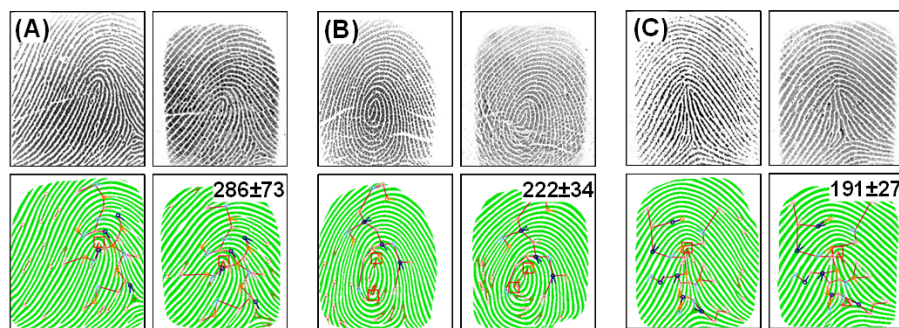


Figure 3-2: Matching of 3D PDMS phantoms with original fingerprints. (A) Fingerprint with a loop core. (B) Fingerprint with a whorl core. (C) Fingerprint with a tented arch core. Top row of each section: optical images of actual finger (left) and corresponding phantom (right) output from the same fingerprint scanner. Bottom row: binarized representation of fingerprint pattern with results of minutiae identification and matching algorithm overlaid. Similarity scores between original and phantom are displayed on the binarized phantom images (top left corner).

The quality of the PDMS phantoms was first examined for their fidelity with the original fingerprints they were copied from. Figure 3-2 depicts the matching of three representative fingerprints with corresponding phantoms; both were collected with the same digital fingerprint scanner (Secugen Hamster Plus). The fingerprints in (A), (B), and (C) belong to three most popular fingerprint classes (based on the core), *i.e.*, a loop (65% of the population's fingerprints), a whorl (30%), and an arch (5%) respectively.⁵ Appraisal between the optical images of original fingerprint (left) and phantom fingerprint (right) illustrates the exceptional quality of the PDMS fingerprint phantoms; the phantom images are practically indistinguishable from the original fingerprints as the position and size of ridges match perfectly. The dimensions of phantom ridges are clearly defined, subtleties in ridge width and height are recorded by the scanner allowing details such as pores and

ridge contours to stand out. Artificially designed finger ridges, such as those produced by 3D printing of fingerprint phantoms, do not include variation in ridge width and depth that naturally occur.⁹ Such distinct features will aid in optimizing scanners for imaging real fingerprints. In Figure 3-2, below each fingerprint image is a binary representation; anywhere that the fingerprint matching software (Verifinger SDK) detects a ridge is displayed as solid color on a pure white background. These binarized representations allow the software to match fingerprints readily based on the location of minutiae (unique fingerprint ridge arrangements). From a research perspective it shows us where the scanner identifies ridges. Like real fingerprints, phantom fingerprints can be accurately converted to a binarized image; moreover, the locations of binarized ridges are identical to source ridges indicating that real and phantom ridges are interpreted similarly by the scanner.

Several fingerprint matching algorithms are currently available, which all operate on the same principle of comparing minutiae.⁵ Particularly, the software identifies the location and direction of minutiae (e.g., where a ridge ends or splits) and compares them between fingerprints.¹⁴⁰ The output is a similarity score (Figure 3-2, bottom row of each section). The colored circles overlaying the binarized fingerprints represent minutiae identified by the system, vectors protruding from the circles identify the direction of minutiae, and the red box identifies the location(s) of the core origins.^{135,140} Minutiae that match (based on direction and location relative to the core) between the original and phantom fingerprints are connected with lines to form a “tree”, differences in the distance between matched minutiae and the number of matches contribute to the similarity score.^{135,140} The scores displayed in Figure 3-2 are an average from three phantoms constructed independently of each source fingerprint. According to the specifications of Verifinger, a similarity score of 33 represents a false acceptance rate of 0.01%, which is considered sufficient for fingerprint matching. The score for all phantoms (>190) are well above this matching threshold, indicating the ridges are faithfully copied and detectable when imaged by a standard optical fingerprint scanner. Engelsma *et al.* also achieved similarity scores ranging from 100-300 when matching their 3D-printed phantoms and the original fingerprint image.¹³² This comparison confirms that our naturally derived (*via* PC molding) PDMS phantoms should fulfill the purpose of testing the performance of fingerprint scanners and the embedded matching algorithms.

3.3. Microscopic imaging of the mold and phantom

The exceptional quality of PDMS phantoms was further validated based on the reproduction (between mold and phantom) of the three levels of physical details that exist within a fingerprint pattern.^{5,141} The first level of details is the location and arrangement of fingerprint ridges in relation to each other; the second level details (minutiae) are unique ridge patterns formed where ridges come together and differentiate.¹⁷⁸ Dimensional attributes of fingerprint ridges represent the third level of detail, including the width, edge contours, shape, the location and size of sweat pores and other permanent details such as creases or scars.^{141,142} Highly distinctive third level features are excellent for examining partial prints; as few as 20-40 pores (size and location) are adequate for a positive identification.¹⁴²

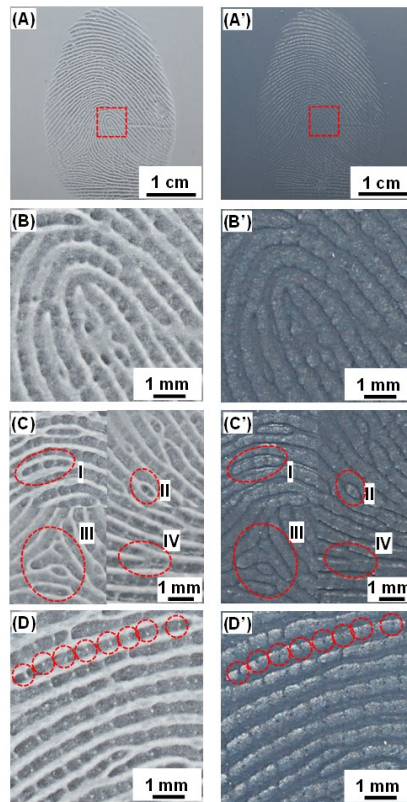


Figure 3-3: Optical imaging of the PC fingerprint mold (left) and PDMS phantom (right). (A)/(A') shows the entire fingerprint, which represents the first level details; (B)/(B') a magnified section showing the fingerprint core; (C)/(C') selected second level details such as islands (I), incipient (under developed) ridges (II), delta (III), and bifurcation (IV); (D)/(D') a high magnification image showing the third level details, i.e., sweat pores along a fingerprint ridge (as highlighted).

The complete fingerprint mold and phantom images are displayed in Figure 3-3A and A', respectively to show the reproduced first level details, *i.e.*, an overview of the discernible individual ridges. Figure 3-3B/B' highlights the fingerprint core in the PC mold and PDMS phantom, the essential feature to align fingerprints for matching.¹⁴² In Figure 3-3C and Figure 3-3C' several second level details are clearly defined, *i.e.*, an island(I), an incipient ridge (II), a delta (III), and a bifurcation (IV) as highlighted in red dash-line circles. Comparison of the first level and second level details between the mold and phantom illustrates the accuracy of our molding approach; all minutiae recorded in the mold are present in the phantom and their relative locations are identical. The minimal size and depth of third level details such as sweat pores can make them difficult to identify and define; these distinctive features however, can be perfectly recorded in the PC mold and reproduced in the PDMS fingerprint phantoms (a series of pores are highlighted along a ridge in Figure 3-3D/D'). Other third level details, such as ridge width and contours are also replicated well.

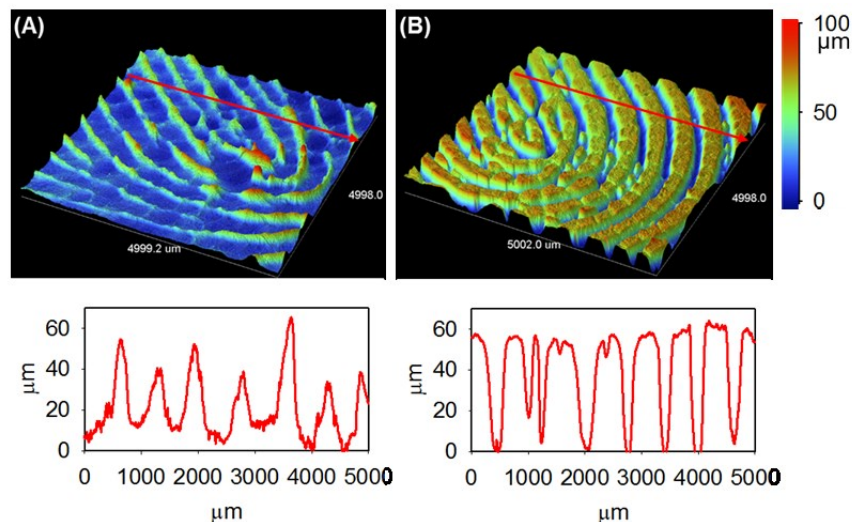


Figure 3-4: Profilometry imaging of PC fingerprint mold and PDMS phantom. Profiled 3D images of (A) PC mold, (B) PDMS phantom, and their respective cross section along the red line.

The other key feature of our phantoms is the capability of recording the depth of fingerprint ridges on PC mold and reproducing them into PDMS phantom, *i.e.*, the creation of a 3D polymeric replica of the original fingerprint. To illustrate this unique feature, both the fingerprint PC mold and PDMS phantom were imaged with a profilometer to examine the 3D morphology (Figure 3-4). For the particular fingerprint replicated, the average ridge width is between 500 and 700 μm and the height ranges from 40 to 60 μm , which is well

within the range of ridge dimensions of human fingerprints.¹⁴³ Along the ridges of the PC mold (Figure 3-4A) minute changes in depth are visible, while the peaks (corresponding to the space between ridges in the original fingerprint) have more obvious variability in height (as shown in the inset below Figure 3-4A). The PDMS phantom effectively copied the ridge impressions to reproduce subtle minutiae of the original ridges. The image in Figure 3-4B shows that the ridges were reproduced down to the third level details of a fingerprint; differences in the steepness of ridges and the depth of valleys between them can be differentiated. Along ridges variations in height manifest as pore impressions and undulations in finger tissue. Subtleties such as the angle of ridge edges partially developed and shallow ridges were also well duplicated. The cross-section profile (inset below Figure 3-4B) shows an incipient ridge and two pores located at 1200 μm , 1600 μm , and 2300 μm , highlighting the reproduced microscale details. 3D recording of third level details in fingerprint phantoms confirms that the topography of the PC mold (fingerprint impression) was effectively reproduced to the PDMS phantom. These PDMS phantoms have the advantage over other 2D image-derived phantoms because of their defined 3D morphological information,^{11,131} which is imperative for confirming proper fingerprint reading in sensor development and accuracy testing.

The fingerprint PC molds and PDMS phantoms were also imaged with SEM to probe microstructural details and examine how accurately they were transferred during nanocontact molding and casting. When swollen with a solvent (e.g., acetone), PC not only forms a malleable surface, but also undergoes rearrangement at the molecular level. Solvent molecules penetrate between polymer chains, which push them apart and increases their free volumes.^{54,65} Greater free volumes allow PC which originally existed in an amorphous state (polymer chains are too rigid to crystallize from melting) to adopt ordered configurations and crystallize into spherulites (i.e., spherical semi-crystalline regions inside non-branched linear polymers).^{54,65} Spherulites in PC range from 5 to 10 μm in size, consisting of ~ 100 nm crystalline PC tendrils which grow and branch outward from a central nucleation point with amorphous PC filling space between the tendrils.^{54,65} Evidence of PC spherulite impressions in PDMS would indicate that PDMS can mold features at least as small as spherulites or their tendrils (at micrometer and nanometer scale, respectively).

Figure 3-5A presents a low magnification SEM image of a fingerprint impression in PC; ridges are well defined; raised sections along ridges corresponding to pores (in red

circles) are visible. Figure 3-5A' displays the same area of the PDMS phantom casted from the PC mold in Figure 3-5A. Visually phantom ridges match the PC impression and their similarity to actual ridges is striking; the sweat pores can be identified as slight depressions along the ridge (highlighted in red circles). Further examination of ridge impressions (Figure 3-5B) revealed that PC forms a porous surface, as the PC chains rearranges into spherulites after swelling with acetone.^{54,65} The entire phantom surface is covered with uniformly distributed "protrusions" (Figure 3-5B'), which conform to the porous surface of the PC mold. As shown in Figure 3-5C, the PC spherulite surfaces are rough and they are interconnected with each other; their sizes vary from 5 to 10 μm . These high magnification SEM images show that the PDMS phantom (Figure 3-5C') in fact copies microscopic features as small as the spherulites from the PC perfectly. Even more remarkable, the shape of an individual spherulite can be "casted" on the PDMS phantom with the details corresponding to protruding tendrils (Figure 3-5D/D'). The surface of spherulite impressions on the PDMS phantom (Figure 3-5D') are rough at the nanometer scale, as a result of PDMS conforming to the surface of spherulites (formed on the PC mold). These SEM studies illustrate that the PC molding procedure accurately reproduces the microscopic details of the original fingerprint. A Fourier-transform infrared spectroscopy (FT-IR) spectrum of the PDMS surface (Figure A1) indicates no PC is transferred to the PDMS during casting.

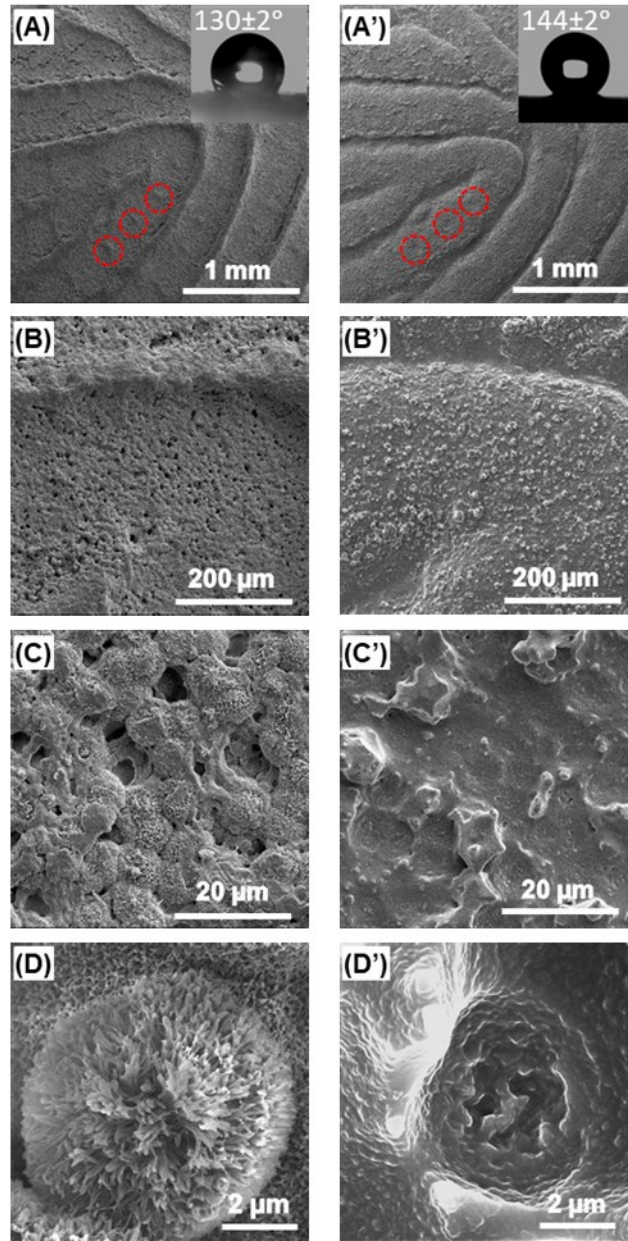


Figure 3-5: Scanning electron microscopy (SEM) imaging of PC fingerprint mold (left) and matching PDMS fingerprint phantom (right). (A)/(A') Low magnification images of ridges; (B)/(B') images of a single ridge surface; (C)/(C') images of spherulites in PC mold and their impressions in the PDMS phantom; (D)/(D') high magnification images of an individual spherulite and its impression. The insets in (A)/(A') display water drops on the respective surfaces and corresponding contact angles.

The other surface property pertaining to the above described nanostructured morphology is the wettability. As shown as the inset in Figure 3-5A, the water contact angle on the PC mold is $130\pm 2^\circ$, which is significantly higher than that of an unmodified

PC surface ($90\pm 2^\circ$). The PDMS phantom in fact has an even higher water contact angle ($144\pm 2^\circ$, inset of Figure 3-5A'). Such a near-superhydrophobic surface should be resistant to contamination, which ensures imaging reproducibility and is suitable for long-term applications.

3.4. Optimization of phantom fabrication

As mentioned above, fingerprint scanners rely on various means of detecting ridges (optical, conductivity, or ultrasound) and may use additional measures to verify the authenticity of fingerprints. Although PDMS is a great physical analog of skin in terms of strength and elasticity, their optical and electrical properties are very different, which can lead to unreadable phantoms. While the fingerprint matching shown in Figure 2-6 was successfully performed with an optical scanner, possible additives to further improve their performance were identified. To approximate tissue optical properties, a flesh colored silicone pigment (pantone 488C) can be added at low weight percent to the PDMS during curing (Figure A2). Pigmentation provides the necessary scattering and absorption for optical scanners to resolve ridges clearly.^{128,129} Many different pigments can be chosen or combined to mimic a wide range of skin tones. Biological additives (blood cells, collagen, and lipids) cannot serve this purpose in PDMS phantoms as they do not disperse well and decompose rapidly.¹²⁸

Fabrication of PDMS phantoms for reading with capacitive scanners is also feasible; these phantoms must achieve an electrical resistance of $\sim 16 \text{ M}\Omega/\text{cm}$ to properly simulate human tissue.¹³¹ There is a degree of flexibility in achieving readability by capacitive scanners because they are built to detect fingerprints with a high rate of success by accepting large variations in conductivity. Silver nanowires and particles may be applied, however large percentages (18%) are required to reach the percolation threshold and achieve the desired conductivity.¹⁴⁴⁻¹⁴⁵ At such high additive ratios, PDMS becomes less elastic and conforms to the mold surface poorly.¹⁴⁵ Commercially available conductive PDMS precursors with silver coated aluminum nanoparticles dispersed at their percolation threshold may be tested.¹³² Silicone thinner (5%) should be added to decrease viscosity and ensure complete molding of fingerprint impressions along with flesh colored pigment to produce an electrically and optically realistic fingerprint phantom.¹³² Ultrasound based

scanners should not require any additional modification as PDMS possesses a similar density to human tissue.¹⁸

3.5. Conclusion

Unconventional PC molding has been shown to be an effective technique to construct 3D fingerprint phantoms, i.e., fingerprint molds made of solvent-softened PC plate serve as robust templates to cast flexible and highly detailed PDMS replicas (fingerprints phantoms). By matching the PDMS phantoms with source fingerprints, it was confirmed that the ridge patterns are faithfully reproduced and all three levels of fingerprint details are transferred in 3D. These refined phantoms are excellent tools to expedite and advance the development of biometric fingerprint scanners for security and law enforcement applications. This represents an example of the novel benchtop fabrication method that can be applied to the mass production of many other polymeric nanostructures and devices.

3.6. Experimental

Polycarbonate (PC) sheets were purchased from Bayer (Sheffield, USA), which are protected by a plastic film on both sides upon receiving. Acetone (99.8%) and ethanol (95%) were purchased from Fisher Scientific. Sylgard 184 polydimethylsiloxane (PDMS) kit (which contains an elastomer base and elastomer curing agent) was purchased from Ellsworth Adhesives (Germantown, USA). Deionized water (>18.3 M Ω ·cm) was produced with a Barnstead Easypure UV/UF water system (Thermo Scientific, Waltham, USA).

To mold fingerprints a 1.5" \times 1.5" piece of PC chip was cut from the large sheet and the protective film removed from one side. The bare surface was washed with deionized water and ethanol, then dried with N₂. 1.0-mL of acetone was dispensed onto the PC surface with an automatic pipette and left for 45 s. A finger was then either pressed with mild force or rolled to produce a fingerprint impression on the surface. The PC plate was left to dry in ambient conditions to solidify the fingerprint impression (the mold). The fingerprint phantoms were constructed by casting a PDMS replicate using the PC mold. Briefly, the two precursors supplied in the PDMS kit, the elastomer base (part A) and the curing agent (part B) were mixed in a 10:1 ratio by manual stirring and vortexing. The precursor solution was poured over the PC mold, degassed for 45 min in a vacuum

chamber, and then cured in an oven at 80 °C for 2 h. The PDMS phantom is then cut and carefully peeled from the PC mold.

Optical images were captured with a stereo microscope (Motic SMZ-168 Series) equipped with a 10 Mpixel digital camera (Moticam10+, Motic Instruments Inc., Richmond, Canada). Digital imaging of fingerprints and fingerprint phantoms was conducted with a Hamster Plus Fingerprint Scanner (SecuGen Co., Santa Clara, USA), and a DigitalPersona Eikon Touch 710 Fingerprint Scanner (DigitalPersona Inc., Redwood City, CA) was used to capture digital images of fingerprints and fingerprint phantoms. Digital fingerprint images were converted to 8-bit, 500 DPI gray-scale pictures. Fingerprints were verified and matched with Verifinger 11.0 SDK, a software program developed by NEURO technology (Vilnius, Lithuania).

Scanning electron microscopy was employed to examine the morphology of the PC molds and PDMS phantoms. An FEI NanoNova 430 SEM was used to obtain high resolution images; the samples were coated in a Hummer 6.2 gold sputtering system and sputtered in pulse mode for 6 min to deposit a conductive gold layer to the surface. The depth of the ridge impressions was measured using a Bruker Dektak XT (Billerica, USA) profilometer. Contact angle measurements were performed with a VCA Optima System (AST Products Inc.; Billerica, USA).

3.7. Supporting Information

Additional experimental details including the fabrication of skin-color PDMS phantoms and further optical and spectroscopic characterization of the PC mold and PDMS replica are also presented.

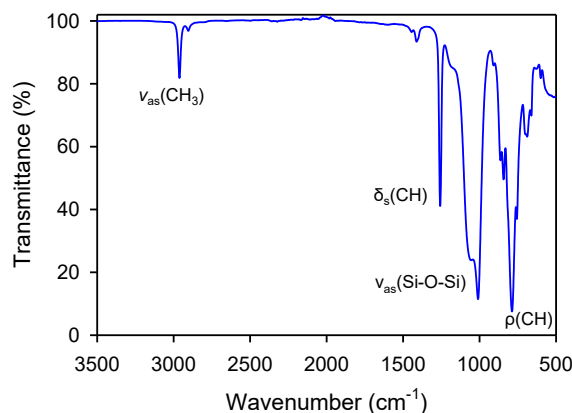


Figure A1. FT-IR spectrum of a PDMS plate casted from a PC mold. The major peaks associated with PDMS are present, e.g., $\nu_{as}(CH_3)$ C-H bond stretch at 2950 cm^{-1} , $\delta_s(CH)$: bending of C-H at 1250 cm^{-1} , $\nu_{as}(Si-O-Si)$: stretching vibrations of Si-O-Si bonds at 1000 cm^{-1} , and $\rho(CH)$: C-H rocking at 800 cm^{-1} (Berdichevsky *et al.*, *Sens. Actuators B* 2004, 97, 402-408). No carbonyl peak is present ($\nu(C=O)$ at $1670\text{-}1820\text{ cm}^{-1}$) in the spectrum, indicating that no significant transfer of PC (or precursor) residues to the PDMS replica occurs during the casting process

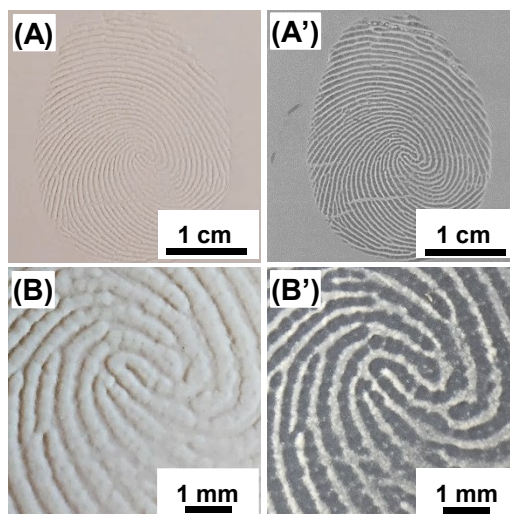


Figure A2. Photos of a skin-color PDMS phantom (left) and the PC mold (right). (A/A') shows the entire fingerprint, which represents the first level details; (B/B') a magnified section showing the fingerprint core. The pigment used to dope the phantom, Silc Pig Pantone 488C, is a commercial silicone dye for the entertainment industry to make props and fake limbs. The skin-color phantom in Figure A1(A) has similar optical properties as human skin. More importantly, the doping with pigments does not affect the casting of the phantom from the PC mold, i.e., the third level details (pores) are replicated accurately along the finger ridge impressions.

Chapter 4. Three-Dimensional Conductive Fingerprint Phantoms Made of Ethylene-Vinyl Acetate / Graphene Nanocomposite for Evaluating Smartphone Scanners

Fingerprints consist of unique patterns of skin ridges and valleys and are commonly described by three levels of feature details. Most fingerprint identification systems rely on matching only first- and second-level details; their calibration using unrealistic targets combined with human sampling are cumbersome and time-consuming. We have developed a true-to-life fingerprint phantom with optimized conductive properties and third-level fingerprint details for developing more reliable matching algorithms for popular capacitive fingerprint scanners. An impression of a live finger is made into a solvent-softened polycarbonate template, which is subsequently adapted to thermally mold ethylene-vinyl acetate graphene (EVA-G) nanocomposite of satisfactory conductivity ($1.2 \pm 0.1 \times 10^{-3}$ S/m) and mechanical flexibility. It was confirmed with SEM, optical, and profilometry imaging that the phantom made of EVA-G nanocomposite replicates the three-dimensional morphology of fingerprint with high fidelity, including well-defined third-level details. The EVA-G phantoms can operate capacitive scanners in popular brands of smartphones and tablets with either iOS or Android operating systems (>80% success rate). As these permanent phantoms include defined third-level details based on real fingerprints, their potential application as calibration standards for developing the next generation of scanners with improved security is warranted.

Note: this chapter is adapted with modifications from a recently published manuscript:

Schultz, C. W., Fawzy, M., Nasirpouri, F., Kavanagh, K., Yu, H.-Z., Three-Dimensional Conductive Fingerprint Phantoms Made of Ethylene-Vinyl Acetate / Graphene Nanocomposite for Evaluating Smartphone Scanners, *ACS Appl. Electron. Mater.* **2021**, 3, 2097–2105. Copyright (2021) American Chemical Society.

This work is a collaboration with Dr. Karen Kavanagh's lab. I performed most of the experimental work and drafted the paper. Mirette Fawzy performed initial electronic characterization and fabricated phantoms. Dr. Hogan Yu and Dr. Karen Kavanagh supervised the entire project and, along with Dr. Farzad Nasirpouri helped with writing and proof-reading the paper.

4.1. Introduction

Fingerprint identification is an indispensable technique in forensic science, as every human fingerprint is unique (even between identical twins).⁵ It is also widely adapted for biometric authentication in security systems at international borders, airports, workplaces, and most popularly in portable electronic devices (laptops, tablets, and smartphones). In practice, a finger is placed onto a sensor/scanner that constructs an image of the fingerprint, typically via optical, capacitive, or ultrasound signals; the image is then compared to a previously recorded fingerprint via an automated fingerprint identification system (AFIS) to confirm a match.^{5,146} Fingerprint scanners are becoming ubiquitous nowadays;¹²⁵ with more than 5 billion users in the world and the high turnover rate of smartphones,¹⁴⁷ more than one billion smartphones with fingerprint scanners were sold in 2019.¹⁴⁸ As more and more of our daily lives are managed through a smartphone, the personal and financial information protected by these biometric systems becomes more valuable, and its security more vital.

The uniqueness of fingerprints is derived from the three-level of details present.⁵ The general arrangement of ridges and pattern type for classification (i.e., whorls, loops, and arches) represents the first level. The second level consists of fingerprint “minutiae”, i.e., characteristic arrangements of fingerprint ridges into common patterns where ridges merge or differentiate. The locations of these second level details are compared in the majority of current fingerprint AFIS. A similarity score is generated by matching minutiae in fingerprint images and comparing deviations, while allowing slight deformations resulted from fingerprint malleability. Third level details include the width and contours of fingerprint ridges, creases, and sweat pores. They are smaller (<50 μm), require high resolution sensors (>40 pixels per mm) to identify, and are more susceptible to errors (for example, from variations in skin dryness).¹⁴⁹ Pre-existing low-quality fingerprint images in databases and latent prints may not resolve third-level details clearly, which prevented their application for fingerprint matching. With improved imaging and cataloging techniques, third-level details like sweat pores (number and location) can be included in AFIS matching algorithms to provide additional identifying information, strengthening matches, especially when only small or partial prints are available.¹⁵⁰

Although fingerprints are inherently unique, existing AFIS are not always secure. They have significant vulnerabilities primarily because their matching algorithms may not

utilize all the information present on fingerprints. Smaller partial prints containing less minutiae are often recorded by the fingerprint scanner in phones. A recent study by Roy et al. showed that the same simulated “MasterPrint” with common arrangements of minutiae can find a match to 10% of phone users.¹² It is also becoming easier to make illicit forgeries of fingerprints from images in a database or latent fingerprints; as such inkjet and 3D printing of spoofing fingerprints have been reported recently.^{11,106} These issues highlight the urgent need for better fingerprint scanning resolution and matching algorithms.

Fingerprint scanners are developed to meet application specifications and tested using actual fingerprints. In fact, sampling real people is expensive, time-consuming, and faces many uncontrollable variables (finger condition, sweat levels, pressure, fingerprint type, and skin color).¹³¹ Manufacturers desire alternatives in order to reduce costs, and demand for analogs/targets that emulate the complex 3D structure and physical characteristics of human fingerprints. In medicine, tissue analogs with reproducible properties are known as phantoms,^{127-129,151,152} which range in complexity from blocks of gelatin and water to full-body phantoms with differentiated tissues, organs, and bones. They have facilitated precise calibration of medical imaging instruments including magnetic resonance, computed tomography, magnetoencephalography, and ultrasound machines.^{127-129,151,152} Fingerprint phantoms may solve many of the problems associated with human testing: physical properties can be controlled by doping or coating the phantom; automated systems can be employed to control user variables and perform long-term durability tests (unlimited repeating tests). Testing on real fingerprints will always be the final stage prior to production, but most of the interim testing and development could be performed with phantoms.

Fingerprint phantoms have been initially constructed from gelatin-based materials;¹³⁰ although approximate many of the properties of fingerprints well, they quickly dry out and shrink. PDMS (polydimethylsiloxane) phantoms have been cast from simulated ridge patterns then coated with gold to improve their conductivity.¹⁵³ Another type of PDMS phantoms cast from patterns etched in silicon has been applied for the development of ultrasound scanners.¹⁸ Conductive PDMS in conjunction with 3D printing technique has been recently adapted to create fingerprint phantoms as well.^{131,154} Further advancement in the accuracy and complexity of fingerprint phantoms (such as including

simulated subdermal blood vessels¹⁵⁵) will essentially accelerate the development of next-generation scanners and matching algorithms with improved reliability and security.¹⁵⁶⁻¹⁵⁸

We have previously reported the fabrication of PDMS fingerprint phantoms with third-level details for developing optical fingerprint scanners with improved secure biometric authentication.¹⁵² Particularly, an impression of a real finger is molded into acetone-softened polycarbonate (PC), which is subsequently used as the negative to cast a PDMS phantom. This practical, benchtop approach does not require any advanced instrumentation and fabrication facilities. Those PDMS phantoms, however, are electrically insulating, which do not possess the conductivity of real fingers necessary for capacitive scanners. In fact, capacitive scanners are favored in today's smartphones and tablets for their low profile and are less vulnerable to forgeries because they are sensitive to topographical variations.^{107,148} By incorporating commercially available metallic nanoparticles, the conductivity of PDMS for molded fingerprint phantoms can be manipulated.^{131,152} However, incorporating conductive fillers is deleterious to the mechanical integrity of PDMS, whereas its conductivity is still insufficient to be detected by smartphone fingerprint scanners.¹⁵²

In this work, we explore a novel polymer/nanomaterial blend, i.e., ethylene-vinyl acetate (EVA) embedded with low-cost graphene nanoplatelets produced by industrial scale, mechanochemical exfoliation of graphite,¹⁵⁹ for the fabrication of fingerprint phantoms. Graphene nanomaterials have unique and desirable properties,¹⁶⁰ i.e., high thermal conductivity, large surface area, and good electrical conductivity, which make them attractive for a compendium of practical applications.¹⁶¹ Besides the preparation of composite materials as an additive, graphene has been employed in the fabrication of various biomedical devices, sensors, electronics, electromechanical systems, and many more.¹⁶²⁻¹⁶⁴ In this study, EVA was chosen as the matrix for its compatibility with high amounts of graphene nanoplatelets while remaining thermally moldable, flexible, and durable.¹⁶⁵ The EVA-graphene (EVA-G) nanocomposite replicates the 3D morphology of fingerprint ridges more precisely than PDMS, with well-defined third-level details (e.g., ~50 μm pores and <1 μm variations in ridge contours) and fewer defects, as characterized using scanning electron microscopy (SEM), optical microscopy, and profilometry. We will compare the capacitive sensor images from real finger with our phantoms to illustrate the high-fidelity in the replication of fingerprints. We will demonstrate that our phantoms have similar electrical properties as skin, can operate the majority of capacitive scanners from

an array of iOS and Android-based smartphones with a high success rate, and that these robust and flexible phantoms can be reused for a prolonged period of time.

4.2. Fabrication and characterization of 3D fingerprint phantoms made of EVA-G

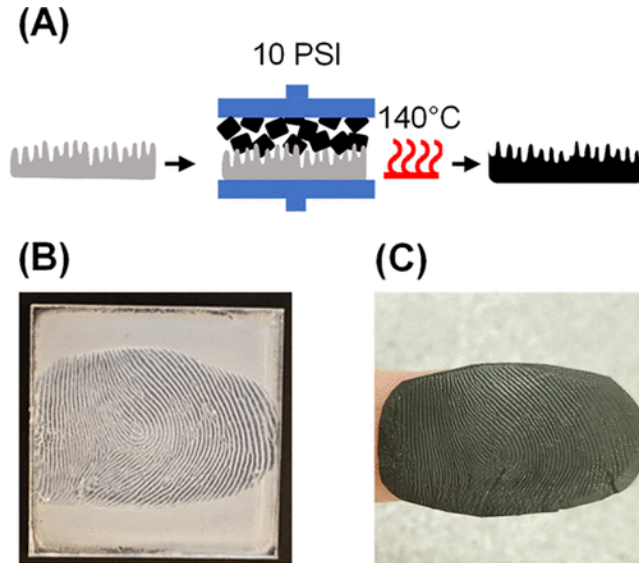


Figure 4-1: Fabrication of EVA-G fingerprint phantom from a real finger via thermal molding. (A) Schematic view of the thermal molding process (grey: PC, black: EVA-G). (B) PC with molded impression of fingerprint on the surface. (C) EVA-G phantom cast from the PC mold.

Our method of fabricating polycarbonate (PC) molds of real finger impressions was adapted for thermally molding conductive fingerprint phantoms made of EVA-G. Such a simple, benchtop fabrication process is illustrated in Figure 4-1A. A PC plate is first coated with a thin film of acetone (~1 mL for a 4 × 4 cm² piece) and left for 45 s. Once the solvent has swollen and softened the PC as visualized from a decrease in transparency, a finger is pressed onto the PC surface creating a negative impression (Figure 4-1B).¹⁵² To cast a phantom, pellets of EVA-G (30 wt % graphene) are heated to 140 °C and pressed against the PC mold with a pressure of 10 PSI (Figure 4-1B). A commercial anti-adhesion spray must be used prior to the molding to prevent the EVA-G from adhering to the PC negative and breaking during demolding. The thermally melted EVA-G fills the features of the fingerprint negative, and after cooling the EVA-G can be separated from the PC mold revealing a one-to-one replica of the original fingerprint. The EVA-G fingerprint phantom produced (Figure 4-1C), can be cut to desired size and is extremely flexible, i.e., it can be wrapped around one's finger or mounted onto a glove.

The replication fidelity was examined with optical and electron scanning microscopy. While Figure 4-2A shows the source fingerprint, the magnified image (Figure 4-2B) displays its well-defined morphology with minutiae easily identified in the ridge pattern. Several minutiae, the core (I), a delta (II), islands (III), and a bifurcation (IV) were highlighted with red circles. The optical image in Figure 4-2C shows the same area of the fingerprint on the phantom surface. The individual ridges surrounding it can be easily distinguished from each other. The same minutiae observed on the source fingerprint (Figure 4-2B) can be clearly identified in the ridge pattern as highlighted with red circles, illustrating the accurate replication of second-level details conventionally used to match fingerprints. An optical image of the phantom with even higher magnification is presented in Figure 4-2D, where distinctive third-level details including sweat pores (highlighted in blue circles), cracks, and ridge undulations are clearly visible.

SEM images of a set of ridges on the EVA-G phantom are displayed in Figure 4-2E. The surfaces of ridges appear smooth at this scale, no defects such as voids and cracks are visible, and the surface of ridges and valleys has natural variations in morphology. When we magnify further, as shown in Figure 4-2F, morphological details of a single ridge begin to be resolved. Ridges are not completely flat; undulations in height and edge contours that are characteristic of real finger ridges are present.¹⁶⁶ A sweat pore can be identified near the top of the ridge (circled in blue). Some low-aspect ratio bumps are visible on the surface, which are derived from the PC mold rather than the original finger.¹⁵² Our PC molds are covered in spherulites (5–10 μm) and small voids (>10 μm), as a result of solvent-induced recrystallization.¹⁵² Fortunately, when the EVA-G is thermally molded with the PC negative, it does not “copy” these rough surface features.

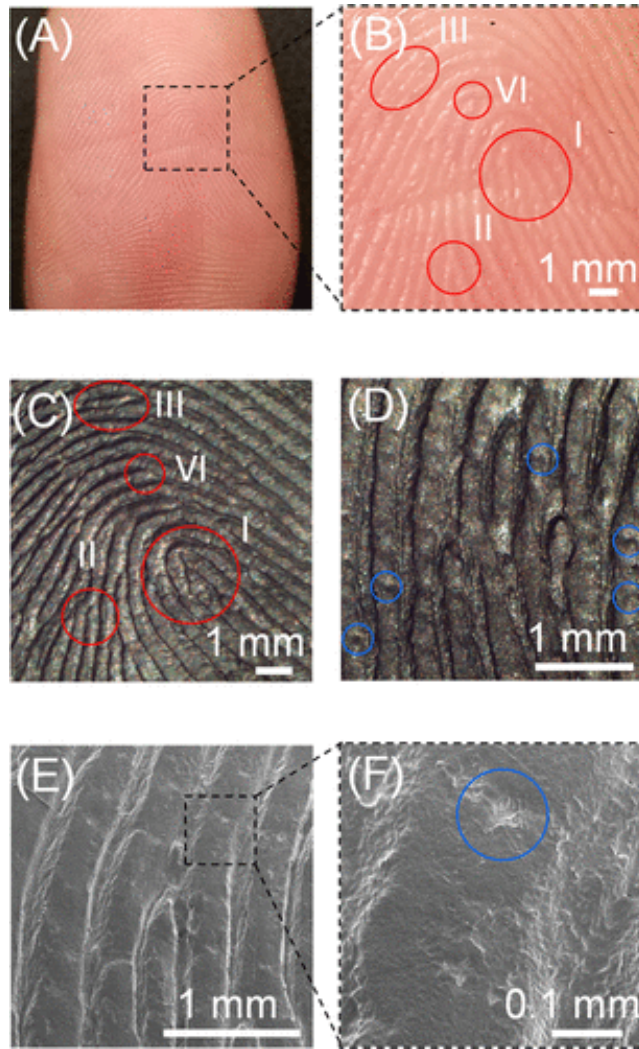


Figure 4-2: (A) Optical image of the source fingerprint on a fingertip; (B) magnified optical image of fingerprint ridges at the fingertip core; (C) optical image of the fingerprint phantom corresponding to the fingerprint shown in (B); (D) Magnified optical image of several ridges on the phantom; (E) SEM image of fingerprint ridges on the phantom; (F) magnified SEM image of the highlighted region in E. Various pairs of matching minutiae (second-level details) are highlighted in B and C with red circles, such as the core (I), a delta (II), an island (III), and a ridge bifurcation (IV). Third-level details (sweat pores) are circled in blue in D and F.

To further examine the surface topography of EVA-G phantoms, we have obtained profilometry images of both the PC mold and EVA-G phantom of the same fingerprint. 3D scans of the surfaces ($5 \times 5 \text{ mm}^2$) were performed by taking parallel profiles (with a step size of $2 \mu\text{m}$) and “stitching” them together to provide a microscale map of the surface (Figure 4-3). The profilometer tip had a radius of $2.5 \mu\text{m}$ and a vertical resolution of 10 nm , both are much smaller than fingerprint third-level features.

The image of the PC mold in Figure 4-3A shows a pattern of wide depressions that appear blue in the topographical false color. These are the impressions of fingerprint ridges molded into the PC. Several third-level details are recorded in these depressions: height differences along ridges are clearly visible at the edges and along top surfaces; the small green dots along the ridges and bisecting the edges are closed and open sweat pores, respectively; and variations in ridge widths are accurately recorded. The depth of the PC ridge impressions is between 20 to 40 μm separated on average by 0.5 mm. The full width at half-maximum (fwhm) of narrower valleys, or furrows, in between ridges, are 100 to 200 μm . Figure 4-3B displays a profilometry image of the corresponding EVA-G fingerprint phantom that was cast from the PC mold (Figure 4-3A). Because the scan from the phantom is a mirror image of the PC mold, the original scan image was inverted to align their patterns. It is clear that the PC ridge depressions (ridges and valleys) have been reproduced in the EVA-G phantom, as well as the critical third-level details.

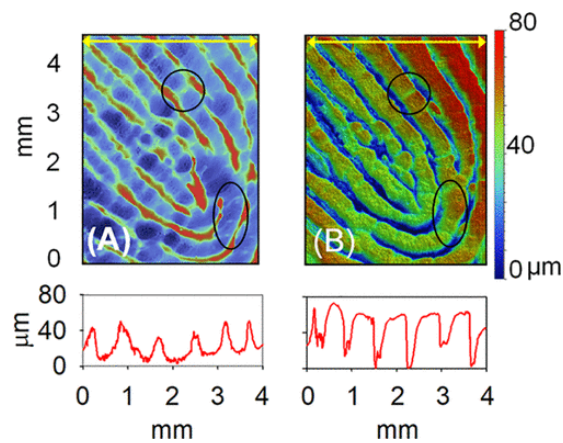


Figure 4-3: Profilometry images of (A) PC mold with the impression of a fingerprint and (B) the corresponding EVA-G phantom. The bottom insets show cross-section profile along the red line in the associated image.

Below each of the 3D images shown in Figure 4-3 is a profile plot of the fingerprint taken across the same region, as indicated by the yellow line. The profiles were leveled and the heights were rezeroed for direct comparison. Five ridges/impressions can be identified in each line profile, with varying height and shape. A disparity in height is apparent in the profiled ridges, impressions in the PC are between 20 and 40 μm deep whereas the EVA-G ridges are 40–60 μm tall. Consistent ridge height distortion is the result of variable pressures used when making PC impressions. Real fingerprint ridges deform under pressure, as such, each PC impression from the same finger would have a slightly different 3D morphology. In this case, the PC template may have been made with

higher pressure than the one the EVA-G phantom was molded from, with compressed and widened finger ridges.^{166,167} This finding might be further explored to design phantoms that simulate fingers with different ridge heights, such as worn hands after prolonged manual work.

Though ridge height in the phantom may be amplified, more importantly, realistic 3D features on the fingerprint ridges (i.e., pores, cracks, and variable minutiae) are replicated in high fidelity. Along the ridges, undulations identical to those in the template are also visible (e.g., the crack highlighted in the upper portion of the image), as is the varying slope of the valleys at the ridge edges. Sweat pores are reproduced along the ridges; at the bottom right corner of each image, three sweat pores are highlighted in both the phantom and mold. Pores may not look identical, even on the same print, as they can change from open to closed between instances of molding or fingerprinting. Whereas pore shapes may be variable, the position along a ridge is reproducible. Previously developed phantoms do not include this level of details, having ridges with constant height as they were created from 2D images.^{18,131,153}

The composition of the EVA-G nanocomposite (30 wt %) was chosen for its balanced mechanical (durability and flexibility) and electrical properties.^{159,168} The conductivity of EVA-G generally improves upon increasing the amount of GNP filler; at low weight percent (<15%), the conductivity is poor but becomes much better at 30 wt % with the formation of a percolation network.¹⁵⁹ We have particularly performed Impedance spectroscopy on the molded EVA-G nanocomposite at this composition (30 wt %) to confirm its satisfactory electrical properties. As shown in Figure 4-4A, the representative Nyquist plot exhibits a single semicircle between 100 Hz to 1 MHz (the frequency in the middle is 26 kHz), which can be ascribed to the simple conductivity-permittivity relation of the bulk nanocomposites (indicating the formation of a homogeneous, well dispersed EVA-G composite).¹⁶⁹ A linear correlation between the DC voltage and the measured current was found (inset of Figure 4-4A); such an Ohmic response further confirms its satisfactory conductivity. In addition, we have shown that these measurements are reproduceable and the EVA-G nanocomposites with low percentages of GNP are much less conductive (Supporting Information). On the other hand, the conductivity remains constant at low frequencies (<1 kHz) and increases significantly at high frequency (>100 kHz) (Figure 4-4B). Such a “DC plateau” is characteristic of conductive polymer nanocomposites and confirms the formation of a percolation network.^{170,171} Our measured

conductivity is in fact lower than that reported previously,^{159,169} for which the molding process may have influenced the graphene dispersion in the nanocomposites. The complex permittivity, also shown in Figure 4-4B, decreases with increasing frequency as the degree of polarization induced in the EVA-G composite diminishes. A similar trend (frequency-dependent conductivity and permittivity) has been observed by Gabriel et al. for human skin,¹⁷² indicating that EVA-G phantoms might be effective targets for operating/calibrating capacitive scanners.

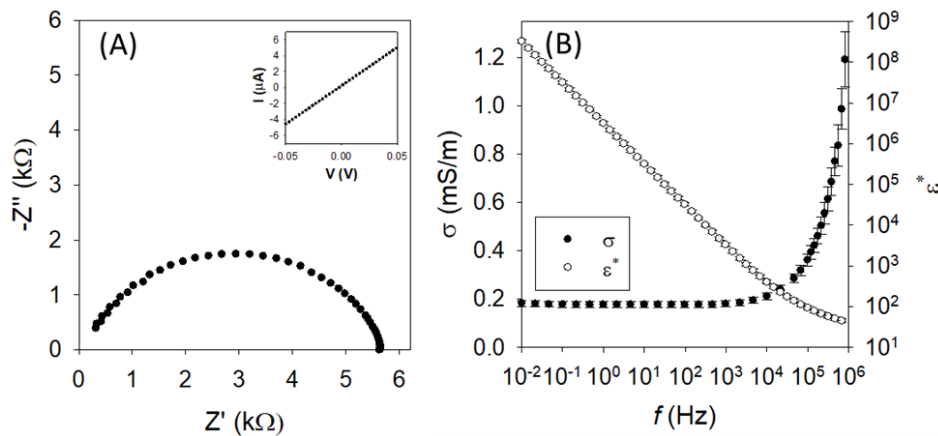


Figure 4-4: Impedance spectroscopy of thermally molded EVA-G nanocomposites (30 wt %). (A) Representative Nyquist plot. The top-right inset displays the current as a function of applied DC voltage. (B) Electrical conductivity (σ) and complex permittivity (ϵ^*) of as a function of the frequency (f) for the impedance measurements.

For capacitive scanning, both the conductivity and permittivity of the target (finger or phantom) are critical; conductivity is required for charge to flow during charging and discharging, whereas the permittivity of a material determines how much it is polarized by the electric field of the scanner.^{173,174} The parasitic capacitance between the scanner and target is also inversely correlated with the distance, which facilitates the differentiation of feature (ridge) heights. The conductivity of EVA-G phantoms is $1.2 \pm 0.1 \times 10^{-3}$ S/m, and the complex permittivity is 42 ± 4 ; both are about an order of magnitude lower than that of dry human skin ($2.0\text{--}2.5 \times 10^{-2}$ S/m, and 550–1100 respectively).¹⁷² Although less conductive and polarizable than human skin, the EVA-G still induces a detectable capacitive response with fingerprint scanners (vide infra), possibly because its conductive surface comes closer to the scanner than human skin, in which the conductive hydrated cells are buried below a few layers of keratinized cells (drier and less conductive). It should be noted that the properties of skin vary significantly;¹⁷² ultimately, fingerprint scanners

are built to differentiate ridges and valleys rather than precisely determine the electrical properties.

Nonetheless, higher filler concentrations would stiffen the composite such that the phantom cannot properly conform to surfaces for imaging. The decrease in flexibility at higher amount required for better conductivity explains why previous attempts to construct conductive PDMS phantoms were unsuccessful.¹⁵² GNPs were chosen over other carbon-based conductive additives for their balanced affordability and function.¹⁷⁵ Although their percolation threshold may be higher than carbon nanotubes (CNTs), GNPs are significantly cheaper and easier to produce through bulk solution exfoliation.¹⁵⁹ Our Raman spectroscopy analysis show that the GNPs used in this work contain very few defects and are not significantly oxidized (Supporting Information). GNPs that have a percolation threshold of ~15 wt % are comparable to carbon black (10 wt %) and outperform other conductive fillers such as metal nanoparticles.^{159,175}

4.3. Phantom Testing with Standalone Capacitive Scanner and Smartphones

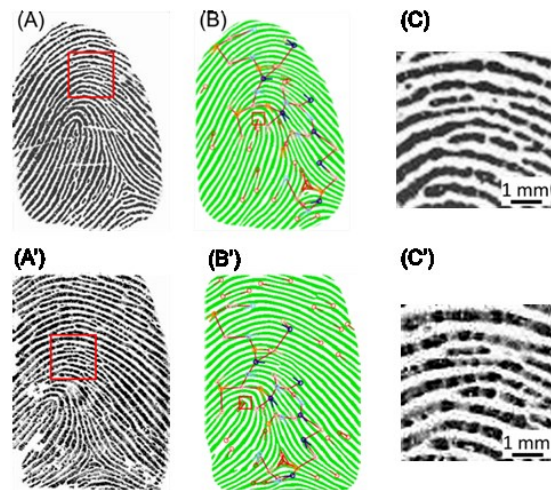


Figure 4-5: Fingerprint matching between the original fingerprint and the EVA-G phantom with a capacitive scanner. (A) Image of a real fingerprint captured with a capacitive scanner used to make the PC mold. (A') Image of the EVA-G fingerprint phantom cast from the PC mold. (B) Binarized depiction of the original fingerprint with location of minutiae indicated by tailed circles. (B') Binarized depiction of the image of the EVA-G phantom, the circles connected with a red line are minutiae for matching. (C) Magnified image of the highlighted area in (A); (C') Magnified image of the corresponding area in the EVA-G phantom.

To test their compatibility with commercial capacitive scanners, we initially imaged and matched EVA-G phantoms with their source fingerprints using a standalone fingerprint scanner (Digital Persona EikonTouch 710) with the biometric matching software (Verifinger 11.1 SDK) at specified resolution of 20 pixels/mm (500 pixels/inch). A capacitive scanner differentiates the high and low points of fingerprint ridges with an array of “cells” containing two coplanar capacitive plates per cell.^{5,176} The finger acts as a third capacitive plate, based on the capacitance decrease between the cell plates (which would vary according to the distance from the skin) the system determines if a specific region is a ridge or a furrow.¹⁷⁶ By placing on the scanner surface, the source fingerprint was imaged with a capacitive scanner (Figure 4-5A). Ridges and furrows have high contrast, first- and second-level details can be easily identified. The scanner did not adjust the contrast, indicating that the finger surface is rather conductive (far above the minimum threshold to elicit a change in capacitance), though absolute readings were not available for further analysis.

Figure 4-5A' shows the corresponding image of an EVA-G fingerprint phantom that was cast from a PC mold of the source fingerprint. Like the original, first- and second-level details are clearly resolved. Both fingerprints are detected and recognized, but the darkness of ridges in the phantom image was lower than the source fingerprint image, likely due to a lower capacitance. The contrasts of phantom images in Figure 4-5A' and 5C' were maximized for easier comparison with the source fingerprint. Differences are expected since the contrast of a phantom fingerprint will be less influenced by humidity, whereas a real fingerprint depends on the skin dryness (dry skin is less conductive) and suppleness (harder skin cannot conform as easily to the scanner surface).^{149,177} Variation in contrast along ridges in the phantom indicates that the phantom is not as “supple” as the real finger upon conforming to the scanner. To simulate different finger conditions, which have variable properties and morphologies (Supporting Information), the contrast of EVA-G phantoms could be controlled by further adjusting the malleability of EVA or the amount of GNP additives.

The fingerprint images produced by the finger and phantom were compared using the biometric matching software (*Verifinger 11.1 SDK*). The fingerprint images are first “binarized” for feature extraction (Figure 4-5B and B'), particularly minutiae (where ridges end, separate, or differentiate) are detected by the system and labeled with tailed circles. Because of intraclass variation in fingerprints made by malleable fingers, minutiae cannot

be directly compared; instead, the most similar minutiae pair in each fingerprint is used to align the fingerprint then other minutiae are compared.^{5,149} Matching minutiae (those in similar locations in the two fingerprints) are connected on the same fingerprint with lines. The relative distances between minutiae pairs (represented by the length of connecting lines) on each fingerprint are compared to generate a matching/similarity score.^{5,149} The matching score between images of the phantom and the source finger is 290 ± 10 , indicative of a very strong match by this algorithm. To put this score in perspective, multiple images of the same fingerprint, matched with each other, scored 255 ± 10 . Remarkably, the matching score of the phantom with its source fingerprint is comparable to previously reported artificial fingerprint phantoms.^{131,153}

Along some of the ridges above the fingerprint core in both the source finger and phantom, small “white spots”, i.e., sweat pores, are observed, even though they are much smaller ($\sim 50 \mu\text{m}$) than minutiae (second-level details). Other third-level details such as ridge contours (1 to $10 \mu\text{m}$ variations in ridge height and width) can be also identified on the phantom. Magnified sections of the finger and phantom images are shown in Figure 4-5C and C', respectively, to highlight these features. Most of the sweat pores are molded successfully to the phantom, illustrating how these features could be used to match fingerprints (even on very small partial prints). In contrast, other phantoms constructed from conductive PDMS or linear low-density polyethylene/ethylene butyl acrylate were unable to achieve the balance between its conductivity and flexibility required to imitate a real finger (Supporting Information).

Fingerprint scanners on smartphones are typically small, but are able to capture several partial prints to match with the prerecorded fingerprint in its database; each partial print is compared with an image from the scanner and if any match, the phone unlocks. These partial prints may only have a few minutiae for the algorithm to compare with, so that even a relatively poor replica may unlock the phone. As mentioned above, this vulnerability is exemplified by hacking fingerprint databases with so-called “MasterPrints”.¹² Moreover, artificial phantoms derived from fingerprint images (no third-level details) have achieved strong matches on standalone capacitive scanners and smartphones.^{131,107} This should be alarming as these scanners can be easily fooled it becomes vital to improve their security via calibration with true-to-life phantoms (beyond standard calibration or extensive human testing).

The EVA-G phantoms were tested on capacitive fingerprint scanners of several iOS and Android-based smartphones/tablets where the source fingerprint had been enrolled, as depicted in Figure 4-6A. Figure 4-6B presents an example of the array of partial prints recorded during enrollment of the source fingerprint into the catalogue of fingerprint profiles within the device. The smartphone saves only the relative location of minutiae, as indicated by the triangles. Minutiae from the phantom fingerprint image are compared with all enrolled profiles. If enough minutiae match with any of the profiles (green triangles indicate a match) the phone would unlock (Figure 4-6C).

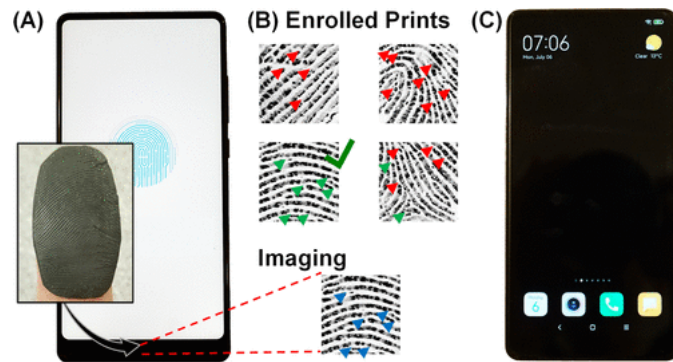


Figure 4-6: Operation of smartphones with an EVA-G fingerprint phantom. (A) EVA-G phantom taped to a finger and imaged with the smartphone fingerprint scanner. (B) Examples of enrolled fingerprint profiles, partial fingerprints captured by the scanner during the initial enrollment; triangles indicate minutiae locations. Minutiae in the prospective and enrolled fingerprints are compared for a match. Green triangles in the enrolled profiles indicate matching minutiae, red indicate no-match. An accepted match is indicated by a green checkmark. (C) Smartphone unlocked after matching the phantom with an enrolled fingerprint profile.

Table 4-1: Imaging of fingerprint phantoms with several smartphone capacitive scanners

Device Type	Phantom Detection	Success Rate
iPhone 6	yes	95%
iPhone 7	yes	90%
iPhone SE (2020)	yes	100%
iPad Pro 2018	yes	90%
Macbook Pro 2019	yes	85%
Samsung S8	no	NA
Huawei Honor	yes	80%
Huawei P30	yes	0%
Huawei Y Max	yes	90%
Xiaomi Redmi 5 Plus	yes	0%

Table 4-1 lists the smartphones/tablets tested and if the phantoms can be detected and successfully match with the enrolled fingerprint to unlock the device. A pair of fingerprint phantoms (left and right thumb of the same operator) were tested on each of the devices after the original fingerprints were enrolled. Once an area of the phantom that matches with the enrolled fingerprint profile is found, which often took 2–4 attempts, that area was repeatedly “applied” to the fingerprint scanner (10 times). Apart from the Samsung S8, all capacitive scanners recognized the phantom as a “true” finger. For most devices that detected the phantoms, the matching success rate was above 80%; however, two of the phones that recognized the phantom did not detect it as a match, surprisingly. The Huawei P30 has an in-screen fingerprint scanner, which is embedded “deeper” in the device; phantoms required higher pressure than a real fingerprint to be detected owing to the limited elasticity of the EVA-G phantom compared to real finger tips. The phantom could have been rejected also by “liveness” detection of the touch screen (other than those of standalone fingerprint scanners) or strengthened algorithm, unfortunately the exact reason for a nonmatch was not provided by the software for security purposes. While extensive testing with many more devices is warranted for the practical application of the EVA-G phantom as a calibration target, the high success rate achieved across a range of mobile devices highlights the effective replication of all levels of details of fingerprints and their conductive properties. Beyond being excellent replicas, our phantoms are durable, i.e., when used repeatedly, no signs of damage from testing or degradation over time (>3 months) were observed. They are resistant to oxidation (tested with a UV-ozone treatment) and withstand physical deformation such as folding and scratching.

As described above, these EVA-G phantoms with natural 3D features are capable of operating capacitive scanners either standalone or on mobile devices. The third-level details we can reproduce on the phantoms will be key to developing new scanners that can image them accurately, along with upgraded algorithms that match third-level details. Even small fingerprint scanners (the smaller, the better for phones, nonetheless) that capture only a few ridges would be exponentially more secure if every sweat pore along the fingerprint ridge could be detected for matching.^{12,149} At the same time, algorithms can become more strict, making the fabrication of fingerprint forgeries and illicit “MasterPrints” more difficult.¹⁰⁷

4.4. Conclusions

The capacitive fingerprint phantoms made of EVA-G nanocomposites, are permanent, conductive, and contain third-level features from real fingerprints as illustrated with optical, SEM, and profilometry imaging. These phantoms are capable of matching real fingerprints recorded by capacitive scanners, including those typically found on smartphones. This work highlights their potential as imaging standards for developing improved fingerprint scanners, which are currently highly vulnerable to fraudulent access. It is conceptually simple to cast replicas from a fingerprint impression; we therefore must assume that nefarious individuals have developed similar techniques and have similar capabilities. By providing the best artificial fingerprint possible, developers can make better scanners with improved algorithms capable of recognizing third-level fingerprint details, and that can learn to detect high-quality forgeries. Moreover, industrial graphene nanoplatelets are low cost, which will facilitate extensive testing during critical development and quality control.

4.5. Experimental Section

Ethanol (95%) and acetone (99.8%) were purchased from Fisher Scientific (Waltham, MA). Sheets of polycarbonate (PC) were bought from Bayer (Sheffield, AL), in which the top and bottom surfaces are covered with plastic films for protection during shipping. Sylgard 184 polydimethylsiloxane (PDMS) kits were purchased from Ellsworth Adhesives (Germantown, MD). A PDMS kit contains an elastomeric base and curing agent, which are mixed in a 10:1 ratio before casting. A Barnstead Easypure UV/UF water system was used to produce deionized water ($>18.2 \text{ M}\Omega \text{ cm}$) (Thermo Scientific, Waltham, MA).

EVA infused with different weight percents (1–30 w/w%) of graphene nanoplatelets (GNPs) were supplied by NanoXplore Inc. (Montreal, QC). The GNPs (GrapheneBlack 3X) were generated in large scale from crystalline graphite through mechanochemical exfoliation. The mean thickness of GNPs is 6–10 layers; agglomerate flakes are $38 \mu\text{m}$ on average in size.¹⁷⁸

To mold fingerprints, we cut a $4 \times 4 \text{ cm}^2$ PC plate from the large sheet. The protective film was peeled from one side; the PC plate was washed with deionized water

and ethanol, and subsequently dried with N₂ gas. Acetone (1.0 mL) was applied to the surface using an automatic pipet. After 45 s the source finger was rolled and pressed into the PC with mild force, producing an impression of the fingerprint. To solidify the impression the PC plate was left to dry in air. Prior to the EVA-G casting, the PC mold was covered with a commercial demolding spray to prevent adhesion (Smooth-On Inc., Machungie, PA). The fingerprint phantoms were constructed by placing 0.5 g of EVA pellets (loaded with 30 wt.% GNP) onto the mold, heating to 140 °C, then pressing together using an automatic swing-away heat press (DC8AP, Geo Knight & Co. Inc., Brockton, MA) with a constant pressure of 10 PSI (Figure 4-1A). After air cooling for 5 min, the EVA-G phantom was carefully separated from the PC mold with a spatula.

Optical images were captured with a stereo microscope (Motic SMZ-168 Series) equipped with a 10 Mpixel digital camera (Moticam10+, Motic Instruments Inc., Richmond, BC). A DigitalPersona Eikon Touch 710 Fingerprint Scanner (DigitalPersona Inc., Redwood, CA) was used to capture digital images of fingerprints and fingerprint phantoms. Digital fingerprint images were converted to 8-bit, 500 DPI gray scale pictures. Fingerprints were verified and matched with *Verifinger 11.0 SDK*, a software program developed by NEURO technology (Vilnius, Lithuania).

An SEM system with a field-emission source (FEI NanoNova 430) operating at an accelerating voltage between 10–15 kV was used to collect secondary electron images of PC molds and EVA-G fingerprint phantoms. Samples were coated with 10 nm of iridium (Leica EM ACE600 Carbon & Iridium Coating System) to reduce surface charging. 3D morphology of the PC mold and EVA-G phantom was obtained with a profilometer (Bruker Dektak XT, Billerica, MA) in the MapScan mode (tip radius: 2.5 μm). Particularly, a series of 2500 lines (5 mm long; 2 μm apart) were scanned and “stitched” together to construct a 3D profile of the surface (5 × 5 mm²).

Impedance spectroscopy measurements of the EVA-G composites were performed using a CHI 1040A electrochemical analyzer (CH Instruments, Austin, TX) with a voltage (rms) amplitude of 0.01–0.05 V and a frequency range of 0.01 Hz to 1 MHz. All the samples for electrical characterization were prepared by hot pressing the as-received pellets at 140 °C for 5 min. Rectangular slabs (2 × 2 cm²) were cut from the ~100 μm thick hot-pressed discs and both sides were sputter-coated with 10 nm of iridium to minimize

contact resistance. The slabs were then placed between two copper electrodes that were connected to the impedance analyzer.

4.6. Supporting Information

Additional experimental results including impedance spectroscopy and Raman spectroscopy studies of thermally molded EVA-G, fingerprint images from different individuals (to highlight their natural variations), and fingerprint phantoms constructed using other polymer-GNP composites.

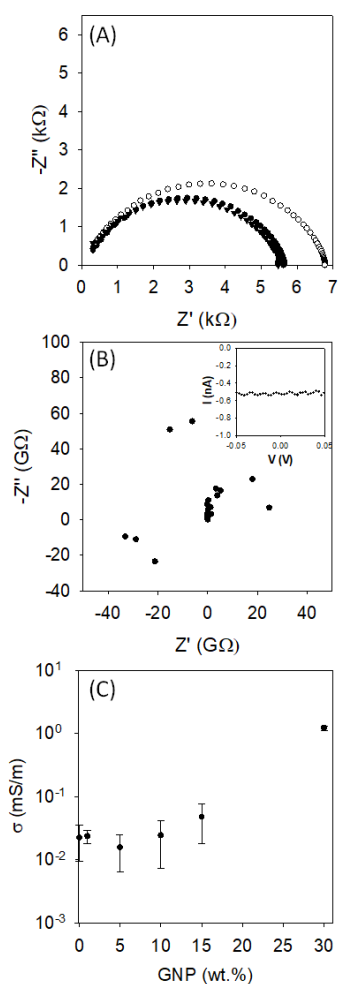


Figure B1: Impedance spectroscopy of thermally molded EVA-G nanocomposites. (A) Nyquist plots of three interpedently prepared EVA-G samples (30 wt.%). (B) A representative Nyquist plot for a 15 wt.% EVA-G sample; the top right inset displays a DC I-V measurement of the same sample. (C) Electrical conductivity of EVA-G nanocomposites as a function of the GNP wt.%.

Impedance spectroscopy measurements were performed on a CHI 1040A electrochemical analyzer (CH Instruments, Austin, TX). The electrical response of 30 wt.% EVA-G (Figure B1A) was rather reproducible; all samples produced a single semi-circle, differences in the impedance data are likely the result of slight variations in the exact composition and the molding process. The data from samples with lower GNP percentages (15 wt.% and below) were quite poor; as shown in Figure B1B there is a region in the middle associated with high frequencies where the impedance data seem to be reliable, but at lower frequencies the data fluctuates randomly. The DC measurement (inset of Figure B1B) also confirmed its very low conductivity (i.e., very high impedance). Using the high frequency impedance data (10^6 Hz), we have also investigated the conductivity of EVA-G composites with varied GNP wt.% (Figure B1C). At low wt.% the conductivity is low and increases slightly as more GNPs are added. There is a sudden increase in the conductivity between 15% and 30% associated with the formation of a conductive network upon reaching the percolation threshold.

The conductivity of the EVA-G composites was determined across a wide range of frequencies based on the impedance spectroscopy data (Figure 4-4A). Conductivity was calculated using the equation:

$$\sigma_{AC} = 2\pi f \varepsilon_0 \varepsilon'' \quad (1)$$

where f is the frequency in Hz, ε_0 is the permittivity of free space (8.854×10^{-12} F m⁻¹), and ε'' is the imaginary part of the complex permittivity.¹⁷⁴ ε'' is calculated from the impedance by:

$$\varepsilon'' = \frac{Z''}{2\pi f (\varepsilon_0 \frac{A}{d}) Z^2} \quad (2)$$

The real part of the complex permittivity is calculated with:

$$\varepsilon' = \frac{Z'}{2\pi f (\varepsilon_0 \frac{A}{d}) Z^2} \quad (3)$$

where Z' is the real part and Z'' is the imaginary part of the complex impedance, A is the area of the sample, d is the thickness, and Z is the complex impedance.¹⁷⁴ The complex impedance (Z) is determined from the real (Z') and imaginary (Z'') components by:¹⁷⁴

$$|Z| = \sqrt{Z'^2 + Z''^2} \quad (4)$$

The complex impedance (ε) as displayed in the Bode plot of Figure 4B is calculated from ε' and ε'' :^{S1}

$$|\varepsilon| = \sqrt{\varepsilon'^2 + \varepsilon''^2} \quad (5)$$

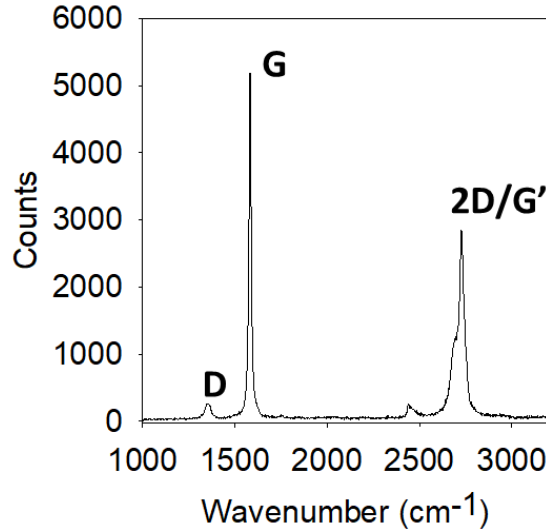


Figure B2: Raman spectrum of GNPs taken with a laser excitation at 514 nm using an inVia Raman Microscope (Renishaw, Mississauga, ON). The G band (1582 cm⁻¹) and D band (1350 cm⁻¹) in the spectrum come from the Raman active sp² carbon network and defects in that network, respectively.^{179,180} Such a small D band indicates rather defect free carbon layers. In single-layer graphene the 2D/G' band appears as a single peak, the shoulder on the 2D/G' band (2730 cm⁻¹) of the GNP spectrum reveals that GNPs consist of several layers (6-10, as specified by the manufacture¹⁷⁸).



Figure B3. Fingerprint images from four different individuals to highlight the natural variabilities. The darkness of ridges is variable, even within the same finger, some ridges saturate the scanner while others elicit a weaker response (A). The contrast is influenced by the skin moisture, which improves the conductivity of the finger tissue. Ridge contours present another difference; some are well defined (B) while others (C) are not. Ridge height differences can be identified as well, e.g., those in image (D) are heavily laden with large pores, while others have fewer pores (A). These differences make developing scanners that can detect all types of real fingers, while not being susceptible to illicit fingerprint forgeries exceedingly difficult.

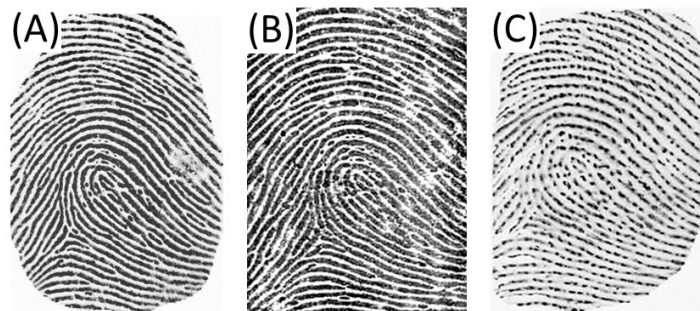


Figure B4: Fingerprint phantoms fabricated from other GNP-polymer composites. Capacitive fingerprint sensor images of the original finger (A), the GNP-PDMS phantom (B), and the GNP-LLDPE/EBA phantom (C), respectively.

For comparison, we have attempted to construct capacitive fingerprint phantoms with a variety of polymers loaded with conductive filler, e.g., polydimethylsiloxane (PDMS) and linear low-density polyethylene/ethylene butyl acrylate (LLDPE/EBA), respectively. We have previously tested a commercially available conductive PDMS for preparing fingerprint phantoms; the overall conductivity and mechanical flexibility of the resulting phantom were too low.¹⁷² With a protocol adapted from Filippidou et al.,¹⁶⁸ we have explored the creation of conductive PDMS with infused GNPs. Particularly, GNPs were first dissolved in a 7:3 hexane/isopropyl alcohol mixture and sonicated for 30 min. After which PDMS base was added, and the solution was sonicated for 12 h. The mixture was then mechanically stirred for 24 h. The PDMS curing agent was then added in a 10:1 ratio with the PDMS base (with infused GNP) and the mixture was stirred until the solvents evaporated. Then the GNP-PDMS composite was poured onto a PC mold (of fingerprint) and cured in an oven at 60° C for 24 h to a fingerprint phantom. We have found that PDMS could be loaded with up to 30% w/v GNPs before failing to demold; Figure B4B shows an image of such a GNP-PDMS fingerprint taken with a standalone capacitive scanner. Compared with the original fingerprint image (Figure B4A) ridges in the GNP-PDMS phantom were wider but in the proper location. Small partial ridges and depressions from pores that match the original were present in the replica. Unfortunately, the conductivity of the PDMS was still not high enough to be a satisfactory analog for human skin. Getting the GNP-PDMS phantom to be detected by the capacitive scanner proved a challenge and it was not recognized by any smartphone capacitive scanners we tested it on.

A copolymer of linear low-density polyethylene/ethylene butyl acrylate (LLDPE/EBA) loaded with GNPs was also tested for fabricating phantoms. Like the EVA-G phantoms, these phantoms were thermally molded using the PC fingerprint molds. When imaged with a capacitive scanner (Figure B4C) the LLDPE/EBA phantom was detected, but the image quality is poor. Ridges had varied contrasts and critical third level details like pores (which show up in optical images) were not resolved by the scanner. More importantly, these LLDPE/EBA phantoms cannot be recognized by any of the smartphone scanners we have tested.

Chapter 5. Benchtop one-to-one replication across length scales from 100 nm to 10 cm via ambient polycarbonate molding

Herein, a benchtop technique to create one-to-one plastic replicas of nanostructured “masters” of various materials and dimensions via polycarbonate (PC) molding under ambient conditions is described. Instead of conventional thermal molding of PC under high temperature and pressure, it is explored to adapt solvent-assisted method that has been traditionally unpopular due to the alteration of its morphology induced by swelling and recrystallization. A thorough study of how polymer spherulites (spherical domains of semicrystalline polymer chains) develop and whether their growth can be inhibited by nanocontact molding is conducted; it demonstrated not only how molding drastically limits crystallization but also how the crystallization can be controlled in the process of replicating micro/nanostructures. The efficacy of one-to-one replication across length scales from 100 nm to 1 mm over large areas ($>5 \text{ cm}^2$) has been confirmed with high-resolution scanning electron microscopy and atomic force microscopy. The durable monolithic PC replicas can be used as templates for casting polydimethylsiloxane (PDMS) devices, allowing expensive lithographically designed masters to be preserved and accelerating production by multiplexing. The simplicity and low cost of this benchtop approach augment the feasibility of nanofabrication in resource-limited settings with reduced costs and processing time.

Note: this chapter is adapted with modifications from a recently published manuscript:

Schultz, C. W., Yu, H.-Z., Benchtop one-to-one replication across length scales from 100 nm to 10 cm via ambient polycarbonate molding. *Adv. Eng. Mater.* **2021**, 2100048. Copyright (2021) Wiley.

I performed most of the experimental work and drafted the paper. Dr. Hogan Yu supervised the entire project and helped with writing and proof-reading the paper.

5.1. Introduction

Miniaturization has been paramount to technological advancement over the past few decades and will continue to be a main driver of improvement in scientific, industrial, and consumer settings.^{20,23,181} This is most evident in state-of-the-art electronics, e.g., mobile phones have advanced from simple bulky devices to fully capable pocket-sized “computers.”¹⁸² Technologies reliant on micro and nanoscale structures are also being applied in important fields such as biomedicine, optics, sensors, and material sciences. Optical properties can be controllably altered for security applications;¹⁸³ nanostructures in bioassays and microfluidics are being used for directing fluid flow;^{142,184} and, completely waterproof self-cleaning surfaces are constructed from micro/nanoscale patterns on and of desired materials.^{185,186}

Traditionally, micro and nanostructures are fabricated via lithographic techniques. Generally, a mask controls where a resist is exposed to the light (photolithography) or an electron beam is applied serially to specified locations (electron beam lithography). The resist, which is spin coated onto the substrate (e.g., silicon), is then chemically etched to develop the pattern.²³ Samsung and Intel have recently advanced these techniques to produce <10 nm features in their microchips.¹⁸¹ These lithography techniques have limitations; the fabrication of photomasks is expensive and time consuming; electron beam lithography is an inherently slow serial process; nonplanar materials are difficult to pattern; and expensive lithography equipment (precise mask aligners and exposure lamps) must be housed in a cleanroom.²³

To address the challenges of traditional lithography, nanoimprint lithography (NIL) and soft lithography techniques have been developed.^{20,23,187,188} NIL refers to a pressure-induced transfer of patterns from a rigid mold to a UV cured or thermally softened polymer.²⁰ Soft lithography encompasses a number of techniques that use an elastomeric stamp (often polydimethylsiloxane, PDMS) to print, mold, or emboss a pattern onto a surface.^{20,23,187} In both cases, their primary purpose is to prepare a negative copy of an existing “master” (designed or natural). A wide array of substrate materials (e.g., polymers, glass, and gold film) and surface morphologies can be handled with these techniques, expanding the application of nanofabricated structures.^{20,23,138,187} Particularly, polymethylmethacrylate (PMMA) and polystyrene (PS) has been proven versatile for copying microscale patterns by thermal NIL.¹⁸⁹ Polycarbonate (PC) is conventionally

molded via NIL to mass-produce optical discs; with properly controlled temperature and pressure, sub-50 nm structures can be replicated.^{190,191} It has been recently adapted for making one-to-one replicas of lithographically fabricated masters by thermally molding PDMS negatives.¹⁹² Sub-nanometer patterns have been also imprinted into polyurethane (PU) by exposing uncured prepolymer to UV light while in conformal contact with a “master.”^{193,194}

Solvent-assisted molding techniques, a subset of soft lithography, further simplifies the fabrication procedure by taking advantage of different interactions of solvent with the mold and substrate to eliminate the need of heat and high pressure.^{30,195,196} Although the mold is relatively impervious (or at least insoluble) to solvent, the substrate is compatible and becomes inundated with solvent, either swelling or dissolving. Solvent-assisted molding of PS and PMMA has been explored in the past two decades to achieve sub-100 nm resolutions.^{20,,30,195,196} PC is prone to recrystallization upon solvent treatment,^{54,65} as a result it has not been considered as a suitable substrate, i.e., a solvent-assisted molding protocol for convenient nanoscale replication with PC has not been explored.¹⁹⁷ Nonetheless, PC has excellent durability, impact resistance, and optical clarity, which lend to its broad application in safety goggles, greenhouses, skylights, bulletproof glass, and automobile headlights.¹⁹⁸ Adapting solvent-assisted molding to PC (with a similar resolution to thermal-NIL of PC) would reduce the complexity and equipment costs, and facilitate the incorporation of functionalities derived from micro and nanoscale features to PC-based structures and devices.

Herein, we report a nanocontact replication technology to create durable one-to-one monolithic PC replicas of any micro or nanostructures (with a lateral resolution of ≈ 100 nm) that are compatible with PDMS. Unlike thermal molding which requires specialized equipment and precise conditions, our protocol is conducted on a benchtop at ambient conditions. It should be emphasized that this is not a conventional molding technique where a master is used to prepare a negative copy, but a reproduction technique where the negative template is adapted for rapidly creating identical replicas of the masters. Such replicas can be used as masters to preserve the original and to perform multiplex fabrication. With this in mind, particular attention is paid to efficient pattern transfer from a master to the PDMS template and the fidelity among the master, PDMS template, and PC replica. In specific, optimized replication of both micro and

nanostructured masters (arrays of pits and holes) will be presented, whereas microfluidic channel plates and commercial security labels with subwavelength diffractive structures are replicated to demonstrate the broad adaptability of this technology in academic and industrial settings.

5.2. Nanocontact replication using PC at the Micro- and Nanoscale

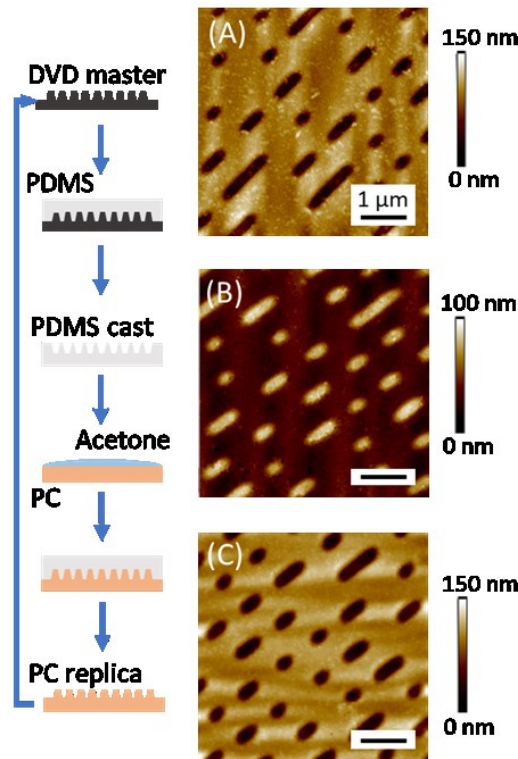


Figure 5-1: Benchtop one-to-one nanocontact replication of a DVD-ROM master to create an identical PC replica. Schematic illustration of the preparation of a PDMS template and the subsequent solvent-assisted molding to create a PC replica of the original DVD master; AFM images of (A) the original DVD-ROM as the master, (B) the PDMS template cast from the DVD-ROM, (C) the PC replica.

Previously (in Chapter 3) I fabricated 3D PDMS fingerprint phantoms (calibration targets) for developing more reliable fingerprint scanners by first making fingerprint impressions into a PC surface that was swollen and softened by a short period (45 s) acetone treatment.¹⁵² After solvent had evaporated, the PC impression was applied as a template to cast a PDMS fingerprint replica (organic dyes were added to emulate the optical properties of skin).¹⁵² Upon examining the fidelity of finger ridge replication on the

PDMS phantom, we observed that impressions of nanostructured micro-spherulites formed on the PC surface are precisely copied into PDMS phantoms cast from them. We envisioned this novel approach as a benchtop technique for reproducing designed micro/nanostructures simply and economically, with an ultimate goal of formulating a protocol for the simple, rapid, and cost-effective replication of material nanostructures. The generalized protocol to produce a one-to-one PC replica of a master without involving high heat and pressure is shown in Figure 5-1. In this first example, the “structural master” shown in Figure 5-1A, is the base of a digital versatile disc-read only memory (DVD-ROM) that consists of an array of pits. By casting the master with PDMS, an elastomeric negative (PDMS template) of the master is prepared (Figure 5-1B). The PDMS template was then used to mold a PC plate that was treated briefly with acetone, i.e., the PDMS template was placed on the softened PC surface under slight pressure (<10 PSI) to achieve conformal contact. Comparison of the DVD-ROM master and PC replica (Figure 5-1C) indicates no defects formed on the surface and the edges of pits remain well defined.

Table 5-1: Feature dimensions of the DVD-ROM master, PDMS template, and PC replica fabricated by benchtop one-to-one nanocontact replication.

	DVD Master	PDMS stamp	PC Replica
Width (nm)	260 ± 10	250 ± 10	260 ± 10
Length 1× (nm)	400 ± 5	400 ± 15	400 ± 15
Length 2× (nm)	740 ± 5	770 ± 5	720 ± 25
Length 3× (nm)	1350 ± 15	1300 ± 20	1250 ± 50
Height (nm)	85 ± 5	50 ± 5	60 ± 5

Listed in Table 5-1 are the dimensions, determined from the AFM images shown in Figure 5-1, of the features on the DVD-ROM master, PDMS template, and PC replica, respectively. It should be noted that data are encoded into optical discs in such a way that result in pits of three different lengths but the same width. The smallest pits are 400 ± 5 nm long in the DVD-ROM, the corresponding features in the PDMS template and the PC replica were both 400 ± 15 nm. Though the variability in pit length increased, overall, the features were not distorted. Midsize pits in the DVD-ROM and PC replica were the same length, though the PDMS “peaks” were slightly large. On the longest pits some distortion appeared, pits in the PC replica (1250 ± 50 nm) are slightly smaller than those on the DVD-ROM (1350 ± 15 nm). The height of features in the PDMS (50 ± 5 nm) were lower than on the DVD (85 ± 5 nm) indicating the PDMS did not completely impregnate features. As a

result, the features in the PC replica are slightly shorter (60 ± 5 nm), this issue will be addressed in later experiments. This simple protocol only requires PC, acetone, and a PDMS kit, and the whole process can be conducted on benchtop without any specialized equipment. The PC replica can be used to replace the master for future molding applications (vide infra). As long as the prospective “master” is unaffected by the solvents in the PDMS kit (<1% ethyl benzene and xylene) and does not stick to or become inundated with PDMS (preventing demolding),^{72,78} a PDMS template can be prepared and the one-to-one nanocontact replication to a PC replica is feasible.

The fabrication of functional structures often involves a large range of feature sizes (e.g., the hierarchical roughness of superhydrophobic surfaces);^{185,191} compatibility with macro, micro, and nanoscale features would broaden the possible applications of our protocol.^{188,195} In fact, the molding protocol described herein has already been successfully applied for precisely replicating fingerprints, which have a lateral feature size of ≈ 0.5 mm and a depth of ≈ 50 μm .^{152,199}

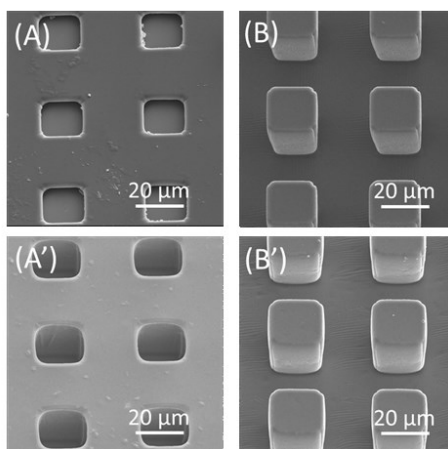


Figure 5-2: SEM imaging of microscale pit arrays prepared via benchtop nanocontact replication. (A) Silicon/SU8 master, (B) PDMS template cast from the master, (A') PC replica of the master, (B') Second generation PDMS template cast from the PC replica. All images are tilted at 30° to measure the feature height/depth.

To test the fidelity of our replication protocol at the micrometer scale, a silicon/SU8 master with 20 ± 1 μm wide and 25 ± 1 μm deep square pits (Figure 5-2A) was used to cast a PDMS template (Figure 5-2B). The PDMS template was subsequently used to mold a PC replica (Figure 5-2A'), from which a second-generation PDMS template was created (Figure 5-2B'). The samples were tilted for imaging the feature heights, even so

the depth of pits in the master cannot be accurately measured. The PC replica shown in Figure 5-2A' is adorned with $21 \pm 1 \mu\text{m} \times 21 \pm 1 \mu\text{m}$ square pits, identical in size to those on the original master (Figure 5-2A); moreover, the square pits in the PC replica are $25.0 \pm 0.5 \mu\text{m}$ in depth, which is also consistent with the designed depth of the square pits in the master (Figure 5-2A). The PDMS template used to mold the PC replica (Figure 5-2B) is adorned with a negative of the master; $20 \pm 1 \mu\text{m}$ wide pillars with notched corners, indicating these micrometer features were precisely reproduced. However, the pillars in the PDMS template measured $26.5 \pm 0.5 \mu\text{m}$ in height, slightly higher than the pit's depth in the master and PC replica. The features on the second-generation PDMS template (Figure 5-2B') are of identical dimensions ($21 \pm 1 \mu\text{m}$ width and $25.5 \pm 0.5 \mu\text{m}$ in height) as those on the original template (Figure 5-2B); the pillars are shown to have smooth edges and notched corners like the original.

Two important conclusions can be drawn from this experiment: 1) microscale features on silicon/SU8 masters can be readily copied into a PC replica; 2) PC replicas can replace the masters for subsequent PDMS casting without any distortions of the feature dimensions. To define the ultimate resolution of our nanocontact replication protocol, a nanohole array lithographically prepared on a thin film of PMMA (spin coated on silicon substrate) was used as the "master." The array of nanoholes have diameters ranging from 50 to 300 nm, which are ideal choices to test our replication protocol.

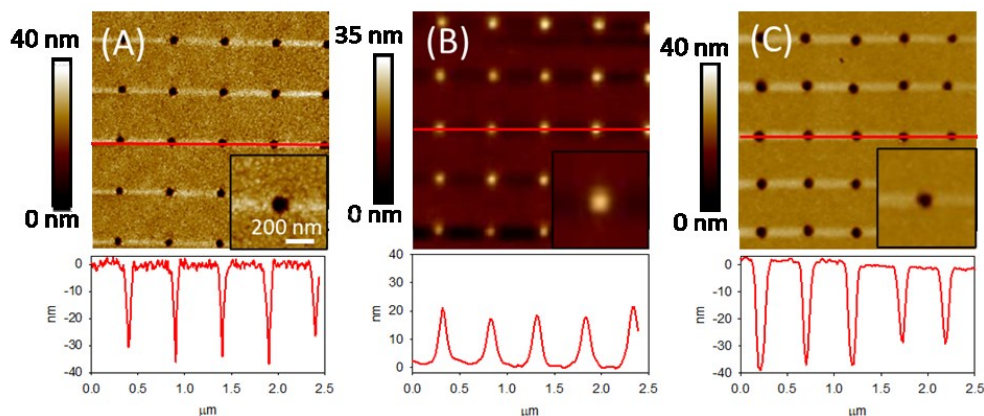


Figure 5-3: Nanocontact replication of nanohole arrays. Atomic force microscopy (AFM) images of a nanohole array fabricated on a thin PMMA film on a silicon substrate (A), the PDMS template cast from the "master" (B), and the PC replica molded from the PDMS template (C). Inset below each image is the profile of the respective surface along the red line. Inset in each image is a zoom-in of a single nanoscale feature.

The successful replication of such a nanostructured master is shown in Figure 5-3, from casting the PDMS negative to molding a PC replica. As confirmed with AFM imaging (Figure 5-3A), the array of pits in the PMMA film are 500 nm apart, whereas slight variation in the shapes of pits is evident. The pits are well defined having a mean diameter of 105 ± 5 nm, and the depth of pits is 33 ± 4 nm. The diameter of pillars on the PDMS template (a negative of the original) is much larger at the bottom (190 ± 10 nm); they also appear significantly shorter (19 ± 2 nm) than expected based on the measured depth of the nanoholes. The PC replica molded with the PDMS template is shown in Figure 5-3C; visually it appears very similar to the master and defect-free. Remarkably, the average diameter of pits on the PC replica is 125 ± 10 nm, which is consistent with the dimensions on the master; the depth of the pits is 34 ± 5 nm, the same as the pits on the master (33 ± 4 nm). It is unexpected that the features on the PDMS template showed different dimensions; AFM imaging distortions likely cause this inconsistency, the softness of PDMS may “depress” the feature height, and the AFM tip contacting and adhering to the features can distort the profile as well.^{120,200}

This series of AFM images illustrates how our benchtop nanocontact replication protocol can be used to replicate structures down to ≈ 100 nm with only minor distortions if the aspect ratio is not too high. When the pit diameters are smaller than 100 nm, the PDMS precursors may fail to fill the features, leading to missing or partially formed pillars. In the subsequent PC replica, missing holes and shallow pits are scattered across the array. The replication of a larger scale PMMA master with a wide range of nanohole sizes, along with the PDMS template and PC replica, are shown in Figure C2, Supporting Information).

5.3. Optimization of Replication Parameters

The same swelling process that makes the PC surface malleable eventually leads to recrystallization of the polymer network; solvent molecules penetrate the polymer network, and push the polymer chains apart to increase their free volume.^{54,65} With a greater free volume, the polymer chains have more freedom to move, rotate, and slip past other polymer chains, lowering the T_g below room temperature and putting the polymer in a rubbery state. The small size of acetone facilitates its penetration into the polymer network; however, it is a relatively poor solvent for PC.^{92,108} Without adequate polymer–solvent interaction (dissolution), the mobile PC chains conform with one another and adopt

more energetically favorable conformations by crystallizing into spherulites (a spheroidal arrangement of crystallized polymer chains emanating radially from a central nucleation point).^{54,65} As the spherulites in PC range from 2 to 10 μm in diameter, their formation during solvent-assisted molding would inherently disrupt nanoscale features. Therefore, thorough understanding and potential control of spherulite formation during the molding process is imperative to optimize the nanocontact replication protocol.

With the aforementioned consideration, morphological changes of PC upon treating with acetone and nanocontact molding have been examined via scanning electron microscope (SEM) imaging systematically. As shown in the top inset of Figure 5-4, PC plates were treated with acetone for the indicated time period then either had the solvent rapidly removed with a stream of air until dry (Figure 5-4A) or were molded with a PDMS template (Figure 5-4B). The PDMS template (5 cm \times 5 cm), cast from a blu-ray disc-recordable (BD-R), was adorned with a line grating (pitch of 320 nm). It was pressed onto the PC plate (2.5 cm \times 2.5 cm) with <10 PSI of pressure and left until acetone had evaporated (<5 min). When PC was not molded, small spherical nodules began to form randomly on the surface after as short as 10 s of acetone treatment. On the 20 s sample, the initial nodules had grown significantly larger, some of them became completely exposed from the surface while others remain embedded. Very significant changes occur at 45 s, well-developed PC spherulites emerge from the amorphous polymer surface, and radial arrangements of tendrils on top of spherulites are visible. On the PC plate treated for 60 s much of the amorphous surface is consumed and incorporated into spherulites that have grown further to impinge on each other. With the amorphous polymer chains at the surface consumed, underlying layers of spherulites have developed.

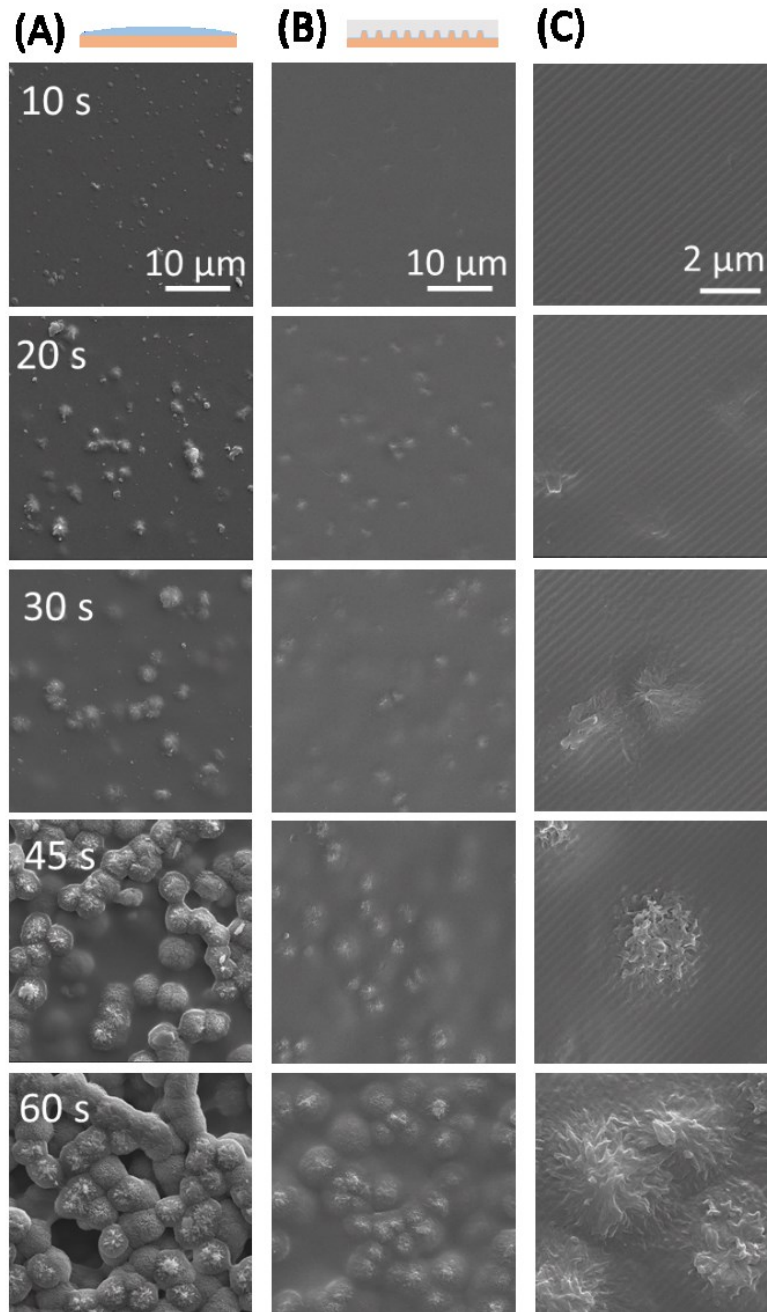


Figure 5-4: Crystallization of acetone-treated PC plates confined by nanocontact molding. (A) PC treated with acetone for the indicated period of time. (B) PC molded with a PDMS template (cast from a BD-R disc) right after the solvent treatment for the same period of time as in (A). Simple schematics of the treatment applied to the PC surface are displayed as the top insets. (C) High-magnification images of the molded PC plates shown in (B).

In contrast, considerably retarded morphological changes have been observed when the surface was molded with the PDMS template right after the solvent treatment (Figure 5-4). The PC molded after 10 s of acetone treatment has very few defects on the surface. Small nodules became visible on the surface of PC molded after 20 s acetone treatment but were still less pronounced than on the corresponding unmolded sample. On the PC surface treated for 30 s before molding, tendrils of growing spherulites can be seen emerging from and growing along the surface (Figure 5-4C). Spherulites in the sample molded after 45 s of treatment remain embedded in the polymer matrix whereas tendrils at the tops of spherulites have reached the surface, in comparison spherulites had fully emerged in the sample that was not molded. On the 60 s molded sample spherulites have grown, but are still not separated from the amorphous matrix; in the high-magnification image, spherulites can be seen beginning to impinge upon each other and disrupting most of the grating, even between spherulites the grating is incomplete and deformed. The degree of crystallization was also assessed by the decrease in optical transmittance through a PC plate caused by light scattering by the formed spherulites. Transmittance decreased at a slower rate on molded samples indicating reduced spherulite formation (Figure C3, Supporting Information).

It is evident that if the solvent treatment were limited within a short period of time (<20 s), the PC surface should be free of defects and suitable for subsequent molding of nanoscale features. This was further confirmed by replicating a PC diffraction grating (from a DVD-R base); prolonged treatment of the PC prior to molding would essentially disrupt the formation of sub- μm scale gratings for which the interference pattern of the laser shining atop is no longer visible (Figure C4, Supporting Information). More importantly, the morphological change particularly the development of spherulites in the molded sample are much less pronounced than on the corresponding unmolded surface. This indicates that molding essentially suppresses the development of spherulites, which is beneficial for the replication of nanoscale structures (below the μm -size of typical spherulites).

We can conclude that by molding solvent-treated PC with a PDMS template, the disfavored crystallization process can be retarded, but why is this so? Placing the PDMS template in contact with the solvent-treated PC plate physically displaces acetone from the surface, decreasing the amount available to swell and crystallize PC further. Another source of acetone removal is being absorbed into the PDMS template, which swells up to 6% in length when immersed in acetone for prolonged period of time.⁷¹ Figure 5-5A shows

the partitioning of acetone into PC and PDMS with time. When treated with 250 μL acetone for 10 s before molding, the PC absorbs $22 \pm 1 \mu\text{L}$ and the PDMS absorbs $16 \pm 1 \mu\text{L}$. As treatment time before molding is extended, the amount of acetone absorbed into PC increases whereas the amount absorbed into PDMS decreases. The amount absorbed into PC plateaus at $27 \pm 1 \mu\text{L}$ after 45 s, which corresponds to the significant development and growth of spherulites at the surface. After 60 s, the amount of acetone in both the PC and PDMS begins to decrease; it has become more difficult for additional acetone to penetrate the now semicrystalline PC.^{65,201} In this case, both air blowing or PDMS molding can effectively remove much of the excess solvent at the surface.

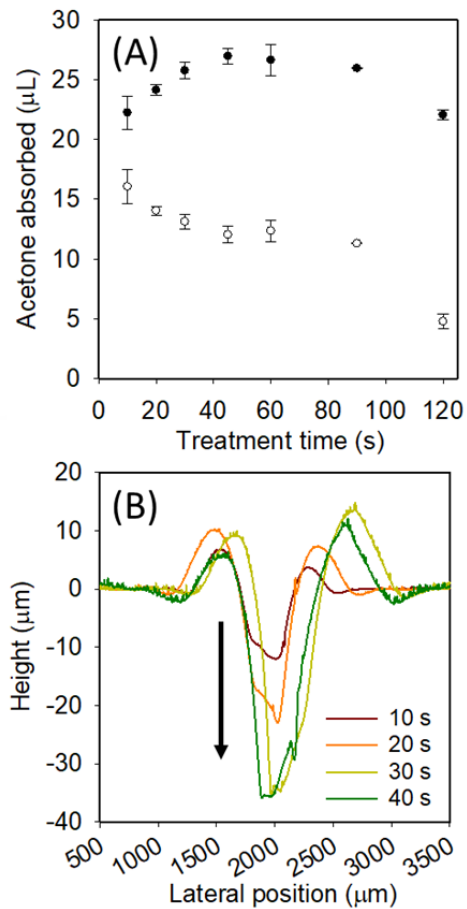


Figure 5-5: (A) Volume of acetone absorbed by the PC plate (solid circles) and PDMS template (open circles) during nanocontact replication as a function of acetone treatment time before molding. (B) Profiles of PC molded with the back of a boxcutter (Exacto blade) after acetone treatment. PC was treated for 10 to 40 s as color coded in the corresponding curves; the arrow indicates the direction of increased treatment time.

The depth of acetone penetration to PC is important as it determines the thickness of the “moldable” layer, and therefore defines the maximum “height” of features that can be replicated. Particularly, the “depth” of acetone penetration to PC was examined by pressing the flat edge of a box cutter (Exacto blade) into the PC plate after treating PC with acetone for different periods of time (Figure 5-5B). It is remarkable that in 10 s, the PC plate was “softened” to a depth of $18 \pm 4 \mu\text{m}$, and by 20 s, it increased to $25 \pm 3 \mu\text{m}$. The moldable layer increased to $40 \pm 8 \mu\text{m}$ by 30 s where it starts to be plateaued. This result confirms that acetone treatment time can be adjusted depending on the height of features to be replicated; by selecting the shortest treatment time required based on the feature height, the size and prevalence of crystallization defects can be minimized.

We have also examined the pressure required to mold a solvent-softened PC plate with a PDMS template by placing a pressure sensitive film under the PC plate during the molding. A pressure of only 5–25 PSI is required to achieve conformal contact and ensure the entire area is molded successfully. Successful molding over a low but wide pressure range is valuable in situations that special apparatus to apply high and/or consistent pressure are not available.

5.4. Distinction from Conventional Single-step Molding and Application Potential

The results presented in Figures 5-1 to 5-3, illustrated how the nanocontact replication protocol can functionally produce a one-to-one PC replica of various “masters” adorned with microscale and nanoscale features. For academic and on-site fabrication applications where a lithographically prepared silicon master is used repeatedly to cast PDMS templates (stamps), cutting, demolding, and constant handling will eventually damage the master (Figure S5, Supporting Information). PC replicas can alleviate these issues because they are easily replaceable and durable (they do not delaminate or crack like silicon wafers) (Figure S6, Supporting Information). Moreover, PC and PDMS easily demold from each other because PC has a much lower surface energy than silicon wafers, which generally require the application of a silane-based antiadhesion coating.^{202,203}

Patterning large areas is difficult with many nanofabrication methods;^{20,30,181,193-195} in contrast, as large as $10 \text{ cm} \times 10 \text{ cm}$ of defined micro/nanostructures can be replicated quickly and with ease by our method (*vide infra*). The highest lateral resolution

we achieved (≈ 100 nm) is on par with that of thermal molding of PC (50 nm),^{190,191} as well as solvent-assisted molding of PMMA and PS (sub-100 nm).^{30,195,196} Table 5-2 lists the resolutions of thermal and solvent-assisted molding techniques on several engineering polymers for further comparison.

Table 5-2: Resolutions of traditional nanoreplication methods on popular engineering plastics.

Material	Method	Resolution
Poly(lactic acid) (PLA), Polyethylene Naphthalene (PEN)	Hot emboss PLA and PEN with a fluorosilane coated Si master.	~ 1 μm (microfluidic channels and wells) ¹⁸⁹
Acetonitrile Butadiene Styrene (ABS)	ABS film is molded with PDMS stamp with solvent (acetone) applied to it.	~ 300 nm (nodes connected by thin bridges) ³⁰
Polycarbonate (PC)	PC film treated with chloroform vapors for 2 hours, PVA mold placed on surface.	~ 700 nm (diffraction grating) ²⁰⁴
Polycarbonate (PC)	PC is molded with an AAO roller at 160 C and 33 kPa of pressure.	50 nm (nanopillars) ⁵⁹
Polyurethane (PU)	PU prepolymer is put in contact with h-PDMS mold and irradiated with UV light.	0.5 nm (molecular steps on crystal) ²⁰⁵
Polymethylmethacrylate (PMMA)	PMMA dissolved in trichloroethylene is placed on Si and molded with PDMS stamp.	80 nm (high aspect ratio lines) ²⁰⁶
Polymethylmethacrylate (PMMA)	PMMA is loaded into a heated press, molded at 170 C and 30 bar pressure.	100 nm (nanowells) ¹⁹⁵
Polystyrene (PS)	PS film treated with chlorobenzene then molded with a PDMS stamp.	~ 500 nm (diffraction grating) ²⁰⁷
Polystyrene (PS)	PS is loaded into a heated press, molded 85 C and 70 psi pressure.	100 μm (microfluidic channels) ²⁰⁷
Our work	PC molded with solvent assistance.	125 nm (nanodot array)

To further demonstrate the advantages of the nanocontact replication protocol discussed earlier, we have created a PC replica of a silicon/SU8 master (Figure 5-6A) that is used for preparing PDMS microfluidic microchannel plates (Figure 5-6B). It is a standard procedure to mold PDMS microchannel plates from lithographically created silicon/SU8

masters, which enables the benchtop fabrication of functional microfluidic devices. As shown in Figure 5-6C, the PC replica has the same pattern of the rectangular relieves as the master, which is now used in place of the master to cast a “second-generation” PDMS microchannel plate (Figure 5-6D). We have shown that such a PDMS microchannel plate works well when attached to a flat glass substrate. As illustrated with a blue dye solution, the microchannels performed perfectly as follows: 1) the solution is wicked along the channels; 2) the fluid flow is consistent and smooth, without any bubbles formed in channels; and 3) the channels do not leak or bleed at their edges. This result shows that the durable and inexpensive PC replicas can be used in place of more precious silicon/SU8 masters for making microfluidic devices.

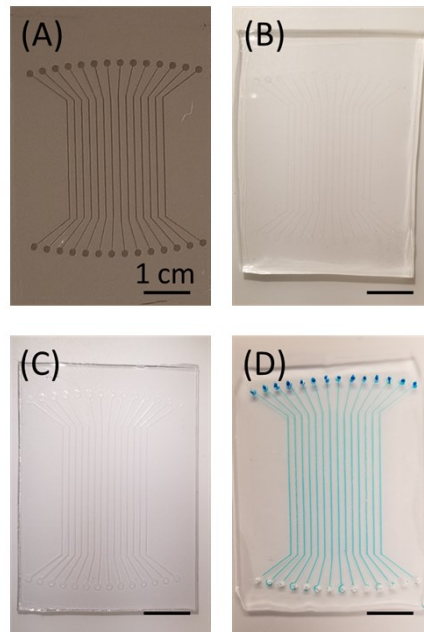


Figure 5-6: Fabrication of PDMS microchannel plates from the PC replica of a silicon/SU8 master. (A) Lithographically prepared silicon/SU-8 master with 14 rectangular relieves (0.5 mm wide and 50 μm high); (B) PDMS template cast from the master, adorned with microfluidic channels; (C) PC replica of the master molded with the PDMS template; (D) Second-generation PDMS microchannel plate cast from the PC replica. Inlet holes were punched into the PDMS plate, which was adhered to a glass substrate; embedded microchannels were filled with a dye solution to test their efficacy.

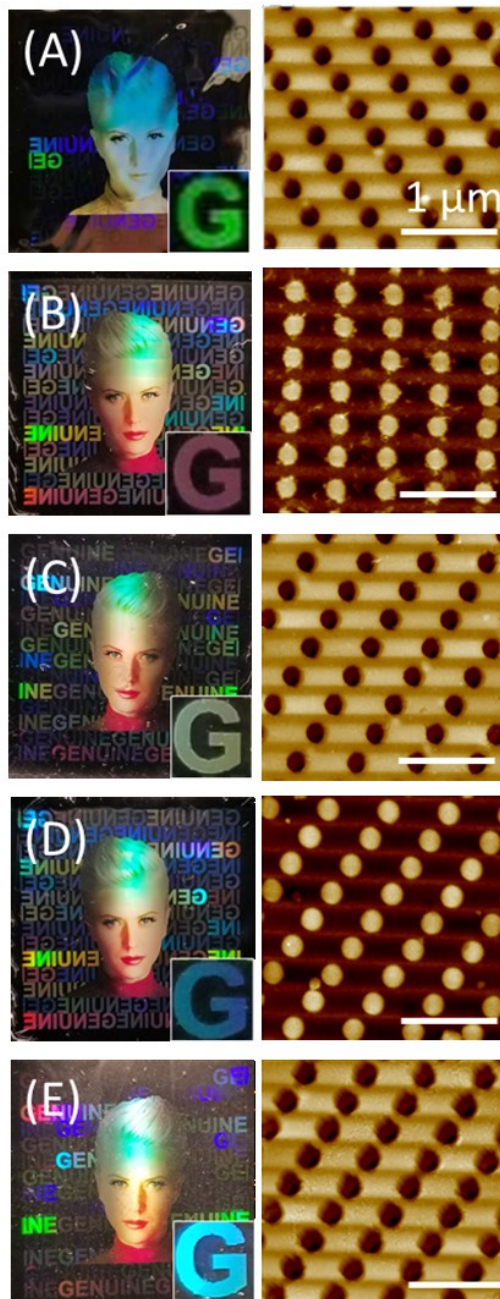


Figure 5-7: Nanocontact replication of a security label with subwavelength diffractive structures. (A) Nickel master for making security labels provided by Nanotech Nanosecurity Corp.; (B) PDMS template cast from the nickel master; (C) PC replica molded from the PDMS template; (D) Second-generation PDMS template cast from the PC replica; (E) Second-generation PC replica molded from the second-generation PDMS template. In all cases, optical images are shown on the left, while the corresponding AFM image showing the microscopic morphology is shown on the right. The bottom-right Inset in each optical image is a magnified section (letter G).

A nickel master with nanometer-sized pits and troughs (Figure 5-7A) used to prepare security labels was chosen to demonstrate the capability of our protocol to replicate commercial products with rather complex structures. The specific arrangement of subwavelength diffractive structures causes light to reflect, diffract, and interfere in such a way to produce a vibrant pattern of colors.^{204,205} The portrait of a woman that it generates provides a convenient method to visually evaluate replication fidelity.²⁰⁶ Via the preparation of a PDMS template (Figure 5-7B), a one-to-one PC replica of the Ni master (Figure 5-7C) was successfully created. Illustrating how the original master can be replaced by a PC replica, a second-generation PDMS template (Figure 5-7D) and the second-generation PC replica (Figure 5-7E) were fabricated subsequently. Throughout the replication process, the image colors remained consistent and vibrant. The AFM images of the surface confirmed the fidelity of replicating the nanoscale features. The dimensions of features (arrayed nanoholes for this particular section of view) in the master and PC replica are identical; the feature depth is 40 ± 2 and 42 ± 2 nm and width 200 ± 5 and 210 ± 5 nm, respectively. The arrayed nanoholes created in the second-generation PC replica are slightly larger (44 ± 2 nm deep and 220 ± 5 nm wide), but the image is essentially unperturbed. In both industrial and academic settings, multiple PC replicas of a single master can be combined into a single monolithic mold to exponentially increase production.

As demonstrated earlier, the application of this nanocontact replication protocol is broad; its future potential is manifold. Particularly, PC-based devices and parts (vehicle headlights, skylights, safety glasses, greenhouse siding, medical tubing connectors, etc.) can be augmented with embedded micro and nanostructures to control light,²⁰⁷ wetting,²⁰⁸ and reduce biofouling.^{209,210} For example, bacterial infections caused by medical devices can be reduced by applying nanoscale, antibacterial features to the PC components.^{209,210} In the meantime, the studies of molding-confined crystallization will shed lights on investigating molding other polymeric materials that have been overlooked in the past.

The one-to-one benchtop replication of micro/nanostructures into PC will benefit industry and academic labs by reducing the cost for device fabrication and accelerate the adoption of micro and nanotechnology. Fast and economic replication of masters will enable researchers to scale up fabrication by multiplexing and share their designs, whereas the relative simplicity of our protocol will help promote interdisciplinary work that

relies on such masters. In comparison with concurrent exploration of heat molding with PDMS to create PC replicas by Sonmez et al.,¹⁹² our solvent-assistant replication protocol is even faster, less reliant on specialized apparatus, and has a better resolution.

5.5. Conclusion

A benchtop method of nanocontact replication has been demonstrated for replicating features ranging from 0.5 mm to 100 nm in resolution with high fidelity, which can be scaled up to templates as large as $10 \times 10 \text{ cm}^2$. Thus produced PC replicas can be repeatedly used as low-cost replacements for molding PDMS templates, preserving the original, precious “masters”. It was also discovered that molding a PC plate with a PDMS template can inhibit the recrystallization at the surface by physically disrupting the crystallization process and absorbing the solvent. The ideal conditions for effective molding while simultaneously limiting crystallization were defined; the recrystallization does not induce significant structural disruption to the replicated features upon carefully controlling the solvent treatment time. The success in replicating various “masters”, from microfluidic channel plate to nanostructure-embedded security labels exemplifies the potential application of this bench-top nanocontact replication protocol in both academic and industrial settings.

5.6. Experimental

Materials and reagents. PC sheets were purchased from Bayer (Sheffield, AL), which were protected by a polyethylene masking film on both sides upon receiving. Acetone (99.8%), toluene (99.9%), hexane (99.9%), and ethanol (95%) were purchased from Fisher Scientific (Hampton, NH). Sylgard 184 PDMS kit (consisted of an elastomer base and an elastomer curing agent) was purchased from Ellsworth Adhesives (Germantown, WI). Hard PDMS (h-PDMS) kit was purchased from Gelest Inc. (Morrisville, NY). Fujifilm Prescale Films were purchased from Sensor Products Inc. (Madison, NJ). Deionized water ($>18.2 \text{ M}\Omega \text{ cm}$) was produced with a Barnstead Easypure UV/UF water system (Thermo Scientific, Waltham, MA).

Preparation of masters, casting PDMS templates, and molding PC replicas. Several “masters” adorning micro and nanoscale structures either prepared via standard lithography or adapted from optical discs were prepared and used for the replication

studies, for which detailed preparation instructions are provided in Figure S1, Supporting Information.

To cast PDMS templates from masters or PC replicas, the two precursors included in the kit, the elastomer base (part A) and the curing agent (part B) were mixed in a 10:1 ratio by manual stirring and vortexing. The solution was then poured over the master or PC replica, degassed in a vacuum chamber for 45 min, and cured in an oven at 80 °C for 2 h. The PDMS template was then cut and peeled from the master (or PC replica).

For casting templates with nanostructures (<250 nm) or with a high aspect ratio, a thin layer of h-PDMS diluted with toluene was cast first; the ratio of toluene was dependent on the resistance of the template to organic solvents (e.g., 75 wt% when casting a metal master and 20 wt% when casting a PC replica). The elastomer (part A) and curing agent (part B) were mixed in a 1:1 ratio then toluene was added. Upon manual stirring and vortexing, the solution was poured over the master or PC replica, degassed in a vacuum chamber for 45 min, and cured in an oven at 80 °C for 30 min. A regular PDMS film was prepared (as outlined) on top of the h-PDMS layer to create a flexible backing; after curing an additional 2 h at 80 °C, the composite PDMS template was cut out.

To mold micro and nanostructures onto PC plates (2.5 cm × 2.5 cm), the protective masking film was removed from one side, and the exposed surface was then covered with 0.25 mL of acetone. The solvent was left on the surface for 10–60 s (depending on the feature size to be molded). The PDMS template was placed onto the PC plate and pressure was applied (7–25 PSI) with a t-shirt press to achieve conformal contact. The PC and PDMS template were left in contact for 5 min or until there were no signs of solvent.

To observe partitioning of solvent during molding PC plates with a PDMS templates, the PC plate and PDMS template were weighed immediately prior and immediately after molding with an analytical balance.

Characterization and instrumentation. A FEI NanoNova 430 SEM (Thermo Fisher Scientific, Hillsboro, OR) was used to obtain high-resolution images, for which an accelerating voltage between 10 and 15 kV was used. The samples were coated in a Leica EM ACE600 high vacuum coating system (Concord, ON) with a 7–10 nm iridium layer to improve the conductivity. Atomic force microscopy (AFM) images were taken with a Dimension Icon scanning probe microscope (Bruker; Billerica, MA) using a ScanAsyst-Air

silicon nitride tip with a resonance frequency of 70 kHz. The maximum molding depth was measured using a Bruker Dektak XT (Billerica, MA) profilometer.

5.7. Supporting Information

Detailed procedures to prepare micro- and nanoscale “masters”; additional experimental results including replication of the nanohole array used to determine the protocol’s resolution, replication of a diffraction grating with different acetone treatment time, UV-Vis measurement of acetone treated PC, demonstration of the damaged silicon masters, and the durability test of PC replica used as a “replacement master” for polydimethylsiloxane (PDMS) casting.

Preparation of replication masters

The nanostructured masters used for the replication depicted in Figure 5-1 of the main text were prepared from DVD-ROM discs by removing the bottom PC substrate (see Figure C1A) with a craft knife. The top PC substrate with pits (for storing data) were cleaned by sonication in water then rinsing with ethanol before casting PDMS.

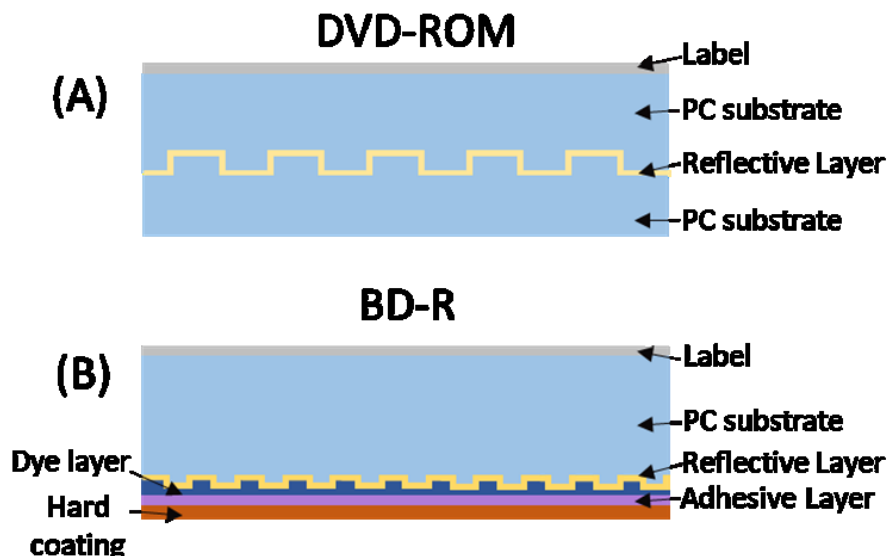


Figure C1. PC substrates of optical discs adapted as “masters” by removing additional protective/dye layers. Schematic view of the layered structure of (a) DVD-ROM (A) and (b) BD-R (B).

Microstructured masters used in the experiments shown in Figure 5-2 were constructed by standard photolithography; a 25 μm thick SU-8 film was first spin coated onto a Si wafer with a Laurell WS-400B-6NPP-LITE spin coater (North Wales, PA). Designs created in CleWin (WieWeb software, Helengo, Netherlands) were etched into a chrome mask, which was then used to confine the UV irradiation (at 254 nm for 6 s). A USHIO 500 DUV lamp (Cypress, CA) and an OAI MBA mask aligner (San Jose, CA) were used for the process. The irradiated wafer was then treated with a SU-8 developer solution (1-methoxy-2-propanol acetate) for 4 min to develop the pattern. The wafer was cleaned by rinsing with acetone, then isopropyl alcohol, and finally water.

Nanostructured masters used for the resolution tests shown in Figure 5-3 were prepared from a PMMA film spin coated onto a silicon wafer with the Laurell WS-400B-6NPP-LITE spin coater. The array-format features were created by electron beam lithography with a Raith GmbH e_LiNE system (Dortmund, Germany), followed by development with a 1:3 methyl isobutyl ketone: isopropyl alcohol solution.

Nanostructured masters for studying PC crystallization (Figure 5-4) were made from recordable Blu-ray discs (BD-R). The disc (Figure C1B) was first scored with a blade then a pair of tweezers were used to slowly peel off the scratch-resistant layer; it was then sonicated in ethanol and water sequentially (5 min each) to remove the dye layer and the reflective layer. Thus obtained PC substrate with a nanoscale grating structure was thoroughly cleaned with water, and dried with N_2 .

The Si/SU-8 masters for preparing microfluidic microchannel plates (experiments presented in Figure 5-6) were also constructed by standard photolithography as described above, but with a 50 μm thick SU-8 layer which was developed for 6 min.

To test the commercial replication potential of our protocol (Figure 5-7), a nickel master with subwavelength diffractive structures was supplied by Nanotech Security Corp.

Replication of a nanohole array with varied feature sizes

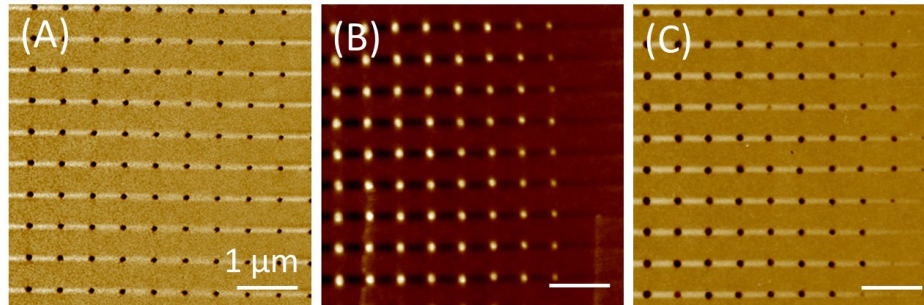


Figure C2. Replication of a nanohole array with varied feature sizes. AFM images of (A) the nanohole array (“master”) prepared on polymethylmethacrylate (PMMA) using standard e-beam lithography. (B) the PDMS mold casted from the master, (C) the PC replica molded with the PDMS negative.

The nanostructure “master” used to determine the resolution of our nanocontact replication procedure consists of arrayed nanoholes of different diameters. Figure C2A shows part of the array with nanoholes, from 50 nm to 300 nm in diameter, which were fabricated with different electron beam irradiation time. Figure S2B shows the h-PDMS template cast from the “master”; once the hole size decreases to a certain point (52 ± 2 nm), the h-PDMS is unable to fill the holes. This results in incomplete molding to the PC replica (Figure S2C), where the last row of holes is missing.

Transmittance through acetone treated and nanocontact molded PC

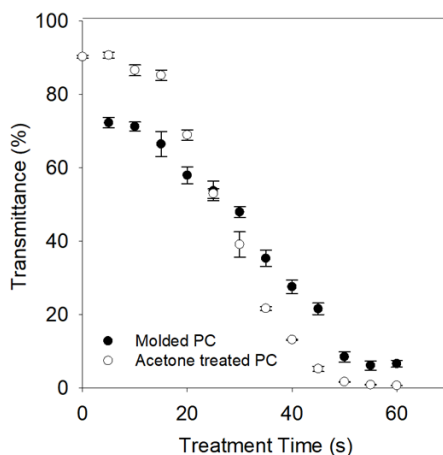


Figure C3. Transmittance through acetone treated and nanocontact molded PC.

To track crystallization in molded and acetone treated PC, PC plates were treated with acetone for a period of time and then either molded or had the excess acetone blown

off with a stream of air. After treatment, the transmittance was measured and compared. Initially the molded PC had a lower transmittance due to scattering by molded structures (grating) on the surface. With increasing treatment time, the transmittance through both types of PC decreased. However, it decreased slower in molded PC and plateaued at a higher value, this is attributed to the inhibition of crystallization at the surface by molding.

Fidelity of nanocontact replication influenced by the acetone treatment time

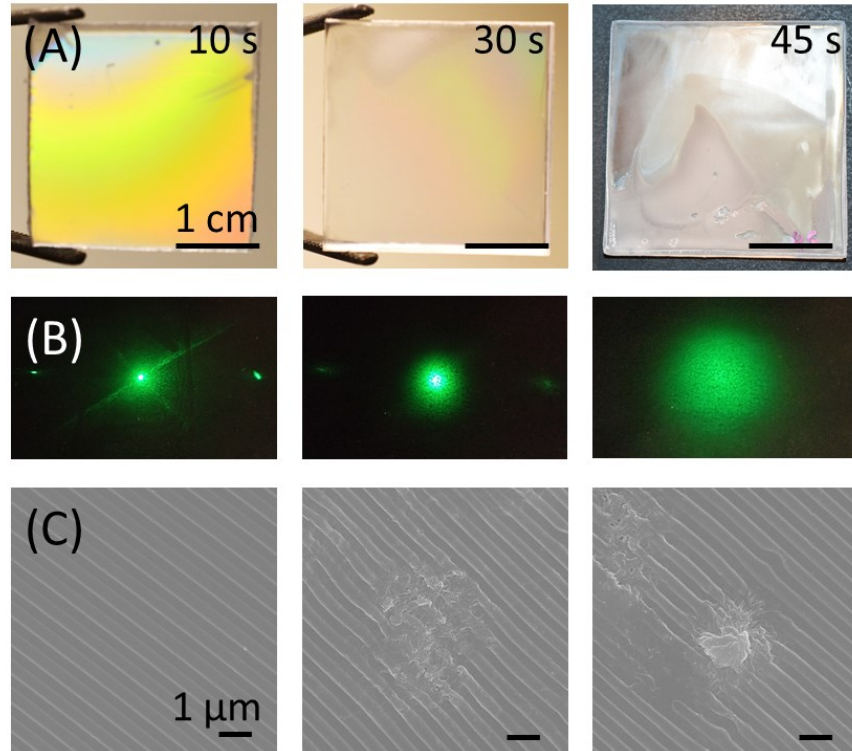


Figure C4. Nanocontact replication of a PC diffraction grating (DVD-R base). (A) Optical images of the PC replicas of the DVD-R base; (B) Diffraction patterns of a laser shining on the PC replicas; (C) SEM images of the PC replicas. PC was treated with acetone for 10 s, 30 s, and 45 s as indicated in the top-right insets of Figure B2A prior to the molding with the PDMS template.

A PC diffraction grating was replicated from the base of a DVD-R with our protocol. Optical images of the diffraction gratings in Figure C2A show how the vibrance of the grating decreases when increasing the acetone treatment time. A simple test of the diffraction was performed by shining a laser on the grating (Figure C2B), initially (10-s acetone treatment) the interference pattern is clear, which become faint and diffusive (30 s), and disappeared (45 s). The fidelity of the diffraction gratings were examined with SEM (Figure C2C); the 10 s treated sample perfectly replicated the grating and no evidence of

distortion was observed; on the 30-s sample the formation of spherulites begin to disrupt the grating, and on the sample treated for 45 s spherulites are prevalent and completely “destroyed” the grating.

Damage on the silicon masters during routine PDMS casting

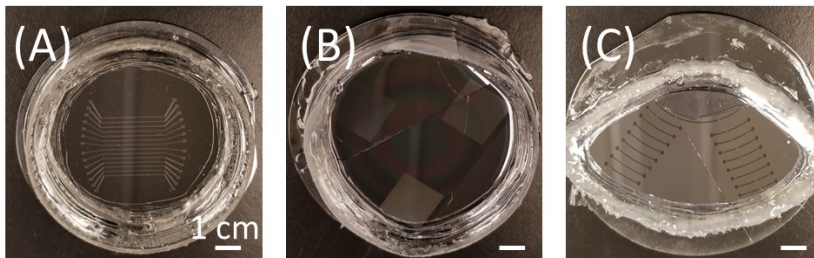


Figure C5. Scratched and damaged silicon masters. (A) Silicon master heavily scratched by cutting out PDMS templates. (B) Silicon master that cracked during cutting. (C) Silicon master that cracked during demolding.

The images in Figure C3 show damaged silicon masters from routine lab operations. All these masters were damaged through repeated casting and demolding of PDMS templates (microfluidic microchannel plates). Cutting the PDMS template out can cause damage to the silicon surface; the demolding process can cause the surface to crack. Once the silicon master is cracked it can no longer be used. Constructing durable 1-to-1 PC replicas of silicon masters has two primary advantages: (1) the master can be preserved by casting PDMS templates from the PC replica; (2) many PC replicas can be prepared from a single master, which drastically increases the fabrication output.

Durability of 1-to-1 PC replicas as “masters” for casting PDMS templates

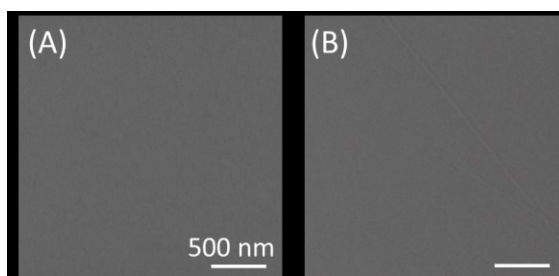


Figure C5. Durability test of a PC replica used as the “master” for casting PDMS templates. SEM images of a pristine PC surface (A) and after casting 10 PDMS templates (B).

PC replicas must be able to withstand casting many PDMS templates without becoming damaged or distorted to be considered a viable alternative of casting from the

silicon master directly. To evaluate the durability of PC replicas, a piece of pristine PC was used as a “master” for repeatedly casting PDMS templates. Pristine PC was used because it is practically featureless; any damage or changes to the surface could only come from the casting procedure. The SEM image in Figure C4A shows that the pristine PC is indeed completely flat and featureless before being used as a “master” for PDMS casting. The PC plate used as a “master” for 10 times remains flat and free of defects. The faint 50-nm wide groove on the surface could be due to the solvents in the PDMS kits; however, their remaining concentration during the casting process are low so that no significant damage to the PC morphology is expected.

Chapter 6. Superhydrophobic Polydimethylsiloxane via Nanocontact Molding of Solvent Crystallized Polycarbonate: Optimized Fabrication, Mechanistic Investigation, and Application Potential

Herein is described a benchtop protocol to create superhydrophobic polydimethylsiloxane (PDMS) via nanocontact molding of polycarbonate (PC) that was crystallized by controlled solvent treatment. The crystallized PC chains rearrange into a network of spherulites (spherical semi-crystalline domains); the overall surface is rough on the μm -scale while the spherulites themselves consist of nanoscale features. It was confirmed via conventional spectroscopic and high-resolution microscopic investigation that such hierarchical roughness is key to the development of superhydrophobic PC and the substantial enhancement upon PDMS molding. Thus prepared PDMS surface has excellent superhydrophobicity with an optimized contact angle of $172\pm 1^\circ$ and a sliding angle of $< 1^\circ$, superior to those prepared from more elaborate techniques, such as plasma sputtering and laser etching. The present method is potentially scalable, as large areas of PC can be treated to prepare the template. More importantly, the knowledge acquired regarding the structural transition and superhydrophobicity development would be beneficial to engineering and evaluating templates for many other polymeric nanostructures and functional surfaces.

Note: this chapter is adapted from:

Schultz, C. W., Ng, C. L. W., Yu, H.-Z., Superhydrophobic Polydimethylsiloxane via Nanocontact Molding of Solvent Crystallized Polycarbonate: Optimized Fabrication, Mechanistic Investigation, and Application Potential *ACS Appl. Mater. Interfaces*, **2020**, 12, 3161-3170. Copyright (2020) American Chemical Society.

I performed most of the experimental work and drafted the paper; Cliff Ng (an undergraduate student in Yu lab) helped with initial experimental design and manuscript proof-reading. Dr. Hogan Yu supervised the entire project and helped with writing the paper.

6.1. Introduction

Polydimethylsiloxane (PDMS) is an incredible class of materials that are chemically inert, optically clear, non-toxic, and easily fabricated into devices by micro/nanocontact molding.²⁰ PDMS consists of a siloxane backbone with bounded methyl moieties,^{75,76} which is typically prepared by mixing the liquid base and curing agent (crosslinker) in a 10:1 ratio, followed by degassing mixture and curing at 60 - 80 °C while in contact with a mold. The liquid base primarily contains 70% vinyl-terminated polydimethylsiloxane, and 30% dimethylvinylated and trimethylated silica.^{32,75} The curing agent is comprised of copolymers of methylhydrosiloxane and dimethylsiloxane.^{32,76} Reactions between the curing agent and base generates a heavily crosslinked durable elastomer³² In the past two decades, PDMS has been widely used in applications ranging from contact lenses, medical device parts, to food and shampoo additives.^{86,185}

Micro/nanofabrication techniques, particularly soft lithography, rely on the creation of PDMS stamps or molds, for which the liquid PDMS precursors are applied to a designed micro/nanostructured template to produce an elastomeric negative after curing.²⁰ The durability and inherent flexibility of PDMS allow the mold/stamp to conform to non-ideal surfaces without imprinting failing or mold breaking, and to be used repeatedly. The most notable application of PDMS is to create microfluidic devices because of its optical clarity and ability to reversibly bond to microchip surfaces, allowing for reuse.^{211,212} A wide range of devices such as microreactors, microchips, and microarrays have been constructed for biomedical applications,²¹²⁻²¹⁴ as cell culturing, cell separation, and biomolecular detection can be easily performed in these devices with low sample volume.^{185,211-215} The properties of surfaces within PDMS microfluidic devices can be tuned to control liquid transport, droplet formation, and sample loading; thus facilitating development of more complex and highly automated systems.²¹⁶⁻²¹⁸ Other functional materials with self-cleaning,^{59,62,219,220} anti-icing,^{221,222} and anti-fouling surface properties⁶² can be made with PDMS via micro/nanocontact molding. All these applications, particularly microfluidics, would be even more effective if the surface can be modified to be highly water repellent (i.e., superhydrophobic) to improve the performance.²²³

By and large, superhydrophobic surfaces are used extensively in our everyday lives; examples range from raincoats and shoes to windshields and building materials. By limiting wetting and fouling, these superhydrophobic products can last longer and remain

pristine even under heavy usage. PDMS is naturally hydrophobic, because of its intrinsically low surface energy (21.3 mJ/m^2)²²⁴ The first superhydrophobic PDMS was produced by treating the entire surface of PDMS with a CO_2 -pulsed laser.²²⁵ Laser irradiation was applied in a controlled manner to etch various nano/micro-structures into PDMS which achieves contact angles of up to 162° .^{62,63,226,227} Another method of preparing superhydrophobic PDMS is depositing PDMS-polystyrene block copolymer under humid conditions.²²⁸ ZnO nanoparticles dispersed onto partially cured PDMS²²⁹ and PDMS molded with calcinated candle soot²³⁰ has also produced superhydrophobic surfaces.

Benchmark approaches to construct superhydrophobic PDMS have been explored via the adaptation of soft lithography.^{59,60,231,232} Initially, simple structures such as arrays of PDMS pillars were cast from etched silicon masters and achieved modest contact angles of $\sim 150^\circ$.²³¹ The naturally superhydrophobic lotus leaves were employed as the molds and the PDMS replicas showed an identical contact angle to the original leaf ($\sim 160^\circ$).⁵⁹ Other templates such as Ni/NiO which possess hierarchical roughness produced similarly superhydrophobic PDMS as long as the feature aspect ratio is high enough.⁶⁰

Herein is described a benchmark protocol to prepare superhydrophobic PDMS via nanocontact molding of polycarbonate (PC) substrates that were recrystallized by controlled solvent treatment. Not only the optimization of preparation conditions, but also the mechanistic investigation of the correlation between structural transition and superhydrophobicity development will be presented in detail. In addition to spectroscopic (UV/Vis absorbance) and microscopic (profilometry and scanning electron microscopy) studies, I will also compare the present method with the state-of-arts and discuss the potential applications of thus fabricated ultra-water-repellent polymeric materials.

6.2. Optimized fabrication of superhydrophobic PDMS via nanocontact molding of solvent treated PC

In our previous work of replicating fingerprints into a PC plate (upon softening with acetone), it was noticed the PC mold and PDMS replica have high water contact angles, i.e., 130 ± 2 and $144 \pm 2^\circ$ respectively. Based on these previous observations and the early study of Yilbas et. al.,²³² I decided to explore the creation of superhydrophobic PDMS via a similar, but optimized procedure. As shown in Figure 6-1, a $2.5 \times 2.5 \text{ cm}^2$ amorphous PC plate (Figure 6-1A) was covered with a thin film of acetone ($\sim 250 \text{ }\mu\text{m}$) and allowed it to

evaporate completely (in about 10 min under ambient conditions). During the evaporation process the PC plate first became hazy then turned opaque (Figure 6-1B). The water contact angle increased from slightly hydrophobic ($90\pm 2^\circ$) to superhydrophobic ($151\pm 2^\circ$), as shown in the inset images. PDMS fabricated by molding a replica of the PC mold (Figure 6-1C) has a similar opaque appearance but a higher contact angle of $157\pm 1^\circ$. This simple fabrication process, illustrated in the scheme beside the images of Figure 6-1 on the right, can be scaled up to much larger areas.

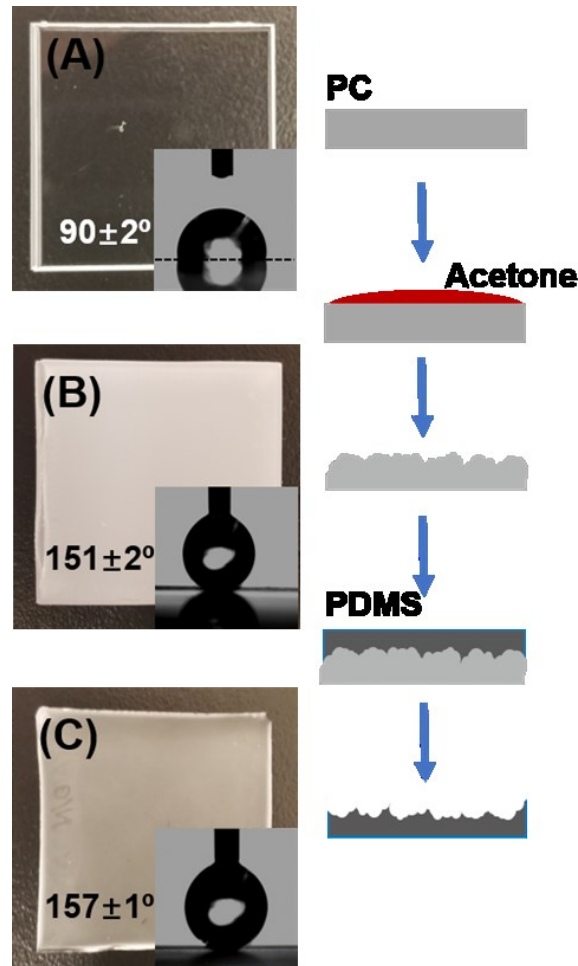


Figure 6-1: Fabrication of superhydrophobic PDMS via nanocontact molding of solvent-treated PC. (A) PC plate ($2.5\times 2.5\text{ cm}^2$) before acetone treatment. (B) PC plate after acetone treatment. (C) PDMS molded from the acetone-treated PC template. The bottom right inset of each image shows a water droplet on the surface and the measured contact angle. The right side inset is a schematic representation of the fabrication process (gray: PC, red: acetone, dark grey: PDMS).

A comprehensive array of reaction conditions was tested to improve the performance of superhydrophobic PDMS fabricated; the conditions tested include: (1)

choice of solvent (acetone vs. ethyl acetate) and the treatment time; (2) quenching reagent/methods, e.g., water, methanol washing vs. air drying to stop the reaction between the solvent and the PC substrate; (3) PDMS dilution (e.g., adding 20% toluene or hexane to the PDMS) or mixing h-PDMS (a “harder” PDMS formulation with shorter polymer chains and more crosslinkers) with regular PDMS.

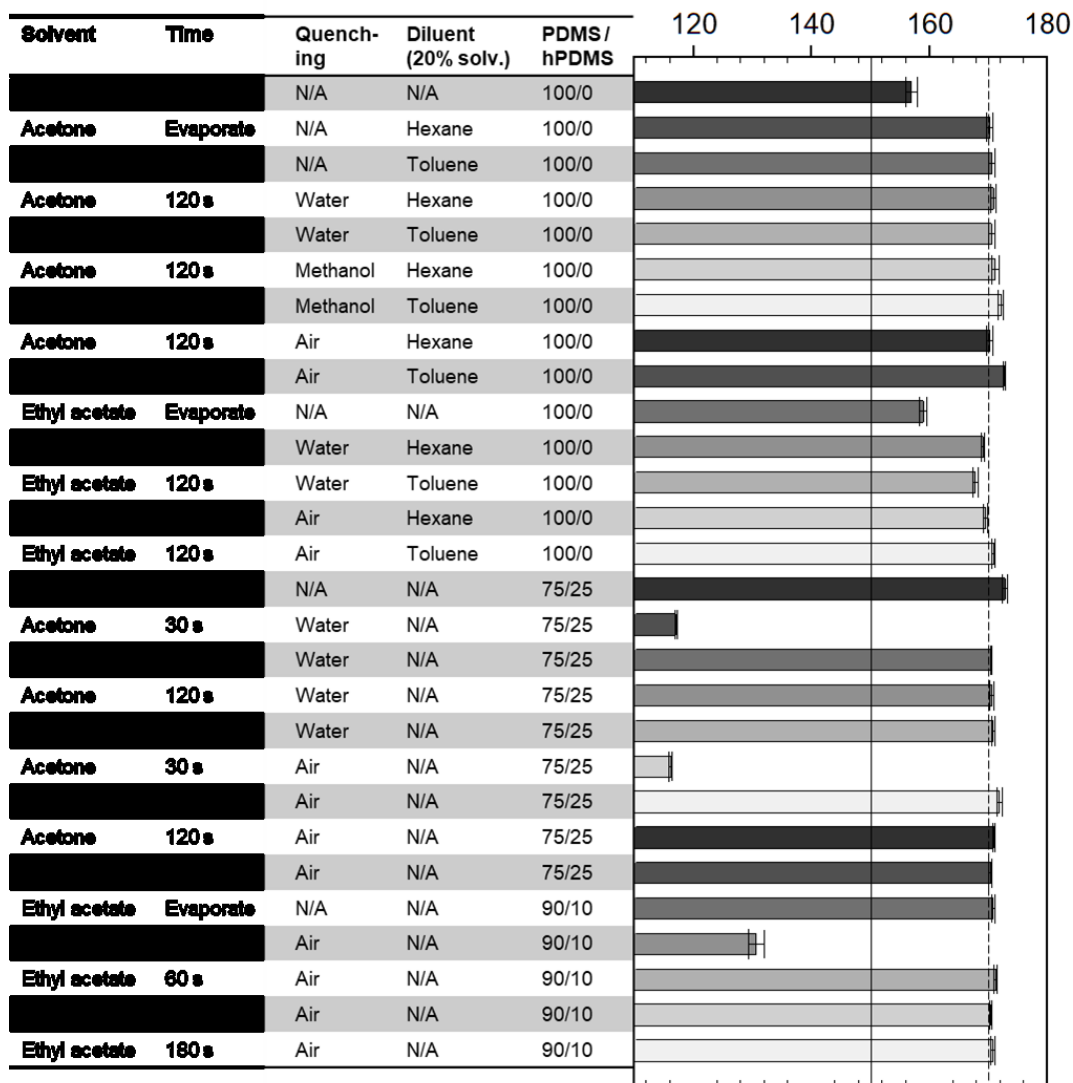


Figure 6-2: Optimization of the preparation protocol for superhydrophobic PDMS. PC treatment and PDMS casting conditions are listed in the left inset table. Solvent: solvent used to treat PC; Time: how long solvent is applied; Quenching: non solvent used to stop the treatment; Diluent: solvent used to dilute PDMS; PDMS/h-PDMS: ratio of PDMS to h-PDMS (wt %). The solid black line indicates a contact angle of 150° (superhydrophobic) and the dashed line denotes a contact angle of 170°.

As shown in Figure 6-2, most of the treated samples exhibited contact angles above the “cut-off” for superhydrophobicity (150°), and many of them achieved contact angles close to 170° , which is extremely promising. Upon closer analysis of the results, it was identified that only the samples treated with solvent for short time periods (e.g., 30 s) were not superhydrophobic, with contact angles between 110 to 130° . The other two less remarkable situations (150 – 160°) happened when the solvent was left for complete evaporation (no quenching reagents applied) and when the PDMS was not diluted (without adding 20% toluene or hexane). The highest water contact angles achieved on the PDMS molded from acetone and ethyl acetate treated PC are $172\pm 1^\circ$ and $171\pm 1^\circ$, respectively. In both cases the PC surfaces were treated for 120 s; the reactions were stopped by either methanol quenching or compressed air drying, and the diluted PDMS was used for molding.

The next series of samples in Figure 6-2 were prepared with mixtures of PDMS and h-PDMS, which have been previously used to improve the resolution of PDMS molding.¹⁹⁴ This was also to compare with the dilution approach as described above. When a ratio of 75/25 (PDMS/h-PDMS) was tested, all the samples treated with acetone for over 30 s are superhydrophobic with contact angles as high as $170\pm 1^\circ$. It was surprising to note that the sample molded from PC on which solvent was allowed to evaporate has the highest contact angle ($172\pm 1^\circ$). When ethyl acetate was used to treat the PC instead of acetone, it was found that only low ratios of h-PDMS (10%) can be demolded successfully; higher ratios of h-PDMS suffered from adhesion to the PC template and broke when demolding. Ethyl acetate is less polar than acetone and can penetrate more deeply into the polymer network, generating a rough surface with higher aspect ratio features that enhances the adhesion between the PDMS and the PC. Nonetheless, these samples also showed excellent water repellent properties (contact angles $> 170^\circ$). While not the focus of this research a brief characterization of PDMS molded from ethyl acetate treated PC is included in the supporting information (Figure D1).

As a benchtop protocol, the toxicity of the organic solvents used (acetone, ethyl acetate, hexane, and toluene) must be considered. Acetone and Ethyl acetate are both fairly safe; exposure to them can cause slight mucous membrane and skin irritation.¹³⁶ Toluene and hexane are more problematic, both being central nervous system

depressants.^{233,234} These solvent should only be used in well ventilated environments using gloves that are resistant to their absorption.

Based on above comparison, it can be concluded that (1) acetone is the best solvent to treat PC because samples have consistently high contact angles. Wetting is time dependant with 120 s of treatment producing the most hydrophobic PDMS. (2) For acetone treated samples, quenching the reaction instead of allowing acetone to evaporate improved contact angles; the method of quenching did not matter. (3) Diluting the PDMS with solvent or using a mixture of PDMS/h-PDMS caused contact angle to increase in acetone and ethyl acetate treated samples. The highest contact angle achieved ($172\pm 1^\circ$) is significantly higher than the 153° achieved by Yilbas et al.²³² with a similar protocol. The differences between the protocols (quenching acetone treatment, modifying PDMS composition) will be elaborated on below.

6.3. Structural characterization and Mechanistic Insights

As demonstrated above, the solvent treatment time is key to produce superhydrophobic PDMS with superior water contacts angles ($> 170^\circ$). Therefore, I have monitored the contact angles of both the PDMS samples and PC templates and their optical properties (optical transmittance) as a function of the solvent treatment time.

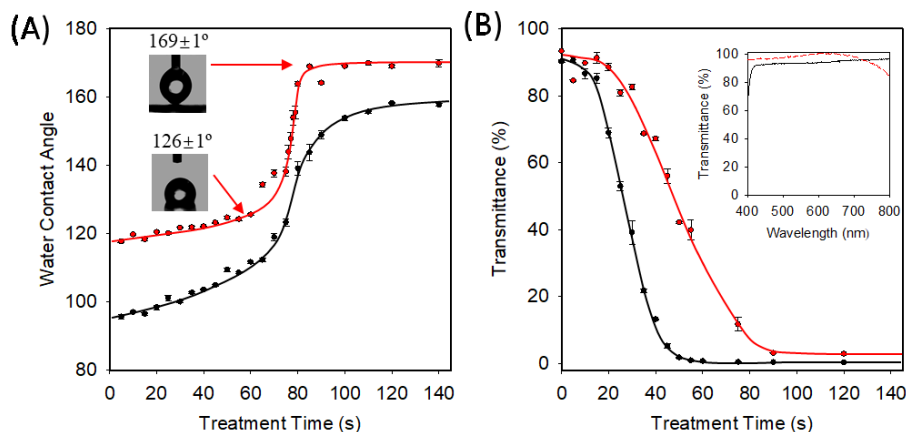


Figure 6-3: Contact angle (A) and optical transmittance at 500 nm (B) through PC (black) and PDMS (red) as a function of solvent treatment time. The inset photos in (A) show water droplets on the molded PDMS surfaces prepared from 60 and 80 s treatment of PC with acetone. The top right inset in (B) shows the optical transmittance of unmodified PC and PDMS across the visible spectrum, respectively.

As shown in Figure 6-3A, the unmodified PC surface has a contact angle of $92\pm 1^\circ$; upon treatment with acetone, the contact angle of PC increases gradually at the beginning. After 60 s the contact angles of PC surfaces begin to increase rapidly, increasing from $111\pm 1^\circ$ to $139\pm 2^\circ$ on the 80-s treated PC. It was noted that the measured uncertainties of the contact angles are significant. On PC treated for 120 s and longer, the contact angles of samples begin to level off and reaches a maximum of $158\pm 1^\circ$. PDMS is naturally more hydrophobic than PC; the contact angle of featureless PDMS is $107\pm 1^\circ$. As shown in Figure 6-3A, the contact angle rises to $126\pm 1^\circ$ on the PDMS cast from PC that was treated for 60 s, and like PC, the contact angle begins to increase much more rapidly after 60 s, and reaches a “plateau” ($169\pm 1^\circ$) on the PDMS cast from a PC plate treated for 85 s. Interestingly, the hydrophobicity of PC increases at a faster rate than PDMS, even though one would expect them to have similar changes in surface morphology.

In Figure 6-3B, the optical transmittance at 500 nm of the solvent-treated PC and the molded PDMS as a function of the reaction time is shown. Both untreated PC and PDMS are optically transparent in the wavelength range of 400 to 800 nm (inset of Figure 6-3B), i.e., the transmittance is above 80% in both cases. If PC is treated for 15 s, the transmittance decreases slightly; but on samples treated for 20 s or longer, the transmittance begins to decrease significantly, with only $\sim 10\%$ transmittance upon acetone treatment for 40 s. It decreases further to $\sim 1\%$ at 60 s then levels off. The transmittance of the molded PDMS starts at a similar value to PC, which begins to decrease at a later time (30 s) and at a slower rate. In general, the PDMS is significantly more transparent than the corresponding PC mold; at 60 s the transmittance of the molded PDMS is still 38%, but eventually decreases to 3% upon treatment for 90 s and longer.

Several conclusions can be drawn from the above results. The rapid increase in contact angle occurs for both materials at the same time indicating that whatever change in physical structure of the PC surface that increased the contact angle of PC induces similar changes to the surface of the PDMS molded from it. The water contact angles reach the maximum at 120 s, indicating that the surface morphology does not change appreciably with extended solvent treatment time. Visual inspection of the PC and PDMS suggests that the light is not absorbed but scattered when passing through the samples. Their dull white appearance results from the structural inhomogeneities within and on the surface of the materials.

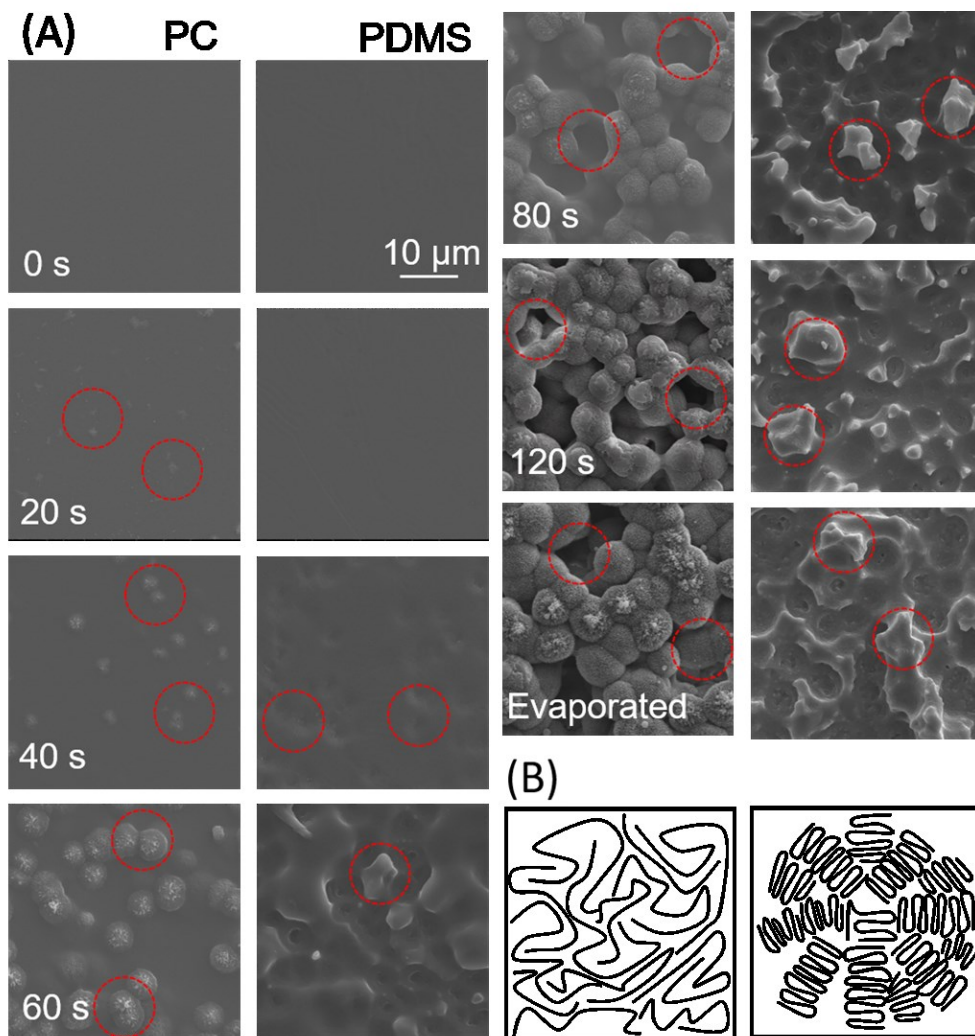


Figure 6-4: SEM images of acetone treated PC plates and PDMS casts. (A) PC was treated with acetone for up to 120 s, then the acetone film was blown off with compressed air or left to evaporate. These PC plates (left) were used as templates for molding the corresponding PDMS (right). Acetone treatment conditions for each row are shown on the PC image. Areas of interest are highlighted with red circles. (B) Schematic view of amorphous PC (left) and of a semi-crystalline PC spherulite (right).

The intriguing wetting and optical property changes of the solvent-treated PC and particularly the molded PDMS motivated us to further characterize both materials with scanning electron microscopy (SEM) to examine their microscopic morphological variations. SEM images in Figure 6-4A display the changes in surface morphology during the time series (Figure 6-3). Before acetone treatment the PC is flat and featureless because it is supplied in an amorphous glassy state. Randomly distributed features begin to emerge in the PC after 20 s of treatment and start to assume a spherical shape at 40

s. Spherical structures are beginning to emerge from the plane of the surface and impinge on each other after 60 s. At this point the developing features can be identified as so-called spherulites, i.e., spherical semi-crystalline domains. PC is known to crystallize by forming microsize spherulites, especially when swollen with organic solvents (e.g., acetone),^{54,65,92} as they are capable of swelling the polymer network but cannot dissolve the polymer. The PC that initially exists in the amorphous state (schematically shown in Figure 6-4B, left) swells as solvent molecules diffuse between polymer chains; swelling increases the free volume of polymer chains allowing them to rearrange.^{65,92} During acetone treatment and upon solvent evaporation or quenching with air/non-solvent, the PC adopts more energetically favorable arrangements by crystallizing into spherulites, as shown schematically in Figure 6-4B (right). A more detailed description of the crystallization process is presented in Figure D2 and the associated text of the supporting information. Spherulites initially form as tendrils of crystalline lamellae that grow out radially from initial seeds.⁹² Crystalline PC grows radially because tendrils of stacked lamellae that form drive crystallization in the surrounding amorphous polymer. Either by putting strain on amorphous polymer or seeding by partially incorporated polymer chains, new tendrils of lamellae are formed at or beside existing tendrils. New tendrils splay outward from and initiate further crystallization, successive splaying cause the spherulite to eventually form a spherical domain.⁹¹ As indicated in the SEM images, the initial seeds are visible in the 20 s sample, while radial growth of tendrils can be seen developing between the 40 s and 60 s of solvent treatment.

From 60 s to 80 s, the morphology of treated PC changes dramatically; spherulites grow larger and many more grow out of the amorphous polymer matrix. This timeframe is also when the water contact angle increased dramatically; as shown in the highlighted areas, pores have been developed between spherulites creating an additional level of microscale surface roughness with high aspect ratios. After 120 s, the amorphous polymer chains are consumed and incorporated into spherulites, as they are no longer visible between spherulites and at the bottom of pores. The morphology of PC after 120 s appears similar to those on which acetone was left to evaporate, confirming that the PC surface can be thoroughly crystallized within 120 s of solvent treatment.

After 120 s, additional crystallization in the form of lamellae thickening, nucleation of secondary lamellae, rearrangement of pre-existing lamellae, and development of fringed micelle structures are possible.⁹¹ Thickening occurs on the lamellae of spherulite

tendrils if crystallized conditions are maintained after spherulites form.^{67,235} Pre-existing tendrils can also nucleate fringed micelles and secondary lamellae by destabilizing their surroundings and providing existing lamellae for polymer to conform with.⁹¹ Tendrils of polymer can also combine if they are in close proximity.⁹¹ All these effects can decrease the amount of and aspect ratio of nanoscale features, which explains the slightly higher contact angle of samples quenched at 120 s. Supplementary SEM images and schematics to illustrate these effects are included in Figure D2 along with a short discussion of secondary crystallization. X-ray diffraction measurements (Figure D3) confirmed the development of crystallization upon acetone treatment.

PDMS samples casted from the solvent treated PC were also imaged with SEM for comparison (Figure 6-4A). The PDMS plate casted from PC molds treated for 20 s or less are completely featureless. Small impressions of embedded spherulites become visible after 40 s; by 60 s the PDMS surface is covered with microscale features as spherulites protrude from the template surface creating such impressions. In the next 20 s the morphology of PDMS changes significantly; micro-sized pillars form in the pores between spherulites. Like the morphological and corresponding wettability change observed for PC, the development of micro-sized features at 80 s corresponds with the transition to superhydrophobicity. The solvent-evaporated sample appear very similar to those prepared from 80 s and 120 s samples, characterized by a random arrangement of impressions and pillars.

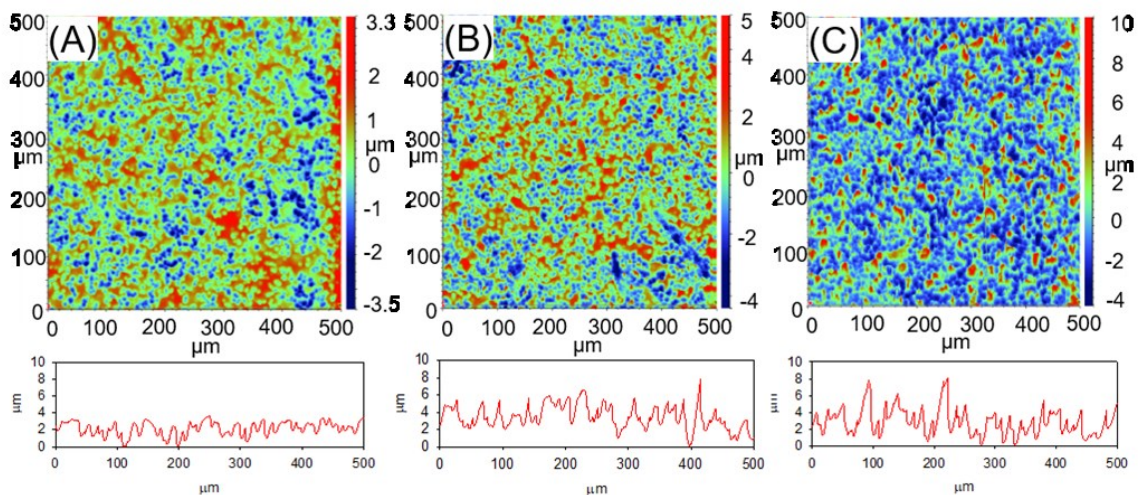


Figure 6-5: 3D Profilometry images of PDMS molded from PC templates treated with acetone for 60 s (A), 75s (B), and 80 s (C), respectively. The vertical relief is represented on a color scale bar from blue to red. Cross-section profiles are shown as insets below each image.

To assess the microscale morphology of the surface, particularly the height of surface features molded to the PDMS, profilometry was used to examine the “key” samples on which the transition from hydrophobic to superhydrophobic occurs (PDMS plates casted from the PC templated treated with acetone for 60 s, 75, and 80 s respectively). The profilometry image of the PDMS sample casted from a PC template treated for 60 s (Figure 6-5A) is the cast on which the water contact angle starts to increase rapidly. At this point the arithmetic average roughness (Ra) is 0.68 μm , and the surface is composed of semi-circular impressions which form randomly distributed hills and valleys. Figure 6-5B displays the 3D profilometry scan of a PDMS cast from the PC template treated for 75 s (contact angle of $138^\circ \pm 1^\circ$). The Ra increased to 0.96 μm as spherulites in the template are larger and no longer as deeply embedded in the amorphous matrix. Despite the increased roughness, the overall morphology is similar to the 60 s sample. It is remarkable that the morphology of the 80 s sample (Figure 6-5C) evolved to a random distribution of pillars, i.e., the image appears as a large amount of “blue” and the peaks are well separated. More interestingly, the Ra has increased dramatically to 1.46 μm , confirming the formation of micrometer scale pillars. The cross-section profiles as the bottom inset in Figure 6-5 further illustrates the transition of the micrometer scale morphologies, i.e., as the solvent treatment time increases, the surface features become larger and more peak-like structures emerge. If the solvent is allowed to evaporate completely (> 3 min, without using quenching solvent or rapid air drying), the molded PDMS surface has a similar morphology as the 80 s sample, but with a slightly larger Ra value (1.80 μm). Analysis of Figure 6-5C shows that pillars on the PDMS are rather evenly distributed on the surface, each $100 \times 100 \mu\text{m}$ area contains between 5 to 7 microscale pillars. The density of pillars is consistent between samples cast from multiple identically treated PC templates as well. Histograms of roughness feature height (Figure 6-6) illustrate the evolution of surface roughness. At 60 s roughness is distributed mainly between 1.5 and 3 μm , and slightly skewed towards peaks. The mean height was 2.1 μm with a standard deviation of 0.8 μm . At 75 s the height of features increases significantly, and the distribution of roughness features becomes more symmetrical, at this stage the mean height has increased to 3.4 μm with a standard deviation of 1.4 μm . On the 80 s sample the peak of the distribution shifts further to the left. More importantly, there is an increase in the frequency of the tallest features ($>6 \mu\text{m}$) associated with pillars forming from pores in PC. The relative rarity of tall features is consistent with the sparse distribution of pillars, which helps to minimize contact between the surface and a water drop resting

on it. This shift to a distribution of isolated peaks is reflected in the mean height, which decreases to 2.8 μm while the standard deviation increases to 1.5 μm because of the increase in the tallest features.

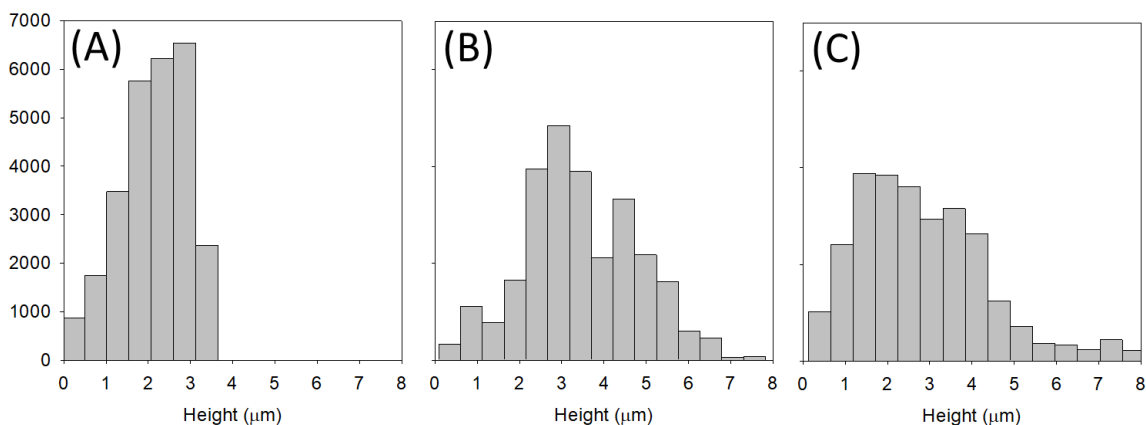


Figure 6-6: Histograms of roughness features on PDMS molded from PC templates treated with acetone for 60 s (A), 75s (B), and 80 s (C), respectively.

The other important discovery from the survey experiments (Figure 6-2) is the significant improvement of the hydrophobicity (157° to 170°) upon adapting h-PDMS or diluting PDMS with an organic solvent. As there were no changes in the morphology of the PC template, the enhanced superhydrophobicity must be derived from a better replication process (i.e., structural details at nanometer scale can be projected well from the PC templates to PDMS casts). The SEM images in Figure 6-7 show explicitly such a favorable phenomenon for molding a typical PC spherulite (Figure 6-7A). With conventional PDMS, the nanoscale structural features are not “copied” as displayed in Figure 6-7B, i.e., the impression of the spherulite appears as a micrometer size “dent”. Notably, no sharp edges are visible, and the impression appears rather smooth. The use of h-PDMS has shown to improve replication by decreasing the viscosity of the liquid precursor during casting (h-PDMS has lower viscosity of 500–750 mPa·s than regular PDMS at 4500 mPa·s) and increases the stability of sharp structures in the resulting cast.^{194,236} In Figure 6-7C a spherulite impression cast with pure h-PDMS is shown, in which nano-sized nodules are replicated with a much higher fidelity in comparison with pure PDMS molding. Nanoscale roughness in the impression is more pronounced; defined nanostructured features with high aspect ratios on the surface are more apparent. Unfortunately, h-PDMS is brittle and therefore very difficult to demold from the PC

template (i.e., easily breaks into small pieces when demolded). One of the options is to use a mixture of regular PDMS and h-PDMS; the spherulite impression in Figure 6-7D was molded with such a 75/25 w/w mixture that shows satisfactory results. While not as high fidelity as the pure h-PDMS cast, replicated nanostructures were more detailed and sharper than using neat PDMS without compromising the durability.

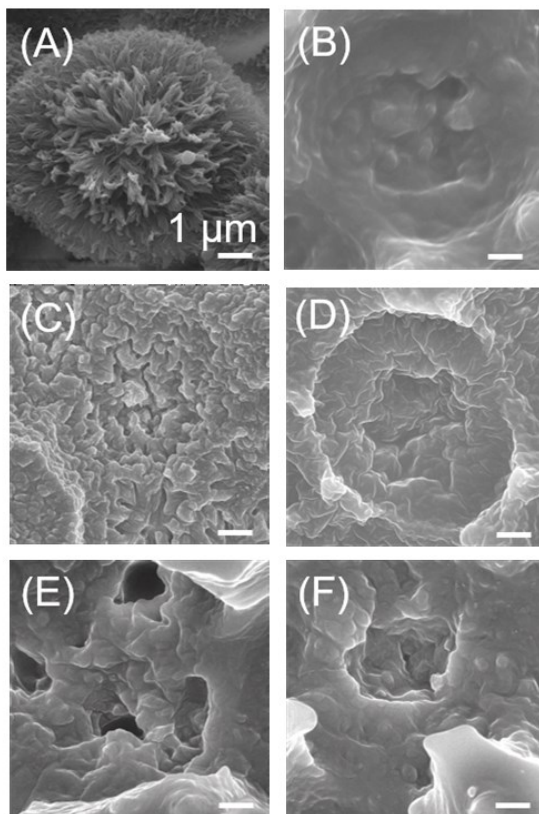


Figure 6-7: SEM images of a PC spherulite (A) and the impressions molded with neat PDMS (B), h-PDMS (C), 75/25 (w/w) PDMS/h-PDMS (D), PDMS diluted with 20% (w/w) hexane (E), and PDMS diluted with 20% (w/w) toluene (F), respectively.

Along the same line of decreasing the viscosity of PDMS precursors, I have also tested the effect of diluting PDMS with hexane or toluene.^{237,238} By testing with a series of PDMS/solvent ratios (10–50% w/w), it was discovered that with high solvent ratio (> 30%), the samples failed to demold, i.e., the PDMS broke and stuck to the PC surface. The PC template showed signs of solvent damage as well. The sample diluted with 20% hexane showed satisfactory results (Figure 6-7E), i.e., the nanostructures appear more defined and have higher aspect ratios than the neat PDMS. The sample diluted with 20% toluene (Figure 6-7F) appears similar to the hexane sample in terms of nanofeature replication; compared with neat PDMS a similar increase in the complexity of nanoscale roughness

was observed. These results highlight how nanoscale morphology can be better molded by mixing PDMS with h-PDMS or diluting with an organic solvent at optimized ratios; in both cases, the superhydrophilicity of the molded PDMS can be greatly enhanced due to the retaining the nanoscale features from the PC templates.^{59,60,231,232}

Our comprehensive characterization of PDMS casts described above raise two main questions: (1) why does the development of micrometer sized pillars drastically increase the hydrophobicity? (2) why does the improved replication of nanoscale details increase the hydrophobicity? To answer these questions, one must understand the origin of superhydrophobicity. The roughness of a solid surface increases the area of the solid-liquid interface in contact with a water droplet, which amplifies the intrinsic hydrophobicity of the surface. If the water droplet is in full contact with the rough surface, it is classified as being in a Wenzel state; the water contact angle increases meanwhile the adhesion of the droplet to the surface is strong due to the increased contact area of the interface.²³⁹ If the water droplet is not in full contact with the rough surface, a composite interface of both the solid and trapped air forms that is known as a Cassie-Baxter state.²²³ As the ratio of solid surface in contact with the droplet (f) decreases the contact angle increases (Equation 1).²²³

$$\cos \theta_c = f(\cos \theta_1 + 1) - 1 \quad (1)$$

On superhydrophobic surfaces, water droplets adopt the Cassie-Baxter state; water drops cannot make full contact with the rough surface, and the limited contact between the surface and droplet drastically reduces the adhesion, allowing droplets to roll off easily. The Cassie-Baxter state is induced by surface roughness on multiple (micro and nano) scales.

By forming microscale pillars and improving the fidelity of nanoscale replication, an ideal surface morphology for achieving superhydrophobicity on PDMS was developed. The abrupt increase in water contact angle of the PDMS samples (Figure 6-3A) coincides with the formation of microscale pillars (Figure 6-5). Once the microscale roughness becomes large enough that droplets become suspended on top of microstructures, a Cassie-Baxter state is achieved and contact angle rapidly increases.^{54,219,240} A similar trend occurs for PC; however, the porous surface geometry creates higher ratio of solid-liquid

contacts between the surface and water than an analogous pillar geometry formed on the PDMS.

6.4. Comparison with state-of-the-arts and application potentials

Table 6-1: Comparison of the state-of-the-art methods of preparing superhydrophobic PDMS. Wetting properties (contact angle and sliding angle) and calculated f value of superhydrophobic PDMS substrates fabricated via different methods.

Ref.	Authors	Fabrication Method	Water contact angle	Sliding angle /hysteresis	f
62	Jin et al.	Pulse laser etched PDMS	162°	>5°	6.9%
124	Sun et al.	Nanocasting Lotus leaf with PDMS	160°	2°	8.5%
219	Cortese et al.	Replication of SU-8 master followed by plasma treatment	170°	4°	2.1%
226	Yong et al.	Femtosecond laser etched PDMS	160°	1°	8.5%
60	Zhang et al.	Nanocasting porous Ni template with PDMS	159°	2°	9.4%
232	Yilbas et al.	Nanocasting crystallized PC with PDMS	153°	7°	19.0%
240	Boscher et al.	PDMS film deposited by plasma discharge	170°	5°	2.1%
This work		Nanomolding crystallized PC with PDMS	172°	1°	1.4%

As compared in Table 6-1, our technique produces superhydrophobic PDMS that outperforms those samples prepared with state-of-the-art methods. First of all, I have archived the highest water contact angle, $172\pm 1^\circ$. The 2° improvement from the best performed samples prepared via plasma etching^{219,240} is significant when approaching the limit of superhydrophobicity ($>170^\circ$). In fact, such an incremental improvement is also indicated by the fraction of solid-liquid interface (f) that was calculated using the Cassie-Baxter equation (Eq. 1) with known water contact angle of the superhydrophobic PDMS (θ_c) and that of an unmodified sample ($\theta_1 = 107\pm 1^\circ$). Particularly the f value of our PDMS sample with a contact angle of $172\pm 1^\circ$ is calculated to be 0.014, i.e., 1.4% of the interface is water/PDMS (the rest is between water/air). In comparison, the f value of the superhydrophobic PDMS prepared by Yibas et al. in a similar manner with a contact angle of 153° was calculated to be 0.19 (19%).²³² Even compared with the PDMS surfaces of

170° water contact angle ($f = 2.1\%$),^{219,240} I have achieved a 50% reduction of the liquid/solid interfacial contact! Such a drastic decrease in the solid-water interface fraction is a result of improved PC template preparation (quenching with a non-solvent to limit the lamellae thickening)²⁴¹ and optimized PDMS nanomolding protocol (solvent dilution or h-PDMS composite). Practically, the superhydrophobic robustness would be enhanced upon limiting the contact area with water, as it provides less surface for droplet adhesion and spreading to occur.

Second, I have achieved the lowest sliding angle of superhydrophobic PDMS. Contact angle is not the only means to measure the water-proof property of a surface; rather, a low sliding angle for water droplets on the surface (water droplets can move or expand with very little resistance)^{62,223} is also an important consideration. A low sliding angle is indicative of minimized wetting hysteresis, which is integral to achieving self-cleaning capabilities on superhydrophobic surfaces. As listed in Table 6-1, the sliding angle of water droplets on the PDMS samples prepared herein sets a new record (1°), i.e., other techniques to fabricate superhydrophobic PDMS that achieved > 170° water contact angles had much higher sliding angles (4-5°).^{219,240}

The self-cleaning property of thus prepared superhydrophobic PDMS were demonstrated by testing with samples that are covered with sand and activated charcoal, which can be completely removed by simply dropping water onto the surface (Figure D4). For such an application, low-cost methods that can produce large scale substrates are desired. Our technique embodies both qualities; templates are produced simply by treating PC plates with a readily available solvent and there is no practical limit to the size of the template. Nevertheless, large areas would require a significant amount of PDMS precursors, which are rather expensive compared to consumer plastics.

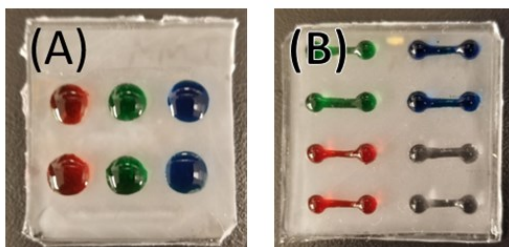


Figure 6-8: Superhydrophobic PDMS (2.5×2.5 cm²) patterned by UV/Ozone treatment. (A) Array of hydrophilic spots, (B) Array of hydrophilic spots connected by channels. Diluted color ink solutions were used for better visualization.

Microfluidic devices also take advantage of using superhydrophobic PDMS substrates to improve their performance. Superhydrophobic channels can improve liquid flow by minimizing friction along the channel walls.^{62,215,242} Other small microfluidic parts such as nozzles can also have their performance improved by reducing friction when using superhydrophobic PDMS.²³⁹ The technical challenge is to pattern superhydrophobic PDMS substrates to create hydrophilic regions that can be subsequently used as reaction zones or channels. To test the potential of superhydrophobic PDMSs prepared herein for microfluidic applications, simple hydrophilic patterns were generated by UV/Ozone treatment (Figure 6-8). Firstly, an array of circular spots was reactivated (Figure 6-8A) where aqueous solutions are well contained. The pattern reactivated in Figure 6-8B is of two small spots connected by a channel. When water was deposited on one side it wicks to cover the whole reactivated region. Sophisticated PDMS microfluidics could be constructed by adapting our protocol; superhydrophobic PDMS could be used as a base or cover layer in microfluidics to generate channels with unique combinations of wettability and flow characteristics.

6.5. Conclusion

The protocol for replicating PC spherulites into PDMS described in this paper promises a method to produce superhydrophobic polymeric materials at a low cost. It has been confirmed that the solvent-induced crystallization of PC produces a template with both micro and nanoscale roughness as spherulites form and separate from each other into a porous network. It was also discovered that the nanomolding protocol can be improved by modifying the PDMS via solvent dilution or mixing with h-PDMS. Most importantly, I have shown that thus fabricated PDMS has superior performance in comparison with state-of-art methods in terms of both ultrahigh water contact angle ($172\pm 1^\circ$) and record-low sliding angle (1°), resulting from the smallest ratio of solid-liquid contact (1.4%) at the interface. The application potential of thus made superhydrophobic PDMS has been further illustrated for its self-cleaning property and microfluidic patternability via conventional UV/ozone irradiation.

6.6. Experimental

Materials and reagents. Makrolon 2600 ($M_w \sim 26,000$) Polycarbonate (PC) sheets ($4 \times 2 \text{ m}^2$) were purchased from Bayer (Sheffield, AL), which are protected by a plastic film on both sides upon receiving. Acetone (99.8%), toluene (99.9%), hexane (99.9%), and ethanol (95%) were purchased from Fisher Scientific (Hampton, NH). Slygard 184 Polydimethylsiloxane (PDMS) kit (which contains an elastomer base and a curing agent) was purchased from Ellsworth Adhesives (Germantown, WI). Hard PDMS (h-PDMS) kit was purchased from Gelest Inc. (Morrisville, NY). Deionized water ($> 18.3 \text{ M}\Omega\text{-cm}$) was produced from a Barnstead Easypure UV/UF water system (Thermo Scientific, Waltham, MA).

Preparation of PC templates and superhydrophobic PDMS. To create PC templates for subsequent molding with PDMS, small pieces of PC plates ($2.5 \times 2.5 \text{ cm}^2$) were cut from the large sheet and the protective film was removed from one side. The PC plate was washed with deionized water and ethanol, then dried with compressed N_2 gas. 0.25 mL of acetone or ethyl acetate was dispensed onto the surface with an automatic pipette, to covers the entire surface with a $\sim 2 \text{ mm}$ thick film. The solvent was left to evaporate under ambient conditions ($20 \text{ }^\circ\text{C}$, 35% relative humidity). For experiments where solvent treatment time was varied, the solvent was removed at the specified time with a blast of compressed air or immersed in water/methanol to quench the reaction. PC plates were placed in an oven at $60 \text{ }^\circ\text{C}$ for 1 h to ensure complete drying before being used as molds.

For molding PC templates, PDMS precursors were prepared following standard literature protocol.⁶⁰ Briefly, the elastomer base (part A) and the curing agent (part B) were mixed in a 10:1 ratio by manual stirring and vortexing. The precursor solution was poured over the PC mold, degassed for 45 min in a vacuum chamber, and then cured in an oven at $80 \text{ }^\circ\text{C}$ for 2 h. The PDMS replica was then cut and carefully peeled from the mold. For molding with h-PDMS, except for the mixing ratios between elastomer (part A) and curing agent (part B) (1:1), all other steps followed essentially the same procedure as regular PDMS.

A PSD Series Digital UV/Ozone System (Novascan Technologies, Inc., Boone, IA) equipped with both 185 nm and 254 nm UV lamps was used to create hydrophilic regions

on superhydrophobic PDMS. Samples were covered with an aluminum mask that was fixed to the PDMS plate with binder clips and placed in the UV/Ozone system for 4 h.

Characterization and instrumentation. Contact angle measurements were performed with a VCA optima goniometer (AST Products Inc., Billerica, MA). A 1.5-2 μL drop of deionized water was brought in contact with the surface by a syringe mounted on the goniometer. Each reported angle is calculated as the average of 5 measurements at different locations on the sample, with each sample run in triplicate. UV-Vis spectra were obtained with an Ocean Optics DH-2000-BAL UV Spectrometer (Largo, FL); a piece of either PDMS or PC plate was placed in the cuvette holder perpendicular to the light beam, with the molded side facing the incident light.

An FEI Nova NanoSEM 430 SEM (Thermo Fisher Scientific, Hillsboro, OR) was used to obtain high-resolution images with an accelerating voltage between 10–15 kV. PDMS and PC plates were coated with a 5–10 nm thick iridium layer using a Leica EM ACE600 Carbon & Iridium Coating System (Leica Microsystem Inc., Concord, ON) to improve the conductivity of the surface. The microscale relief of PC molds and PDMS templates was measured using a Bruker Dektak XT (Billerica, MA) profilometer set to “map scan” mode; PDMS or PC was affixed to the stage using vacuum suction to prevent the sample from moving and distorting the scan.

6.7. Supporting Information

Additional experimental results and characterization, including: (1) preparation of superhydrophobic PDMS from PC treated with ethyl acetate as a crystallizing solvent, (2) demolding precautions for superhydrophobic PDMS, (3) a schematic explanation of polycarbonate crystallization which highlights the changes in morphology caused by secondary crystallization, (4) X-ray diffraction characterization of the PC surface, and (5) investigation of the self-cleaning properties of superhydrophobic PDMS.

Ethyl Acetate as a crystallizing solvent

Several other solvents besides acetone were tested to determine if they can crystallize PC to form spherulites. Strong solvents dichloromethane, hexane, and toluene all cause PC to swell and form a gel-like layer on the surface. However, these solvents dissolve PC which prevents polymer chains from forming crystalline moieties. Ethyl

acetate was a success in general; when treated, PC quickly crystallized and formed an opaque white layer at the surface. PC samples treated with ethyl acetate for various durations were used as templates for PDMS molding. The water contact angle of PDMS casts plateaued at $160 \pm 1^\circ$ (Figure D1A) when PC was treated for 60 s, indicating a rather rapid recrystallization process (in comparison with acetone).

SEM imaging of a PDMS cast from a PC templates treated by covering the surface in ethyl acetate and allowing it to evaporate (Figure D1B) reveals a similar structure to that of acetone treated PC. Spherulite impressions are consistent in size ($\sim 7 \mu\text{m}$), and the nanoscale morphology seems to be uniform cross the entire surface. More interestingly, a couple PC spherulites were retained in the PDMS (bottom left corner), indicating that spherulites formed by ethyl acetate treatment are less fused.

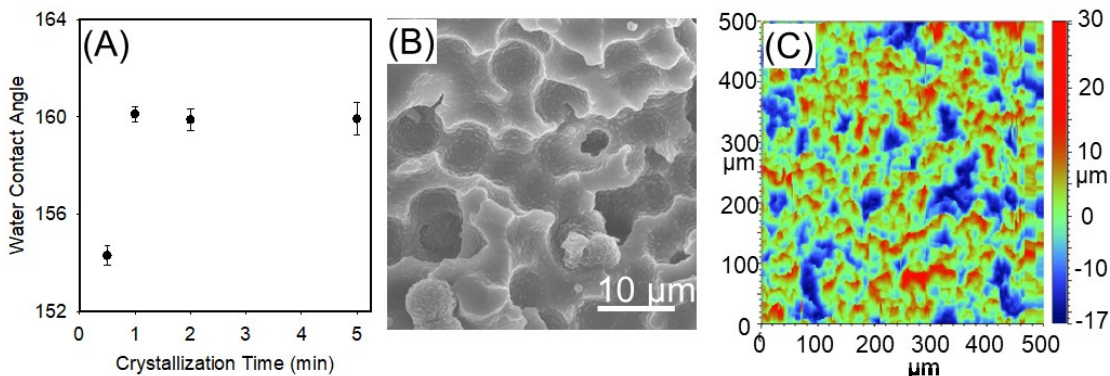


Figure D1. Characterization of PDMS cast from ethyl acetate treated PC template. (A) Water contact angles of PDMS molded from PC treated with ethyl acetate for different times. (B) SEM image of PDMS cast from a PC template treated with ethyl acetate. (C) Profilometry image of the PDMS cast.

As shown in Figure D1C, the profilometry profile shows that the PDMS surface is adorned with spherical impressions and protrusions. The ethyl acetate crystallized samples have much taller and more pronounced protrusions. The R_{pm} (average maximum peak height) of the ethyl acetate sample was $29.4 \mu\text{m}$ and the R_{vm} (average maximum valley depth) was $-16.8 \mu\text{m}$, much higher than the acetone crystallized samples which have an R_{pm} and R_{vm} of $12.0 \mu\text{m}$ and $-7.3 \mu\text{m}$ respectively. The R_a also reflects this; $6.2 \mu\text{m}$ for ethyl acetate compared to $1.8 \mu\text{m}$ for acetone. It is interesting that the water contact angles are very similar to acetone treated PC, nonetheless.

Precautions during demolding of superhydrophobic PDMS

Some precautions must be taken when preparing the PC mold and demolding the PDMS. The PC surface contracts slightly when crystallizing, causing the PC to “bow” if a large enough area is treated. This is problematic when trying to generate large areas with consistent thickness but can be mitigated by treating both sides of the PC template with the solvent.

PC should be fixed to the bottom of the container to prevent the viscous PDMS flowing below the PC and making the resulting cast uneven. Adhesion between the PC and PDMS can be significant during demolding because of the enormous surface area and high degree of conformal contact between them. To reduce the risk of tearing, PDMS must be cut to the edges of the PC template and all edges demolded before removing the entire PDMS. When demolding PDMS that contains h-PDMS, the risk of PDMS breakage increases.

Further understanding of crystallization of PC: morphological development in both micro and nanometer scales

PC is difficult to thermally crystallize because the aromatic rings along the polymer backbone limit its rotation; the melt crystallization of pure PC is extremely slow for which the half-life time is 12 days at 190 °C.²³⁵ When held at this temperature for a prolonged period of time PC is prone to degradation.⁶⁵ In contrast, crystallization of PC when exposed to swelling solvents can occur at room temperature and is rapid, terminating after only 3-4 min.⁹² The crystallization is significantly accelerated because the swelling solvent can penetrate between the polymer chains and increase the free volume of the chains, allowing them to have greater freedom to conform and rearrange.^{65,92} This swelling process is depicted in Figure D2A to C. With more freedom to move, the glass transition temperature of the polymer decreases; once it is below the room temperature the polymer can begin to adopt more energetically favorable arrangements. As shown in Figure D2D polymer begins to fold together and align the polymer into lamellae.^{65,92} From these initial crystalline regions further crystallization is nucleated, and the ordered regions of polymer provide a lower energy site for other polymer chains to begin folding and conforming (Figure D2E). As PC crystallizes, the swelling solvent is ejected into the amorphous matrix surrounding the developing spherulite until the spherulite is mature (Figure D2F). The spherulite growth process begins at the surface; Figure D2K shows that as the solvent

penetrates the polymer, multiple layers of spherulites begin to develop. Ouyang et al. have reported that acetone penetrates the surface at a constant rate; within the first 10 min the crystalline region penetrates 125 μm into the polymer,²⁰² enough for 10-25 layers of spherulites to form. Once the growing spherulites begin to impinge on each other, their growth stops; in PC these spherulites reach between 5 to 10 μm in size.

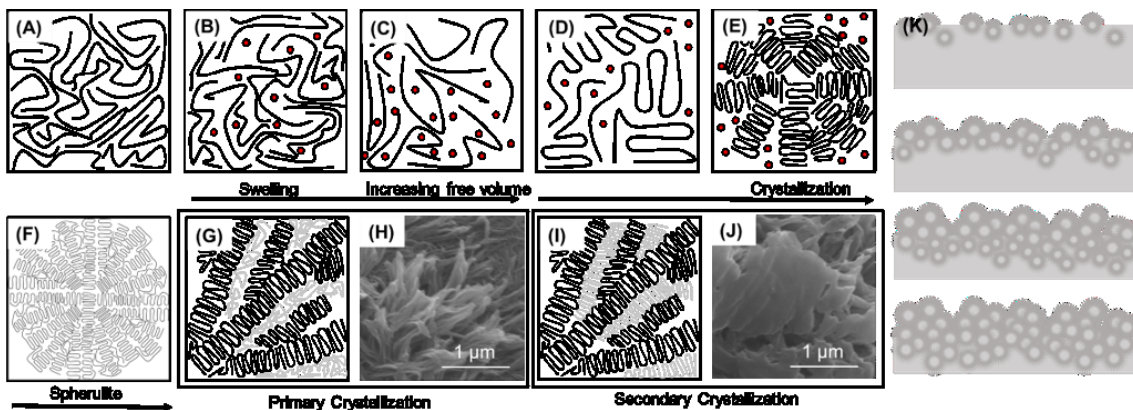


Figure D2. Schematic view of solvent-induced crystallization of PC. Black and grey lines in the diagrams represent polymer chains, red circles represent acetone molecules. (A) Amorphous PC. (B) PC beginning to swell with acetone. (C) PC swollen with acetone. (D) PC beginning to form crystalline domains. (E) Initial spherulite development from crystalline “seed”. (F) A mature spherulite. (G) Tendrils of PC spherulite immediately after formation (in black) surrounded by amorphous PC (in grey). (H) SEM image of tendrils formed by primary crystallization. (I) Secondary crystallization on spherulite tendrils (secondary crystals are shown in grey). (J) SEM image of secondary crystallization on spherulite tendrils. (K) Schematic view of the spherulite development on the polymer surface throughout the solvent-induced crystallization process.

Once spherulites have stopped growing, the primary crystallization process is complete. The schematic in Figure D2G depicts the branching tendrils of crystallized polymer that make up the spherulite. This is confirmed with the SEM image of PC treated with acetone for 2 min then immediately dried with air shown in Figure D2H. When PC is exposed to acetone for additional time, additional crystallization can occur, i.e., amorphous polymer that remains around crystalline regions can crystallize onto the surface of existing lamellae.^{67,91,124,241} New crystalline regions are nucleated by pre-existing lamellae.¹²⁴ Figure D2I depicts the secondary growth of crystalline regions (in grey) between the primary crystals (in black).²⁴¹ The SEM image in Figure D2J shows a spherulite on PC immersed in acetone for 2 min (the acetone on the surface was allowed

to evaporate). Additional polymer has crystallized onto the primary crystals, creating wider and shorter features on the spherulite surface. Secondary crystallization decreases the overall roughness of the spherulites, which can negatively influence the superhydrophobicity of PDMS cast by reducing the overall nanoscale roughness.

Secondary crystallization develops from constrained amorphous polymer surrounding crystallized regions. Being constrained, rearrangement into lamellae is often impossible and chains reorganize through a clustering process and form fringed micellar structures.²⁴¹ Constrained polymer may be in the form of cilia of partially crystallized chains, loose folds, and tie chains.²⁴¹ The initial stages of secondary crystallization are characterized by an Avrami exponent of 1/2, significantly different from the range for primary crystallization (2-4).²⁴¹ Secondary crystallization can be identified by multiple melting behavior associated with the melting of primary, and less perfect secondary crystals.²⁴¹

PC commonly displays two melting peaks, indicating the presence of secondary crystallization.^{108,109,241} In the case of PC, polymer chains near primary crystals (which have limited translational freedom and an abundance of partially incorporated chains) have reduced entropy making the less favored arrangements of polymers (i.e. fringed micelles) possible.^{108,241} When crystallizing conditions were extended the melting peak associated with secondary crystallization moved to higher temperatures indicating further reorganization, in contrast the melting peak of the primary crystals is unchanged as lamellae cannot reorganize.^{108,241}

X-ray Diffraction (XRD) analysis of Amorphous and Crystalline PC

XRD was performed with a Bruker D8 Advance X-ray Diffractometer (Bruker, Billerica, MA) using Cu K α radiation with a wavelength of 1.5406 nm. The instrument was operated at a voltage of 40 kV and a current of 40 mA.

Examination of the XRD patterns (Figure D3) provides insight into the evolution of crystalline regions in PC with varied acetone treatment time. The unmodified sample (red) appears completely amorphous, having a large amorphous halo and no diffraction peaks.⁶⁷ Upon initial exposure to acetone, PC quickly forms spherulites (~120 s) as tendrils of crystalline PC develop from an initial “seed”. The sample treated for 2 min (black) has a small peak, as spherulitic tendrils that rapidly grew have considerable

branching and are quite disordered so that the total crystallinity is low. With extended treatment time the crystalline peak becomes larger and more defined; the PC sample treated by immersion (green) has a much larger peak than other samples, and a small shoulder peak also appears on the right. The larger and sharper diffraction peaks indicate that more polymer chains are crystallizing into lamellae, and that crystals are becoming more “perfect” as the average lamellae size increases via lamellae thickening.^{67,91} This confirms what was observed in the SEM image (Figure D2H); if crystallizing conditions are maintained, such as in the case of immersion, amorphous polymer can slowly rearrange and conform to pre-existing crystallites.⁶⁷

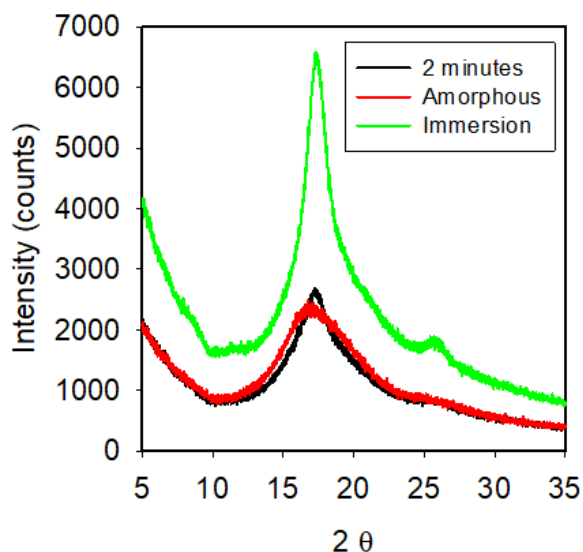


Figure D3. XRD patterns of PC plates before and after solvent treatment. The red curve corresponds to amorphous PC. The black curve shows the PC treated with acetone for 2 min then immersed in water to quench the reaction. The green one corresponds to PC immersed in acetone for 30 min.

Self-cleaning property of superhydrophobic PDMS

Superhydrophobic materials can exhibit self-cleaning properties, especially when the sliding angle of water droplet is low.^{124,220} On these surfaces, water droplets that form on or fall onto the surface will easily roll off. While the droplet is moving on the surface contaminants like dust and particles are picked up by the water droplet and carried off the surface. Figure D4 depicts the self-cleaning properties of our PDMS when covered with particulate contaminants (sand and activated charcoal). In Figure D4A the

superhydrophobic PDMS is “fouled” with sand, water dropped on the surface with a slight tilt (5°) can pick up all the sand in its path and remove it from the surface. By continually dropping water on the surface all the sand can be removed. Figure D4B shows the superhydrophobic PDMS covered with activated charcoal, which is much smaller than sand and more hydrophobic. Water removes much of the charcoal upon dropping on the surface; the charcoal left behind can be removed by a subsequent droplet.

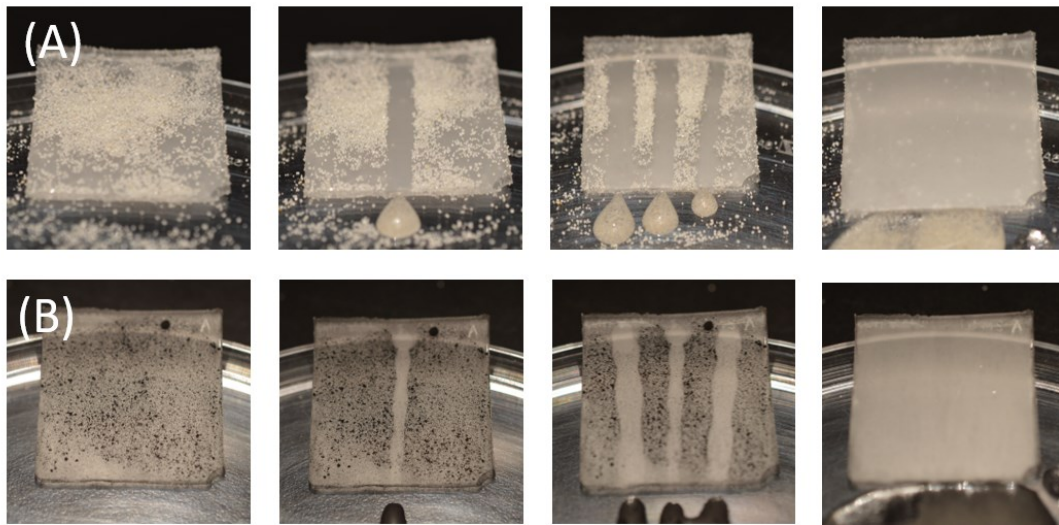


Figure D4. Self-cleaning property of superhydrophobic PDMS. (A) Cleaning of sand from superhydrophobic PDMS using water droplets. (B) Removing of activated charcoal from superhydrophobic PDMS with water droplets.

Chapter 7. Concluding Remarks and Future Directions

7.1. Concluding Remarks

The nanoreplication protocol developed herein is more than just another soft lithography technique. It is an adaptable and convenient method to duplicate structures across several length scales; exact replicas or negatives can be fabricated onto either PC or PDMS, these copies can be used to continue the replication for another step or can be the functional end product. This interchangeability and freedom regarding the process steps and endpoint is the true beauty of this work, with creativity this protocol can be applied a plethora of masters encompassing academic, consumer, and industrial settings. Since this entire procedure can take place on a benchtop, it is uniquely suited resource limited and especially interdisciplinary settings where specialized replication equipment is unavailable.

The closer the optical and conductive phantoms developed herein become to real fingerprints in terms of properties and structure, the more they can be used instead of more costly human testing. The highly detailed nature of our phantoms will provide the required feature density to properly test greater pixel density in future devices and algorithms which detect and match 3rd level fingerprint details. These phantoms will be superior to real fingerprints, which can't be extensively mapped in 3D to sub-micrometer resolutions. Better phantoms are desperately needed considering the simple fabrication of fingerprint spoofs¹³⁴ and masterprints¹² from 2D fingerprint images demonstrated in recent literature. A patent, (U.S. patent application number 16/383393; Nanocontact Molding and Casting: from 3D Fingerprint Phantoms to Designed Nanostructures – Schultz, C. W.; Wong, J. X. H.; Yu, H.-Z), was filed with the support of SFU TLO on June 18, 2020 to facilitate its commercialization.

Replication across length scales from 100 nm to 10 cm is possible via the protocol detailed herein. The method is also versatile, any material compatible with PDMS can be used as a “master” to make 1-to-1 PC replicas. The solvent application is also quite robust, extra solvent applied to the PC is simply pushed away by the stamp, unlike other solvent-assisted methods where the polymer/solvent mixture must be quite precise.²⁰ Since a single PC replica can be used to generate more of itself, replicas can easily be replaced

and shared at very low cost. By making replicas of replicas, production can be scaled up through multiplexing, especially for designing medium to large scale feature arrays, where small distortions and occasional errors are not deleterious (i.e. superhydrophobic surface, diffraction grating, holographic pattern).

Superhydrophobic PDMS cast from crystallized PC in this work had exceptional water contact ($172\pm 1^\circ$) and sliding (1°) angles. The solid-liquid contact area under the droplet was reduced to 1.4%, due to extensive multiscale roughness. It was demonstrably shown to have self cleaning properties and could be patterned to be hydrophilic with UV/ozone. Large-scale PC templates and PDMS casts can easily be generated, only availability of material limits the size of PC that can be treated.

7.2. Future Directions

7.2.1. Development of Universal Phantoms

In this work fingerprint phantoms specialized for either optical or conductive scanners were designed in chapter 3 and chapter 4, respectively. Development of a truly universal fingerprint phantom is the next logical improvement. Not only would a universal phantom be suitable for any type of fingerprint sensor it would also facilitate development of liveness detection, where another property of fingerprints is measured to determine if it is a real finger. Phantoms could be used to hone liveness detection algorithms to one of its fingerprint emulating properties (density, conductivity, optical properties) or challenge algorithms to identify them as a “fake” through properties/features it cannot emulate (temperature, pulse, sub-dermal blood vessels).

Universal phantoms could be developed with higher quality conductive fillers; the conductive additives used in this research were low-cost and mass produced, high ratios required to achieve suitable conductivity prevented inclusion of other additives. Lower percolation thresholds can be achieved with more expensive higher performance additives such as carbon nanotubes, which have percolation thresholds below 5%.^{168,176} At such low concentrations deleterious effects of additives on the mechanical properties are limited, additional dyes and thinner could be included to hone the optical properties and density while maintaining a skin-like elasticity.

So far, development of conductive phantoms has relied on conductive fillers within polymers to attain the desired combination of electrical and mechanical properties. By constructing phantoms from conductive polymers, the deleterious effects of fillers could be eliminated. Polyaniline is a conductive polymer that can be grafted to elastomeric polymers for stretchable electronic applications.²⁴³ If compatible with organic dyes (optical properties) and some form of molding/casting, polyaniline-based phantoms could be constructed from our PC impressions. Hydrogels are another alternative, water is the source of conductivity in finger tissue so hydrogels with a similar water content would be excellent analogs in terms of conductivity. Water soluble dyes could be used to emulate the optical properties of tissue. For example, a durable hydrogel made from polyvinyl alcohol and polyethyleneimine which maintains a stable water content of 60% is a potential phantom material.²⁴⁴

7.2.2. Extended Nanoreplication Applications

With specialized equipment the replication technique developed herein could be further optimized. A thermal press could be used to examine the relationship between pressure and molding fidelity, particularly at high pressures where crystallization behavior may be altered. With an automated molding apparatus, solvent treatment time can be more precisely optimized, especially in the first few seconds where manual control becomes too erroneous. Solvent application method may be optimized as well; simple spraying systems and solvent vapor treatment could be viable pre-treatment methods. Spraying and vapor treatment offer improved control over the amount of acetone applied and are more conducive to curved surfaces and conventional fabrication procedures.

Nanoreplication as an educational tool

This protocol can be an excellent teaching tool for high school and post-secondary students. The entire process from making a cast of the original to molding the PC replica can be conducted in a few hours and can be condensed to minutes if a cast of the master is provided. The wide range of feature sizes that can be replicated (0.5 mm to 100 nm) provides flexibility as to what can be molded. For younger students, immediately gratifying patterns such as a fingerprint, diffraction grating, or superhydrophobic surface can be generated to maintain interest more easily. Older students can replicate smaller structures

that may only be visible with different forms of microscopy or modify other less obvious material properties.

Most importantly, students can conduct the process completely on their own, providing an invaluable hands-on learning experience. Because the materials are rather low-cost and non-toxic, more students can perform the experiment with a limited budget and students can leave with souvenirs, helping to cement the principles learned. Further “hands-on” experience can be achieved through fingerprinting on the PC; students can physically feel the swollen polymer conform to their finger, helping to understand the interface of a molding process. Acetone, as part of nail polish remover, is safe for physical contact, especially at the low volumes needed.¹³⁶

Confined crystallization of solvent-treated PC

One of the challenges in current nanoreplication is that what can be replicated is inherently limited by the master; from a given master only a negative or replica of its morphology can be generated. It is possible to, by modulating polymer crystallization through molding, create many novel surface morphologies and adjust properties with a single master. This concept, which was briefly explored on the diffraction gratings molded in Figure C4, can be expanded upon. Molding of simple optical elements like micro lenses or filters after extended acetone treatment should be explored and would have applications in vehicle headlights which are made primarily from PC. Fabrication of microfluidic channels with tunable hydrophobicity should be explored. 3D PDMS channels cast from such PC replicas would have unique surface morphology, particularly on the PDMS sidewalls, which are traditionally difficult to pattern. Roughness should render sidewalls more hydrophobic, if Cassie-Baxter state superhydrophobicity is achieved friction in channels would be greatly reduced.

Confined crystallization takes the relationship between molding and crystallization one step further. By crystallizing the polymer while molding it with features similar in size to the crystalline structures that would develop from melt, the morphology of crystals can be controlled by the molding template. Researchers working with several polymers such as poly(ethylene oxide),²⁴⁷ poly(butadiene)/poly(caprolactone) block co-polymer,²⁴⁸ and poly(vinylidene fluoride),²⁴⁹ have shown that when a polymer is molded with specifically sized micro and nano features the long range ordering between polymer chains can be disrupted. Increased control over crystallization, either in degree of or crystal orientation,

is valuable for designing plastics with specific properties based on crystallinity or crystallographic orientation such as flexibility, durability, conductance, and optical properties.²⁵⁰ When AAO was used as a template, polymer crystals aligned with the direction of pores, likely driven by nucleation from the AAO side walls.²⁴⁷ Long channels and sine gratings were used as templates, polymer crystals would orient along the direction of the channels or perpendicular depending on the size of channels and polymer.^{248,250}

Application of confined crystallization to solvent-assisted molding of PC has not been studied, confined crystallization is typically applied to thermally molded polymers. Structural materials could be fabricated, taking advantage of crystal orientation to control material properties. For example, crystallization alters the impact resistance and flexibility of PC. To test this PC should be molded with a range of templates such as AAO with controllable defined feature size, the low cost of AAO make it a convenient first mold to test proof of concept. If successful, other masters with features similar in size to crystallites can be applied such as gratings and lithographically fabricated masters.

The bulk of the material can act to limit the effect of confinement on thermal crystallization,²⁵⁰ since solvent induced crystallization may behave differently, thick and thin PC films should be tested. Free standing PC can be purchased as thin as 1 mm, for thinner films PC would need to be dissolved in a compatible solvent (i.e. dichloromethane) and cast onto a substrate such as a glass slide or Si wafer by spin coating. Crystal orientation can be characterized by polarized optical microscopy, IR spectroscopy, and X-ray diffraction analysis.^{250,251} SEM and AFM can be used to observe physical signs of crystal orientation.^{250,251}

Molding other polymer with crystallizing solvents

Our replication protocol is a rather unique nanomolding method because the solvent applied to soften the polymer also crystallizes it, in most cases a good solvent or one that just swells the polymer is applied for solvent-assisted molding. The solvent must be removed quickly after application to prevent significant crystallization, but because solvent does not dissolve the polymer it may be easier to create a moldable interface (just pour the solvent on).

There are likely several polymers or polymer/solvent pairs (i.e. PS/dichloromethane) on which solvent-assisted molding has gone unexplored due to solvent-induced crystallization. The studies and protocols described herein could be applied to these other polymers to discover new nanoreplication materials. Initially, through varied application methods (vapor, spray, immersion, etc.), short solvent treatment times would be explored and the growth of crystallites at the surface tracked. Next, solvent treated polymer would be molded and also analyzed for evidence of crystallization to determine if molding inhibits crystallization and define the optimized treatment time before molding.

7.2.3. Improved and Applied Superhydrophobic Surfaces

Our superhydrophobic PDMS could be significantly improved by exploring the lower size limits for microscale features to improve the optical clarity. Larger microscale features characteristic of our material cause incoming light to scatter, resulting in surfaces that are opaque. Some optically transparent superhydrophobic materials have been developed by minimizing the size of microscale features while still maintaining enough surface roughness for superhydrophobicity.^{45,252} Microscale features in our PDMS are derived from the pores formed when PC crystallizes into spherulites. To reduce the size of pores the crystallization of PC must be adjusted to reduce the overall size of spherulites, rendering the pores between them smaller. Conducting crystallization at reduced temperatures would increase nucleation and decrease growth rate to form more and smaller spherulites. The formulation of PC could also be modified, lower molecular weight PC could more easily reorganize while higher molecular weight PC would be more stable in crystalline morphologies. Both extremes should be explored to expand the possible morphologies that can be developed in the PC template.

Real-world testing of self-cleaning PDMS

Self-cleaning PDMS generated via casting from crystallized PC was tested (Figure D4). Sand and charcoal were tested as hydrophilic and hydrophobic contaminants respectively, and both could be effectively removed. The self-cleaning potential of these surfaces should be more extensively explored; these idealized scenarios do not represent real world contaminants, which are much more complex and variable. Complex contaminants like wine, paint, honey, detritus, and markers should be tested. Dry

contaminants can be deposited from inside water droplets, as a particulate spray, or by direct contact; resistance to all deposition routes should be investigated.²⁵³

Long term testing of the self-cleaning properties of PDMS under outdoor conditions would give insight into the effect of weather on the surface as well as test the resistance to biofouling. Biofouling is particularly problematic as once life gets a foothold it begins to bury hydrophobic surface features with films of hydrophilic biological molecules.²⁵⁴ UV/Ozone treatment of PDMS can oxidize the surface and increase surface energy, rendering the PDMS hydrophilic.^{245,246} Over the long periods of time self-cleaning materials are expected to persist in the environment UV damage could be significant. The stability of superhydrophobic PDMS to UV damage from sunlight should be tested.

Another form of damage to be encountered in the real world is physical damage. Because superhydrophobic surfaces are reliant on their surface structure, any disruption of it is detrimental to hydrophobicity. The most common and well-established test of physical durability are abrasion tests, where an abrasive material (usually sandpaper) is scraped along the surface.²⁵⁵ Since the PDMS is one continuous material it is expected to be resistant to delamination, but this needs to be confirmed.

Fabrication of microfluidic devices through selective oxidation

Briefly explored in Figure 6-8, the surface of superhydrophobic PDMS can be selectively oxidized by UV/Ozone treatment to render it superhydrophilic and capable of wicking; the potential for developing microfluidics and reaction wells should be explored. The resolution of this technique is a pressing question, if sufficiently small it could be a viable alternative to imprinted microfluidic channels. The volume of liquid held in these regions should be determined along with the possibility of loading the treated area with reagent. If reagents could be easily loaded into hydrophilized regions, microfluidics for point-of-care and on-site detection could be designed with reagents stored on the PDMS surface.

Microfluidics incorporating hydrophilic PDMS are held back by the hydrophobic recovery of PDMS. Within the PDMS matrix some uncured polymer chains exist, these along with rearrangement of crosslinked PDMS can restructure to bury the higher energy oxidized surface and replace it with pristine PDMS which has a lower surface energy (increasing the hydrophobicity and inhibiting wicking).^{245,246} Keeping the surface in contact

with water slows the recovery, our oxidized PDMS retained its ability to wick water for 6 months when stored in water. Recovery can also be slowed by soaking the PDMS in good solvents to remove uncured PDMS, but no methods to fully prevent it have been developed.^{245,246} A combination of these methods or a novel technique to stabilize the PDMS would greatly enhance the feasibility of microfluidics designed this way.

Anti-icing surfaces via slippery, liquid-infused porous surface (SLIPS)

While research into superhydrophobic surfaces has seen substantial progress over the past 20 years, developing surfaces which water rolls off at nearly 0°, water continues to pose a challenge at freezing temperatures. Freezing temperatures change how water is deposited onto a surface and how the surface-liquid interface forms. Excess moisture in the air tends to coalesce and deposit onto surfaces as the amount of water vapor it can contain decreases, especially if the surface is colder than the air and cools it further.²⁵⁶ While it can initially be difficult for water to condense and adhere to a superhydrophobic surface, eventually a small enough drop may form and remain in place. Once some water has condensed onto the surface it incites a runaway process of condensation.²⁵⁶ Under normal conditions additional water would form on the droplet and it would roll off once large enough or perturbed, but under freezing conditions this initial water droplet freezes and adheres to the surface.^{256,257} As more water is condenses onto the frozen droplet it too freezes and slowly the contact area between the droplet and surface grows, strengthening adhesion to the surface.²⁵⁶ From these initial points of failure the entire surface can be frozen over.

The situation becomes more dire when a surface is exposed to repeated weathering events. At points of contact roughness features press into the droplet, during freezing the expansion of water pushes water further down the features and compresses them.^{258,259} If the surface features are too rigid or not robust they can be damaged, this process is shown in Figure 7-1A to B, where ice breaks the top of roughness features. This begins a catastrophic cycle wherein water can more easily adhere to the surface and the next droplet will penetrate a little further down (note that the ice has reached deeper roughness features). Once enough roughness is damaged water will fully penetrate surface features and subsequent freezing water will strongly adhere to the surface. Adhesion becomes worse than on a theoretical flat surface because the interface between ice and the surface is larger.²⁵²

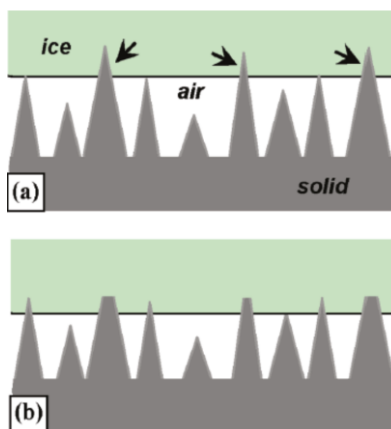


Figure 7-1: (a) Ice on a superhydrophobic anti-icing surface. The asperities with tips indented into the ice (indicated by arrows) are very likely to be damaged during icing (water solidification) and/or deicing (ice removal). (b) Ice on the same surface sitting lower on the asperities during the next icing events. The ice-solid contact area increases from (a) to (b).

Reprinted with permission from Ref. 259. Copyright (2011), American Chemical Society.

Since ice damages the structures responsible for superhydrophobicity, other avenues to water repellency were explored. Even if a rough surface has low surface energy, the small points of contact provide anchor points for freezing, so researchers explored “removing” the surface altogether. This was accomplished by filling porous surfaces with a hydrophobic liquid (oils, uncured polymer) which forms a thin layer. The hydrophobic liquid layer is flat, so the surface does not benefit from the increase in interfacial size, instead the icephobicity is derived from the fluid nature of the liquid. Adhesion is reduced because the droplet has nowhere to “pin” to the surface, and since the liquid layer is mobile the droplet can more easily slide along the surface. These materials are known as “slippery liquid-infused porous surfaces” (SLIPS). PDMS has been shown to be an excellent candidate for SLIPS, by copying a template to produce a porous structure then adding hydrophobic liquid or incorporating the hydrophobic liquid during curing.^{260,261} Roughened PDMS inundated with hydrophobic liquids, such as uncured PDMS or paraffin oil, has also demonstrated reduced ice adhesion.^{260,262}

Our superhydrophobic PDMS could be adapted to create a SLIPS surface following both the strategies successfully applied to create SLIPS. The array of microscale pillars on the PDMS can serve as a reservoir for the hydrophobic liquid. In this configuration the liquid is more susceptible to physical removal but can be easily restored

by adding more hydrophobic liquid.²⁶³ Hydrophobic liquid can also be incorporated during the casting of PC templates to generate a surface with an internal reservoir.²⁶¹

Both these strategies have undergone preliminary testing and showed a decrease in ice adhesion over conventional superhydrophobic PDMS and unmodified PDMS. Further testing should be performed with a specialized ice adhesion measurement system which consists of a force probe that is pressed perpendicularly into ice columns with defined contact areas.²⁶⁴ The durability of the applied hydrophobic liquid layer should be investigated, and the ideal ratio of hydrophobic liquid added during curing should be quantified. Many potential liquids exist which would be compatible with PDMS; silicon oils of varying molecular weight and viscosity should be tested, as should biodegradable naturally derived oils.

Anti-microbial surfaces

Bacterial growth on medical equipment causes infections in modern healthcare. Hospital acquired infections (HAIs) effect over 2 million patents in the United States and leads to 100,000 deaths annually.²⁶⁵ While antibiotics are a powerful tool to combat infections, antibiotic resistant bacteria are becoming more prevalent, i.e. penicillin-resistant *Staphylococcus aureus*.²⁶⁵ Infections are often associated with the formation of biofilms on medical equipment, which exacerbates the problem, as these colonies can be 1000x more resistant to antibiotics.²⁶⁶ It is urgent that we develop strategies to reduce HAIs without the use of antibiotics, to preserve their efficacy. The recent pandemic highlights the tragic effects of HAIs, many of the deaths are due to pneumonia and other opportunistic infections contracted while receiving treatment for COVID-19.

Inhibiting the initial settlement of bacteria onto a surface is critical to preventing the eventual development of a biofilm.²⁶⁵ The extracellular matrix of biomolecules helps more bacteria grow and provides protection.²⁶⁵ Recently superhydrophobic surfaces which significantly reduce bacterial adhesion have been developed.²⁶⁵ Their low surface energy ease protein detachment and inhibit adhesion in the first place.²⁶⁵ The formation of trapped air also reduced contact between the surface and fluids, limiting opportunities for bacterial adhesion. Superhydrophobic anti-microbial surfaces can be constructed from various low surface energy polymers such as PDMS, poly(lactic acid), and poly(vinylidene fluoride).²⁶⁵

Superhydrophobic surfaces typically delay the adhesion of bacteria, but to actively prevent it anti-bacterial additives are incorporated into polymers. Materials with known antibacterial activity such as silver nanoparticles and copper compounds have been applied to enhance anti-bacterial superhydrophobic surfaces.^{265,267} Many antibiotic additives work by disrupting the walls/membranes of bacterial cells, however the cells of a patient can also be affected by additives.^{265,267} Silver nanoparticles and crystals can cause localized inflammation.^{265,267} Reducing or eliminating the need for additives will help make antibacterial materials safer and less intrusive.

Another strategy developed to inhibit biofouling and biofilm formation is through specifically designed surface patterns which reduce bacterial adhesion. When microfeatures on the surface were similar in size or smaller than bacteria, the cells were unable to attach to the tops of these features.^{266,268} If features were larger than bacteria they would form biofilms between and on top of features, with a preference for recessed regions of the pattern.^{247,249} While bacteria still settled between microfeatures, the rate of attachment and overall coverage was reduced.^{266,268} Hydrophobicity further reduced bacterial adhesion in conjunction with micropatterns.²⁶⁸

It could be possible, through a combination of molding and controlled crystallization, to develop antimicrobial PC and PDMS surfaces. Microstructures can be replicated and additional superhydrophobic functionality could be imparted by spherulite formation. Common bacterial strains (*E. coli*, *S. aureus* and *P. aeruginosa*) could be tested against PC and PDMS with 2-20 μm features and varying degrees of spherulite derived nanostructures. Both materials are applied in medical devices, PC as connectors in medical tubing and PDMS is commonly applied as on medical devices for its low surface energy and compatibility with additives as mentioned previously.

References

1. Hicklin, R. A. Anatomy of Friction Ridge Skin. In: Li S.Z., Jain A. (eds) *Encyclopedia of Biometrics*, Springer, Massachusetts, **2009**.
2. Jablonski, N. G. *Skin: A Natural History*; University of California Press, California, **2013**.
3. "Purpose of Fingerprints Is Questioned" (**2009**) (<https://www.livescience.com/3684-purpose-fingerprints-questioned.html>) Retrieved 2019-12-4.
4. Vanderkolk J. R. Examination Process: The Fingerprint Sourcebook U.S. Department of Justice, **2013**.
5. Maltoni, D.; Maio, D.; Jain, A. K.; Prabhakar, S.; Handbook of fingerprint recognition, Springer, London, **2009**, pp. 1–5.
6. Jain, A. K.; Feng, J.; Nandakumar, K.; Fingerprint Matching, *IEEE Computer Society*, **2010**, 36-44.
7. Kanjan, N.; Patil, K.; Ranaware, S.; Sarokte, P.; A Comparative Study of Fingerprint Matching Algorithms *IRJET*, **2017**, 11, 1892-1896.
8. Maltoni, D.; A Tutorial on Fingerprint Recognition *ASB'03 Proceedings of the 1st international conference on Advanced Studies in Biometrics*, **2003**, 43-68.
9. Jain, A. K.; Chen, Y.; Demirkus, M.; Pores and Ridges: Fingerprint Matching Using Level 3 Features *18th International Conference on Pattern Recognition (ICPR'06)*, **2006**, 1-4.
10. "Understanding Biometric Performance Evaluation" (**2014**), (<https://precisebiometrics.com/wp-content/uploads/2014/11/White-Paper-Understanding-Biometric-Performance-Evaluation.pdf>) Retrieved 2020-05-31
11. Espinoza, M.; Champod, C.; Margot, P.; Vulnerabilities of fingerprint reader to fake fingerprints attacks *Forensic Sci. Int*, **2011**, 41-49.
12. Roy, A., Memon, N. & Ross, A. MasterPrint: exploring the vulnerability of partial fingerprint-based authentication systems. *IEEE T. Inf. Foren. Sec.* **2017**, 12, 2013–2025.
13. Majekodunmi, T. O.; Idachaba, F. E.; A Review of the Fingerprint, Speaker Recognition, Face Recognition and Iris Recognition Based Biometric Identification Technologies *Proceedings of the World Congress on Engineering 2011*, **2011**, 2, 1-7.

14. Memon, S.; Sepasian, M.; Balachandran, W.; Review of Fingerprint Sensing Technologies *Proceeding of the 12th IEEE International Multitopic Conference*, **2008**, 23-24.
15. "History of Biometrics" (<https://www.biometricupdate.com/201802/history-of-biometrics-2>) Retrieved 2020-05-31
16. Xia, X.; O'Gorman, L.; Innovations in fingerprint capture devices *Pattern Recognit.*, **2003**, 36, 361-369.
17. Kang, H.; Lee, B.; Kim, H.; Shin, D.; Kim, J.; A study on performance evaluation of fingerprint sensors *Audio- and Video-Based Biometric Person Authentication*, Springer, Berlin, **2003**.
18. Lu, Y.; Teng, H.; Fung, S.; Wang, Q.; Tsia, J. M.; Daneman, M.; Boser, B. E.; Horsley, D. A. Ultrasonic fingerprint sensor using a piezoelectric micromachined ultrasonic transducer array integrated with complementary metal oxide semiconductor electronics. *Appl. Phys. Lett.* **2015**, 106, 1-5.
19. Savoia, A.; Caliano, G.; Iula, A.; Longo, C.; Caronti, A.; Carotenuto, R.; Pappalardo, M.; Design and Fabrication of a cMUT Probe for Ultrasound Imaging of Fingerprints, *IEEE International Ultrasonics Symposium Proceedings*, **2010**, 1877-1880.
20. Gates, B. D.; Xu, Q.; Stewart, M.; Ryan, D.; Wilson, G.; Whitesides, G. M., New Approaches to Nanofabrication: Molding, Printing, and Other Techniques. *Chem. Rev.* **2005**, 105, 1171-1196.
21. Chen, Y., Nanofabrication by electron beam lithography and its applications: A review, *Microelectron. Eng.* **2015**, 135, 57-72.
22. https://blog.phenom-world.com/tungsten-ceb6-electron-source_ Retrieved 2019-05-31
23. Liddle, J. A.; Gallatin, G. M., Nanomanufacturing: A Perspective, *ACS Nano*. **2016**, 10, 2995-3014.
24. Voinigescu, S.; High-Frequency Integrated Circuits. *Cambridge University Press*. **2013**, pp. 164. ISBN 9780521873024.
25. Shilov, A. "Samsung Completes Development of 5nm EUV Process Technology". *AnandTech*. (<https://www.anandtech.com/show/14231/samsung-completes-development-of-5-nm-euv-process-technology>) Retrieved 2020-05-31.
26. Schor, D. "TSMC Starts 5-Nanometer Risk Production". *WikiChip Fuse*. (<https://fuse.wikichip.org/news/2207/tsmc-starts-5-nanometer-risk-production/>) Retrieved 2020-06-07.

27. Xia, Y.; Kim, E.; Zhao, X.-M.; Rogers, J. A.; Prentiss, M.; Whitesides, G. M., Complex Optical Surfaces Formed by Replica Molding Against Elastomeric Masters, *Science*, **1996**, 273, 347-349.
28. Zhao, X.-M.; Xia, Y.; Whitesides, G. M.; Fabrication of three-dimensional microstructures: Microtransfer molding, *Adv. Mater.* **1996**, 8, 837-840.
29. Kim, E.; Xia, Y.; Whitesides, G. M., Polymer microstructures formed by moulding in capillaries, *Nature*, **1995**, 376, 581-584.
30. Kim, E.; Xia, Y.; Zhao, X.-M.; Whitesides, G. M., Solvent-assisted microcontact molding: A convenient method for fabricating three-dimensional structures on surfaces of polymers *Adv. Mater.* **1997**, 9, 651-654.
31. Liang, C. C.; Lin, C.-H.; Cheng T.-C.; Shieh J.; Lin, H.-H. Nanoimprinting of Flexible Polycarbonate Sheets with a Flexible Polymer Mold and Application to Superhydrophobic Surfaces, *Adv. Mater. Interfaces* **2015**, 2, 1500030.
32. Xia, Y.; Whitesides, G. M., Soft Lithography, *Annu. Rev. Mater. Sci.* **1998**, 28, 153-184.
33. Shirtcliffe, N. J.; McHale, G.; Atherton, S.; Newton, M. I., An introduction to superhydrophobicity, *Adv. Colloid Interface Sci.* **2010**, 161, 124-138.
34. Ma, M.; Hill, R. M., Superhydrophobic surfaces, *Curr. Opin. Colloid Interface Sci.* **2006**, 11, 193-202.
35. Schrader, M. E. Young-Dupre Revisited. *Langmuir* **1995**, 11, 3585-3589.
36. Barthlott, W.; Neinhuis, C., Purity of the sacred lotus, or escape from contamination in biological surfaces *Planta*, **1997**, 202, 1-8.
37. Wenzel, R. N., Resistance of Solid Surfaces to Wetting by Water, *Ind. Eng. Chem.* **1936**, 28, 988-994.
38. Wang, S.; Jiang, L., Definition of Superhydrophobic States, *Adv. Mater.* **2007**, 19, 3423-3424.
39. Koch, K.; Bhushan, B.; Jung, Y. C.; Barthlott, W., Fabrication of artificial Lotus leaves and significance of hierarchical structure for superhydrophobicity and low adhesion, *Soft Matter*, **2009**, 5, 1386-1393.
40. Koishia, T.; Yasuokac, K.; Fujikawab, S.; Ebisuzakid, T.; Zeng, X. C., Coexistence and transition between Cassie and Wenzel state on pillared hydrophobic surface, *PNAS*, **2009**, 106, 8435-8440.

41. Nishimotoab, S.; Bhushan, B., Bioinspired self-cleaning surfaces with superhydrophobicity, superoleophobicity, and superhydrophilicity. *RSC Adv.* **2013**, 3, 671-690.
42. Shibuichi, S.; Onda, T.; Satoh, N.; Tsujii, K., Super Water-Repellent Surfaces Resulting from Fractal Structure, *J. Phys. Chem.* **1996**, 100, 19512-19517.
43. Shiu J-Y, Kuo C-W, Chen P. Fabrication of tunable superhydrophobic surfaces. *Proc. SPIE 5648, Smart Materials III*, **2004**, 325–332.
44. Zhang, J. L.; Li, J. A.; Han, Y. C., Superhydrophobic PTFE surfaces by extension. *Macromol. Rapid Commun.* **2004**, 25, 1105-1108.
45. Yabu, H.; Shimomura, M., Single-step fabrication of transparent superhydrophobic porous polymer films. *Chem. Mater.* **2005**, 17, 5231–5234.
46. Xu, L.; Chen, W.; Mulchandani, A.; Yan, Y., Reversible conversion of conducting polymer films from superhydrophobic to superhydrophilic. *Angew. Chem. Int. Ed.* **2005**, 44, 6009-6012.
47. Lau, K. K. S.; Bico, J.; Teo, K. B. K.; Chhowalla, M.; Amaratunga, G. A. J.; Milne, W. I.; Mckinley, G. H.; Gleason, K. K., Superhydrophobic Carbon Nanotube Forests, *Nano Lett.*, **2003**, 3, 1701-1705.
48. Zhang, X.; Shi, F.; Niu, J.; Jiang, Y.; Wang, Z., Superhydrophobic surfaces: from structural control to functional application *J. Mater. Chem.*, **2008**, 18, 621-633.
49. Wu, Y.; Sugimura, H.; Inoue, Y.; Takai, O., Thin Films with Nanotextures for Transparent and Ultra Water-Repellent Coatings Produced from Trimethylmethoxysilane by Microwave Plasma CVD, *Chem. Vap. Deposition*, **2002**, 8, 47-50.
50. Erbil, H. Y.; Demirel, A. L.; Avci, Y.; Mert, O., Transformation of a simple plastic into a superhydrophobic surface, *Science*, **2003**, 299, 1377-1380.
51. Lu, X. Y.; Zhang, C. C.; Han, Y. C., Low-density polyethylene superhydrophobic surface by control of its crystallization behavior. *Macromol. Rapid Commun.* **2004**, 25, 1606-1610.
52. Jiang, L.; Zhao, Y.; Zhai, J., A lotus-leaf-like superhydrophobic surface: a porous microsphere/nanofiber composite film prepared by electrohydrodynamics. *Angew. Chem. Int. Ed.* **2004**, 43, 4338-4341.
53. Cui, Y.; Paxson, A. T.; Smyth, K. M.; Varansi, K. A., Hierarchical polymeric textures via solvent-induced phase transformation: A single-step production of large-area superhydrophobic surfaces. *Colloids Surf. A Physicochem. Eng. Asp.* **2012**, 394, 8-13.

54. Zhao, N.; Weng, L.; Zhang, X.; Xie, Q.; Zhang, X.; Xu J., A Lotus-Leaf-Like Superhydrophobic Surface Prepared by Solvent-Induced Crystallization *ChemPhysChem*, **2006**, 7, 824-827.
55. Zhang, J.; Lu, X.; Huang, W.; Han, Y., Reversible superhydrophobicity to superhydrophilicity transition by extending and unloading an elastic polyamide film. *Macromol. Rapid Commun.* **2005**, 26, 477-80.
56. Li, X.; Chen, G.; Ma, Y.; Feng, L.; Zhao, H.; Jiang, L.; Wang, F., Preparation of a super-hydrophobic poly(vinyl chloride) surface via solvent-nonsolvent coating, *Polymer*, **2006**, 47, 506-509.
57. Feng, L.; Li, S.; Li, H.; Zhai, J.; Song, Y.; Jiang, L.; Zhu, D., Super-Hydrophobic Surface of Aligned Polyacrylonitrile Nanofibers *Angew. Chem. Int. Ed.*, **2002**, 41, 1221-1223.
58. Feng, L.; Song, Y.; Zhai, J.; Liu, B.; Xu, J.; Jiang, L.; Zhu, D., Creation of a Superhydrophobic Surface from an Amphiphilic Polymer *Angew. Chem., Int. Ed.*, **2003**, 42, 800-802.
59. Guo, C.; Feng, L.; Zhai, J.; Wang, G.; Song, Y.; Jiang, L.; Zhu, D., Large-Area Fabrication of a Nanostructure-Induced Hydrophobic Surface from a Hydrophilic Polymer *ChemPhysChem*, **2004**, 5, 750-753.
60. Zhang, E.; Wang, Y.; Lv, T.; Li, L.; Cheng, Z.; Liu, Y., Bio-inspired design of hierarchical PDMS microstructures with tunable adhesive superhydrophobicity† *Nanoscale*, **2015**, 7, 6151-6158.
61. Gao, L.; McCarthy, T. J., Contact Angle Hysteresis Explained *Langmuir* **2006**, 22, 6234-6237.
62. Jin, M.; Feng, X.; Xi, J.; Zhai, J.; Cho, K.; Feng, L.; Jiang, L., Super-Hydrophobic PDMS Surface with Ultra-Low Adhesive Force *Macromol. Rapid Commun.* **2005**, 26, 1805-1809.
63. Yong, J.; Chen, F.; Yang, Q.; Zhang, D.; Bian, H.; Du, G.; Si, J.; Meng, X.; Hou, X., Controllable Adhesive Superhydrophobic Surfaces Based on PDMS Microwell Arrays, *Langmuir* **2013**, 29, 3274-3279.
64. Brydson J. A. *Plastics Materials*, Ch 20 Polycarbonates, *Elsevier*, **1999**.
65. Harron, H. R.; Pritchard, R. G.; Cope, B. C.; Goddard, D. T., An atomic force microscope (AFM) and tapping mode AFM study of the solvent-induced crystallization of polycarbonate thin films, *J. Polym. Sci. B* **1996**, 34, 173-180.
66. Prietschk, A., *Kolloid-Z., Dr. Dietrich Steinkopff Verlag, Darmstadt* **1958**, 156, 1, 8.

67. Fan, Z.; Shu, C.; Yu, Y.; Zaporojtchenko, V.; Faupel, F., Vapor-Induced Crystallization Behavior of Bisphenol-A Polycarbonate *Polym. Eng. Sci.* **2006**, 729-734.
68. V. Dobrescu, V. Cobzaru, Some rheological properties of polycarbonate blends *J. Polym. Sci., Polym. Symp.* **1978**, 64, 27-42.
69. Koo, K. K.; Inoue, T.; Myasaka, K., Toughened plastics consisting of brittle particles and ductile matrix *Polym. Eng. Sci.* **1985**, 27, 741-746.
70. Goldel, A.; Kasaliwal, G.; Potschke, P., Selective Localization and Migration of Multiwalled Carbon Nanotubes in Blends of Polycarbonate and Poly(styrene-acrylonitrile) *Macromol. Rapid Commun.* **2009**, 30, 423-429.
71. Lee, J. N.; Park, C.; Whitesides, G. M., Solvent Compatibility of Poly(dimethylsiloxane)-Based Microfluidic Devices *Anal. Chem.* **2003**, 75, 6544-6554.
72. Mark, J. E. Polymer Data Handbook: Kuo, A. C. M., Poly(dimethylsiloxane), *Oxford University Press*, **1999**.
73. Stafie, N.; Stamatialis, D. F.; Wessling, M., Effect of PDMS cross-linking degree on the permeation performance of PAN/PDMS composite nanofiltration membranes *Sep. Purif. Technol.* **2005**, 45, 220-231.
74. Sturgess, C.; Tuck, C. J.; Ashcroft, I. A.; Wildman, R. D., 3D reactive inkjet printing of polydimethylsiloxane *J. Mater. Chem. C*, **2017**, 5, 9733-9743.
75. Sylgard (R) 184 Silicone elastomer kit (Base), *Dow Corning*, (<https://www.wpiinc.com/media/wysiwyg/pdfs/SDS/sylgard184-base.pdf>) Retrieved 2019-09-13.
76. Sylgard (R) 184 Silicone elastomer kit (Curing agent), *Dow Corning*, (<https://www.wpiinc.com/media/wysiwyg/pdfs/SDS/sylgard184-curing-agent.pdf>) Retrieved 2019-09-13.
77. Lewis, L. N.; Stein, J.; Gao, Y.; Colborn, R. E.; Hutchins, G., Platinum Catalysts Used in the Silicones Industry *Platinum Metals Rev.* **1997**, 41, 66-75.
78. Seethapathy, S.; Górecki, T., Applications of polydimethylsiloxane in analytical chemistry: A review *Anal. Chim. Acta.* **2012**, 750, 48-62.
79. Vojinović, K.; Losehand, U.; Mitzel, N. W., Dichlorosilane–dimethyl ether aggregation: a new motif in halosilane adduct formation *Dalton Trans.*, **2004**, 16, 2578-2581.

80. Johnston, I. D.; McCluskey, D. K.; Tan, C. K. L.; Tracey, M. C., Mechanical characterization of bulk Sylgard 184 for microfluidics and microengineering *J. Micromech. Microeng.* **2014**, 24, 035017.
81. Ng, J. M. K.; Gitlin, I.; Stroock, A. D.; Whitesides, G. M., Components for integrated poly(dimethylsiloxane)microfluidic systems *Electrophoresis* **2002**, 23, 3461-3473.
82. Ros, A.; Hellmich, W.; Duong, T.; Anselmetti, D., Towards single molecule analysis in PDMS microdevices: from the detection of ultra low dye concentrations to single DNA molecule studies *J. Biotechnol.* **2004**, 112, 65-72.
83. Huang, X. Y.; Wang, J. N.; Chen, L.; Ren, J. C., Highly sensitive chemiluminescence detection for PDMS/glass micro-chip electrophoresis *Chin. Chem. Lett.* **2004**, 15, 683-686.
84. Schoening, M. J.; Jacobs, M.; Muck, A.; Knobbe, D.; Wang, J.; Chatrathi, M.; Spillmann, S., Amperometric PDMS/glass capillary electrophoresis-based biosensor microchip for catechol and dopamine detection *Sens. Actuators B.* **2005**, 108, 688-694.
85. Bragg, L.; Qin, Z.; Alaei, M.; Pawliszyn, J., Field sampling with a polydimethylsiloxane thin-film *J. Chromatogr. Sci.* **2006**, 44, 317-323.
86. Eduok, U.; Faye, O.; Szpunar, J., Recent developments and applications of protective silicone coatings: A review of PDMS functional materials *Prog. Org. Coat.* **2017**, 111, 124-163.
87. Wouters, M.; Rentrop, C.; Willemsen, P., Surface structuring and coating performance: Novel biocide-free nanocomposite coatings with anti-fouling and fouling-release properties *Prog. Org. Coat.* **2010**, 68, 4-11.
88. Roppolo, I.; Shahzada N.; Sacco, A.; Tressoa, E.; Sangermano, M., Multifunctional NIR-reflective and self-cleaning UV-cured coating for solar cell applications based on cycloaliphatic epoxy resin *Prog. Org. Coat.* **2014**, 77, 458-462.
89. R.F. Boyer, *Transitions and Relaxations in Polymers*, Wiley, New York, **1967**.
90. Chan, C.-M.; Li, L., Direct Observation of the Growth of Lamellae and Spherulites by AFM, *Adv. Polym. Sci.* **2005**, 188, 1-41.
91. Li, L.; Chan, C.-M.; Yeung, K. L.; Li, J.-X.; Ng, K.-M.; Lei, Y., Direct Observation of Growth of Lamellae and Spherulites of a Semicrystalline Polymer by AFM *Macromolecules* **2001**, 34, 316-325.
92. Turska, E.; Janeczek, H., Liquid-induced crystallization of a bisphenol-A polycarbonate, *Polymer* **1979**, 20, 855-858.

93. Montenegro, R. Crystallization, biomimetics and semiconducting polymers in confined systems. (German Title: Kristallisation, Biomimetik und halbleitende Polymere in räumlich begrenzten Systemen). *Universität Postdam*, **2003**.
94. Toda, A.; Spherulitic Growth in Crystalline Polymers, *Encyclopedia of Polymers and Composites*. **2013**, 1-12.
95. Lei, Y. G.; Chan, C. M.; Li, J. X.; Ng, K. M.; Wang, Y.; Jiang, Y.; Li, L., The Birth of an Embryo and Development of the Founding Lamella of Spherulites As Observed by Atomic Force Microscopy *Macromolecules*, **2002**, 35, 6751-6753.
96. Bassett, D. C.; Vaughan, A. S., On the lamellar morphology of melt-crystallized isotactic polystyrene, *Polymer*, **1985**, 26, 717-725.
97. Bassett, D. C.; Olley, R. H., On the lamellar morphology of isotactic polypropylene spherulites *Polymer*, **1984**, 25, 935-943.
98. Beekmans, L. G. M.; Vancso, G. J., Real-time crystallization study of poly(ϵ -caprolactone) by hot-stage atomic force microscopy *Polymer*, **2000**, 41, 8975-8981.
99. Lei, Y. G.; Chan, C. M.; Wang, Y.; Ng, K. M.; Jiang, Y.; Li, L., Growth process of homogeneously and heterogeneously nucleated spherulites as observed by atomic force microscopy *Polymer* **2003**, 44, 4673-4679.
100. Lauritzen, J. I.; Hoffman, J. D., Theory of formation of polymer crystals with folded chains in dilute solution *J. Res. Natl. Bur. Stand. A Phys. Chem.* **1960**, 64A, 73-102.
101. Flory, P. J. Principles of Polymer Chemistry. *Cornell University Press*, Ithaca, **1953**, 1-672.
102. Lindvig, T.; Michelsen, M. L.; Kontogeorgis, G. M., A Flory–Huggins model based on the Hansen solubility parameters *Fluid Phase Equilibria* **2002**, 203, 247-260.
103. Fredrickson, G. H.; Liu, A. J.; Bates, F. S., Entropic Corrections to the Flory–Huggins Theory of Polymer Blends: Architectural and Conformational Effects *Macromolecules* **1994**, 27, 2503-2511.
104. Icoz, D. Z.; Kokini, J. L., Examination of the validity of the Flory–Huggins solution theory in terms of miscibility in dextran systems, *Carbohydr. Polym.* **2007**, 68, 59-67.
105. Hildebrand, J. H., The Solubility of Non-Electrolytes *Reinhold Pub. Corp.*, New York, **1936**.
106. Barton, A. F. M., (1991). Handbook of Solubility Parameters and Other Cohesion Parameters (2nd ed.). *CRC Press*, Florida, **1991**.

107. Soum, V.; Park, S.; Brilian, A. I.; Kim, Y.; Ryu, M. Y.; Brazell, T.; Burpo, F. J.; Parker, K. K.; Kwon, O.-S.; Shin, K. Inkjet-Printed Carbon Nanotubes for Fabricating a Spoof Fingerprint on Paper, *ACS Omega* **2019**, 4, 8626–8631.
108. Turska, E.; Janeczek, H., Liquid-induced crystallization of a bisphenol-A polycarbonate *Polymer*, **1979**, 20, 855-858.
109. Turska, E.; Benecki, W., Studies of Liquid-Induced Crystallization of Bisphenol A Polycarbonate, *J. Appl. Polym. Sci*, **1979**, 23,3489-3500.
110. Vernon-Parry, K. D., Scanning Electron Microscopy: an *introduction III-Vs Review* **2000**, 13, 40-44.
111. R.F. Egerton, Physical Principles of Electron Microscopy *Springer*, Switzerland **2016**.
112. Reimer, L., Scanning Electron Microscopy: Physics of Image Formation and Microanalysis, *Springer*, Berlin, **1998**.
113. Voigtlander, B., Scanning Probe Microscopy: Atomic Force Microscopy and Scanning Tunneling Microscopy *Springer*, Berlin, **2015**, pp. 1-31.
114. Binnig, G., Rohrer, H., Gerber, Ch., Weibel, E. Surface Studies by Scanning Tunneling Microscopy *Phys. Rev. Lett.* **1982**, 49, 57-61.
115. Binnig, G.; Quate, C. F., Atomic Force Microscope *Phys. Rev. Lett.* **1986**, 56, 930-934.
116. Baykara, M. Z.; Schwarz, U. D. Atomic Force Microscopy: Methods and Applications Encyclopedia of Spectroscopy and Spectrometry, *Elsevier*, **2017**, pp. 70-75.
117. West, P. E., Introduction to Atomic Force Microscopy, Theory Practice Applications *P. West*, **2006**, pp. 68-78.
118. Chung, K.-H., Wear Characteristics of Atomic Force Microscopy Tips: A Review *Int. J. Precis. Eng. Man.* **2014**, 15, 2219-2230.
119. Probes and Cantilevers <https://www.spmtips.com/library-probes-and-cantilevers.lib> (Retrieved 2020-02-27).
120. <https://users.4dlabs.ca/uploads/documents/SOP-AFM.pdf> (Retrieved 2020-02-27).
121. Gillies, G.; Prestidge, C. A.; Attard, P. An AFM Study of the Deformation and Nanorheology of Cross-Linked PDMS Droplets, *Langmuir*, **2002**, 18, 1674-1679.

122. Song, J.; Tranchida, D.; Vancso, G. J., Contact Mechanics of UV/Ozone-Treated PDMS by AFM and JKR Testing: Mechanical Performance from Nano- to Micrometer Length Scales *Macromolecules* **2008**, 41, 6757-6762.
123. Huhtamäki, T.; Tian, X.; Korhonen, J. T.; Ras, R. H. A., Surface-wetting characterization using contact-angle measurements *Nat. Protoc.* **2018**, 13, 1521-1538.
124. Sun, M.; Luo, C.; Xu, L.; Ji, H.; Ouyang, Q.; Yu, D.; Chen, Y., Artificial Lotus Leaf by Nanocasting, *Langmuir*, **2005**, 21, 8978-8981.
125. Pierce, E.; Carmona, F. J.; Amirfazli, A., Understanding of sliding and contact angle results in tilted plate experiments *Colloids Surf. A Physicochem. Eng. Asp.* **2008**, 323, 73–82.
126. Lee, P.; Stewart, D.; Calugar-Pop, C.; Talbot, E.; Mandal, S.; Tarigoppula, A. K., Technology, media and telecommunications predictions, <https://www2.deloitte.com/na/en.html> (Retrieved 2020-02-26).
127. Specifications for Fast Tenprint Capture Devices: National Institute of Standards and Technology, <https://www.nist.gov/sites/default/files/documents/2016/12/07/specifications.pdf> (Retrieved 2018-02-22)
128. Pogue, B. W.; Patterson, M. S. Review of tissue simulating phantoms for optical spectroscopy, imaging and dosimetry, *J. Biomed. Opt.* **2006**, 11, 041102.
129. Greening, G. J.; Istfan, R.; Higgins, L. M.; Balachandran, K.; Roblyer, D.; Pierce, M. C.; Muldoon, T. J., Characterization of thin poly(dimethylsiloxane)-based tissue simulating phantoms with tunable reduced scattering and absorption coefficients at visible and near-infrared wavelengths, *J. Biomed. Opt.* **2014**, 19, 1-14.
130. Wang, T.; Mallidi, S.; Qiu, J.; Ma, L. L.; Paranjape, A. S.; Sun, J.; Kuranov, R. V.; Johnston, K. P.; Milner, T. E., Comparison of pulsed photothermal radiometry, optical coherence tomography and ultrasound for melanoma thickness measurement in PDMS tissue phantoms, *J. Biophoton.* **2011**, 5, 335-344.
131. Matsumoto, T.; Matsumoto, H.; Yamada, K.; Hoshino, S., Impact of artificial “gummy” fingers on fingerprint systems. *Proc. SPIE 4677, Optical Security and Counterfeit Deterrence Techniques IV*, **2002**, 1-15.
132. Engelsma, J. J., Arora, S. S., Jain, A. K., Paulter, N. G. Jr. Universal 3D wearable fingerprint targets: advancing fingerprint reader evaluations, arXiv:1705.07972, **2017**, 1-14.
133. Aharoni, S. M.; Murthy, N. S. Effects of Solvent-induced Crystallization on the Amorphous Phase of Poly(carbonate of bisphenol A). *Intern. J. Polymeric Mater.* **1998**, 42, 275-283.

134. Sabry, R. S.; Al-Mosawi, M. I. Novel approach to fabricate a stable superhydrophobic polycarbonate, *Surface Engineering*, **2018**, 2, 151-157.
135. Identix Corporation White Paper, Minutia vs. pattern based fingerprint templates, http://files.spogel.com/projects/t-000145--Fingerprint_Methods.pdf (Retrieved 2019-02-22).
136. Flowers, L.; Broder, M. W.; Forsyth, C., Toxicological review of acetone, *U.S. Environmental Protection Agency*, Washington, D.C., **2003**.
137. Qin, D.; Xia, Y.; Whitesides, G. M., Soft lithography for micro- and nanoscale patterning, *Nat. Protoc.* **2010**, 5, 491-502.
138. Lima, M. J.; Correlo, V. M.; Reis, R. L., Micro/nano replication and 3D assembling techniques for scaffold fabrication, *Mater. Sci. Eng. C* **2014**, 42, 615-621.
139. Cui, Z.; Nanofabrication principles, capabilities and limits, *Springer*, Switzerland, 2nd Ed.; **2017**, pp. 209-261.
140. Peralta, D.; Galar, M.; Triguero, I.; Paternain, D.; Garcia, S.; Barrenechea, E.; Benitez, J. M.; Bustince, H.; Herrera, F., A Survey on fingerprint minutiae-based local matching for verification and identification: taxonomy and experimental evaluation, *J. Inf. Sci.* **2015**, 315, 67-87.
141. Polski, J.; Smith, R.; Garrett, R., The report of the international association for identification, standardization II committee, *U.S. Department of Justice*, Washington D. C., **2010**, pp. 5-9.
142. Barnes, J. G.; Hutchins, L. A.; Moses, K. R.; Yamashita, B.; French, M., Fingerprint sourcebook, (Eds.: E. H. Holder, L. O. Robinson, J. H. Laub), *U.S. Department of Justice*, Washington D. C., **2010**, pp. 5-15, 96-165.
143. Badal, M. Y.; Wong, M.; Chiem, N.; Salimi-Moosavi, H.; Harrison, D. J., Protein separation and surfactant control of electroosmotic flow in poly(dimethylsiloxane)-coated capillaries and microchips, *J. Chromatogr. A* **2002**, 947, 277-286.
144. Xu, F.; Zhu, Y., Highly conductive and stretchable silver nanowire conductors, *Adv. Mater.* **2012**, 24, 5117-5122.
145. Cong, H.; Pan, T., Photopatternable conductive PDMS materials for microfabrication, *Adv. Funct. Mater.* **2008**, 18, 1912-1921.
146. Singla, N.; Kaur, M.; Sofat, S. Automated latent fingerprint identification system: A review, *Forensic Sci. Intl.* **2020**, 309, 110187.
147. GSM Association, *The Mobile Economy 2020*, GSMA Intelligence, London, UK, **2020**, pp 1-62.

148. Qi, E.; Sharma, P. *Fingerprint Sensors In Smartphones Q2 2019*, Counterpoint: Technology Market Research Inc., Hong Kong, China, **2019**.
149. Jain, A. K.; Chen, Y.; Demirkus, M. Pores and ridges: high resolution fingerprint matching using level 3 features, *IEEE Trans. Pattern Anal. Mach. Intell.* **2007**, *29*, 477–480.
150. Zhang, D.; Lu, G.; Zhang, L. High resolution partial fingerprint alignment. *Advanced Biometrics*, 1st Ed., Springer, London, UK, **2017**, pp. 15–40.
151. Storm, J.-H.; Hoemmen, P.; Hoefner, N.; Korber, R. Detection of body noise with an ultra-sensitive SQUID system, *Meas. Sci. Technol.* **2019**, *30*, 125103.
152. Schultz, C. W.; Wong, J. X. H.; Yu, H.-Z. Fabrication of 3D fingerprint phantoms via unconventional polycarbonate molding, *Sci. Rep.* **2018**, *8*, 9613.
153. Arora, S. S.; Jain, A. K.; Paulter, N. G. Gold fingers: 3D targets for evaluating capacitive readers, *IEEE Trans. Inf. Forensics Secur.* **2017**, *12*, 2067–2077.
154. Arora, S. S.; Jain, A. K.; Paulter, N. G. Design and fabrication of 3D fingerprint targets, *IEEE Trans. Inf. Forensics Secur.* **2016**, *11*, 2284–2297.
155. Peng, C.; Chen, M.; Jiang, X. Under-display ultrasonic fingerprint recognition with finger vessel imaging, *IEEE Sens. J.* **2021**, *21*, 7412–7419.
156. Choi, W. Y.; Kang, K. C.; Park, K. K. Ultrasonic fingerprint sensor in underglass prototype using impedance mismatching, *J. Mech. Sci. Technol.* **2020**, *34*, 531–539.
157. Jian, W.; Zhou, Y.; Liu, H. Densely connected convolutional network optimized by genetic algorithm for fingerprint liveness detection, *IEEE Access* **2021**, *9*, 2229–2243.
158. Sengel, O.; Aydin, M. A.; Sertbas, A. An efficient generation and security analysis of substitution box using fingerprint patterns, *IEEE Access*, **2020**, *8*, 160158–160176.
159. Kurusu, R. S.; Helal, E.; Moghimian, N.; David, E.; Demarquette, N. The role of selectively located commercial graphene nanoplatelets in the electrical properties, morphology, and stability of EVA/LLDPE blends, *Macromol. Mater. Eng.* **2018**, *303*, 1800187.
160. Papageorgiou, D. G.; Kinloch, I. A.; Young, R. J.; Mechanical properties of graphene and graphene-based nanocomposites, *Prog. Mater. Sci.* **2017**, *90*, 75–127.
161. Perreault, F.; Fonseca de Faria, A.; Elimelech, M.; Environmental applications of graphene-based nanomaterials, *Chem. Soc. Rev.*, **2015**, *44*, 5861–5896.

162. Cai, G.; Yu, Z.; Ren, R; Tang, D.; Exciton-plasmon interaction between AuNPs/graphene nanohybrids and CdS quantum dots/TiO₂ for photoelectrochemical aptasensing of prostate-specific antigen, *ACS Sens.* **2018**, *3*, 632–639.
163. Zeng, R.; Luo, Z.; Zhang, L.; Tang, D.; Platinum nanozyme-catalyzed gas generation for pressure-based bioassay using polyaniline nanowires-functionalized graphene oxide framework, *Anal. Chem.* **2018**, *90*, 12299–12306.
164. Shu, J.; Qiu, Z.; Tang, D.; Self-referenced smartphone imaging for visual screening of H₂S using Cu_xO-polypyrrole conductive aerogel doped with graphene oxide framework, *Anal. Chem.* **2018**, *90*, 9691–9694.
165. Azizi, S.; David, E.; Frechette, M. F.; Nguyen-Tri, P.; Ouellet-Plamondon, C. M. Electrical and thermal conductivity of ethylene vinyl acetate composite with graphene and carbon black filler, *Polymer Testing*, **2018**, *72*, 24–31.
166. Champod, C.; Lennard, C. J.; Margot, P.; Stoilovic, M. Friction Ridge Skin and Prints. *Fingerprints and Other Ridge Skin Impressions*, 2nd Ed., Cleavland, OH, CRC Press LLC, **2016**, pp 1-28.
167. Espinoza, M.; Champod, C. Using the number of pores on fingerprint images to detect spoofing attacks, 2011 International Conference on Hand-Based Biometrics, Hong Kong, 2011, pp. 1–5, doi: 10.1109/ICHB.2011.6094347.
168. Filippidou, M. K.; Tegou, E.; Tsouti, V.; Chatzandroulis, S. A flexible strain sensor made of graphene nanoplatelets/polydimethylsiloxane nanocomposite, *Microelectron. Eng.* **2015**, *142*, 7-11.
169. Bonanos, N.; Pissis, P.; Macdonald, J. R. Impedance spectroscopy of dielectrics and electronic conductors. In *Characterization of Materials*, 2nd Ed., Kaufmann E. N. Wiley: New York, **2012**, pp. 1-14.
170. Logakis, E.; Pandis, C.; Peoglos, V.; Pissis, P.; Pointeck, J.; Potschke, P.; Micusik, M.; Omastova, M., Electrical/dielectric properties and conduction mechanism in melt processed polyamide/multi-walled carbon nanotubes composites. *Polymer* **2009**, *50*, 5103–5111.
171. Logakis, E.; Pollatos, E.; Pandis, C.; Peoglos, V.; Zuburtikudis, I.; Delides, C. G.; Vatalis, A.; Gjoka, M.; Syskakis, E.; Viras, K.; and Pissis, P.; Structure-property relationships in isotactic polypropylene/multi-walled carbon nanotubes nanocomposites. *Compos. Sci. Technol.* **2010**, *70*, 328–335.
172. Gabriel, C. Compilation of the dielectric properties of body tissues at RF and microwave frequencies, Occupational and Environmental Health Directorate Radiofrequency Radiation Division, Brooks Air Force Base, TX, **1996**.
173. Hassan, H.; Kin, H.-W. CMOS capacitive fingerprint sensor based on differential sensing circuit with noise cancellation, *Sensors* **2018**, *18*, 2200.

174. Elimat, Z. M. AC-impedance and dielectric properties of hybrid polymer composites, *J. Compos. Mater.* **2015**, *49*, 3–15.
175. Lee, C.; Jug, L.; Meng, E. High strain biocompatible polydimethylsiloxane-based conductive graphene and multiwalled carbon nanotube nanocomposite strain sensors, *Appl. Phys. Lett.* **2013**, *102*, 183511.
176. Nam, J.-M.; Jung, S.-M.; Lee, M.-K. Design and implementation of a capacitive fingerprint sensor circuit in CMOS technology, *Sens. Actuators A.* **2007**, *135*, 283–291.
177. Gusev, V.G.; Demin, A.Y.; Galina, L.M.; Mikhal'chenko, E.S. Study of electrical properties of human skin, *Biomed. Eng.* **2009**, *43*, 124–127.
178. https://www.nanoxplore.ca/wp-content/uploads/2018/11/Nanoxplore-GrapheneBlack-3x-Datasheet_180923.pdf, accessed April 3, 2021.
179. Ferrari, A. C.; Meyer, J. C.; Scardaci, V.; Casiraghi, C.; Lazzeri, M.; Mauri, F.; Piscanec, S.; Jiang, D.; Novoselov, K. S.; Roth, S.; Geim, A. K. Raman spectrum of graphene and graphene layers, *Phys. Rev. Lett.* **2006**, *97*, 187401.
180. Pimenta, M. A.; Dresselhaus, G.; Dresselhaus, M. S.; Cancado, L. G. Studying disorder in graphite-based systems by Raman spectroscopy *Phys. Chem. Chem. Phys.* **2007**, *9*, 1276-1291.
181. Fu, N., Liu, Y., Ma, X., Chen, Z. EUV Lithography: State-of-the-Art Review, *J. Microelectron. Manuf.* **2019**, *2*, 19020202.
182. Jesse, S.; Borisevich, A. Y.; Fowlkes, J. D.; Lupini, A. R.; Rack, P. D.; Unocic, R. R.; Sumpter, B. G.; Kalinin, S. V.; Belianinov A. Directing matter: toward atomic-scale 3D nanofabrication, *ACS Nano*, **2016**, *10*, 5600-5618.
183. Naruse, M.; Tate, N.; Ohtsu, M. Optical security based on near-field processes at the nanoscale *J. Opt.* **2012**, *14*, 094002.
184. Kim, P.; Kwon, K. W.; Park, M. C.; Lee, S. H.; Kim, S. M.; Suh, K. Y. Soft Lithography for Microfluidics: a Review, *Biochip J.* **2008**, *2*, 1-11,
185. Li, X. M.; Reinhoudt, D.; Crego-Calama, M. What do we need for a superhydrophobic surface? A review on the recent progress in the preparation of superhydrophobic surfaces, *Chem. Soc. Rev.*, **2007**, *36*, 1350-1368.
186. Schultz, C. W.; Ng, C. L. W.; Yu, H.-Z. Superhydrophobic Polydimethylsiloxane via Nanocontact Molding of Solvent Crystallized Polycarbonate: Optimized Fabrication, Mechanistic Investigation, and Application Potential *ACS Appl. Mater. Interfaces* **2020**, *12*, 2, 3161–3170.

187. Xia, Y. Whitesides, G. M. Soft Lithography *Annu. Rev. Mater. Sci.* **1998**, 28, 153-84.
188. Kang, S. Micro/Nano Replication: Processes and Applications (Ed: Kang, S.), Wiley, Hoboken, NJ 2012, pp. 1–31.
189. Mills, C.A.; Martinez, E.; Bessueille, F.; Villanueva, G.; Bausells, J.; Samitier, J.; Errachid, A. Production of structures for microfluidics using polymer imprint techniques, *Microelectron. Eng.* **2005**, 78, 695-700.
190. Park, S.; Choi, K.; Kim, G.; Lee, J. Nanoscale patterning with the double-layered soft cylindrical stamps by means of UV-nanoimprint lithography, *Microelectron. Eng.* **2009**, 86, 604-607.
191. Guo, C.; Feng, L.; Zhai, J.; Wang, G.; Song, Y.; Jiang, L.; Zhu, D. Large-area fabrication of a nanostructure-induced hydrophobic surface from a hydrophilic polymer *ChemPhysChem.* **2004**, 5, 750.
192. Sonmez, U. M.; Coyle, S.; Taylor, R. E.; LeDuc, P. R. Polycarbonate Heat Molding for Soft Lithography *Small* **2020**, 16, 2000241.
193. Odom, T. W.; Love, J. C.; Wolfe, D. B.; Paul, K. E.; Whitesides, G. M.; Improved pattern transfer in soft lithography using composite stamps, *Langmuir*, **2002**, 18, 5314-5320.
194. Hua, F.; Sun, Y.; Gaur, A.; Meitl, M. A.; Bilhaut, L.; Rotkina, L.; Wang, J.; Geil, P.; Shim, M.; Rogers, J. A., Polymer imprint lithography with molecular-scale resolution, *Nano Lett.* **2004**, 4, 2467-2471.
195. Khang, D.-Y.; Lee, H. H., Sub-100 nm Patterning with an Amorphous Fluoropolymer Mold, *Langmuir* **2004**, 20, 2445-2448.
196. Ferrell, N.; Hansford, D., Fabrication of micro- and nanoscale polymer structures by soft lithography and spin dewetting, *Macromol. Rapid Commun.* **2007**, 28, 966-971.
197. Wiley, B. J.; Qin, D.; Xia, Y. Nanofabrication at High Throughput and Low Cost *ACS Nano* **2010**, 4, 3554–3559.
198. Lyu, M.-Y.; Choi, T. G. Research Trends in Polymer Materials for Use in Lightweight Vehicles, *Int. J. Pr. Eng. Man.-G.T.* **2015**, 16, 213-220.
199. Schultz, C. W.; Wong, J. X. H.; Yu, H.-Z. Plastic fingerprint replica: solvent-assisted 3D molding and motion-promoted nano-spherulite formation *Can. J. Chem.* **2018**, 96, 431.
200. Montelius, L.; Tegenfeldt, J. O. Direct observation of the tip shape in scanning probe microscopy, *Appl. Phys. Lett.* **1993**, 62 (21), 2628-2630.

201. Ouyang, H.; Wu, M.-T. The study of mass transport of acetone in polycarbonate, *J. Appl. Phys.* **2004**, 96, 7066-7070.
202. Kinlock, A. J. Adhesion and Adhesives: Science and Technology', *Chapman & Hall*, London, **1987**, pp. 1-17.
203. Lee, M. J.; Lee, N. Y.; Lim, J. R.; Kim, J. B.; Kim, M.; Baik, H. K.; Kim, Y. S. Antiadhesion Surface Treatments of Molds for High - Resolution Unconventional Lithography, *Adv. Mater.* **2006**, 18, 3115-3119.
204. Gu, Z.-Z.; Uetsuka, H.; Takahashi, K.; Nakajima, R.; Onishi, H.; Fujishima, A.; Sato, O. Structural Color and the Lotus Effect *Angew. Chem. Int. Ed.* **2003**, 42, 894-898.
205. Luo, X. Subwavelength Artificial Structures: Opening a New Era for Engineering Optics *Adv. Mater.* **2019**, 31, 1804680 (1-12).
206. Whitepaper: Nano-Optic Technology, <https://www.nanosecurity.ca/wp-content/uploads/2020/05/Nanotech-Nano-Optic-Display-Technology.pdf>, (Retrieved 23-11-2020).
207. Shih, T.-K.; Chen, C.-F.; Ho, J.-R.; Chuang, F.-T. Fabrication of PDMS (polydimethylsiloxane) microlens and diffuser using replica molding, *Microelectron Eng.* **2006**, 83, 2499-2503.
208. Bixler, G. D.; Theiss, A.; Bhushan, B.; Lee, S. C. Anti-fouling properties of microstructured surfaces bio-inspired by rice leaves and butterfly wings, *J. Colloid Inter. Sci.* **2014**, 419, 114-133.
209. Freschauf, L. R.; McLane, J.; Sharma, H.; Khine, M. Shrink-Induced Superhydrophobic and Antibacterial Surfaces in Consumer Plastics, *PLOS One*, **2012**, 7, 1-7.
210. Kauser, A. A review of filled and pristine polycarbonate blends and their applications, *J. Plast. Film Sheet.* **2018**, 34, 60-97.
211. Dou, M.; Sanjay, S. T.; Dominguez, D. C.; Lui, P.; Xu, F.; Li, X. Multiplexed instrument-free meningitis diagnosis on a polymer/paper hybrid microfluidic biochip, *Biosens. Bioelectron.* **2017**, 87, 865-873.
212. Dou, M.; Macias, N.; Shen, F.; Bard, J. D.; Dominguez, D. C.; Li, X. Rapid and Accurate Diagnosis of the Respiratory Disease Pertussis on a Point-of-Care Biochip, *EClinicalMedicine* **2019**, 8, 72-77.
213. Dou, M.; Sanchez, J.; Tavakoli, H.; Gonzalez, J. E.; Sun, J.; Bard, J. D.; Li, X. A low-cost microfluidic platform for rapid and instrument-free detection of whooping cough, *Anal Chim Acta* **2019**, 1065, 71-78.

214. Zhou, J.; Ellis, A. V.; Voelcker, N. H. Recent developments in PDMS surface modification for microfluidic devices, *Electrophoresis* **2010**, 31, 2–16.
215. Raj M, K.; Chakraborty, S. PDMS microfluidics: A mini review *J. Appl. Polym. Sci.* **2020**, 48958(1-14).
216. Fraper, M. C.; Crick, C. R.; Orlickaite, V.; Turek, V. A.; Parkin, I. P.; Edel, J. B. Superhydrophobic surfaces as an on-chip microfluidic toolkit for total droplet control, *Anal. Chem.* **2013**, 85, 5405–5410.
217. Liu, C. Rapid fabrication of microfluidic chip with three-dimensional structures using natural lotus leaf template, *Microfluid. Nanofluid.* **2010**, 9, 923–931.
218. Xing, S.; Harake, R. S.; Pan, T. Droplet-driven transports on superhydrophobic-patterned surface microfluidics, *Lab Chip* **2011**, 11, 3642–3648.
219. Cortese, B.; D'Amone, S.; Manca, M.; Viola, I.; Cingolani, R.; Gigli, G., Superhydrophobicity Due to the Hierarchical Scale Roughness of PDMS Surfaces *Langmuir* **2008**, 24, 2712-2718.
220. Lui, H.; Huang, J.; Chen, Z.; Chen, G.; Zhang, K.-Q.; Al-Deyab, S. S.; Lai, Y. Robust translucent superhydrophobic PDMS/PMMA film by facile one-step spray for self-cleaning and efficient emulsion separation, *Chem. Eng. J.* **2017**, 330, 26–35.
221. Li, J.; Zhao, Y.; Hu, J.; Shu, L.; Shi, X. Anti-icing Performance of a Superhydrophobic PDMS/Modified Nano-silica Hybrid Coating for Insulators, *J. Adhes. Sci. Technol.* **2012**, 26, 665-679.
222. Darband, B.; Aliofkhaezrai, M.; Khorsand, S.; Sokhanvar, S.; Kaboli, A. Science and engineering of superhydrophobic surfaces: review of corrosion resistance, chemical and mechanical stability, *Arab. J. Chem.* **2018**, 13, 1763-1802
223. Chen, H.; Song, W.; Zhou, F.; Wu, Z.; Huang, H.; Zhang, J. The effect of surface microtopography of poly(dimethylsiloxane) on protein adsorption, platelet and cell adhesion, *Colloids Surf. B* **2009**, 71, 278-281.
224. Owen, M. J. Physical Properties of Polymers Handbook, J.E. Mark, ed., *AIP Press*, Woodbury, NY, **1996**, p. 669.
225. Khorasani, M. T.; Mirzadeh, H.; Sammes, P. G. Laser induced surface modification of polydimethylsiloxane as a super-hydrophobic material, *Radiat. Phys. Chem.* **1996**, 47, 881–888.
226. Yong, J.; Chen, F.; Yang, Q.; Zhang, D.; Du, G.; Si, J.; Yun, F.; Hou, X. Femtosecond Laser Weaving Superhydrophobic Patterned PDMS Surfaces with Tunable Adhesion, *J. Phys. Chem. C.*, **2013**, 117, 24907-24912.

227. Yong, J.; Chen, F.; Yang, Q.; Zhang, D.; Du, G.; Bian, H.; Si, J.; Yun, F.; Hou, X. Superhydrophobic PDMS surfaces with three-dimensional (3D) pattern-dependent controllable adhesion, *Appl. Surf. Sci.* **2014**, 288, 579–583.
228. Zhao, N.; Xie, Q.; Weng, L.; Wang, S.; Zhang, X.; Xu, J. Superhydrophobic surface from vapor-induced phase separation of copolymer micellar solution, *Macromolecules* **2005**, 38, 8996–8999.
229. Wang, B.-B.; Feng, J.-T.; Zhao, Y.-P.; Yu, T.-X. Fabrication of novel superhydrophobic surfaces and water droplet bouncing behavior — Part 1: Stable ZnO–PDMS superhydrophobic surface with low hysteresis constructed using ZnO nanoparticles, *J. Adhes. Sci. and Technol.* **2010**, 24, 2693–2705.
230. Liu, X.; Xu, Y.; Ben, K.; Chen, Z.; Wang, Y.; Guan, Z. Transparent, durable and thermally stable PDMS-derived superhydrophobic surfaces, *Appl. Surf. Sci.* **2014**, 339, 94–101.
231. He, B.; Lee, J.; Patanker, N. A. Contact angle hysteresis of rough hydrophobic surfaces, *Coll. Surf. A* **2004**, 248, 101–104.
232. Yilbas, B. S.; Ali, H.; Al-Aquuli, N.; Khaled, M.; Abu-Dheir, N.; Varanasi, K. K. Solvent-induced crystallization of a polycarbonate surface and texture copying by polydimethylsiloxane for improve surface hydrophobicity. *J. Appl. Polym. Sci.* **2016**, 133, 43467(1–12).
233. U.S. Environmental Protection Agency. Integrated Risk Information System (IRIS) on Toluene. *National Center for Environmental Assessment*, Office of Research and Development, Washington, D. C. **2005**.
234. U.S. Environmental Protection Agency. Integrated Risk Information System (IRIS) on n-Hexane. *National Center for Environmental Assessment*, Office of Research and Development, Washington, D. C. **1999**.
235. Sundararajan, P. R.; Singh, S.; Moniruzzaman, M. Surfactant-induced crystallization of polycarbonate, *Macromolecules* **2004**, 37, 10208–10211.
236. Gelest®hPDMS 2-Part High Modulus Reprographic Silicone Elastomer (1:1 kit), Gelest Inc. (<https://www.gelest.com/themencode-pdf-viewer/?file=https://www.gelest.com:443/wp-content/uploads/PP2-RG07-Gelest%C2%AE-hPDMS-TDS.pdf>) Retrieved 2019-09-13.
237. Zhou, W.; Zhang, J.; Li, X.; Lui, Y.; Min, G.; Song, Z.; Zhang, J. Replication of mold for UV-nanoimprint lithography using AAO membrane, *Appl. Surf. Sci.* **2009**, 255, 8019–8022.
238. Hamouda, F.; Sahaf, H.; Held, S.; Barbillion, G.; Gogol, P.; Moyen, E.; Aassime, A.; Moreau, J.; Canva, M.; Louritoz, J.-M.; Hanbucken, M.; Bartenlian, B. Large area nanopatterning by combined anodic aluminum oxide and soft UV-NIL technologies for application in biology, *Microelectron. Eng.* **2011**, 88, 2444–2446.

239. Wenzel, R. N. Resistance of solid surfaces to wetting by water, *Ind. Eng. Chem. Res.* **1936**, 28, 988–994.
240. Boscher, N. D.; Vache, V.; Carminati, P.; Grysen, P.; Choquet, P. A simple and scalable approach towards the preparation of superhydrophobic surfaces- importance of the surface roughness skewness, *J. Mater. Chem. A* **2014**, 2, 5744–5750.
241. Sohn, S.; Alizadeh, A.; Marand, H. On the multiple melting behavior of bisphenol-A polycarbonate, *Polymer* **2000**, 41, 8879–8886.
242. Tropmann, A.; Tanguy, L.; Koltay, P.; Zengerle, R.; Riegger, L. Completely superhydrophobic PDMS surfaces for microfluidics, *Langmuir* **2012**, 28, 8292–8295.
243. Stoyanov, H.; Kollosche, M.; Risse, S.; Wache, R.; Kofod, G. Soft Conductive Elastomer Materials for Stretchable Electronics and Voltage Controlled Artificial Muscles *Adv. Mater.* **2013**, 25, 578-583.
244. Wang, C.; Hu, K.; Zhao, C.; Zou, Y.; Liu, Y.; Qu, X.; Jiang, D.; Li, Z.; Zhang, M.-R. Li, Z. Customization of Conductive Elastomer Based on PVA/PEI for Stretchable Sensors *Small* **2020**, 16, 1904758 (1-9).
245. Hillborg, H.; Tomczak, N.; Olah, A.; Schonherr, H.; Vancso, G. J., Nanoscale Hydrophobic Recovery: A Chemical Force Microscopy Study of UV/Ozone-Treated Cross-Linked Poly(dimethylsiloxane) *Langmuir* **2004**, 20, 785-794.
246. Ma, K.; Rivera, J.; Hirasaki, G. J.; Biswal, S. L., Wettability control and patterning of PDMS using UV–ozone and water immersion, *J. Colloid Interface Sci*, **2011**, 363, 371-378.
247. Maiz, J.; Martin, J.; Mijangos, C., Confinement Effects on the Crystallization of Poly(ethylene oxide) Nanotubes *Langmuir* **2012**, 28, 12296-12303.
248. Zhang, P.; Huang, H.; He, T.; Hu, Z., Long-Range Ordered Crystallization Structure in the Micromolded Diblock Copolymer Thin Film *ACS Macro Lett.* **2012**, 1, 1007-1011.
249. Hu, Z.; Baralia, G.; Bayot, V.; Gohy, J.-F.; Jonas, A. M., Nanoscale Control of Polymer Crystallization by Nanoimprint Lithography. *Nano Lett.* **2005**, 5, 1738-1743.
250. Hu, Z.; Jonas, A. M., Control of crystal orientation in soft nanostructures by nanoimprint lithography *Soft Matt.* **2010**, 6, 21-28.
251. Gupper, A.; Kazarian, S. G. Study of Solvent Diffusion and Solvent-Induced Crystallization in Syndiotactic Polystyrene Using FT-IR Spectroscopy and Imaging *Macromol.* **2005**, 38, 2327-2332

252. Deng, X.; Mammen, L.; Butt, H.-J.; Vollmer, D., Candle Soot as a Template for a Transparent Robust Superamphiphobic Coating *Science*, **2012**, 335, 67-70.
253. Maghsoudi, K.; Momen, G.; Jafari, R.; Farzaneh, M. Rigorous testing to assess the self-cleaning properties of an ultra-water-repellent silicone rubber surface *Surf. Coat. Technol.* **2019**, 374, 557-568.
254. Chen, H.; Song, W.; Zhou, F.; Wu, Z.; Huang, H.; Zhang, J.; Lin, Q.; Yang, B., The effect of surface microtopography of poly(dimethylsiloxane) on protein adsorption, platelet and cell adhesion *Colloid Surface B*, **2009**, 71, 275-281.
255. Zhu, X.; Zhang, Z.; Men, X.; Yang, J.; Wang, K.; Xu, X.; Zhou, X.; Xue, Q. Robust superhydrophobic surfaces with mechanical durability and easy repairability *J. Mater. Chem.* **2011**, 21, 15793-15797.
256. Subramanyan, S. B.; Kondrashov, V.; Ruhe, J.; Varansi, K. K., Low Ice Adhesion on Nano-Textured Superhydrophobic Surfaces under Supersaturated Conditions *ACS Appl. Mater. Inter.* **2016**, 8, 12583-12587.
257. Kim, P.; Wong, T.-S.; Alvarenga, J.; Kreder, M. J.; Adrorno-Martinez, W. E.; Aizenberg, J., Liquid-Infused Nanostructured Surfaces with Extreme Anti-Ice and Anti-Frost Performance, *ACS Nano*, **2012**, 6, 6569-6577.
258. Bahadur, V.; Mishchenko, L.; Hatton, B.; Taylor, J. A.; Aizenberg, J.; Krupenkin, T., Predictive Model for Ice Formation on Superhydrophobic Surfaces *Langmuir*, **2011**, 27, 14143-14150.
259. Kulinich, S. A.; Farhadi, S.; Nose, K.; Du, X. W., Superhydrophobic Surfaces: Are They Really Ice-Repellent? *Langmuir*, **2011**, 27(1), 25-29.
260. Zhuo, Y.; Wang, F.; Xiao, S.; He, J.; Zhang, Z., One-Step Fabrication of Bioinspired Lubricant-Regenerable Icephobic Slippery Liquid-Infused Porous Surfaces *ACS Omega* **2018**, 3, 10139-10144.
261. Yeong, Y. H.; Wang, C.; Wynne, K. J.; Gupta, M. C., Oil-Infused Superhydrophobic Silicone Material for Low Ice Adhesion with Long-Term Infusion Stability *ACS Appl. Mater. Inter.* **2016**, 8, 32050-32059.
262. Coady, M. J.; Wood, M.; Wallace, G.Q.; Nielsen, K. E.; Kietzig, A.-M.; Lagugné-Labarthe, F.; Ragogna, P. J., Icephobic Behavior of UV-Cured Polymer Networks Incorporated into Slippery Lubricant-Infused Porous Surfaces: Improving SLIPS Durability *ACS Appl. Mater. Inter.* **2018**, 10, 2890-2896.
263. Wong, T.-S.; Kang, S.-H.; Tang, S. K. Y.; Smythe, E. J.; Hatton, B. D.; Grinthal, A.; Aizenberg, J., Bioinspired self-repairing slippery surfaces with pressure-stable omniphobicity *Nature*, **2011**, 477, 443-447.

264. Wang, C.; Zhang, W.; Siva, A.; Tiew, D.; Wynne, K. J. Laboratory Test for Ice Adhesion Strength Using Commercial Instrumentation *Langmuir*, **2014**, 30, 540–547
265. Eduoka, U.; Szpunara, J.; Ebenso, E., Superhydrophobic antibacterial polymer coatings *Superhydrophobic Polymer Coatings* **2019**, 1, 245-279.
266. Hou, S.; Gu, H.; Smith, C.; Ren, D., Microtopographic Patterns Affect Escherichia coli Biofilm Formation on Poly(dimethylsiloxane) Surfaces *Langmuir* **2011**, 27, 2686-2691.
267. Kottmann, A.; Mejía, E.; Hémerly, T.; Klein, J.; Kragl, U., Recent Developments in the Preparation of Silicones with Antimicrobial Properties *Chem. Asian J.* **2017**, 12, 1168-1179.
268. Lu, N.; Zhang, W.; Weng, Y.; Chen, X.; Cheng, Y.; Zhou, P., Fabrication of PDMS surfaces with micro patterns and the effect of pattern sizes on bacteria adhesion *Food Control* **2016**, 68, 344-351.